Optical properties of hybrid plasmonic thin films with a controlled chiral superstructure

Wenbing Wu

UNIVERSITÉ DE STRASBOURG

ÉCOLE DOCTORALE de Physique et de Chimie-Physique

Institut Charles Sadron – UPR22 – CNRS

THÈSE présentée par :

Wenbing WU

soutenue le : **11 Décembre 2020**

pour obtenir le grade de : **Docteur de l'université de Strasbourg**

Discipline/ Spécialité : Chimie-Physique

Propriétés optiques de films minces plasmoniques hybrides à superstructure chirale contrôlée

THÈSE dirigée par :

M. DECHER Gero	Professeur, Université de Strasbourg

RAPPORTEURS :

Mme TREGUER-DELAPIERRE Mona	Professeur, Université de Bordeaux
M. VERBIEST Thierry	Professeur, Katholieke Universiteit Leuven

AUTRES MEMBRES DU JURY :

M. BATTIE Yann	Professeur, Université de Lorraine
M. GENET Cyriaque	Directeur de recherche, Université de Strasbourg
M. PAULY Matthias	Maître de conférences, Université de Strasbourg

Acknowledgements

This work was carried out at the Institut Charles Sadron (ICS) in Strasbourg.

First, I would like to express my sincere gratitude to my supervisor Professor Gero Decher, for allowing me to join his team and work three years under the best conditions. I thank him for his support and guidance during my doctoral studies and research. I gained a good deal of enlightenment in science from his advice and remarks.

I would like to express my gratitude to Matthias Pauly for his constructive supervision and guidance. I thank him for the regular help that he has continuously provided to me. His insight in science ensured the progress of this work. I am grateful for his support for all the difficulties and challenges that we have met and I salute in particular his benevolence and enthusiasm in life.

I would like to express my gratitude to the jury members of my thesis for spending their time reviewing this dissertation.

I would like to express my gratitude to Yann Battie for all the measurements and simulations that he has done for us. His work makes an important part of this dissertation. I salute his expertise in the field and his high efficiency in the collaboration. I am particularly grateful for his quick replies to my questions.

I would like to thank Cyriaque Genet for the discussions that we had and our collaboration that has already shown promising results and that is going to be an extraordinary project.

I would like to thank the members of our group, Olivier Félix, David Martel, Michel Tschopp, Vincent Lemaire, Jean Muller and Randy Mujica for their suggestions in science and help in life. I thank the master intern Emre Yesil for his contribution to this work.

I would like to thank Alain Carvalho and Marc Schmutz for the SEM training and their help in microscopy. I thank François Schosseler for the training in fluorescence spectroscopy. I thank Christophe Contal for the AFM images.

Last but not least, I thank my family for their unconditional support of all times.

List of abbreviation

AFM	Atomic force microscopy
AgNWs	Silver nanowires
AgM	Silver mirror
AuNPs	Gold nanopaticles
CB	Circular birefringence
CD	Circular dichroism
GIS	Grazing incidence spraying
LbL	Layer-by-Layer
LB	Linear birefringence
LD	Linear dichroism
LSPR	Localized surface plasmon resonance
MMP	Mueller matrix polarimetry
PAH	Poly(allylamine hydrochloride)
PDDA	Poly(diallydimethylammonium) chloride
PEI	Poly(ethylene imine)
PEM	Polyelectrolyte multilayer
PMMA	Poly(methyl methacrylate)
PSS	Poly(sodium 4-styrene sulfonate)
SEM	Scanning electron microscopy
SPP	Surface plasmon polariton
TDBC	5,6-Dichloro-2-[[5,6-dichloro-1-ethyl-3-(4-sulfobutyl)-benzimidazol-2-ylidene]-propenyl]-1-ethyl-3-(4-sulfobutyl)-benzimidazolium hydroxide, inner salt, sodium salt

Propriétés optiques de films minces plasmoniques hybrides à superstructure chirale contrôlée

I . Contexte

La chiralité décrit la propriété géométrique d'un objet qui n'est pas superposable à son image miroir dans un plan. Cette propriété, avant qu'elle ne soit nommée chiralité par Lord Kelvin en 1893, a été mise en évidence au niveau moléculaire via les propriétés optiques qui lui sont associées pour la première fois en 1848 par Louis Pasteur lorsqu'il étudia les 2 énantiomères d'un sel d'acide tartrique. La chiralité peut se retrouver à toutes les échelles, du niveau moléculaire aux galaxies de forme spirale. Considérant son importance primordiale dans les processus naturels, en particulier dans le domaine de la biochimie, la chiralité demeure un sujet de recherche essentiel dans les domaines de la chimie, de la biologie et des matériaux depuis sa découverte.

En particulier, accompagnant le développement des nanosciences et des nanotechnologies, la fabrication de structures artificielles chirales à l'échelle nanométrique a suscité de grands intérêts de recherche partout dans le monde. En particulier, les nanostructures chirales à base de nano-objets plasmoniques telles que les nanoparticules métalliques (or, argent, cuivre) représentent actuellement une direction majeure de recherche, motivée par les propriétés chiro-optiques plus fortes que dans les systèmes moléculaires et leur intégration possible dans de futurs dispositifs optiques et métamatériaux. Ces structures peuvent être fabriquées par différentes techniques *top-down* ou *bottom-up*, le grand défi dans ce dernier cas résidant dans l'organisation hiérarchique des briques élémentaires (nano-objets plasmoniques) à l'échelle nanométrique d'une manière reproductible, contrôlée et/ou sur une grande surface. Les propriétés optiques étant intimement liées à la géométrie de l'assemblage, il est fondamental de

pouvoir contrôler finement les paramètres structuraux et d'analyser le lien entre la structure et les propriétés optiques.

L'objectif de cette thèse est ainsi d'étudier un ensemble de nanostructures plasmoniques chirales composées de nanofils d'argent (AgNWs, *Ag Nanowires*) assemblés en structure hélicoïdale en combinant la pulvérisation à incidence rasante (GIS, *Grazing Incidence Spraying*) et l'assemblage couche-par-couche (LbL, *Layer-by-Layer*). Cette approche permet la fabrication reproductible d'échantillons de structure contrôlée précisément à l'échelle nanométrique sur une grande surface (~ cm^2), conduisant à un très fort dichroïsme circulaire qui peut être modulé dans le domaine UV, visible et proche-IR. De plus, il est possible d'inclure dans la nanostructure un colorant moléculaire à une position bien déterminée et donc d'étudier la modification des propriétés optiques d'une molécule achirale dans un environnement plasmonique chiral.

I I . Superstructures plasmoniques chirales

La pulvérisation à incidence rasante (GIS) (***Figure 1A***) consiste en la pulvérisation à un angle faible (10°−15°) d'une solution d'AgNWs fonctionnalisés par un polyanion sur un substrat recouvert d'un polycation. La buse est alimentée par un fluide et une arrivée d'air, dont les débits sont précisément régulés. Lors du dépôt, la suspension de nanofils d'argent est pulvérisée sur le substrat, créant un film mince de liquide s'écoulant dans la direction de la pulvérisation, induisant l'orientation des nanofils par la force de cisaillement du liquide en mouvement durant

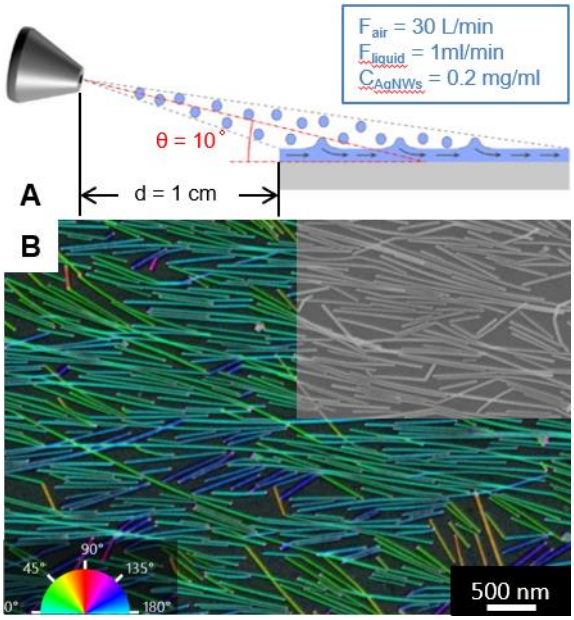

Figure 1. (A) Représentation schématique du GIS et (B) image MEB d'une monocouche orientée d'AgNWs. Les AgNWs sont colorés en fonction de leur

leur adsorbtion sur le substrat par des interactions électrostatiques (***Figure 1B***).

Les nanofils ayant deux modes de résonance des plasmons de surface localisée (LSPR), le mode longitudinal et le mode transverse, les films d'AgNWs obtenus ont des propriétés optiques fortement anisotropes. Le spectre d'extinction d'un film d'AgNWs alignés présente donc un double pic dans la gamme UV-Vis correspondant aux modes transverses de la LSPR des AgNWs et une large bande d'extinction entre 500 nm et 2000 nm correspondant aux modes longitudinaux de la LSPR des AgNWs.

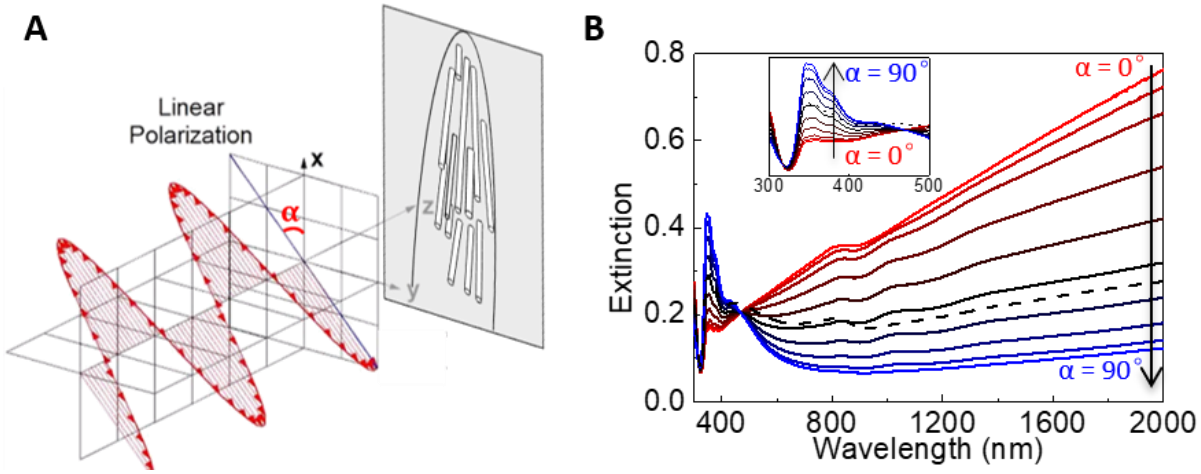

Figure 2. (A) Représentation schématique de la spectroscopie d'extinction avec de la lumière polarisée linéairement à l'angle α par rapport à la direction d'orientation des AgNWs. (B) Spectres d'extinction d'une monocouche de AgNWs alignés mesurés avec une lumière polarisée linéairement. L'angle α varie de 0° à 90° par pas de 10°. La ligne pointillée est le spectre d'extinction mesuré avec un dépolariseur. Les perturbations autour de 900 nm sont un artefact du spectrophotomètre.

Les intensités d'extinction de ces deux modes sont fortement sensibles à la polarisation de la lumière incidente. On décrit l'azimut α de la lumière polarisée linéairement tel que α = 0° lorsque son plan de polarisation est parallèle à l'orientation des AgNWs (***Figure 2A***). On observe que l'extinction entre 320 nm et 450 nm diminue avec α tandis que l'extinction entre 500 nm et 2000 nm augmente avec α (***Figure 2B***), car les modes transverses sont sélectivement excités lorsque α = 0° alors que les modes longitudinaux sont excités préférentiellement lorsque α = 90°. Cela confirme l'excellent alignement des AgNWs et souligne que les propriétés optiques du film monocouche sont fortement anisotropes.

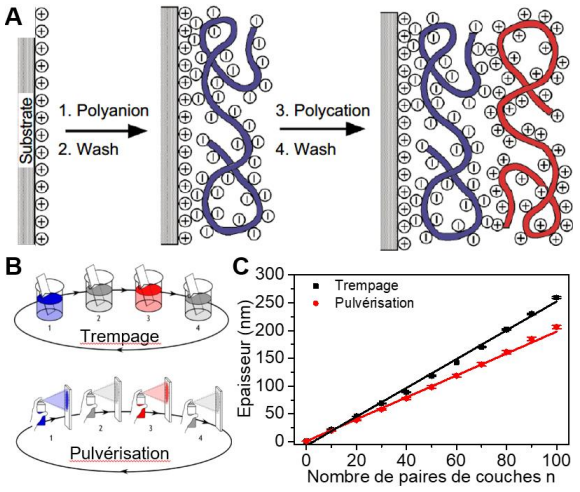

Figure 3. (A) Schéma du principe de l'assemblage LbL par (B) trempage et pulvérisation. (C) L'épaisseur du film avec une structure PEI/(PSS/PAH)$_n$ augmente linéairement en fonction du nombre n de paires de

Des multicouches de polyélectrolytes d'épaisseur contrôlée ont été déposées par LbL sur cette première couche de AgNWs orientés. Le LbL consiste à déposer alternativement des matériaux de charge opposée (***Figure 3A***), notamment des polyélectrolytes, par trempage, pulvérisation (***Figure 3B***) ou *spin-coating*. Cette technique permet de structurer sur toutes sortes de surfaces des films minces multicouches avec une rugosité réduite et une épaisseur bien définie et contrôlable par le nombre de couches de polyélectrolytes déposées (***Figure 3C***). Les principaux polycations utilisés dans cette thèse sont le polyéthylènimine (PEI) et le poly(hydrochlorure d'allylamine) (PAH), le polyanion étant du poly(styrène sulfonate) de sodium (PSS). La structure LbL utilisée en général dans cette thèse est PEI/(PSS/PAH)$_n$/PSS/PEI.

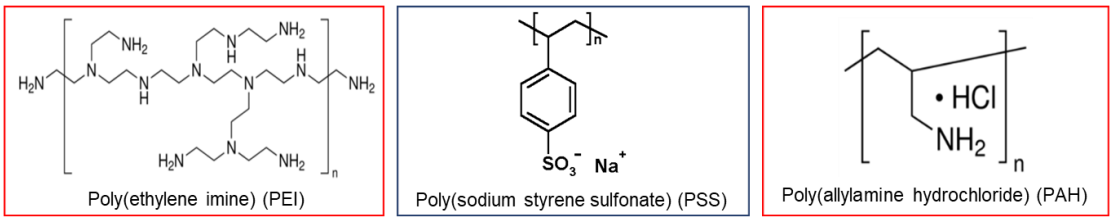

Figure 4. Structures chimiques des polyélectrolytes.

En déposant sur la multicouche de polyélectrolytes une nouvelle couche de AgNWs dont l'orientation peut être choisie indépendamment de la couche précédente, il est possible de créer une structure chirale gauche ou droite. Le processus peut être répété un certain nombre de fois en variant la densité de nanofils, le nombre de couches de polyélectrolytes et la direction d'orientation de chaque couche de AgNWs, et un ensemble de structures chirales d'architecture contrôlée contenant plusieurs couches d'AgNWs orientées dans des directions différentes et séparées d'un espacement différent ont pu être fabriquées (***Figure 5***).

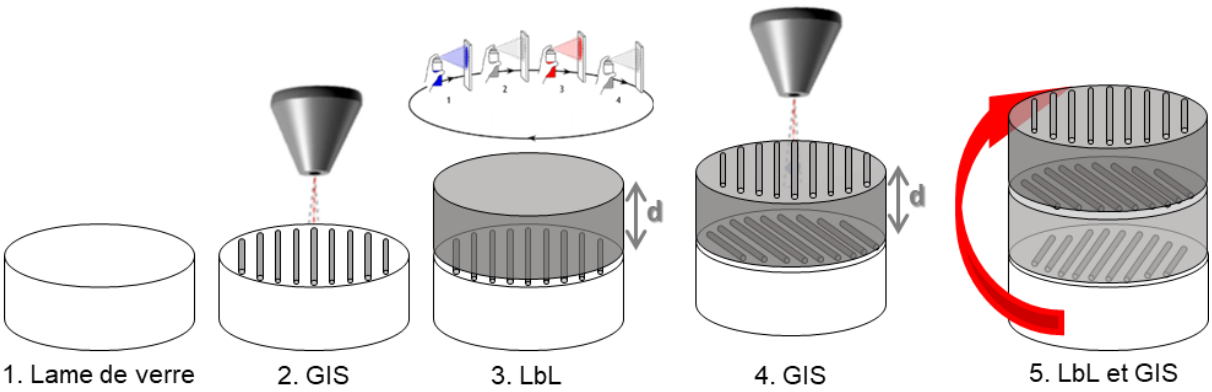

Figure 5. 1. Une lame de verre est fonctionnalisée par un assemblage de couches de polyélectrolytes (PEI/PSS/PAH/PSS/PEI) d'une épaisseur d'environ 5 nm. 2. La première couche d'AgNWs orientée à l'angle 0° est déposé par GIS. 3. Un film multicouche de polyélectrolytes (PEI/(PSS/PAH)$_n$/PSS/PEI) d'épaisseur variable est déposée par LbL. 4. La deuxième couche d'AgNWs orientée à un angle α est déposée par GIS. Cela donne une structure chirale. 5. En répétant le processus, des superstructures chirales d'architecture contrôlée contenant plusieurs couches de AgNWs peuvent être obtenues. La structure obtenue dans les étapes 4 et 5 est une structure « gauche ». Une structure « droite » peut être obtenue en tournant l'échantillon dans l'autre sens.

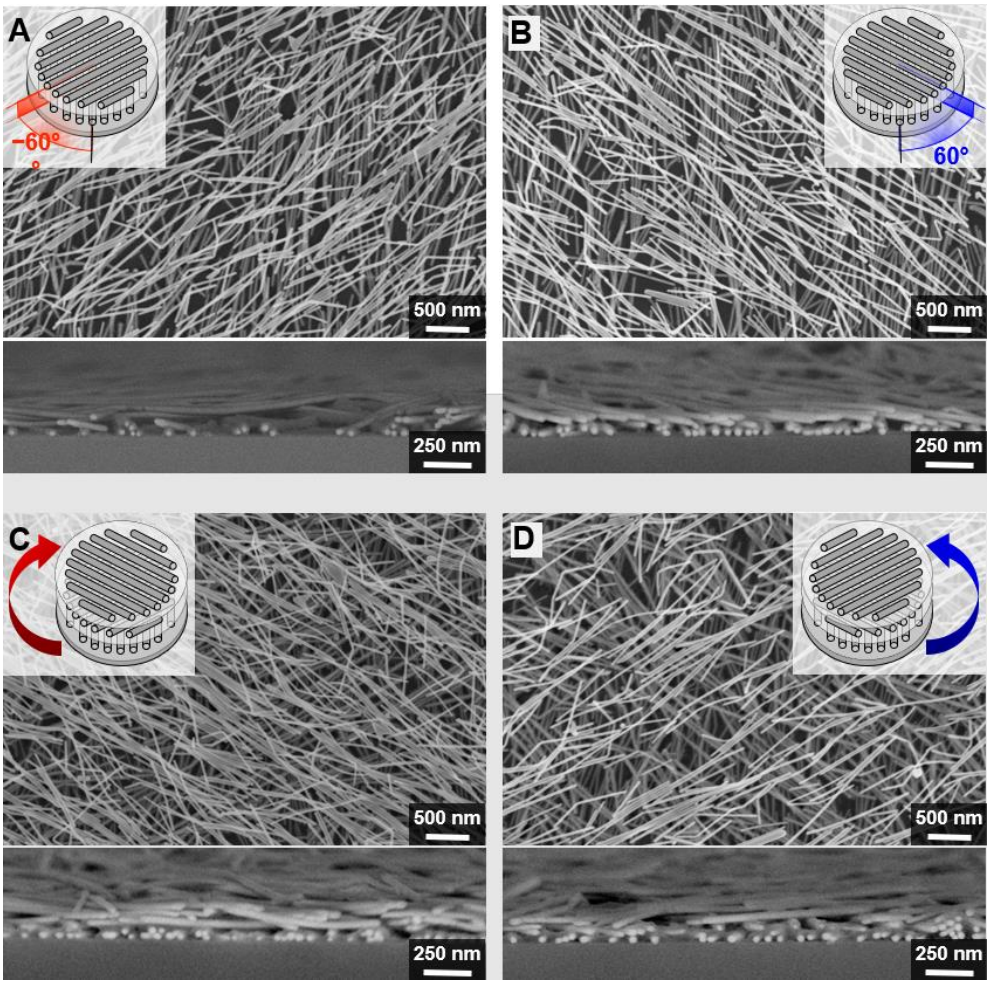

Figure 6. Images MEB de structures gauches (A and C) et droites (B and D) contenant deux (A and B) et trois (C and D) couches d'AgNWs en vue de dessus et en coupe transversale.

La ***Figure 6*** montre des images MEB en vue de dessus et en vue transversale de structures gauches et droites contenant 2 couches et 3 couches d'AgNWs. L'angle entre les couches successives d'AgNWs orientés est de 60° et la distance entre elles est d'environ 13 nm.

Les mesures spectroscopiques du dichroïsme circulaire (CD) et de l'extinction permettent d'accéder au facteur g qui mesure le niveau d'asymétrie en comparant la différence d'absorbance entre la lumière polarisée gauche et droite ($g = \frac{A_{gauche} - A_{droite}}{A} \propto \frac{CD}{A}$), révélant la forte chiralité optique des échantillons avec des valeurs de facteur g très élevées et des propriétés optiques symétriques pour les structures énantiomorphes (***Figure 7***).

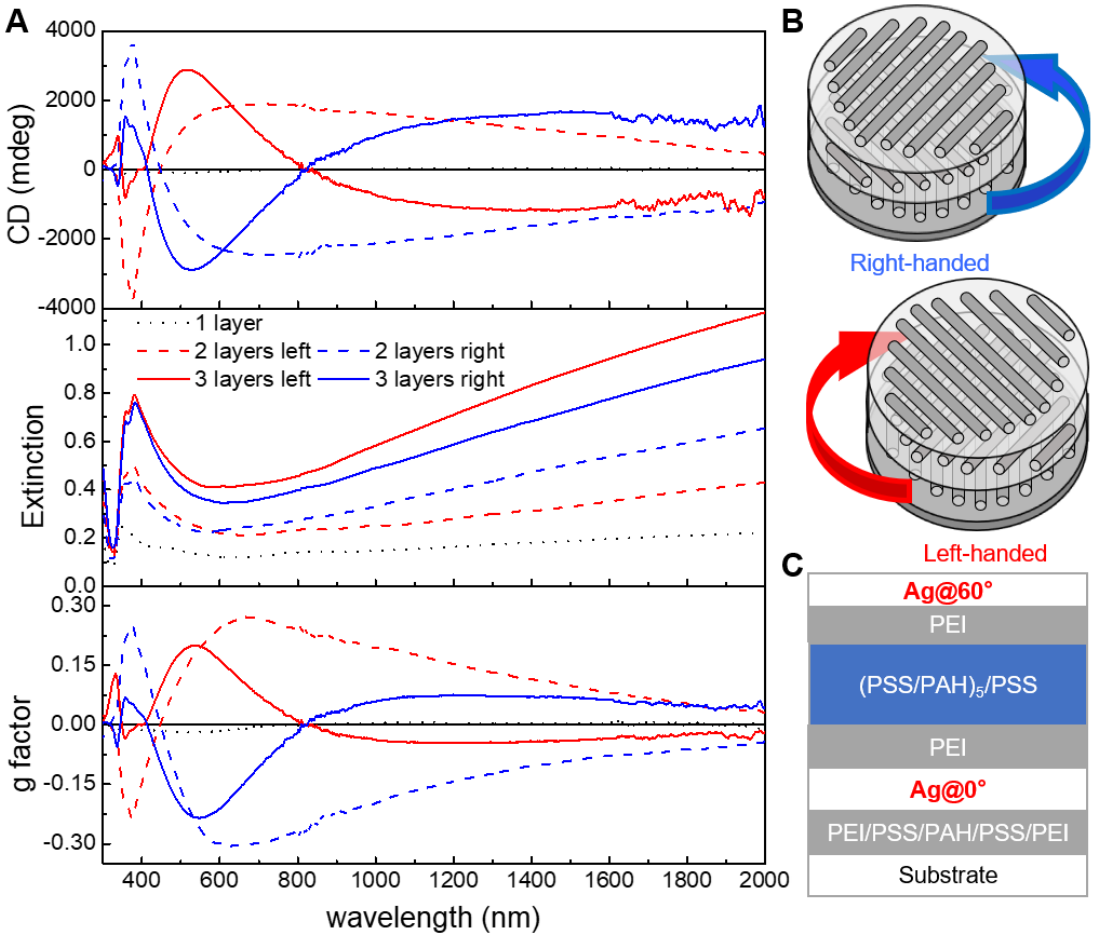

Figure 7. (A) : spectres de CD et d'extinction et facteurs g d'échantillons composés d'une couche (pointillés) d'AgNWs alignés (structure achirale), 2 couches (tirets) et 3 couches (lignes pleines) d'AgNWs avec une chiralité gauche (rouge) et droite (bleue). (B) Schémas de superstructures gauches et droites contenant 3 couches d'AgNW et (C) représentation schématique couche par couche d'une structure à deux couches. L'angle entre deux couches adjacentes d'AgNWs est de 60°, et le multicouche de polyélectrolytes entre elles est PEI/$(PSS/PAH)_5$/PSS/PEI (épaisseur ≈ 13 nm).

Une caractérisation plus poussée des propriétés optiques par Polarimétrie à Matrice de Mueller (MMP) a également été conduite en collaboration avec Yann Battie (Université de Lorraine), et des modélisations par matrices de transfert ont permis de relier les propriétés observées à la structure des échantillons. Les modélisations ont été effectuées à partir des propriétés effectives d'une monocouche orientée de AgNWs mesurées par ellipsométrie et en considérant la structure déterminée par microscopie (en particulier l'espacement entre les couches). À partir de la matrice de Mueller (mesurée et/ou simulée) d'un échantillon qui peut être écrite sous la forme suivante ***(1)***, il est possible, à condition que la dépolarisation soit négligeable, d'extraire les propriétés optiques importantes de l'échantillon, en particulier le dichroïsme circulaire (CD), la biréfringence circulaire (CB), le dichroïsme linéaire (LD) et la biréfringence linéaire (LB).

$$\mathrm{M} = \exp\begin{pmatrix} A & -LD & -LD' & CD \\ -LD & A & CB & LB' \\ -LD' & -CB & A & -LB \\ CD & -LB' & LB & A \end{pmatrix} \qquad \textbf{(1)}$$

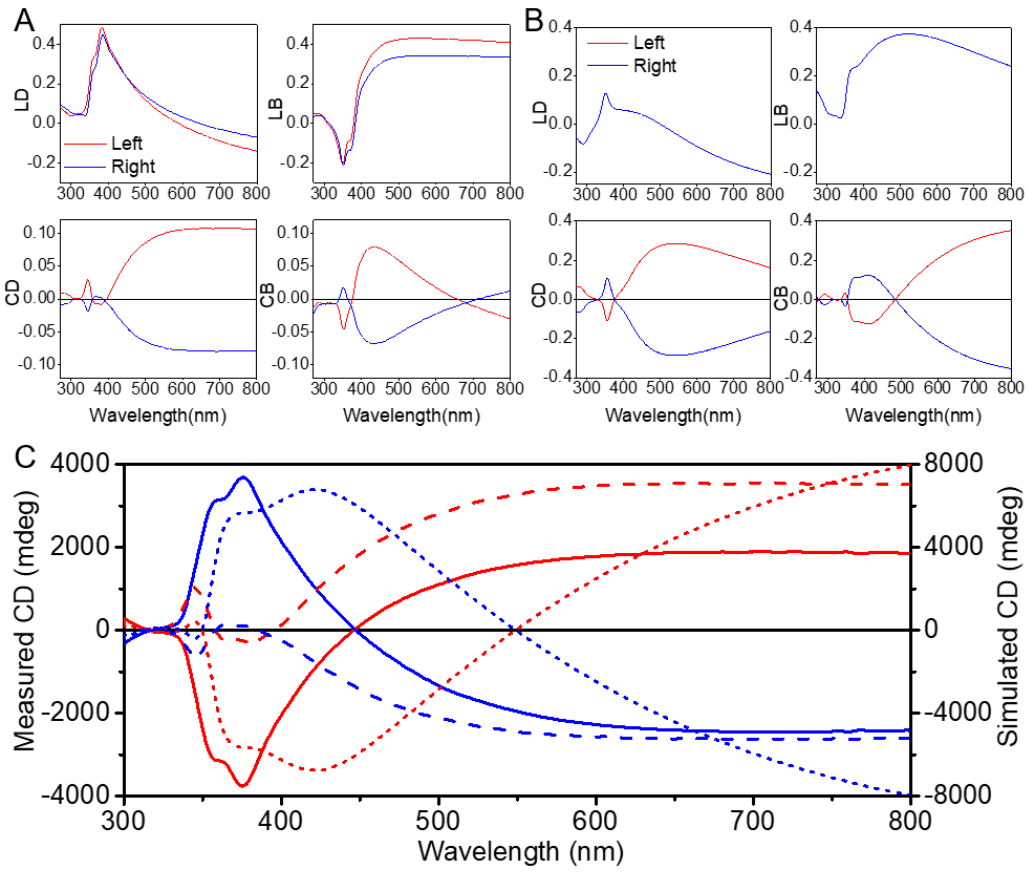

Figure 8. LD, LB, CD et CB pour les structures gauche (rouge) et droite (bleu) à deux couches, extraites de la matrice de Mueller mesurée (A) et simulée (B). (C) Comparaison de CD mesuré par un spectrophotomètre CD commercial (lignes pleines), MMP (tirets) et issu des simulations (pointillés).

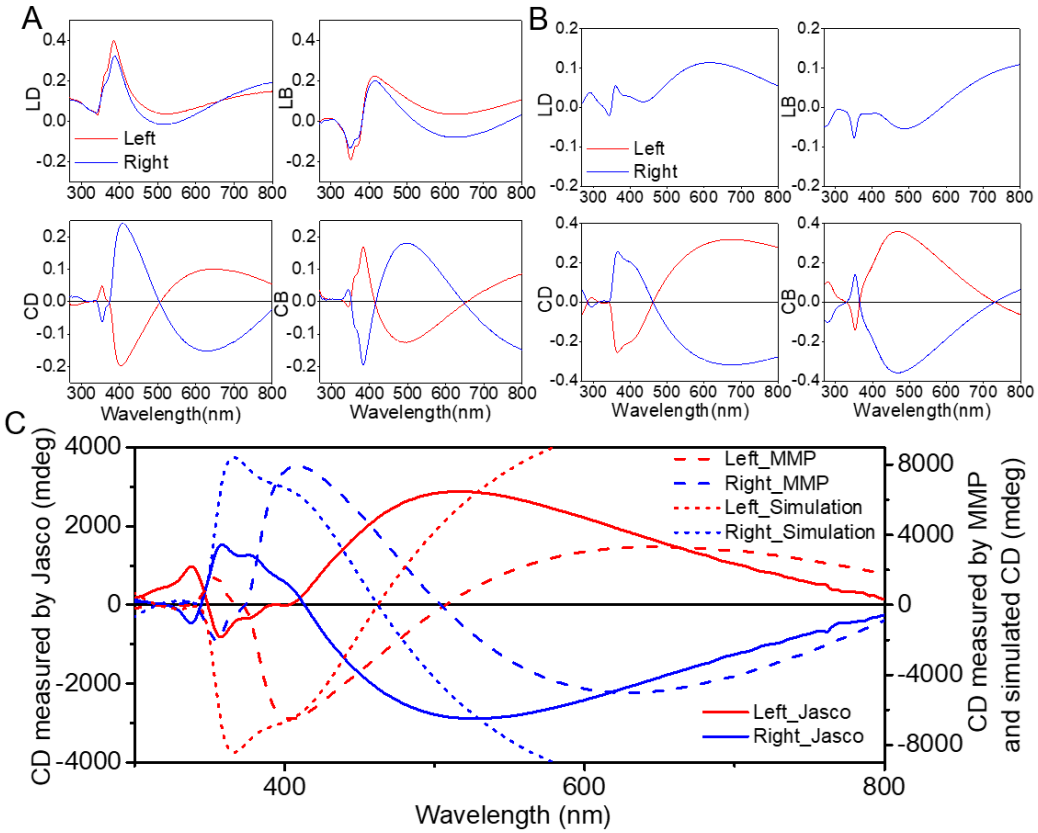

Figure 9. LD, LB, CD et CB pour les structures gauche (rouge) et droite (bleu) à trois couches, extraites de la matrice de Mueller mesurée (A) et simulée (B). (C) Comparaison de CD mesuré par un spectrophotomètre CD commercial (lignes pleines), MMP (tirets) et issu des simulations (pointillés).

Les ***Figure 8*** et ***Figure 9*** montrent le LD, LB, CD et CB mesurés et simulés pour les structures gauches et droites à deux (***Fig. 8***) et trois couches d'AgNWs (***Fig. 9***), ainsi que les comparaisons de CD mesurés et simulé. On observe que les termes linéaires sont similaires pour les échantillons gauches et droites, alors que les termes circulaires sont symétriques en miroir, ceux qui est attendu pour deux énantiomorphes. Le dichroïsme circulaire observé est très important : des valeurs de CD allant jusqu'à 4000 mdeg (soit un facteur g de 0.3) ont été mesurés sur ces structures.

Les simulations réalisées sont basées sur un modèle qui considère un empilement de couches sans interactions. Les principales caractéristiques des spectres sont reproduites par les simulations. Il existe néanmoins des différences entre les mesures et la modélisation, qui peuvent être dues à de petites différences dans la distance entre les couches, au caractère non

idéal des échantillons et au fait qu'aucun couplage des modes de LSPR entre les nanofils des différentes couches n'est considéré dans les simulations.

L'influence des paramètres structuraux des assemblages sur les propriétés chirales (en particulier l'angle α et la distance d entre deux couches d'AgNWs) a été étudiée.

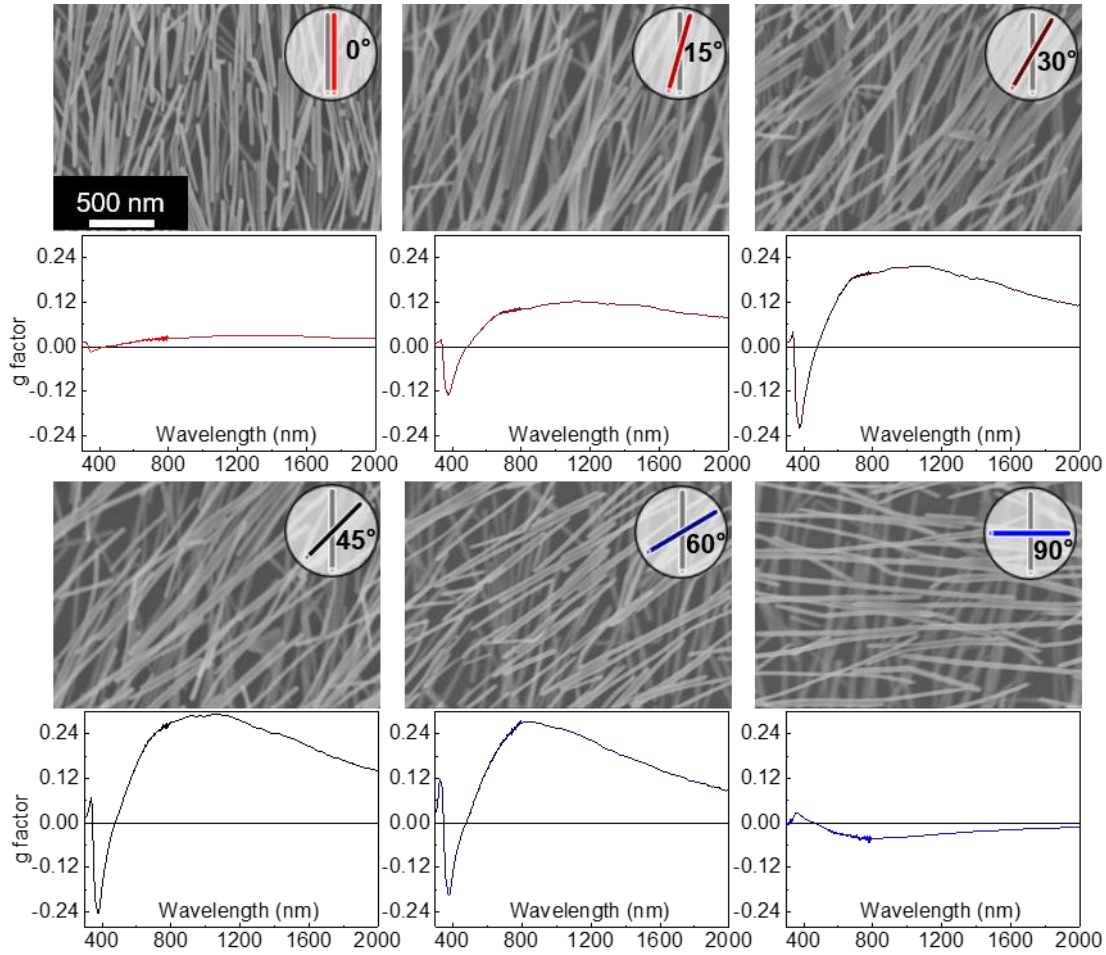

Figure 10. Facteurs g et images MEB correspondantes pour les échantillons avec un angle α entre les deux couches d'AgNWs variable en fixant la distance d entre elles à 13 nm.

Une série d'échantillons à deux couches avec un angle α variable ont été préparées en gardant la distance entre les couches fixée à 13 nm. Le facteur g de chaque échantillon est donné dans la ***Figure 10***. Les échantillons avec α = 0° et 90° ont un facteur g proche de 0, ce qui est cohérent avec le fait qu'il s'agit structures achirales. En revanche, le CD et les facteurs g augmentent avec α entre α = 0° et 45° et atteint un maximum à α = 45°, qui est la superstructure la plus chirale, et diminue de α = 45° à 90°. L'allure du spectre de CD n'est par contre pas modifiée par l'angle entre les couches de AgNWs.

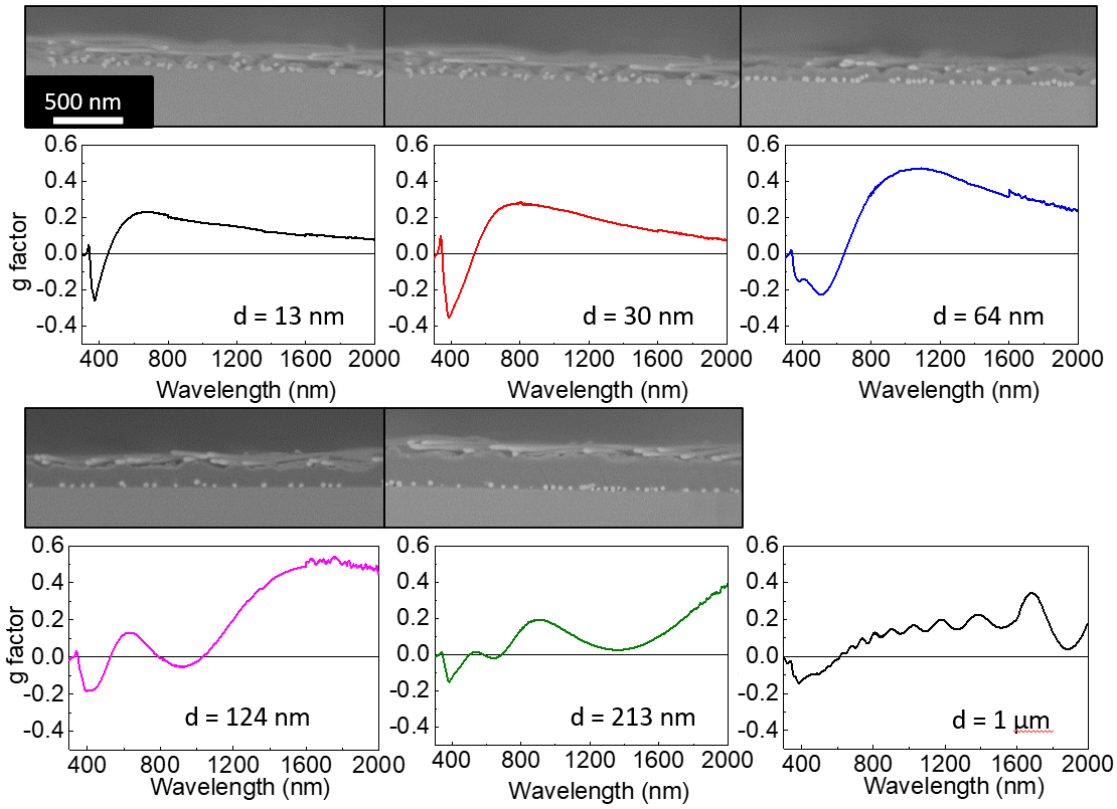

Figure 11. Facteurs g et images MEB correspondantes pour des échantillons avec une distance d entre les deux couches d'AgNWs variable en fixant l'angle α à 60°.

Une autre série d'échantillons à deux couches sont préparés avec une distance d variable en gardant l'angle α fixé à 60°. Le facteur g de ces échantillons sont présentés dans la ***Figure 11***. La distance entre les couches modifie de manière significative le CD du film. Les pics de CD sont décalés vers le rouge avec l'augmentation de la distance et des oscillations dans le spectre de CD ont été observés pour un grand espacement (> 100 nm), similairement à des oscillations de Fabry-Perot observées dans les spectres d'absorbance de couches minces.

III. Couplage d'un colorant achiral aux superstructures chirales

Les nanostructures plasmoniques peuvent modifier les propriétés de molécules placées à leur proximité. Les nanostructures plasmoniques chirales décrites précédemment ont été modifiées en insérant au sein de la structure un colorant achiral, le TDBC. Le TDBC a été sélectionné

pour cette étude car il forme un *J-aggregate* spontanément en solution aqueuse ce qui donne lieu à un pic d'absorbance étroit et intense dans le visible, et que sa charge permet de l'intégrer facilement au sein de la multicouche de polyélectrolytes par assemblage LbL.

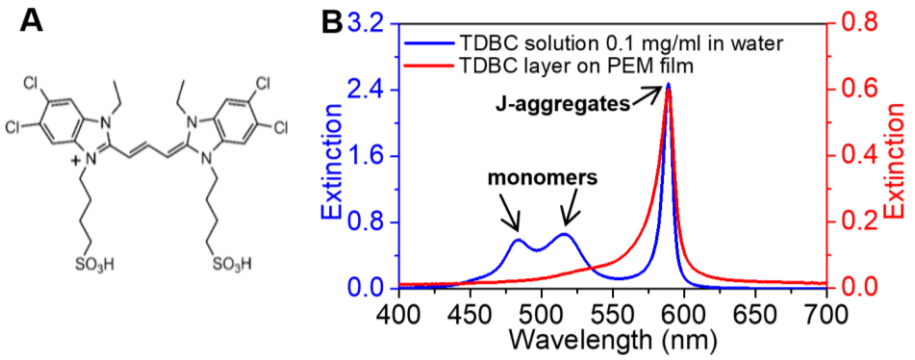

Figure 12. (A) Structure chimique du TDBC. (B) Spectres d'extinction du TDBC en solution et en film.

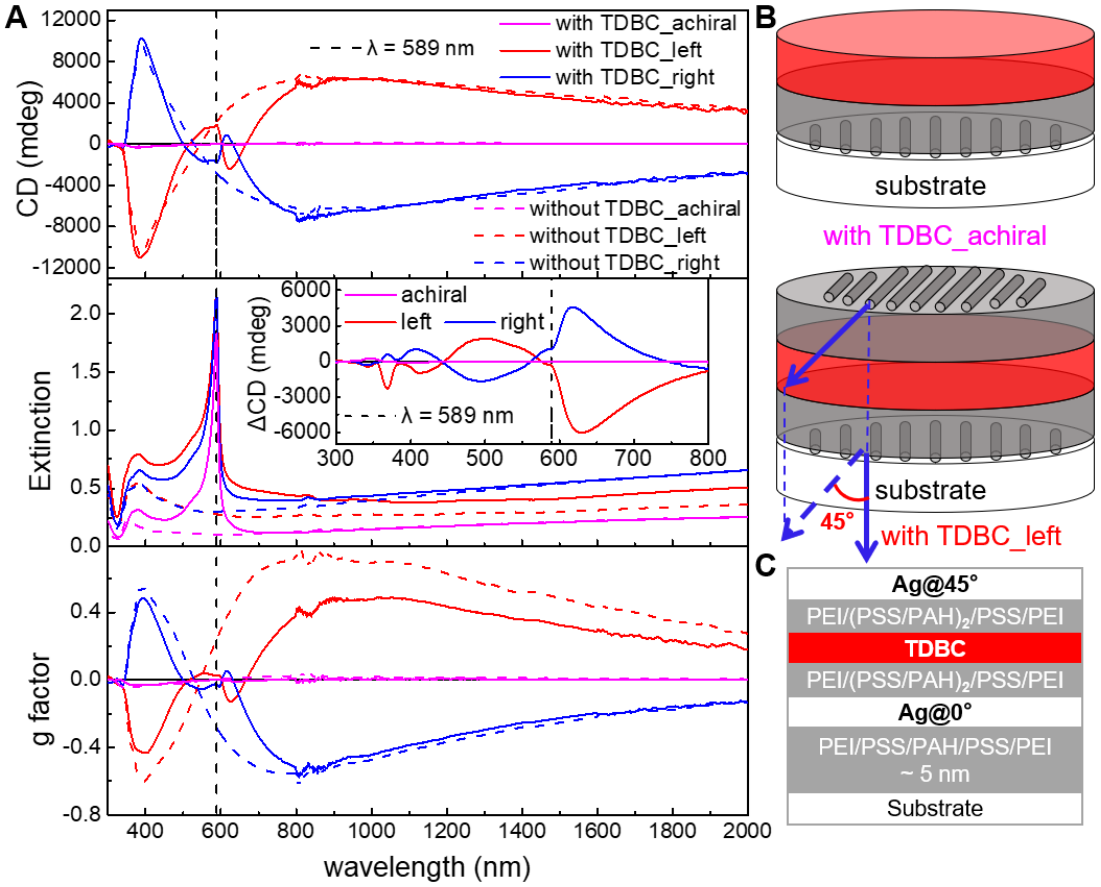

Figure 13. (A) spectres CD, extinction et facteur g d'échantillons constitués de deux couches d'AgNWs avec une couche de TDBC entre elles (lignes pleines) et un échantillon de contrôle (achiral) constitué d'une couche d'AgNWs avec une couche de TDBC. Les structures correspondantes sans TDBC (tiret) sont celles avec un espacement et un angle identiques. Les structures gauche (rouge) et droite (bleu) sont présentées. L'encart montre ΔCD, qui est la différence entre le CD des structures avec et sans TDBC. (B) représentation schématique des superstructures avec la couche de TDBC.

Nous avons développé des superstructures plasmoniques chirales gauche et droite contenant deux couches d'AgNWs avec une couche de TDBC entre elles, ainsi que des échantillons achiraux contenant une couche d'AgNWs et une couche de TDBC. Le processus de fabrication des superstructures plasmoniques chirales utilisant le GIS et l'assemblage LbL présenté dans la ***Figure 5*** a été modifié pour introduire la couche de TDBC. Les conditions de dépôt ont été optimisées pour permettre un assemblage efficace et reproductible du TDBC à une position bien déterminée de la superstructure. Les propriétés chiro-optiques sont fortement influencées par la présence de TDBC : une modification importante du spectre CD de la nanostructure est observée à la longueur d'onde d'absorbance du *J-aggregate* de TDBC alors que le colorant est achiral, ce qui indique une modification des propriétés du TDBC par son environnement chiral. En traçant ΔCD, la différence entre le CD des structures avec et sans TDBC, la modification du CD due à la couche TDBC est mise en évidence (insert de la ***Figure 13A***). Le ΔCD lié à la couche TDBC présente une succession d'extremums positifs et négatifs (effet Cotton) comme le spectre CD de nombreuses molécules chirales, alors que le TDBC lui-même est achiral. Ce ΔCD présente un effet Cotton négatif / positif autour de la longueur d'onde d'absorption du TDBC pour les structures gauches / droites respectivement. De plus, le ΔCD a des valeurs extrêmement élevées (jusqu'à quelques milliers de millidegrés) par rapport aux molécules chirales classiques, qui ont typiquement un CD de quelques dizaines de millidegrés. L'extinction du film se révèle être l'addition des spectres d'extinction des couches AgNW et des couches TDBC, alors que l'intensité d'extinction des J-agrégats de TDBC est significativement renforcée. La structure achirale (une couche d'AgNWs + TDBC) ne présente pas de CD et bien sûr aucune modification de CD, mais le renforcement de l'extinction de TDBC est également observé. Ce phénomène connu sous le nom d'absorption exaltée par le plasmon de surface. Il est dépendant de la distance entre la couche de TDBC et les couches d'AgNWs.

La matrice de Mueller des structures à une et deux couches avec une couche de TDBC a été simulée et mesurée par Yann Battie de l'Université de Lorraine. Les LD, LB, CD et CB mesurés et simulés sont représentés sur la ***Figure 14A*** et ***Figure 14B*** respectivement, ainsi que la

comparaison du CD mesuré et simulé (***Figure 14C)***.

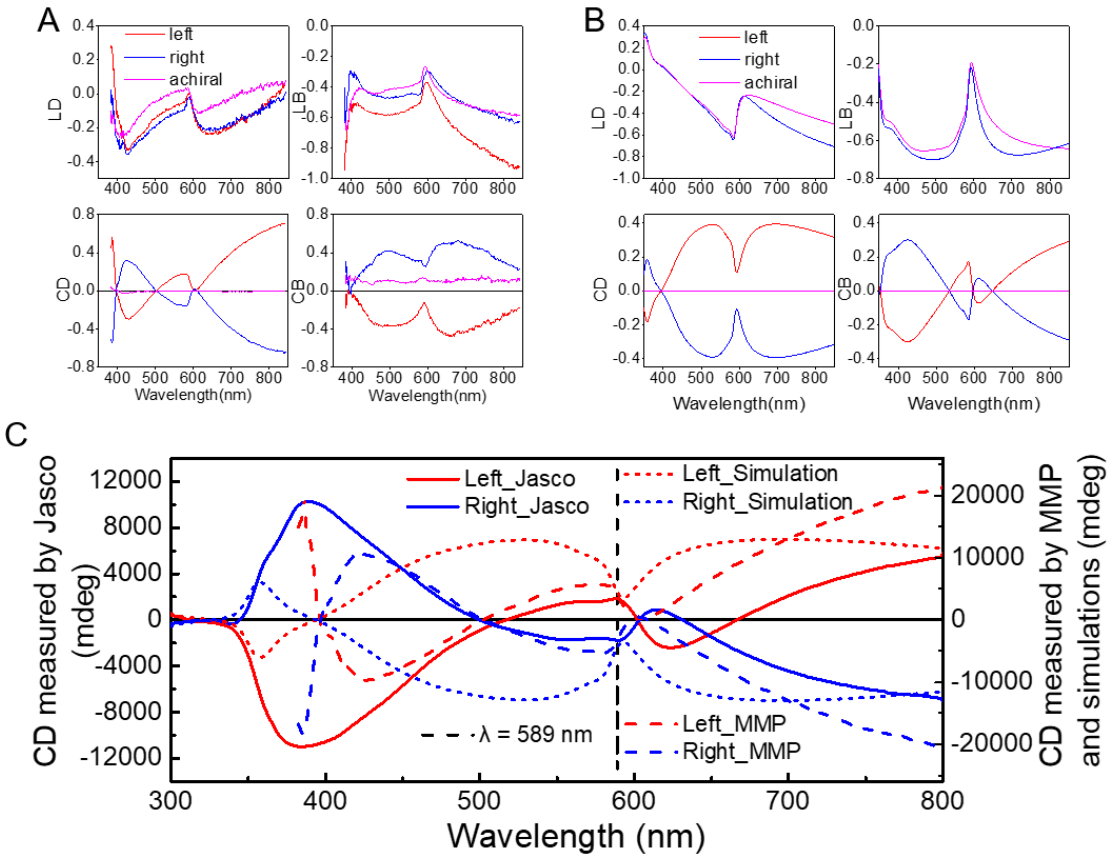

Figure 14. LD, LB, CD et CB pour les structures achirale (rose), gauche (rouge) et droite (bleu) avec une couche de TDBC, extraites de la matrice de Mueller mesurée (A) et simulée (B). (C) Comparaison de CD mesurés par un spectrophotomètre CD commercial (lignes pleines), MMP (tirets) et issu des simulations (pointillés).

Nous avons observé qu'en plus du CD, le LD, LB et CB sont également modifiés par l'introduction de la couche TDBC. Les simulations de CD ne sont pas totalement cohérentes avec les mesures. Cependant, la modification de CD est assez bien reproduite dans les simulations. Cela signifie que le modèle simple considérant les superstructures assemblées en LbL comme des couches indépendantes empilées ensemble est capable de reproduire en partie le changement de CD induit par le TDBC. Cependant, les détails de la modification ne sont pas bien modélisés, et il est donc possible que le couplage entre le LSPR des AgNWs et la couche TDBC contribue également à la modification CD, qui n'a pas été prise en compte dans les simulations.

Les paramètres structurels, y compris la distance entre deux couches d'AgNWs et la position

de la couche TDBC dans le film multicouche de polyélectrolyte, ont une influence majeure sur la modification des propriétés chiro-optiques et ont été systématiquement étudiés.

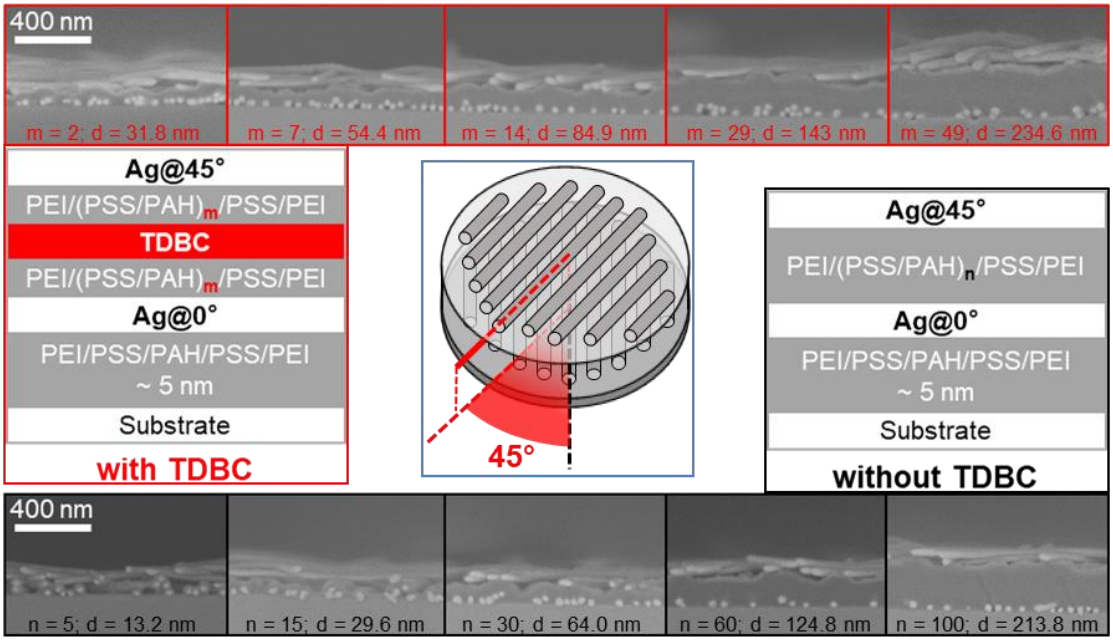

Figure 15. Cadre bleu: les mesures par microscopie de l'épaisseur intercouche ont été réalisées sur des superstructures bicouches avec un angle α = 45 °. Cadre rouge: Images MEB en coupe d'échantillons avec une couche de TDBC, dont la structure est décrite comme PEI/PSS/PAH/PSS/PEI/Ag/PEI/$(PSS/PAH)_m$/PSS/PEI/TDBC/PEI/$(PSS/PAH)_m$/PSS/PEI/Ag (m = 2, 7, 14, 29 et 49). Cadre noir: échantillons sans TDBC, dont la structure est PEI/PSS/PAH/PSS/PEI/Ag/PEI/$(PSS/PAH)_n$/PSS/PEI/Ag (n = 5, 15, 30, 60 et 100). Les épaisseurs sont la distance moyenne entre les deux couches d'AgNW mesurées à différentes positions. m et n pour chaque paire d'échantillons correspondent au même nombre total de couches, lorsque n = 2 (m + 1), entre les couches d'AgNWs.

Afin de mesurer l'épaisseur du film PEM contenant une couche de TDBC placée en son centre, nous avons préparé une série d'échantillons à deux couches d'AgNWs, dont la structure peut s'écrire comme suit: PEI/PSS/PAH/PSS/PEI/Ag/PEI/$(PSS/PAH)_m$/PSS/PEI/TDBC/PEI/$(PSS/PAH)_m$/PSS/ PEI/Ag (m = 2, 7, 14, 29 and 49). Les images MEB ont été prises en vue transversale et l'épaisseur a été mesurée et a été comparée à la structure correspondante sans TDBC ***(Figure 15***). L'épaisseur du film PEM avec une couche de TDBC augmente linéairement à mesure que le nombre de couches de PEM augmente. Pour un nombre total de couches identique entre les AgNWs, l'espacement entre les couches AgNWs d'un film avec TDBC est d'environ 20 nm plus épais que sans TDBC (***Figure 16***).

Le bon contrôle de l'épaisseur du film PEM avec/sans TDBC nous a permis de pourvoir étudier l'influence de l'espacement sur les propriétés chiroptiques. Nous avons donc préparé une série d'échantillons à deux couches d'AgNWs avec une couche TDBC au centre en faisant varier l'espacement d entre les deux couches d'AgNWs (d = 30, 60, 100, 150 et 200 nm). Ces échantillons ont été comparés à des structures sans TDBC avec des espacements identiques. L'angle entre les deux couches d'AgNWs a été fixé à 45°.

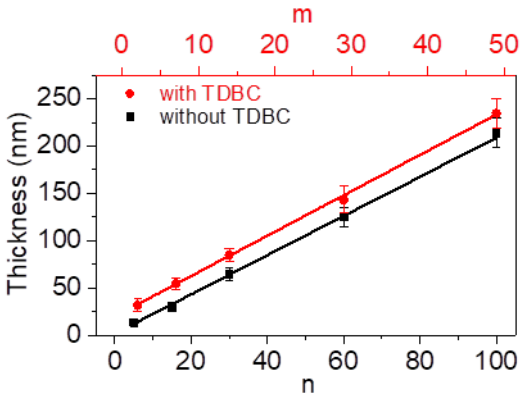

Figure 16. Épaisseurs de films PEM contenant une ou aucune couche de TDBC en fonction du nombre de couche de PEM.

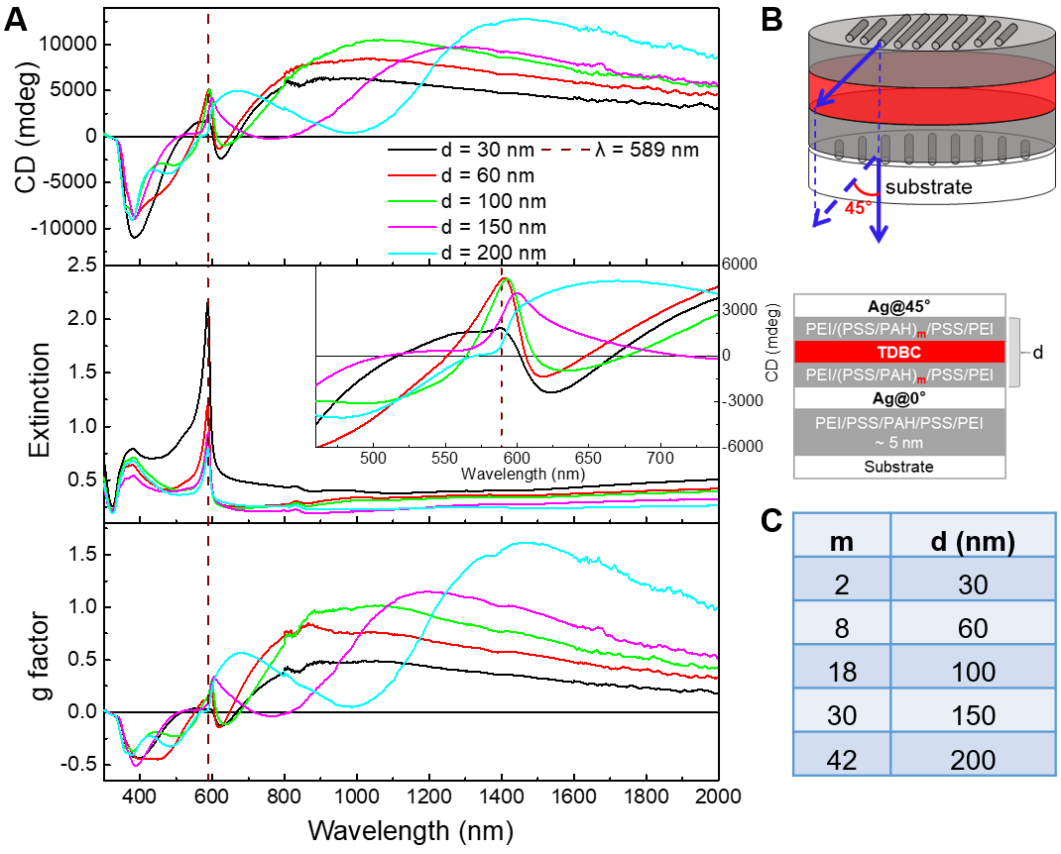

m	d (nm)
2	30
8	60
18	100
30	150
42	200

Figure 17. (A) spectres CD, extinction et facteurs g d'échantillons composés de deux couches d'AgNWs dont l'espacement entre les couches varie de 30 nm à 200 nm, contenant une couche de TDBC au centre et avec l'angle α fixé à 45 °, l'encart est un zoom dans les spectres CD. (B) représentation schématique de la structure et (C) correspondance entre la distance entre les couches de AgNWs et le nombre de paires de couches de PSS/PAH dans les structures notées PEI/PSS/PAH/PSS/PEI/Ag/PEI/$(PSS/PAH)_m$/PSS/PEI/TDBC/PEI/$(PSS/PAH)_m$/PSS/PEI/Ag.

Les spectres de CD et d'extinction et les facteurs g des échantillons avec TDBC sont donnés dans ***Figure 17***. Nous avons observé la modification de CD et du facteur g en fonction de l'espacement entre les couches de AgNWs, ainsi que l'exaltation de l'extinction du TDBC pour les petit espacement (d = 30 nm). Les spectres CD des structures correspondantes avec et sans TDBC sont comparés dans la ***Figure 18*** pour chaque d, ainsi que la différence ΔCD entre le CD avec et sans TDBC pour des espacements identiques.

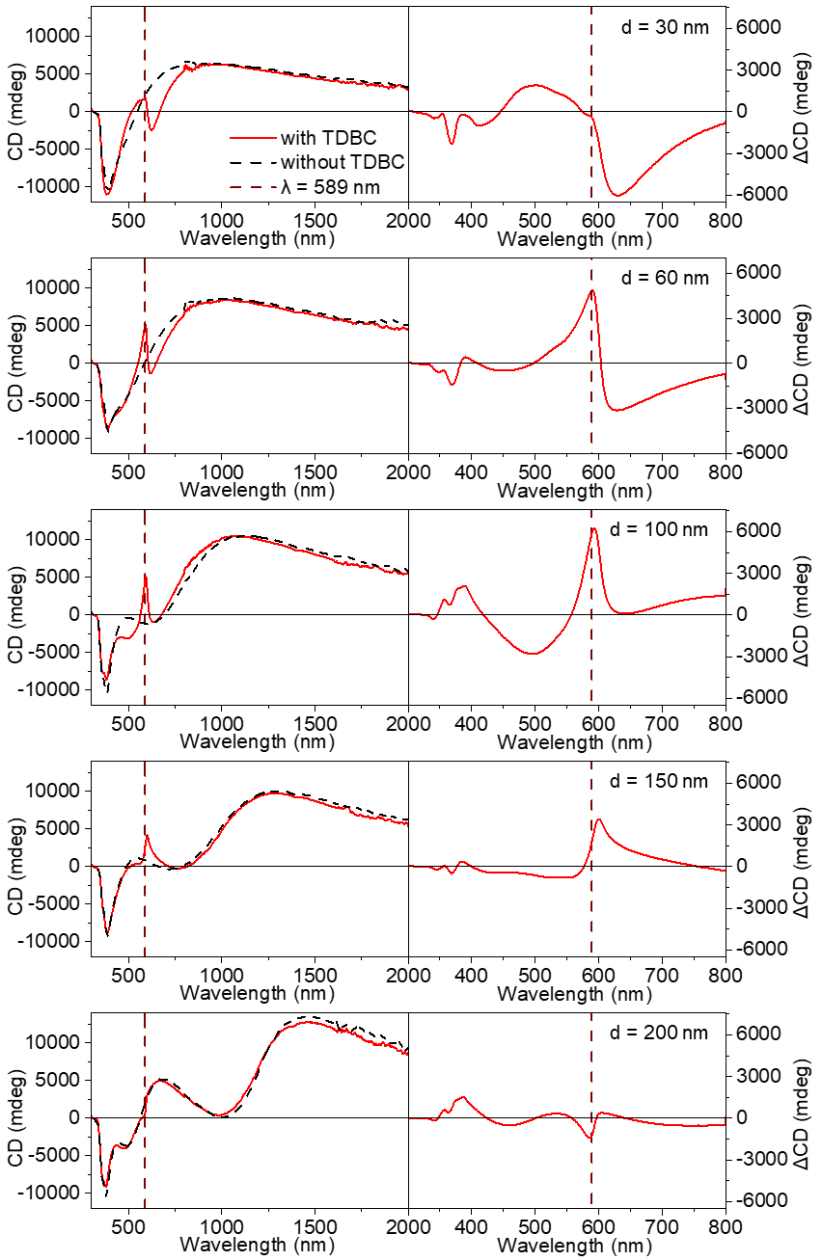

Figure 18. Colonne de gauche: comparaison des spectres CD d'échantillons avec et sans TDBC, avec un espacement identique de d = 30 nm, 60 nm, 100 nm, 150 nm et 200 nm. Colonne de droite: spectres de ΔCD, la différence de CD des échantillons avec et sans la couche TDBC pour un espacement identique entre les deux couches d'AgNWs.

Nous avons observé une excellente reproductibilité des spectres CD pour des échantillons d'espacement identique avec et sans la couche TDBC, ce qui confirme le bon contrôle sur l'épaisseur du film, sachant que les spectres CD sont extrêmement sensibles à l'espacement et que les échantillons nécessitent jusqu'à plus de 200 étapes de dépôt pour les échantillons d = 200 nm. Le ΔCD peut être considéré comme la modification CD due à l'introduction de la couche de TDBC. Le ΔCD a une forme caractéristique d'un effet Cotton. L'espacement entre les couches d'AgNWs a une forte influence sur le changement de CD dû au TDBC. Dans ces structures gauches, pour un faible espacement (d = 30 nm et 60 nm), le ΔCD montre un effet Cotton négatif, décalé vers le rouge avec l'augmentation de d. Pour d = 100 nm et 150 nm, le ΔCD affiche un effet Cotton positif, décalant vers le rouge avec l'augmentation de d et dont l'intensité diminue avec d. Pour d = 200 nm, le ΔCD a un « double effet Cotton » autour de 589 nm avec une intensité faible: un effet Cotton positif à droite de λ = 589 nm et négatif à gauche de λ = 589 nm.

Nous avons étudié ensuite l'influence sur les propriétés chiro-optiques de la position de la couche de TDBC entre deux couches d'AgNWs séparées par une distance fixée. Compte tenu de la propriété semi-réfléchissante des films de AgNWs, une onde stationnaire et / ou des interférences à une longueur d'onde spécifique liée à la largeur de la « cavité » peuvent survenir. Nous avons choisi ici des espacements fixés d = 147 nm et d = 294 nm, correspondant au quart et à la moitié la longueur d'onde d'absorption maximale des J-agrégats du TDBC (589 nm). La structure peut s'écrire comme suit : PEI/PSS/PAH/PSS/PEI/Ag/PEI/$(PSS/PAH)_{\mathbf{m1}}$/PSS/PEI/TDBC/PEI/$(PSS/PAH)_{\mathbf{m2}}$/PSS/PEI/Ag ($m_1 + m_2 = 58$ pour d = 147 nm et $m_1 + m_2 = 128$ pour d = 294 nm). La position de TDBC a été contrôlé en variant m_1 et m_2.

Les spectres de CD et d'extinction et les facteurs g des échantillons avec d = 294 nm sont donnés dans ***Figure 19***. Le ΔCD pour tous les d_1 a un effet Cotton positif avec des positions de pic légèrement décalées et des intensités légèrement différentes. Cette observation rejoint la conclusion de la section précédente : un effet Cotton négatif en ΔCD n'est observé que pour une

petite distance AgNW-TDBC (<20 nm), alors qu'un effet Coton positif est observé pour des distances AgNW-TDBC plus importantes.

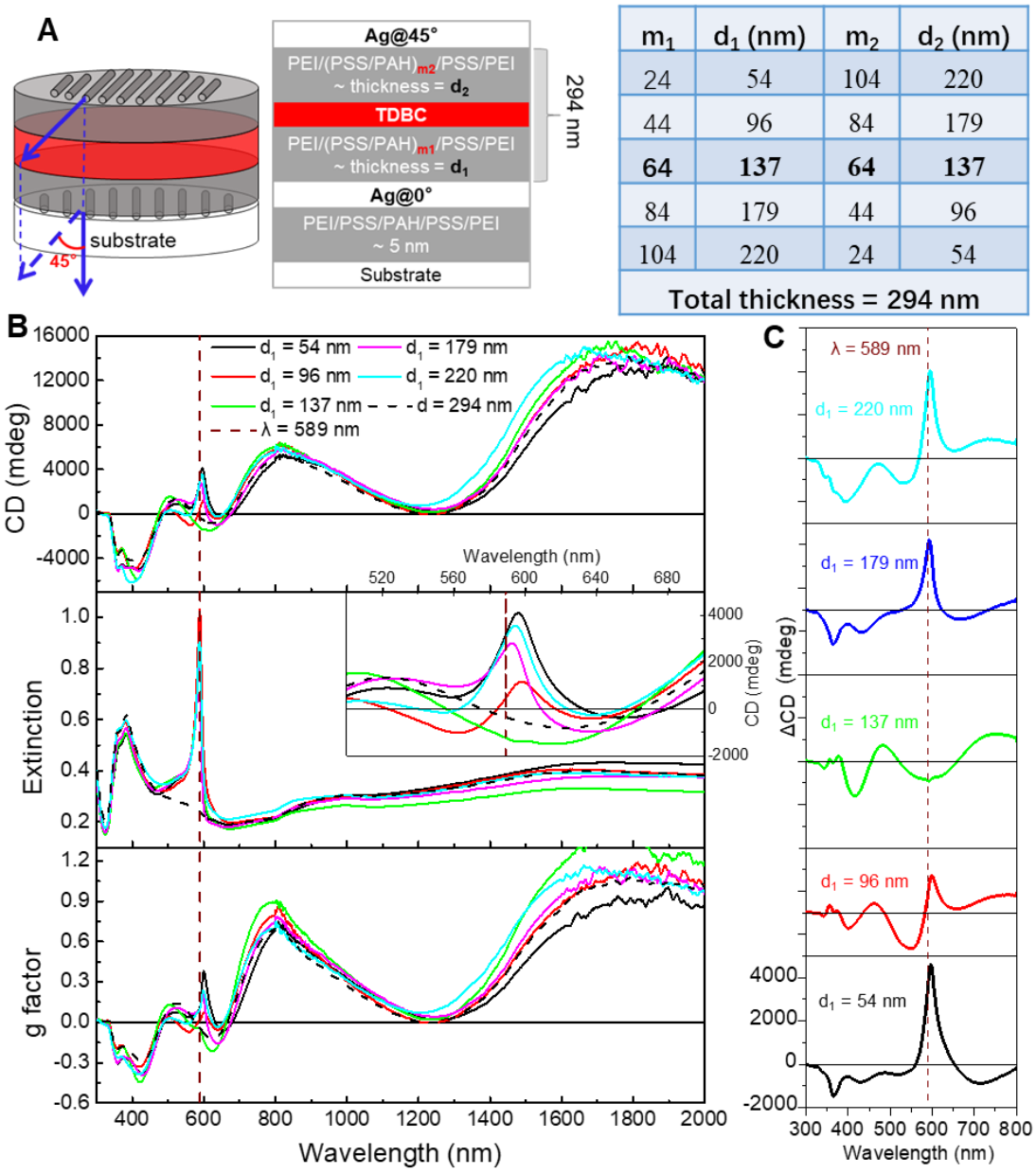

Figure 19. (A) Représentation schématique des structures étudiées. La distance totale entre les deux couches d'AgNWs est fixée à 294nm. La position de la couche de TDBC est modifiée en changeant d_1 (distance de la couche TDBC à la couche inférieure d'AgNWs) et d_2 (distance de la couche TDBC à la couche supérieure d'AgNWs). Lorsque la couche TDBC est au milieu de la structure, $d_1 = d_2 = 137$ nm. (B) spectres CD, extinction et facteurs g des superstructures pour différentes positions de la couche de TDBC (d_1). (C) ΔCD pour différentes positions de TDBC (d_1), l'échelle pour tous les spectres est la même.

Similairement à la série d'échantillons précédente, le ΔCD montre un effet Cotton positif, à une exception près toutefois: lorsque la couche TDBC est placée au milieu entre les deux couches

d'AgNWs (d_1 = 137 nm), le changement de CD est beaucoup plus faible . Ceci confirme notre observation dans la figure 18 (échantillon avec un très grand espacement).

I V . Conclusion et perspectives

En conclusion, nous avons montré que nous sommes capables de construire des nanostructures chirales hybrides bien contrôlées composées de couches d'AgNWs orientées et d'un colorant moléculaire placé à une position précise dans la nanostructure. Bien que la fabrication de telles structures nécessite un grand nombre d'étapes, les structures formées sont très reproductibles et l'architecture peut être facilement modulée avec un contrôle à l'échelle du nm sur les distances entre les différents constituants.

Nous avons ainsi montré que des nanostructures plasmoniques chirales composées de couches de nanofils d'argent orientés présentent un très fort dichroïsme circulaire s'étendant sur toute la gamme de l'UV, du visible et du proche infrarouge, et que les caractéristiques des spectres CD dépendent de l'angle entre l'orientation de chaque couche de nanofils et de la distance entre les couches.

Nous avons également montré que les propriétés optiques d'un colorant organique achiral sont fortement modifiées lorsqu'il est placé à proximité d'une superstructure plasmonique chirale. Cette modification comprend l'exaltation de l'extinction (et de l'émission) du colorant et la modification des propriétés de polarisation, notamment LD, LB, CD et CB, parmi lesquelles nous nous intéressons principalement à la modification CD.

L'extinction exaltée par le plasmon de surface a été observée lorsqu'une couche de TDBC est à proximité d'une ou plusieurs couches d'AgNWs. La modification de CD due à la couche de colorant est caractérisée par ΔCD, la différence entre le CD avec et sans la couche de colorant. Nous avons étudié les paramètres structurels qui ont une influence sur la modification du CD, en particulier la distance entre la couche de colorant et les couches d'AgNWs. En général, ΔCD

a des valeurs relativement élevées (jusqu'à plusieurs degrés) et a une forme caractéristique d'un effet Cotton dépendant de la distance entre la couche de colorant et les AgNWs.

Les propriétés optiques de ces diverses nanostructures ont été modélisées avec un accord raisonnable entre les simulations et les mesures par une approche de matrice de transfert en se basant sur les propriétés effectives mesurées sur une monocouche.

Ce travail ouvre des perspectives dans de nombreux domaines car l'approche proposée est très générale. D'autres molécules pourraient par exemple être intégrés dans de telles nanostructures chirales, en particulier des (bio)molécules chirales dont le spectre CD pourrait être exalté. Il serait aussi intéressant d'étudier si l'intégration de fluorophores achiraux au sein des nanostructures chirales permet de polariser circulairement la lumière émise. Enfin, des résultats préliminaires indiquent qu'en déposant les nanofils d'argent sur des miroirs d'argent il est possible de fabriquer des surfaces semi-réfléchissantes dont la réflexion est polarisée circulairement, ce qui est une première étape vers le couplage fort d'une molécule dans une cavité chirale auto-assemblée.

I . State of the art

I.1. Chirality

Chirality[1] is the geometrical property of an object lacking any planes of symmetry or inversion centers, which distinguishes the original object from its non-superimposable mirror image – a chiral object and its mirror image are called enantiomorphs, or when referring to molecules, enantiomers[2]. Human hands are the most explicit illustration of this concept (***Figure 1***), knowing that the word "chirality" is derived from the word "hand" in Greek.

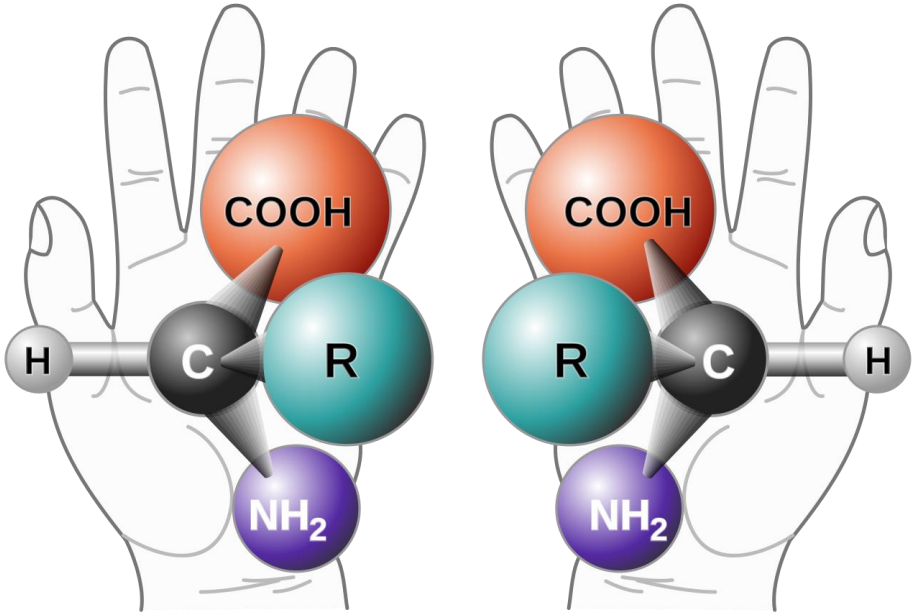

Figure 1. Two enantiomers of a generic amino acid that is chiral[3]

It was Lord Kelvin who coined the term in 1893[4]: "I call any geometrical figure, or group of points, 'chiral', and say that it has chirality if its image in a plane mirror, ideally realized, cannot be brought to coincide with itself", while back in 1848 Louis Pasteur discovered already for the first time the molecular chirality, which he described as "dissymmetry" at that time, investigating the enantiomers of a tartaric acid salt.[5] Pasteur also deduced at the same time the connection between molecular chirality and optical activity, i.e. the rotation of the plane of polarization of light passing through a chiral medium. It was not until 25 years later that Le

Bel[6] and van't Hoff established the basis of molecular stereochemistry by formulating the notion of asymmetrical tetrahedral carbon atom.

Since then, the subject of chirality has been steadily expanding as a major topic in chemistry and biology, owing to its wide existence and paramount importance in nature and of its abundant potential of applications. The fact that, for instance, homochirality[7] is favored in living systems on earth is supposed to be a possible origin of life on earth.[8,9] Indeed, all amino acids (with the exception of glycine) which constitute the essential components of proteins and enzymes are Levogyre and the sugars that are the essential components of DNA and RNA are all Dextrogyre. Nowadays, 80% of active compounds in pharmaceutics are chiral, while in certain cases the enantiomer of a drug is a poison. One tragic outcome of this phenomenon is the "thalidomide scandal"[10], known as the "biggest man-made medical disaster ever". In the 1960s, over 10,000 children were born all over the world with severe birth defects, such as phocomelia, because their mothers consumed thalidomide as a medication to treat morning sickness during pregnancy. Several years later, it was proven that the clinically active component was the (R)-thalidomide, while the (S)-thalidomide was extremely teratogenic (***Figure 2***), yet its pathological mechanism was not understood until 2010.[11] Many other examples advocating the importance of chirality in biology can be given, such as chiral fragrance of molecules[12] of fruits producing different odors like orange and lemon (chiral limonene) or mint and caraway (chiral carvone), to name a few. However, one should bear in mind that chirality is not limited to molecular systems, but may appear at all scales, ranging from spiral galaxy[13] to nanoscale structures[14]. In fact, the upper limit of size scale allowing for detecting an object's chiroptical effects is on the order of the wavelength of light used to probe the optical activity. In this context, accompanying the development of nano-sciences and technologies, fabrication and investigation of artificial chiral nanostructures, from the molecular level[15] and supramolecular (self-)assemblies[16–18] to hybrid chiral

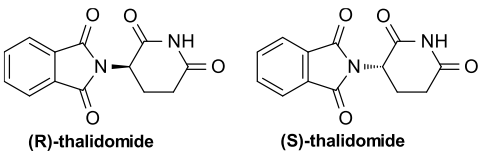

Figure 2. The enantiomers of thalidomide, R and S, can rapidly interconvert (racemize) in body fluids and tissues and form equal concentrations of each form.

nanostructures[14,19,20], have been desirable and attracted interest of researchers all over the world, owing to the vast potential of applications of the chiral nanostructures in biology, pharmacy, chiral catalysis, light manipulation and light-matter interaction (see more in section I.4).

I.2. Chiral inorganic nanostructures

Chiral inorganic nanostructures have been widely investigated in recent years for the following reasons: 1. Such nanostructures exhibit in many cases stronger chiroptical properties by orders of magnitude compared to molecules; 2. They offer more possibilities to be scaled up to metamaterials and metadevices[21]; 3. many fabrication routes are available besides chemical synthesis.

To date, chiral inorganic nanostructures can be classified in various categories, which we will develop in this section: 1. Nanocrystals with intrinsic chirality; 2. individual nanoparticles with chiral shape; 3. nanoparticles in which the chirality is induced by approaching chiral / achiral molecules / ligands; 4. achiral nanoparticles arranged in chiral configurations.

I.2.1. Nanocrystals with intrinsic chirality

The asymmetrical arrangement of atoms or molecules in a crystal lattice is an evident origin of chirality. When dealing with crystals, it involves three levels of chirality: 1. Chirality of the molecule; 2. Chirality of the space group; 3. Chirality of the crystal.[22] One could apply the following dendrogram (***Scheme 1***) to determine the chirality of a crystal.

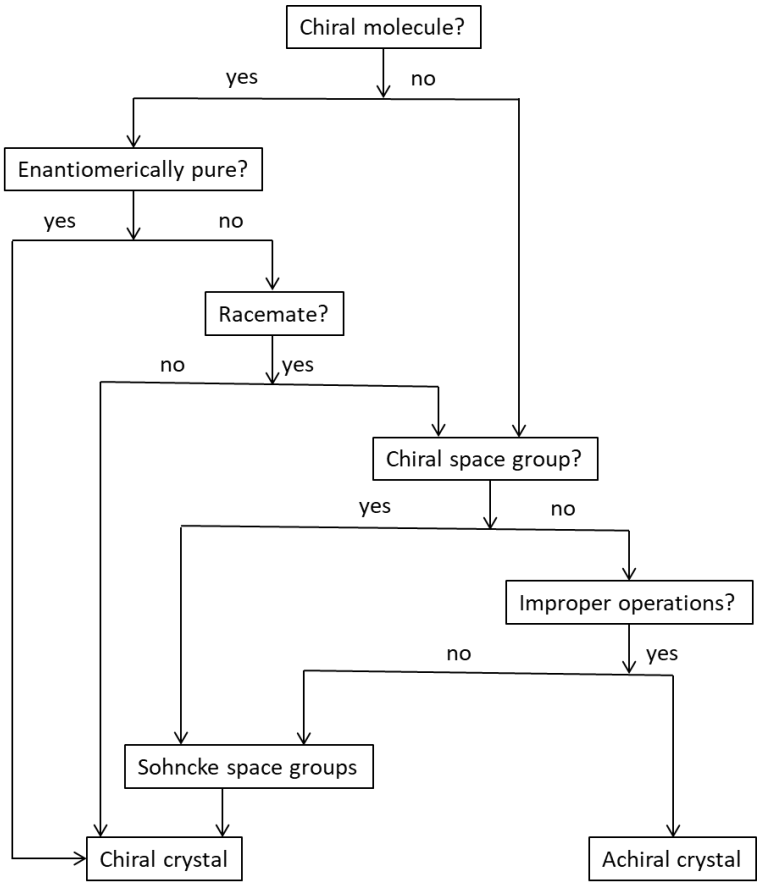

Scheme 1. Determination of crystal chirality

Whether a crystal or an object is chiral or achiral depends on its symmetry group. The symmetry group of a molecule is its point group, that of a crystal is its space group, and that of a space group is its Euclidean normalizer.[23]

There is no achiral crystal formed by chiral molecules. The explanation was given by J. Jacques et al.[24] from a symmetry point of view: the symmetry group of an achiral object contains both proper (viz. translations, rotations and screw rotations) and improper symmetry operations (viz. inversion, reflections, roto-inversions, and glide reflections) in equal numbers, whereas that of a chiral object consists of only proper ones. Thus, the space group of an achiral crystal contains at least one improper symmetry operation. When the latter operates intermolecularly, racemates appear. When operating intramolecularly, achiral molecules are indispensable. Consequently, an achiral crystal is formed either from achiral molecules or from racemates, but never from an enantiomerically pure chiral molecule. In another word, when an enantiomerically pure chiral

molecule crystallizes, it always produces a chiral crystal. The same mechanism works for non-racemate mixtures of chiral enantiomers. The best example of a chiral crystal formed of chiral molecules is Louis Pasteur's discovery of molecular chirality by observing the chiral crystal structures of the two enantiomers of sodium ammonium (2R,3R)-tartrate and sodium ammonium (2S,3S)-tartrate.[5] Enantiomers in Pasteur's case both have $P2_12_12$ space group, the chiral crystals of enantiopure opposite enantiomers, however, do not necessarily display identical space groups.[25] A. Berger et al.[26], for instance, reported the preparation of enantiopure planar chiral cyclopalladated 2-[tricarbonyl(h6-phenyl)chromium] pyridine (***Figure 3***A), as its (+)enantiomer crystallizes in the $P2_1$ space group and the (-)enantiomer in $P2_12_12_1$ one.

On the other hand, as for racemates and achiral molecules, one needs to refer to its space group. 22 space groups (11 enantiomer pairs) out of the total 230, are considered to be chiral (***Figure 3***B), which implies by definition chiral crystals, since they include helical operations. 43 other space groups are actually achiral (containing only proper operations and the 2_1-screw rotation), but result in too invariably chiral crystals (***Figure 3***C), because the asymmetry unit for these 43 symmetries cannot be achiral: if it would have been achiral that is, if it would have contained any improper operation, one could describe the same crystal by a higher symmetry space group from the remaining 165 which encompasses that improper operation.[27] These 65 (22 + 43) space groups are called thereby Sohncke groups, and crystals representing these space groups are chiral.

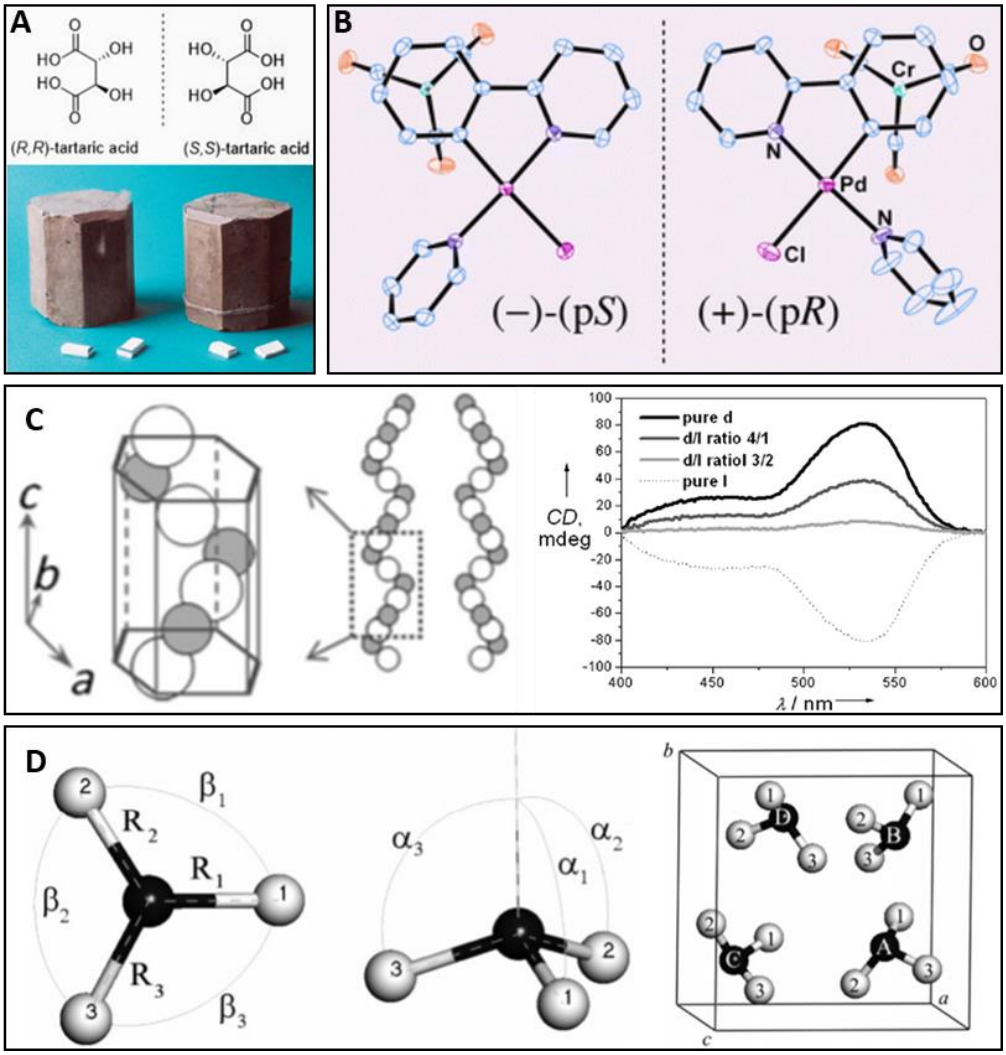

Figure 3. (A) Molecular structure of (R,R)- and (S,S)-tartaric acid (top) and L. Pasteur's own cork models of crystals of sodium ammonium (2R,3R)-tartrate and sodium ammonium (2S,3S)-tartrate.[5] (B) Enantiomers of cyclopalladated 2-[tricarbonyl(h6-phenyl)chromium] pyridine.[26] (C) Schematic illustration of α-HgS nanocrystals in two opposite enantiomorphic space groups, $P3_121$ and $P3_221$ and CD spectra of crystals in different molar ratio of them.[28] (D) Symmetry coordinates of a single NH_3 molecule and its unit cell in a crystal of $P2_13$ group. The molecule and the space group are achiral, while the crystal is.[29]

I.2.2. Individual nanoparticles with chiral shape

Whether a material has an intrinsically chiral crystal structure or not, it is chiral by definition when it has an asymmetrical shape. Nowadays, it is possible to artificially modify the shape of nanoparticles into chiral ones by various strategies (see more in section I.5). Theorists and experimentalists have developed a variety of nanoparticles with different chiral geometries, e.g. tetrahedron (***Figure 4A,B***), metallic clusters (***Figure 4C***), nanohelices (***Figure 4D***), twisted

ribbons (***Figure 4E***), twisted nanorods (***Figure 4F***) and nanotubes (***Figure 4G***), and in diverse materials, e.g. metals (***Figure 4A,C***), semiconductors (***Figure 4B,E,F***), ceramics (***Figure 4D***) and carbonates (***Figure 4G***).

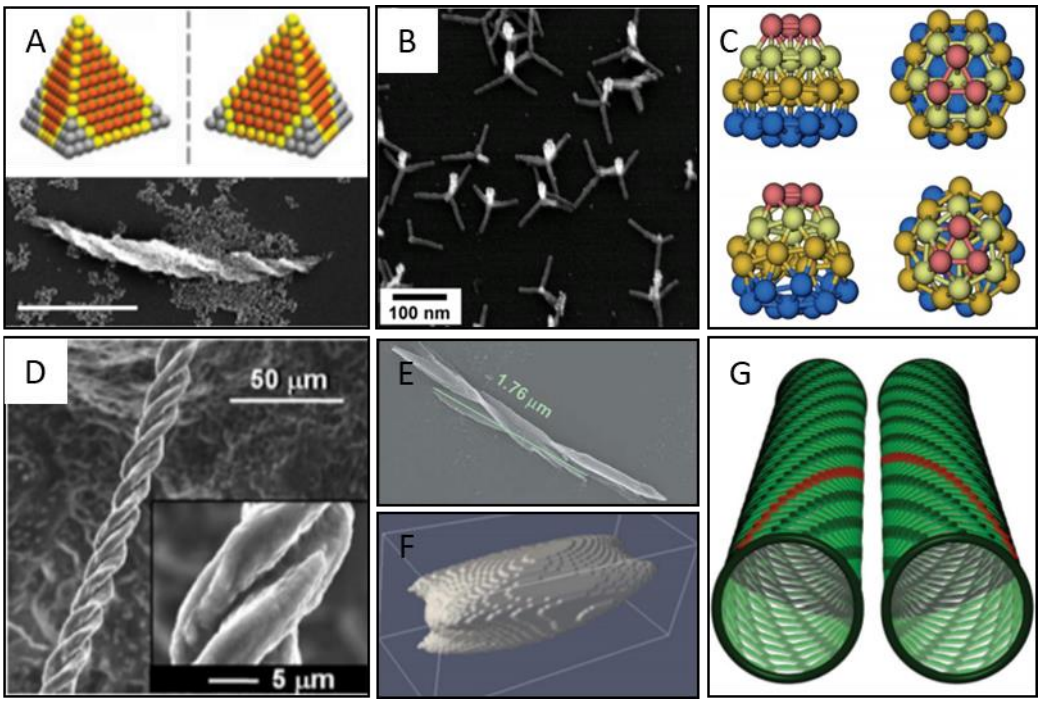

Figure 4. (A) Atomistic models of tetrahedral CdTe nanoparticles with left and right handedness (top) and the SEM image of an experimental assembly of the right handed ones.[30] (B) SEM image of CdTe nano-tetrapods, the bright top arms were modified with Au NPs. Chirality can be induced by respectively modifying each of the four arms.[31,32] (C) Side views (left) and top views (right) of Au_{34} clusters with C_{3v} symmetry (top, achiral) and C_3 symmetry (bottom, chiral).[33] (D)SEM images of a right-handed double helix of silicon (although it is labeled as "left-handed" in the original publication).[34] (E) SEM image of twisted CdTe / CdS nanoribbon.[35] (F) Model chiral shape of twisted tellurium nanorod.[36] (G) Chiral single-walled carbon nanotubes.[37]

Recently, G. González-Rubio et al. reported chiral nanorods with helical wrinkles on the surface (***Figure 5***). Achiral nanorods were used as seeds. Chiral cosurfactants were adsorbed on the surface of the seeds, and directed the seeded growth into chiral nanorods with helical wrinkles on the surface. The obtained chiral nanorods have shown very strong chirality (with g-factors up to 0.2), which depends on the dimensions of the nanorods.

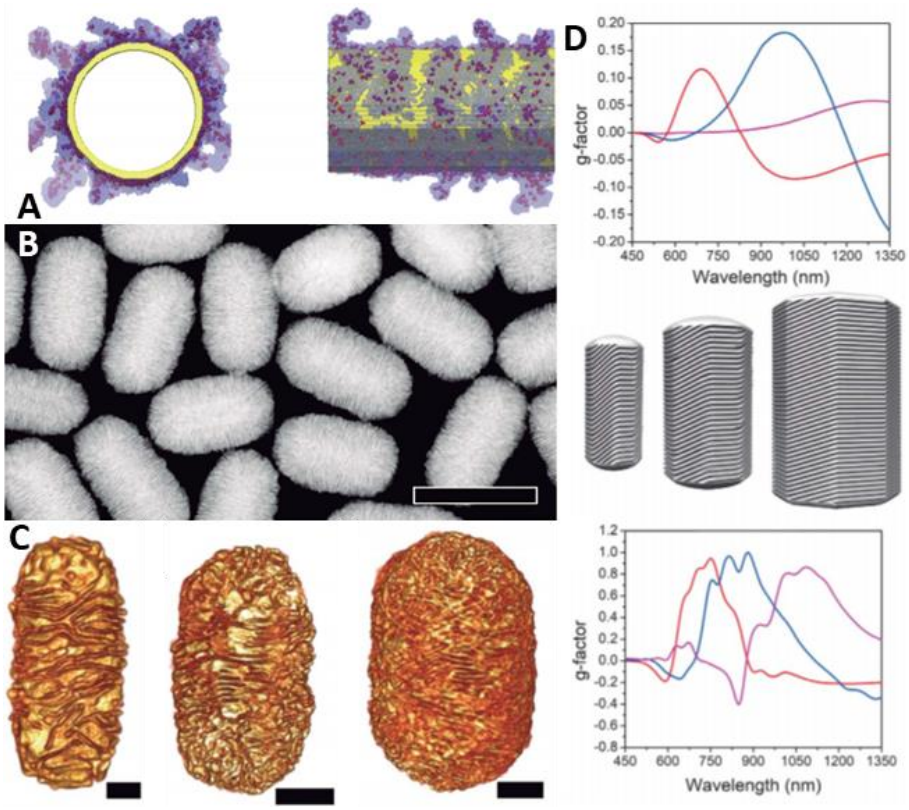

Figure 5. (A) Axial and lateral views of the molecular dynamic simulation of the structure of a right-handed cosurfactant ((R)-BINOL-CTAC) adsorbed on the surface of a gold nanorod. (B) High-angle annular dark-field scanning transmission electron microscopy (HAADF-STEM) image at low magnification of gold nanorods obtained in the presence of a right-handed surfactant ((R)-BINAMINE). (C) Gold nanorods grown with the presence of (R)-BINAMINE of different dimensions. (D) Measured (top) and simulated (bottom) g-factors of the chiral gold nanorods in different dimensions. The gold nanorods from left to right in middle panel correspond to red, blue and magenta lines in the spectra, respectively. All the scale bars are 100 nm.[38]

I.2.3. Nanoparticles with induced chirality

Here we discuss about the chirality induced by surface ligands or molecules on a geometrically symmetrical nanoparticle core. Chiral molecules can impart chirality to closely interacting achiral materials through the chiral field effect (***Figure 6***A-C), which was first demonstrated in 1966[39]. On the other hand, chiral (***Figure 6***D,E) or achiral (***Figure 6***F) surface ligands or molecules may lead to distortion, displacement and / or reconstruction of surface atoms, and thus the destruction of surface symmetry, of the achiral core. It is important to note that the involved surface ligands or molecules are not necessarily chiral. Finally, chirality appears given

the arrangement of the achiral ligands or molecules bound on the particle surface featuring a geometrical handedness (***Figure 6***G-I).

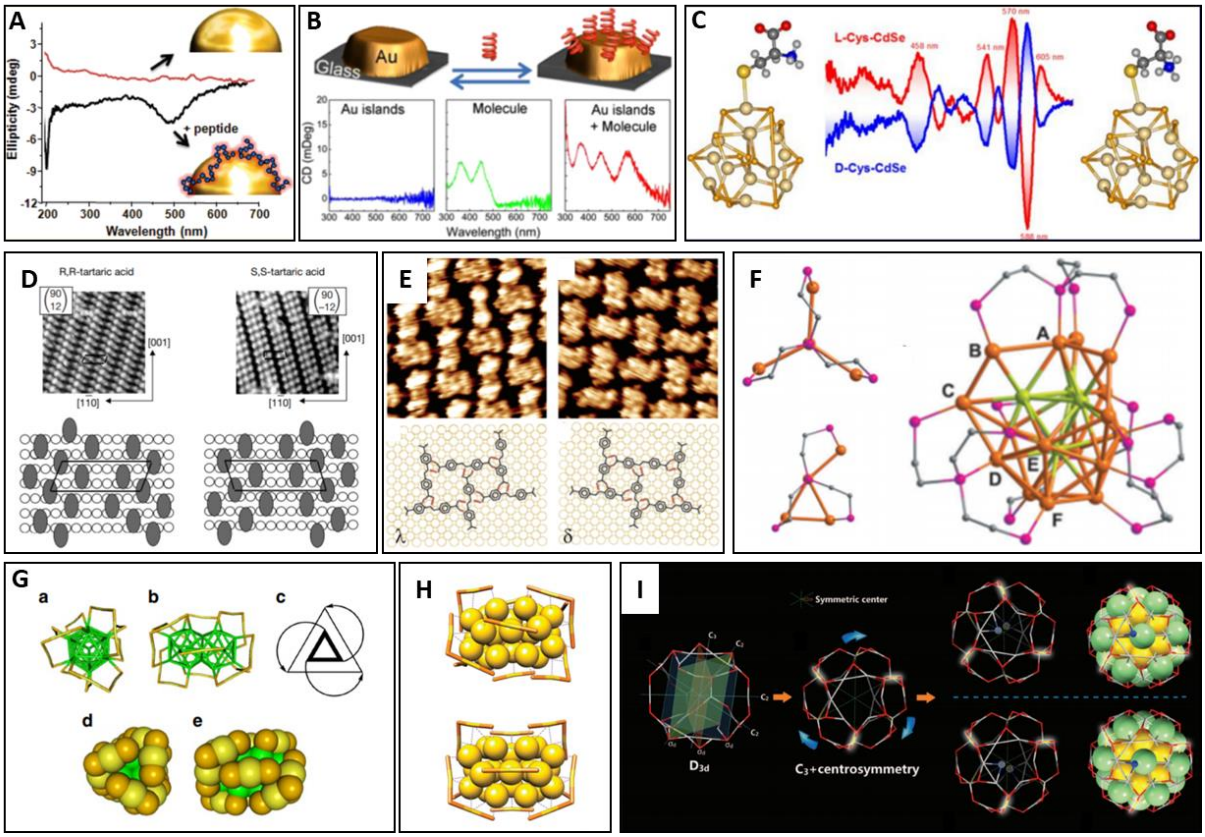

Figure 6. (A) Induced chirality of peptide functionalized gold nanoparticles, CD effects were observed at the plasmonic resonance of the AuNP.[40] (B) Induced chirality of gold nanoparticles by the biomolecule riboflavin, CD not only emerges at the plasmonic resonance of AuNP but also amplifies at biomolecule level.[41] (C) Induced chirality of CdSe quantum dots clusters by chiral thiol capping ligands L- and D-cysteines.[42] (D) STM images of (R,R)- (left) and (S,S)- (right) tartaric acid adsorbed on Cu(110) giving rise to chiral surfaces of Cu.[43] (E) STM images of two enantiomers of chiral stilbene dicarboxylic acid (SDA) bound to Cu(110) leading to chiral configurations Cu surface atoms.[44] (F) Tetradentate phosphine ligands generated chirality of gold nanocluster Au_{20} and two types of the binding modes.[45] (G) Au_{38} clusters protected by achiral ligands. Both the Au_{38} core and the ligands are achiral, while the arrangement of the ligands is chiral.[46] (a) top view; (b) side view; (c) representation of the handedness of arrangement of the ligands; (d) top-view in space-filling representation mode; (e) side-view in space-filling representation mode. (H) Achiral (top) and chiral (bottom) arrangements of thiolate ligands on the surface of Au_{38} cluster.[47] (I) Achiral $Ag_{22}Au_{18}$ core protected by a chiral Au-Ag bimetallic shell.[48]

I.2.4. Achiral nanoparticles arranged in chiral configurations

A large number of research groups all over the world have been making efforts to assemble achiral nanoparticles into chiral configurations, where inter-particle interaction, plasmonic

coupling in particular, engenders chiroptical activity. This sort of chirality opens up the possibilities of hybrid and hierarchical chiroptical systems at the nanoscale and even at larger scales, giving rise to complex superstructures and metamaterials. Superstructures are mesoscale structures composed of nanoobjects assembled with a certain order. Metamaterials are composite materials which exhibit properties that are not found in naturally occurring material, and whose properties depend strongly on the geometrical arrangement of the building blocks rather than of the nature of the constitutive materials.

Figure 7A,B and G depict several examples of chiral plasmonic nanorods dimers, while chiral configurations, such as helices (***Figure 7***D, F) and pyramids (***Figure 7***E), based on plasmonic spherical nanoparticles, are also demonstrated. More complex chiral nanostructures were achieved, such as chiral nanocomposites (***Figure 7***C), multilayer chiral film (***Figure 7***H) and switchable chiral systems (***Figure 7***I). The fabrication approaches leading to such nanostructures will be discussed in section I.5.

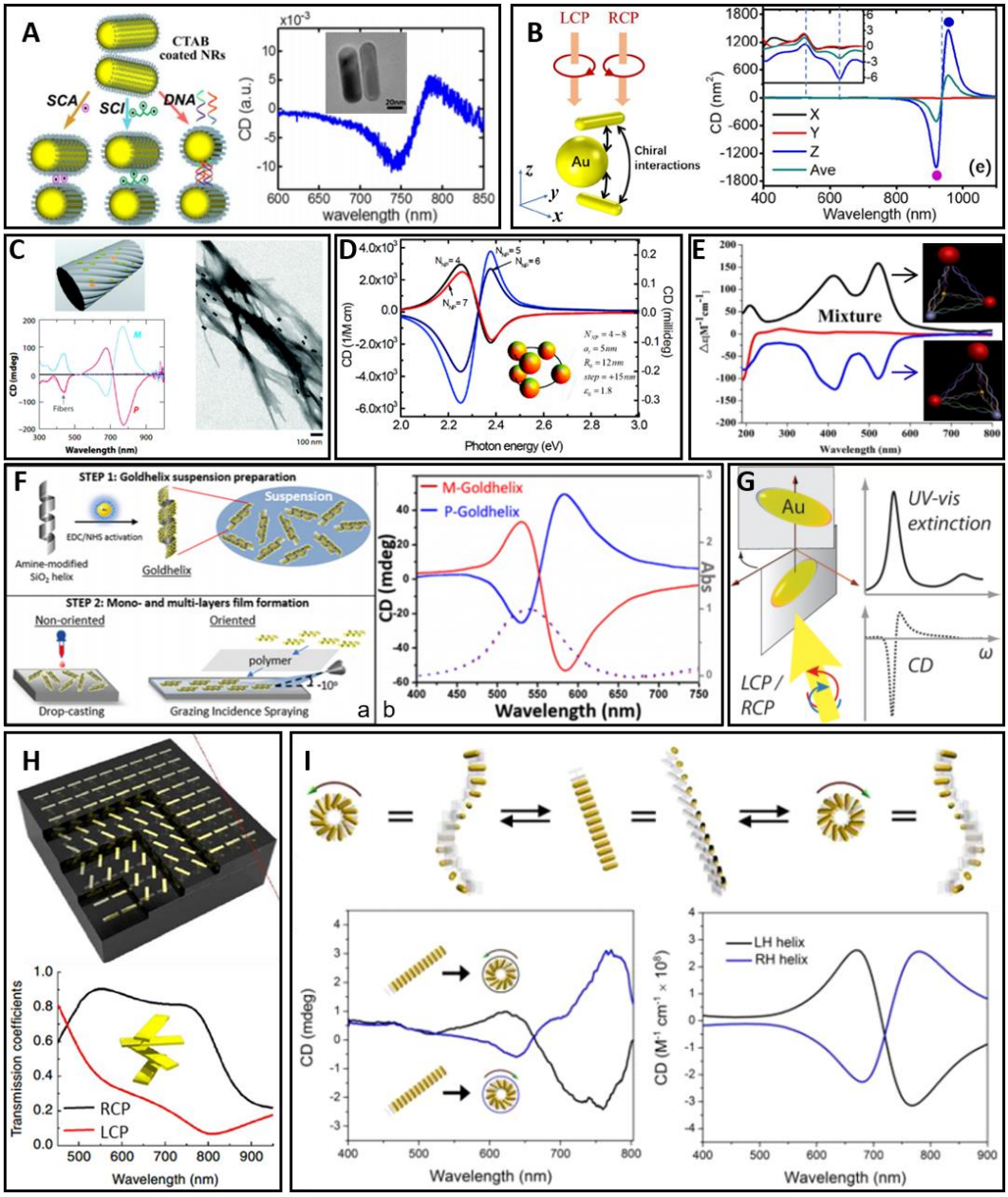

Figure 7. (A) Schematics of chiral dimers of Au nanorods made with sodium citrate (SCI), sodium carbonate (SCA) and DNA (left); TEM image of a twisted dimer and its CD spectrum (right).[49] (B) Au NR-NP-NR chiral structure (left) and its CD spectra detected from different directions X, Y and Z (right).[50] (C) TEM image showing Au NRs absorbed on twisted supramolecular M-fibers (right) and experimental CD spectra for right- (P) and left-handed (M) fibers (left).[51] (D) Calculated CD for helices of Au NPs (number of NPs = 4, 5, 6 and 7).[52] (E) CD spectra of nanoparticle pyramids composed of two Au NPs (of different sizes, red), one Ag NP (grey) and one CdSe@ZnS QD (yellow) of R / S – enantiomers and their mixture.[53] (F) (a) Step 1: Covalent grafting of GNPs on silica nanohelices to form a Goldhelix suspension in water. Step 2: Formation of nonoriented and oriented films by drop-casting and grazing incidence spraying; (b) CD spectra (solid lines) and extinction spectra (dashed lines) of the right-handed (P-Goldhelix) and left-handed (M-Goldhelix) Goldhelix suspension.[54] (G) Au nanorod dimer with certain inter-particle separation and relative orientation (left) and simulated chiroptical responses (right).[55] (H) Multilayer chiral metamaterial composed of 4 layers of Au NRs (top) and its selective transmissions for LCP and RCP (bottom).[56] (I) DNA-Guided Plasmonic Helix with Switchable Chirality.[57]

I.3. Introduction to the localized surface plasmon resonance

In recent years, surface plasmon based structures and devices have emerged as one of the major directions in fundamental and applied research in the nanoscience community. Proposed in 1952 by D. Pines and D. Bohm[58], a plasmon is a quantum of plasma oscillation, or in another word, the oscillation of the electron gas with respect to the fixed positive ions constituting the metal. They can manifest themselves as freely propagating electron density waves along metal surfaces or as localized electron oscillations in metallic nanoparticles. Just like photon is the quantization of the electromagnetic field, plasmon can be recognized as a quasiparticle, which can couple with the photon to create another quasiparticle called a plasmon polariton. In order to understand the nature of plasmons and plasmon polaritons, the interaction of metals with an electromagnetic field has to be introduced.

I.3.1. Electrodynamics of metallic particles

The interactions between metals and electromagnetic fields is determined by the Maxwell's equations, which dictate the highly frequency-dependent complex dielectric function of metals. This dielectric function explains the response of the medium to the external electromagnetic field, while the underlying physics is the change of the induced polarization of the free electron gas according to the driving fields.

$$\nabla \cdot \mathbf{D} = \rho_{\text{ext}} \qquad \textit{(1.a)}$$

$$\nabla \cdot \boldsymbol{B} = 0 \qquad \textit{(1.b)}$$

$$\nabla \times \mathbf{E} = -\frac{\partial \boldsymbol{B}}{\partial t} \qquad \textit{(1.c)}$$

$$\nabla \times \mathbf{H} = \mathbf{J_{ext}} + \frac{\partial \boldsymbol{D}}{\partial t} \qquad \textit{(1.d)}$$

The Maxwell's equations (1) describe the four fundamental electromagnetic fields and their relations in a medium: D (dielectric displacement), E (electric field), H (magnetic field) and B

(magnetic induction), and Jext and ρext are the external current and charge densities. Furthermore, D and E, as well as H and B, have following constitutive relations linked via the polarization P and magnetization M:

$$\mathbf{D} = \varepsilon_0 \boldsymbol{E} + \boldsymbol{P} \tag{2.a}$$

$$\mathbf{H} = \frac{1}{\mu_0} \boldsymbol{B} - \boldsymbol{M} \tag{2.b}$$

where ε0 and μ0 are the permittivity and permeability of vacuum, respectively. In a linear (P and M vary linearly with respect to E and H) and homogeneous (no coordinate dependence) medium, the constitutive relations can be written as:

$$\mathbf{D} = \varepsilon_0 (1 + \chi_e) \boldsymbol{E} = \varepsilon_0 \varepsilon \boldsymbol{E} \tag{3.a}$$

$$\mathbf{B} = \mu_0 (1 + \chi_m) \boldsymbol{H} = \mu_0 \mu \boldsymbol{H} \tag{3.b}$$

where $\varepsilon = 1 + \chi_e$ and $\mu = 1 + \chi_m$ are defined as the permittivity and permeability of the medium, and χ_e and χ_m are called electric / magnetic susceptibility. Being the main characteristics of a material, ε and μ are complex functions of the angular frequency ω. The real part of the permittivity is responsible for the polarization of the material, while the imaginary part for the losses. The $\varepsilon = \varepsilon_1(\omega) + i\varepsilon_2(\omega)$ relation is also known as the dielectric function. The optical properties of a metal over a wide frequency range, including the plasmonic resonance, can be transferred into the problem of solving this dielectric function.

Consider the free electron gas of a metal in an external electric field **E** (the Lorentz force due to the magnetic field can be neglected given that the velocity of the electrons is much lower than the velocity of light), the equation of motion of an electron can be written as:

$$m\ddot{\boldsymbol{x}} + m\gamma\dot{\boldsymbol{x}} = -e\boldsymbol{E} \tag{4}$$

where m and e are the effective mass and charge of an electron, and γ is the inverse of the relaxation time τ of electron (i.e. the mean time between damping collisions of electrons with the metal cations).

For a time-harmonic plane wave, the **E** field is given in the following form with no space dependence taken into account since the velocity of the electrons is estimated much smaller than that of an electromagnetic wave (c):

$$\boldsymbol{E}(t) = \boldsymbol{E_0} e^{-i\omega t} \quad \textbf{(5)}$$

Combining equation ***(5)*** and ***(4)*** leads to a differential equation whose solution is:

$$\mathbf{x}(\mathrm{t}) = \frac{e}{m(\omega^2 + i\gamma\omega)} \boldsymbol{E}(t) \quad \textbf{(6)}$$

This equation of motion reveals that the electrons oscillate in space with the frequency and phase of the external field.

The collective polarization of the free electron gas can be given by:

$$\boldsymbol{P} = -ne\boldsymbol{x} = -\frac{ne^2}{m(\omega^2 + i\gamma\omega)} \boldsymbol{E}(t) \quad \textbf{(7)}$$

n being the volumic density of electrons. Inserting equation ***(7)*** into ***(2.a)*** yields:

$$\boldsymbol{D} = \varepsilon_0 \left[1 - \frac{ne^2}{\varepsilon_0 m(\omega^2 + i\gamma\omega)}\right] \boldsymbol{E}(t) \quad \textbf{(8)}$$

thus,

$$\varepsilon = 1 - \frac{ne^2}{\varepsilon_0 m(\omega^2 + i\gamma\omega)} = 1 - \frac{\omega_p^2}{\omega^2 + i\gamma\omega} \quad \textbf{(9)}$$

This frequency dependent dielectric function is known as the Drude Model, where $\omega_p^2 = \frac{ne^2}{\varepsilon_0 m}$ is defined as the plasma frequency of the free electron gas. For real metals, one needs to integrate also the bound electrons, this equation should then be modified with a dielectric constant ε_∞ (normally $1 \leq \varepsilon_\infty \leq 10$), responsible for the polarization of the bound electrons in response to external electromagnetic fields:

$$\varepsilon = \varepsilon_\infty - \frac{\omega_p^2}{\omega^2 + i\gamma\omega} \quad \textbf{(10)}$$

Consequently, one is capable to extract the real and imaginary components of this complex dielectric function of metal, noting that $\varepsilon = \varepsilon_1(\omega) + i\varepsilon_2(\omega)$:

$$\varepsilon_1(\omega) = \varepsilon_\infty - \frac{\omega_p^2 \tau^2}{1 + \omega^2 \tau^2} \quad \textbf{(11.a)}$$

$$\varepsilon_2(\omega) = \frac{\omega_p^2 \tau}{\omega(1 + \omega^2 \tau^2)} \quad \textbf{(11.b)}$$

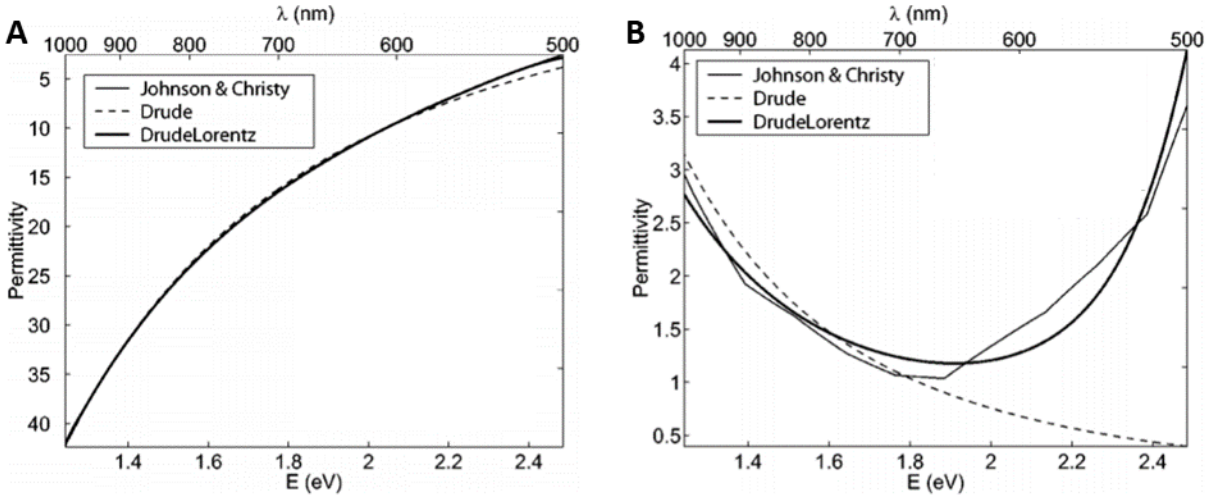

Figure 8. Real part (A) and imaginary part (B) of dielectric function ε(ω) using Drude model and Drude-Lorentz model fitted to the experimental dielectric data for gold.[59,60]

As we can see in ***Figure 8***, the Drude model fits pretty well the measured dielectric function of gold at low frequency, while the fitting of its imaginary part in the visible range deviates strongly from the experimental data. This absorption can be explained by the interband transitions of gold which are not included in the Drude model. For many metals, interband transitions occur for energies larger than 2 eV (corresponding to a wavelength of 620 nm), which is also responsible for the orange and yellow color of copper and gold. Colorless silver, on the other hand, has its interband transitions for higher energies (starting from 4 eV, corresponding to ultraviolet range), which makes it an ideal candidate for plasmonic materials in the visible range. In order to overcome the inadequacy of the Drude model in describing the dielectric function of metals in the UV-Vis range, the Drude model should be replaced by the Drude-Lorentz model by adding one or more Lorentz-oscillator terms of the form $\frac{A_i}{\omega_i^2 - \omega^2 - i\gamma_i \omega}$ to the Drude model in equation ***(10)***.

The dielectric function allows retrieving the response of a metal to an external electric field depending on its frequency. At optical frequencies, the complex refractive index $\tilde{n}(\omega) =$

$n(\omega) + i\kappa(\omega) = \sqrt{\varepsilon\mu} = \sqrt{\varepsilon}$, assuming that $\mu = 1$ for non-magnetic materials. We have therefore:

$$n^2 = \frac{\varepsilon_1}{2} + \frac{1}{2}\sqrt{\varepsilon_1^2 + \varepsilon_2^2} \qquad \textbf{(12.a)}$$

$$\kappa = \frac{\varepsilon_2}{2n} \qquad \textbf{(12.b)}$$

where the real part n of the complex refractive index indicates the phase velocity, and the imaginary part κ is called the extinction coefficient indicating optical absorption of the electromagnetic wave propagating through the medium. The extinction coefficient κ is therefore linked to the absorption coefficient α of the Beer's law ($I(x) = I_0 e^{-\alpha x}$) by the following equation:

$$\alpha(\omega) = \frac{2\kappa(\omega)\omega}{c} \qquad \textbf{(13)}$$

Similarly, ε_1 and ε_2 can be expressed as function of n and κ:

$$\varepsilon_1 = n^2 - \kappa^2 \qquad \textbf{(14.a)}$$

$$\varepsilon_2 = 2n\kappa \qquad \textbf{(14.b)}$$

Having the dielectric function ***(9)***, we are now ready to derive the responses of the free electron gas of metals to an electromagnetic field.

By solving the Maxwell's equations ***(1)***, the following wave equations of a traveling-wave in both time domain and Fourier domain can be obtained:

$$\nabla \times \nabla \times \mathbf{E} = -\mu_0 \frac{\partial^2 \boldsymbol{D}}{\partial t^2} \qquad \textbf{(15.a)}$$

$$\boldsymbol{k}(\boldsymbol{k} \cdot \boldsymbol{E}) - k^2 \boldsymbol{E} = -\varepsilon(\boldsymbol{k}, \omega)\frac{\omega^2}{c^2}\boldsymbol{E} \qquad \textbf{(15.b)}$$

$\boldsymbol{k}$ being the wavevector. For transversal waves, $\mathbf{k}\cdot\mathbf{E} = 0$, we obtain thus the dispersion relation in following form:

$$k^2 = \varepsilon(\boldsymbol{k}, \omega)\frac{\omega^2}{c^2} \quad \textbf{(16)}$$

For longitudinal waves, we have:

$$\varepsilon(\boldsymbol{k}, \omega) = 0 \quad \textbf{(17)}$$

This implies that longitudinal collective oscillation can only occur at frequencies where ε = 0.

- At low frequencies ($\omega \leq \gamma$), $\varepsilon_1 << \varepsilon_2$, the permittivity is predominantly imaginary and thus we have the real part and imaginary part of the complex refractive index of comparable magnitude:

$$n \approx \kappa = \sqrt{\frac{\varepsilon_2}{2}} = \sqrt{\frac{\tau\omega_p^2}{2\omega}} \quad \textbf{(18)}$$

  In this region, metals are mainly absorbing, with the absorption coefficient being

$$\alpha = \sqrt{\frac{2\omega_p^2\tau\omega}{c^2}} \quad \textbf{(19)}$$

- At optical frequencies ($\gamma \leq \omega \leq \omega_p$), $\varepsilon_2 << \varepsilon_1$, the permittivity ε is predominantly real and negative, and the refractive index of metals is predominantly imaginary. This is a characteristic feature of metals, and in this region the metals are mainly reflective with a reflection coefficient R approximately equal to 1.

- At frequencies $\omega \geqslant \omega_p$, ε is predominantly real and $\varepsilon = 1 - \frac{\omega_p^2}{\omega^2}$. Metals are transparent in this spectral region and behave as a dielectric. In particular at $\omega = \omega_p$ and ε = 0, the metals exhibit a volume plasmon resonance and have a maximum transmission coefficient approximately equal to 1. Inserting ε into equation ***(15.a),*** we can obtain the dispersion relation of the free electron gas of metal[61]:

$$\omega^2 = \omega_p^2 + k^2c^2 \quad \textbf{(20)}$$

According to equation ***(17)***, $\varepsilon = 0$ means that ω_p corresponds to the collective longitudinal oscillation of the free electron gas. The plasma frequency ω_p is therefore recognized as the natural frequency of the free oscillation of the electron gas. The quanta of this oscillation of free electron gas (plasma) is called plasmon, or volume plasmon (bulk plasmon) to distinguish from surface plasmon.

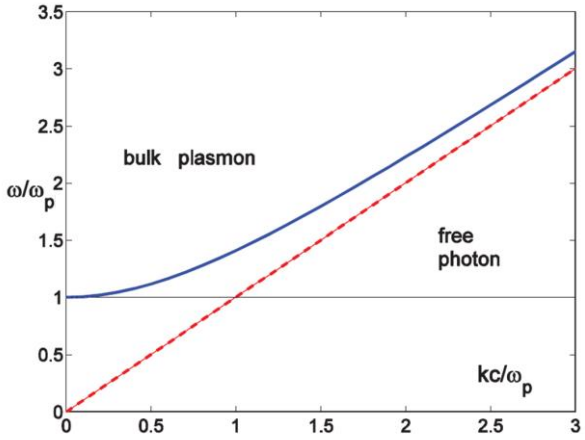

Figure 9. Dispersion relation of volume plasmon. Electromagnetic propagation is only allowed for $\omega > \omega_p$.[61]

I.3.2. Surface plasmon polariton

A plasmon is the quanta of the oscillation of the free electron gas. A surface plasmon is the plasmon existing at the interface between a dielectric and a metal. A surface plasmon polariton (SPP) is the evanescently confined electromagnetic wave propagating along the interface, arising from the coupling of the surface plasmon with external electromagnetic fields. Polaritons are defined as quasiparticles resulting from strong coupling of electromagnetic waves with an electric or magnetic dipole-carrying excitation. There exist in fact polaritons of various origins, for instance, exciton polaritons resulting from the coupling of photons with electron-hole pairs, phonon polaritons from transverse optical phonons in polar lattice, ionic polaritons from ionic charges, Cooper-pair polaritons from Cooper-pair of superconductors, and finally surface plasmon polaritons.

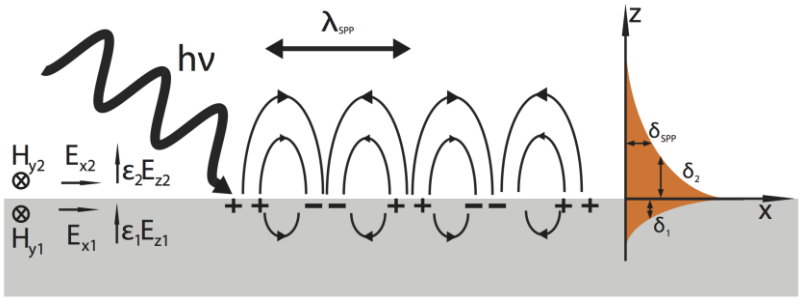

Figure 10. Surface plasmon polariton[62]

To examine the propagating properties of SPP, we need to first solve its wave equation. By calculating the curl of the curl equation from Maxwell's equations in ***(1.c)***, and assuming that there is no external free charge ($\rho_{ext} = 0$) nor current ($\mathbf{j} = 0$), it is easy to obtain the homogeneous wave equation for a non-magnetic ($\mu = 1$) medium in free space:

$$\nabla^2 \boldsymbol{E} - \frac{\varepsilon}{c^2}\frac{\partial^2 \boldsymbol{E}}{\partial t^2} = 0 \qquad \textbf{(21.a)}$$

Similarly,

$$\nabla^2 \boldsymbol{H} - \frac{\varepsilon}{c^2}\frac{\partial^2 \boldsymbol{H}}{\partial t^2} = 0 \qquad \textbf{(21.b)}$$

The solutions to equation ***(21)*** for electromagnetic plane waves in free space are thus:

$$\boldsymbol{E}(\boldsymbol{r}, t) = \boldsymbol{E_0} e^{-i\omega t + i\boldsymbol{k}\boldsymbol{r}} \qquad \textbf{(22.a)}$$

$$\boldsymbol{H}(\boldsymbol{r}, t) = \boldsymbol{H_0} e^{-i\omega t + i\boldsymbol{k}\boldsymbol{r}} \qquad \textbf{(22.b)}$$

Considering a SPP as a wave propagating at the interface along the x direction and decaying in the z direction, and assuming **E** and **H** to be independent on y, equations ***(22)*** can be rewritten as:

$$\boldsymbol{E} = \boldsymbol{E_{0(z)}} e^{-i\omega t + ik_x x} \quad \textbf{(23.a)}$$

$$\boldsymbol{H} = \boldsymbol{H_{0(z)}} e^{-i\omega t + ik_x x} \quad \textbf{(23.b)}$$

The problem here is to obtain the wave equations of SPP in explicit forms and its dispersion relations starting from Maxwell's equations. By expanding ***(1.c)*** and ***(1.d)*** with $\frac{\partial}{\partial t} = -i\omega$ (for harmonic time dependence), we arrive at the following set of equations:

$$\frac{\partial E_x}{\partial y} - \frac{\partial E_y}{\partial x} = -i\mu_0 \omega H_z \quad \textbf{(24.a)}$$

$$\frac{\partial E_z}{\partial x} - \frac{\partial E_x}{\partial z} = -i\mu_0 \omega H_y \quad \textbf{(24.b)}$$

$$\frac{\partial E_y}{\partial z} - \frac{\partial E_z}{\partial y} = -i\mu_0 \omega H_x \quad \textbf{(24.c)}$$

$$\frac{\partial H_x}{\partial y} - \frac{\partial H_y}{\partial x} = i\varepsilon\varepsilon_0 \omega E_z \quad \textbf{(24.d)}$$

$$\frac{\partial H_z}{\partial x} - \frac{\partial H_x}{\partial z} = i\varepsilon\varepsilon_0 \omega E_y \quad \textbf{(24.e)}$$

$$\frac{\partial H_y}{\partial z} - \frac{\partial H_z}{\partial y} = i\varepsilon\varepsilon_0 \omega E_x \quad \textbf{(24.f)}$$

For propagation along x-direction ($\frac{\partial}{\partial x} = ik_x$) and homogeneity in y-direction ($\frac{\partial}{\partial y} = 0$), one is capable of obtaining the Helmholtz equations according to ***(21)*** and ***(24)*** for transverse magnetic (TM) polarization, where E_x, E_z and H_y are nonzero,

$$\frac{\partial^2 H_y}{\partial z^2} - \left(k_x^2 - \varepsilon \frac{\omega^2}{c^2}\right) H_y = 0 \quad \textbf{(25.a)}$$

$$E_x = \frac{-i}{\varepsilon\varepsilon_0 \omega} \frac{\partial H_y}{\partial z} \quad \textbf{(25.b)}$$

$$E_z = \frac{-k_x}{\varepsilon\varepsilon_0 \omega} H_y \quad \textbf{(25.c)}$$

and for transverse electric (TE) polarization, where H_x, H_z and E_y are nonzero:

$$\frac{\partial^2 E_y}{\partial z^2} - \left(k_x^2 - \varepsilon \frac{\omega^2}{c^2}\right) E_y = 0 \quad \textbf{(26.a)}$$

$$H_x = \frac{i}{\mu_0 \omega} \frac{\partial E_y}{\partial z} \quad \textbf{(26.b)}$$

$$H_z = \frac{k_x}{\mu_0 \omega} E_y \quad \textbf{(26.c)}$$

The general solution of Helmholtz equation in upper and in lower medium could be written in the following form for TM polarization:

Upper medium:

$$\mathrm{H}_{y2}(z) = H_{y2,0}e^{ik_x x}e^{-k_{z2}z} \quad \textbf{(27.a)}$$

$$E_{x2}(z) = \frac{ik_{z2}}{\varepsilon_2\varepsilon_0\omega}H_{y2,0}e^{ik_x x}e^{-k_{z2}z} \quad \textbf{(27.b)}$$

$$E_{z2}(z) = \frac{-k_x}{\varepsilon_2\varepsilon_0\omega}H_{y2,0}e^{ik_x x}e^{-k_{z2}z} \quad \textbf{(27.c)}$$

Lower medium:

$$\mathrm{H}_{y1}(z) = H_{y1,0}e^{ik_x x}e^{k_{z1}z} \quad \textbf{(27.d)}$$

$$E_{x1}(z) = -\frac{ik_{z1}}{\varepsilon_1\varepsilon_0\omega}H_{y1,0}e^{ik_x x}e^{k_{z1}z} \quad \textbf{(27.e)}$$

$$E_{z1}(z) = -\frac{k_x}{\varepsilon_1\varepsilon_0\omega}H_{y1,0}e^{ik_x x}e^{k_{z1}z} \quad \textbf{(27.f)}$$

where x, y and z subscripts indicate the components in different directions, and 1 and 2 subscripts indicate the upper and lower medium, respectively.

Inserting ***(27.a)*** into ***(25.a)***, we have

$$k_{z2}^2 H_y - \left(k_x^2 - \varepsilon_2\frac{\omega^2}{c^2}\right)H_y = 0 \quad \textbf{(28)}$$

Thus,

$$k_{z2}^2 = k_x^2 - \varepsilon_2\frac{\omega^2}{c^2} \quad \textbf{(29.a)}$$

Similarly,

$$k_{z1}^2 = k_x^2 - \varepsilon_1\frac{\omega^2}{c^2} \quad \textbf{(29.b)}$$

The boundary conditions at the interface requires that:

$$\mathrm{H}_{y1}(0) = \mathrm{H}_{y2}(0) \quad \textbf{(30.a)}$$

$$E_{x1}(0) = E_{x2}(0) \quad \textbf{(30.b)}$$

Thus,

$$\mathrm{H}_{y1,0} = \mathrm{H}_{y2,0} \quad \textbf{(31.a)}$$

$$\frac{k_{z1}}{\varepsilon_1} + \frac{k_{z2}}{\varepsilon_2} = 0 \quad \textbf{(31.b)}$$

Since both k_{z1} and k_{z2} have positive signs for a wave evanescently confined and decaying in z-direction, it tuns out to be indispensable that the two mediums have permittivity with real part of opposite signs (for example a dielectric and a metal) for the surface wave to exist at their interface.

Furthermore, by solving the system of equations ***(29.a)***, ***(29.b)*** and ***(31.b)***, we have:

$$k_x = \frac{\omega}{c}\sqrt{\frac{\varepsilon_1\varepsilon_2}{\varepsilon_1+\varepsilon_2}} \qquad \textbf{(32)}$$

This is the dispersion relation of SPP for TM polarization.

Similarly, for TE polarization, the field components in upper and lower medium can be expressed as:

Upper medium:

$$E_{y2}(z) = E_{y2,0}e^{ik_x x}e^{-k_{z2}z} \qquad \textbf{(33.a)}$$

$$H_{x2}(z) = -\frac{ik_{z2}}{\mu_0\omega}E_{y2,0}e^{ik_x x}e^{-k_{z2}z} \qquad \textbf{(33.b)}$$

$$H_{z2}(z) = \frac{k_x}{\mu_0\omega}E_{y2,0}e^{ik_x x}e^{-k_{z2}z} \qquad \textbf{(33.c)}$$

Lower medium:

$$E_{y1}(z) = E_{y1,0}e^{ik_x x}e^{k_{z1}z} \qquad \textbf{(33.d)}$$

$$H_{x1}(z) = \frac{ik_{z1}}{\mu_0\omega}E_{y1,0}e^{ik_x x}e^{k_{z1}z} \qquad \textbf{(33.e)}$$

$$H_{z1}(z) = \frac{k_x}{\mu_0\omega}E_{y1,0}e^{ik_x x}e^{k_{z1}z} \qquad \textbf{(33.f)}$$

The boundary conditions at the interface requires that:

$$\mathrm{H}_{x1}(0) = \mathrm{H}_{x2}(0) \qquad \textbf{(34.a)}$$

$$E_{y1}(0) = E_{y2}(0) \qquad \textbf{(34.b)}$$

It turns out:

$$E_{y1}(0)(k_{z1} + k_{z2}) = 0 \qquad \textbf{(35)}$$

Both k_{z1} and k_{z2} are positive, so $E_{y1}(0) = E_{x2}(0) = 0$, and thus no surface mode can exist for TE polarization. In other words, surface plasmon polariton only exists for TM polarization.

With the dispersion relation ***(32)***, we can now plot the dispersion curve of SPP (***Figure 11***)[63]. The dispersion curve of volume plasmon (radiative mode) and SPP (bound mode) divide the whole dispersion plane into three regions. In the region to the left of the upper branch (radiative mode), the electromagnetic waves are propagating in both dielectric and metal media – the metal acquires a dielectric characteristic. In the region between the upper branch and lower branch, the electromagnetic waves are propagating in the dielectric medium and decaying in the metal medium. In the region to the right of the lower region, the electromagnetic waves are decaying evanescently in both media – they are confined and propagating at the interface.

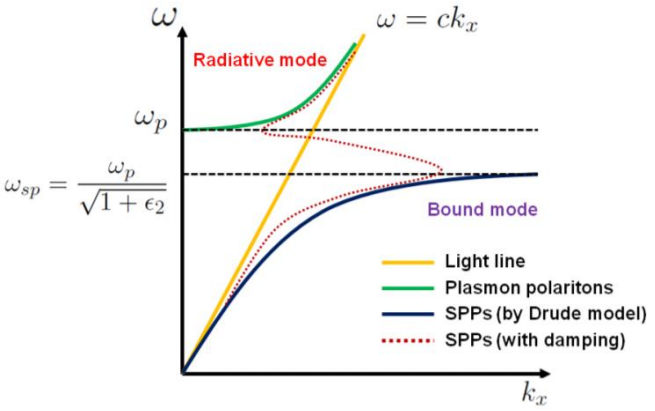

Figure 11. Dispersion relation of SPP from Drude model without damping and a real metal model with damping.[63]

As one can see in the dispersion curve of SPP, the SPP curve does not intersect with the light line. That is to say, a SPP mode has always a momentum mismatch with a photon in air when they are at a resonant frequency. In other words, it is not possible to excite SPPs with light in a direct manner. Several options can be taken to overcome this mismatch of momentum (***Figure 12***), such as frustrated total internal reflection[64,65], grating or notch on the metal surface[66], near field of a tip or light source[67], etc.

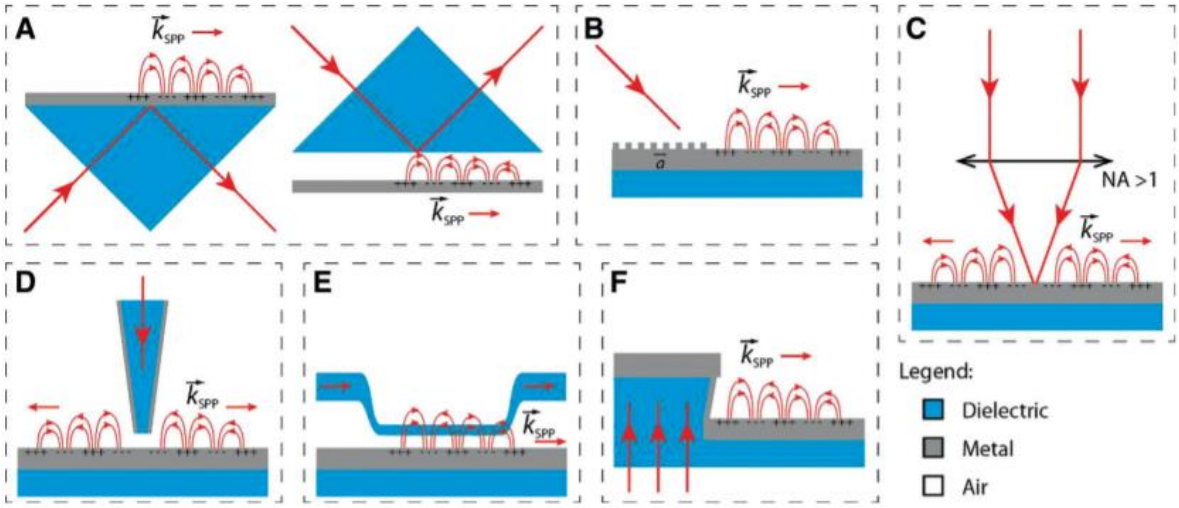

Figure 12. Schematic cartoons illustrating optical excitation schemes for SPPs.[68] (A) Prism coupling schemes, with Kretschmann configuration on the left and Otto configuration on the right. (B) Grating coupling scheme. (C) Highly focused beam coupling scheme. (D) Near-field coupling scheme. (E) End-fire coupling scheme. (F) Step-gap leakage coupling scheme.

I.3.3. Localized surface plasmon resonance

SPPs are evanescently confined and dispersive electromagnetic waves propagating at the interface of a dielectric and a metal. Localized surface plasmons (LSPs) are non-propagating excitation modes of the conduction electrons of metal particles in sub-wavelength scale, due to the coupling with external electromagnetic fields. Generally speaking, it involves the charge density oscillations confined to metallic nanoparticles and metallic nanostructures (***Figure 13***)[69]. Excitation of LSPs by an electric field (light) at an incident wavelength where resonance occurs results in strong light scattering, in the appearance of intense surface plasmon absorption bands, and an enhancement of the local electromagnetic fields. This is what we call localized surface plasmon resonance (LSPR).

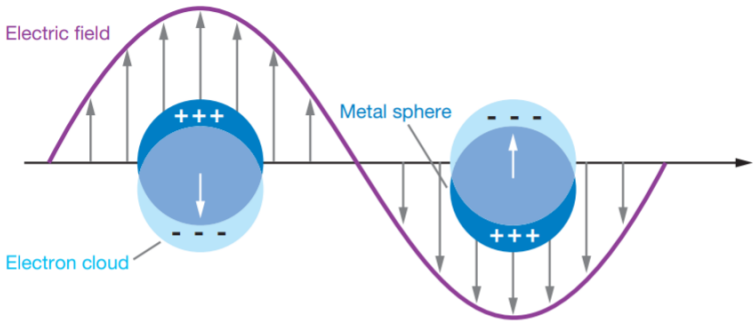

Figure 13. Plasma oscillation of a sphere.[69]

In order to analyze localized surface plasmon resonance, it is easier to start with the simplest geometry, a spherical particle in a quasi-static approximation of subwavelength size, i.e. that $d \leqslant \lambda$.

In the electrostatic approach, the problem turns to be the solution of the Laplace equation for the potential, $\nabla^2 \Phi = 0$.

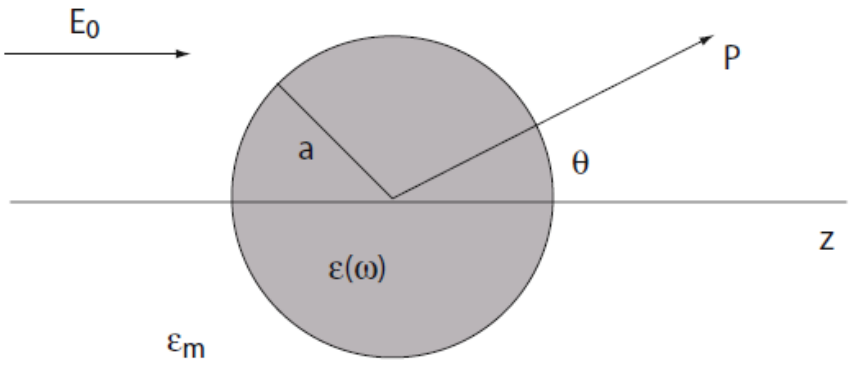

Figure 14. Sketch of a homogeneous sphere placed into an electrostatic field.[70]

The solution of this problem was given by J. D. Jackson[71]:

$$\Phi_{in} = -\frac{3\varepsilon_m}{\varepsilon + 2\varepsilon_m} E_0 r cos\theta \qquad \textbf{(36.a)}$$

$$\Phi_{out} = -E_0 r cos\theta + \frac{\varepsilon - \varepsilon_m}{\varepsilon + 2\varepsilon_m} E_0 a^3 \frac{cos\theta}{r^2} \qquad \textbf{(36.b)}$$

From a physical point of view, Φ_{out} can be regarded as a superposition of the external field E_0 and the field of a dipole due to the polarization of the particle. Thus,

$$\Phi_{out} = -E_0 r cos\theta + \frac{\boldsymbol{p} \cdot \boldsymbol{r}}{4\pi\varepsilon_0\varepsilon_m r^3} \qquad \textbf{(37.a)}$$

$$\boldsymbol{p} = 4\pi\varepsilon_0\varepsilon_m a^3 \frac{\varepsilon - \varepsilon_m}{\varepsilon + 2\varepsilon_m} \boldsymbol{E_0} \qquad \textbf{(37.b)}$$

We can see therefore that the dipole moment inside the particle is induced by the external field. One can introduce the polarizability α, defined by $\mathbf{p} = \varepsilon_0\varepsilon_m\alpha\mathbf{E_0}$, which leads to

$$\alpha = 4\pi a^3 \frac{\varepsilon - \varepsilon_m}{\varepsilon + 2\varepsilon_m} \quad (38)$$

This is the polarizability of a small sphere of sub-wavelength size in the electrostatic approximation. Apparently, α shows a resonant enhancement, when $|\varepsilon + 2\varepsilon_m|$ is minimum. Inserting $\varepsilon = -2\varepsilon_m$ into the Drude model for a metal and neglecting the damping, we obtain the resonance frequency of the localized surface plasmon:

$$\omega_{LSSP} = \frac{\omega_p}{\sqrt{2\varepsilon_m + \varepsilon_\infty}} \quad (39)$$

If $\varepsilon_m = \varepsilon_\infty = 1$ (a Drude metal located in air), $\omega_{LSSP} = \frac{\omega_p}{\sqrt{3}}$.

From the viewpoint of optics, it is interesting to note that another consequence of the resonantly enhanced polarization α is a concomitant enhancement in the efficiency with which a metal nanoparticle scatters and absorbs light. The corresponding cross sections for scattering and absorption C_{sca} and C_{abs} can be calculated via the Poynting-vector[70]:

$$C_{sca} = \frac{k^4}{6\pi}|\alpha|^2 = \frac{8\pi}{3}k^4 a^6 \left|\frac{\varepsilon - \varepsilon_m}{\varepsilon + 2\varepsilon_m}\right|^2 \quad (40.a)$$

$$C_{abs} = kIm[\alpha] = 4\pi k a^3 Im\left[\frac{\varepsilon - \varepsilon_m}{\varepsilon + 2\varepsilon_m}\right] \quad (40.b)$$

Thus, the extinction cross section of a small sphere of sub-wavelength size in the electromagnetic approximation can be written as following:

$$C_{ext} = C_{sca} + C_{abs} = 9\frac{\omega}{c}\varepsilon_m^{3/2} V \frac{\varepsilon_2}{[\varepsilon + 2\varepsilon_m]^2 \varepsilon_2^2} \quad (41)$$

where V is the volume of the sphere, and its dielectric function is $\varepsilon = \varepsilon_1 + i\varepsilon_2$.

For small particles with dimensions below 100 nm, the analysis in electrostatic approximation above is strictly valid, while for larger particles, the electrostatic approximation is no longer justified due to significant phase-changes of the driving field over the particle volume. Gustav Mie developed the so-called Mie theory in order to understand the electromagnetic scattering and absorption of a spherical particle. It was proven to be possible to calculate the polarizability α and the extinction cross section C_{ext} of a sphere of larger diameter free of electrostatic

approximation. Furthermore, the geometry of the nanoparticle has seen also an expansion from sphere to ellipsoid, core shell structure and so on, with specific terms associated with different geometrical factors. In particular, as for anisotropic nanoparticles, multiple LSPR modes may appear at different wavelengths. ***Figure 15***, for instance, shows that transverse and longitudinal modes of LSPR of Au NR manifest themselves by two separate absorption peaks at ~500nm and ~800nm, respectively.

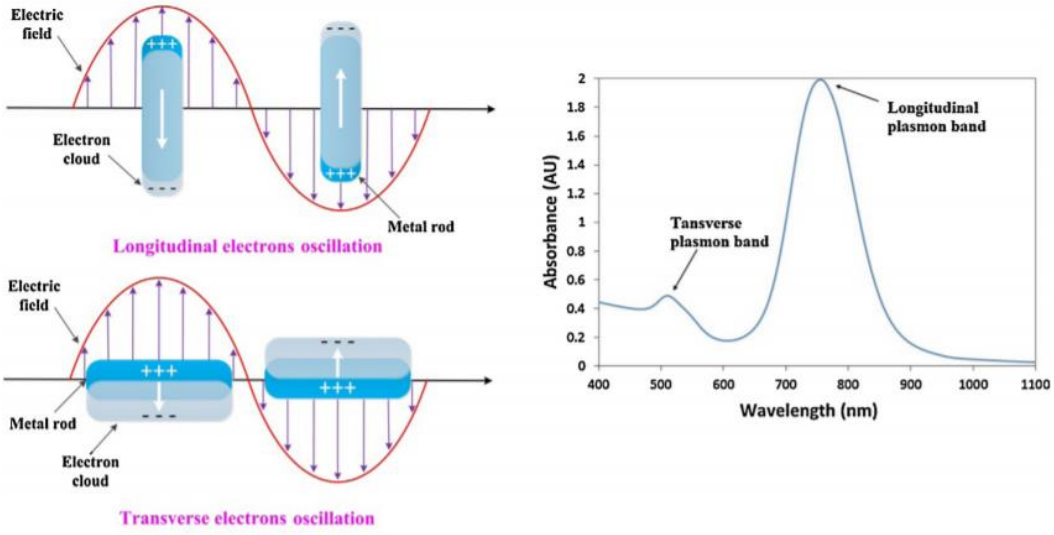

Figure 15. Transverse and longitudinal modes of LSPR of Au NR.[72]

In addition, coupling of a dipolar nature between localized surface plasmons can occur when individual nanoparticles are in close proximity to each other, which leads to a shift in the resonance frequency. The details of these calculations are beyond the scope of this manuscript, while the essence to note here is that the resonance frequency (i.e. extinction wavelength and thus color) and intensity of the LSPR are characteristic of the type of material (typically, gold, silver, or platinum; ***Figure 16***A), and are highly sensitive to the size (***Figure 16***B), the size distribution, the shape of the nanostructures (***Figure 16***C,E), the environments which surround them (***Figure 16***C)[73], and as well as the coupling between the LSPR of individual nanoparticles.

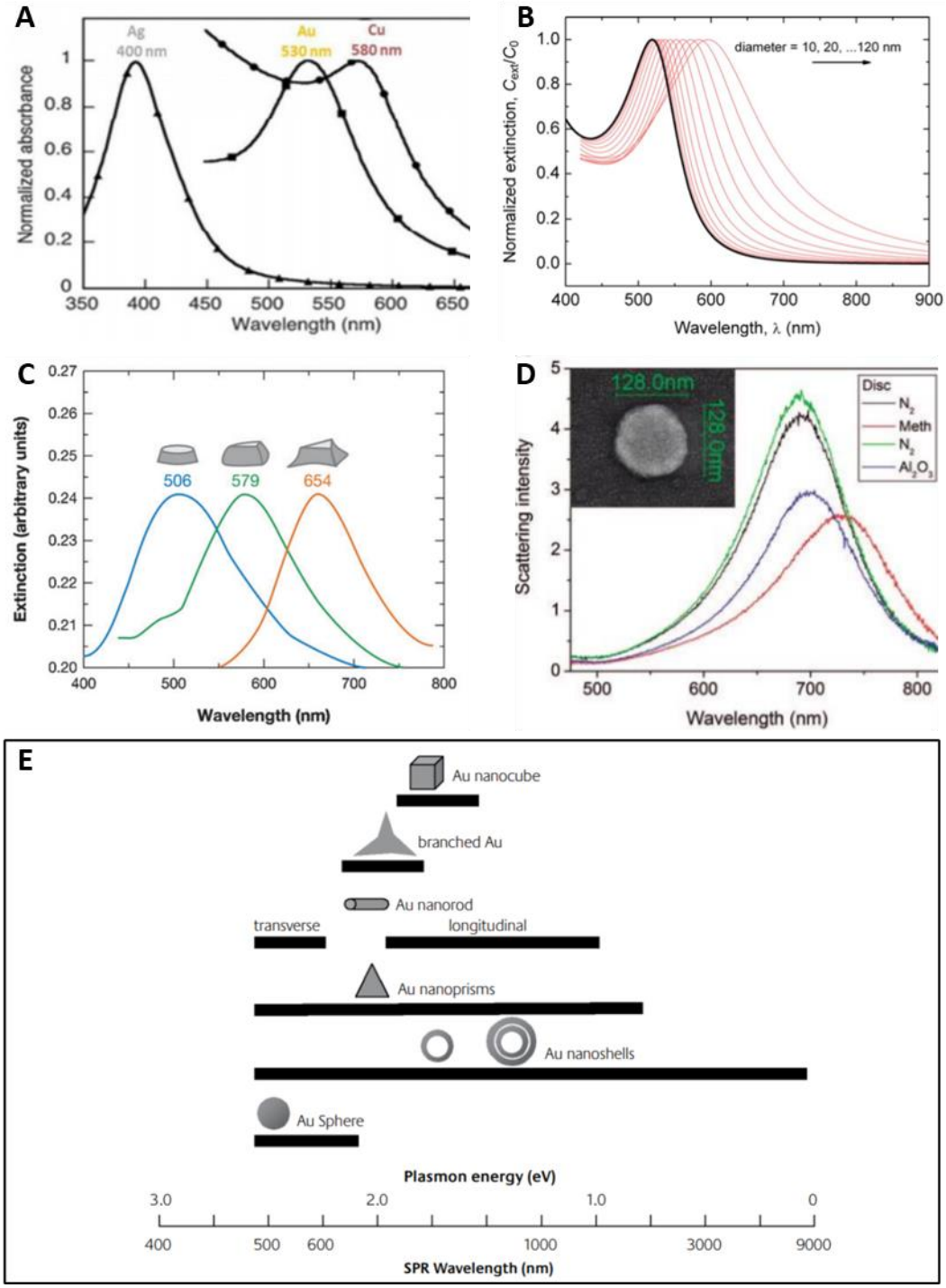

Figure 16. Optical spectra of localized surface plasmon resonance for (A) nanoparticles of different nature.[74] (B) Au NPs of different sizes.[75] (C) Ag NP of different shape.[69] (D) Au NP in different mediums.[76] (E) Range of LSPR of Au NPs depending on their morphology.[77]

Consequently, thanks to its unique ability to confine the incident light and thus enhance the optical responses of the plasmonic systems and allow for characteristic light-matter interactions, including the strong coupling, the plasmon based artificial chiral nanostructures are stepping

into the spotlight.[20] Several examples of chiral plasmonic nanostructures were already illustrated in sections **I.2.3** and **I.2.4** (***Figure 6***, ***Figure 7***), yet their applications are going to be addressed in the following section.

I.4. Applications of chiral plasmonic nanostructures

I.4.1. Biosensing

The excellent ability of LSPR to generate strongly enhanced evanescent fields allows for new possibilities for enantio-recognition / resolution, especially for biosensing, namely probing biomolecules based on the chirality.[78,79]

It has been demonstrated in section I.2.3 (***Figure 6***A,B), that not only the CD signals of a chiral molecule can be amplified when coupled to individual plasmonic nanoparticles, but also new CD peaks appear at the plasmonic resonances,[80,81] due to the exciton-plasmon coupling. This phenomenon was therefore applied to probe chiral biomolecules (***Figure 17***A).[82,83] "Hotspots" of plasmonic dimers (the nanoscale gap between them) can be another alternative to detect chiral biomolecules (***Figure 17***B).[84,85] Finally, chiral plasmonic assemblies and nanostructure have been proven to be effective in tracing not only biomolecules such as markers for a specific disease[86] (***Figure 17***C), but also the concentration of inorganics such as hydrogen[87] (***Figure 17***D).

Molecular chirality (with the dissymmetry factor, g-factors < 10^{-3} in the visible range[88]) is usually much weaker than in plasmonic nanostructures, and in addition, the induced chirality by approaching achiral molecules to chiral ones is even weaker for about an order of magnitude. Therefore, probing molecular chirality by optical methods including CD spectroscopy suffers still from low sensitivity. The strong induced chirality of plasmonic nanostructures allows for a more efficient and sensitive sensing of chiral biomolecules, and quantitative analysis is thus also possible by using the intensity of the CD signal. Furthermore, the molecular transitions are

normally in the UV region, while plasmonic resonances can be found in UV and visible ranges. This leads to a wider use of plasmonic nanostructures in biosensing applications. However, the fabrication of the desired nanostructures can be expensive and time-consuming, and its recognition and / or bonding to biomolecules require also additional efforts.

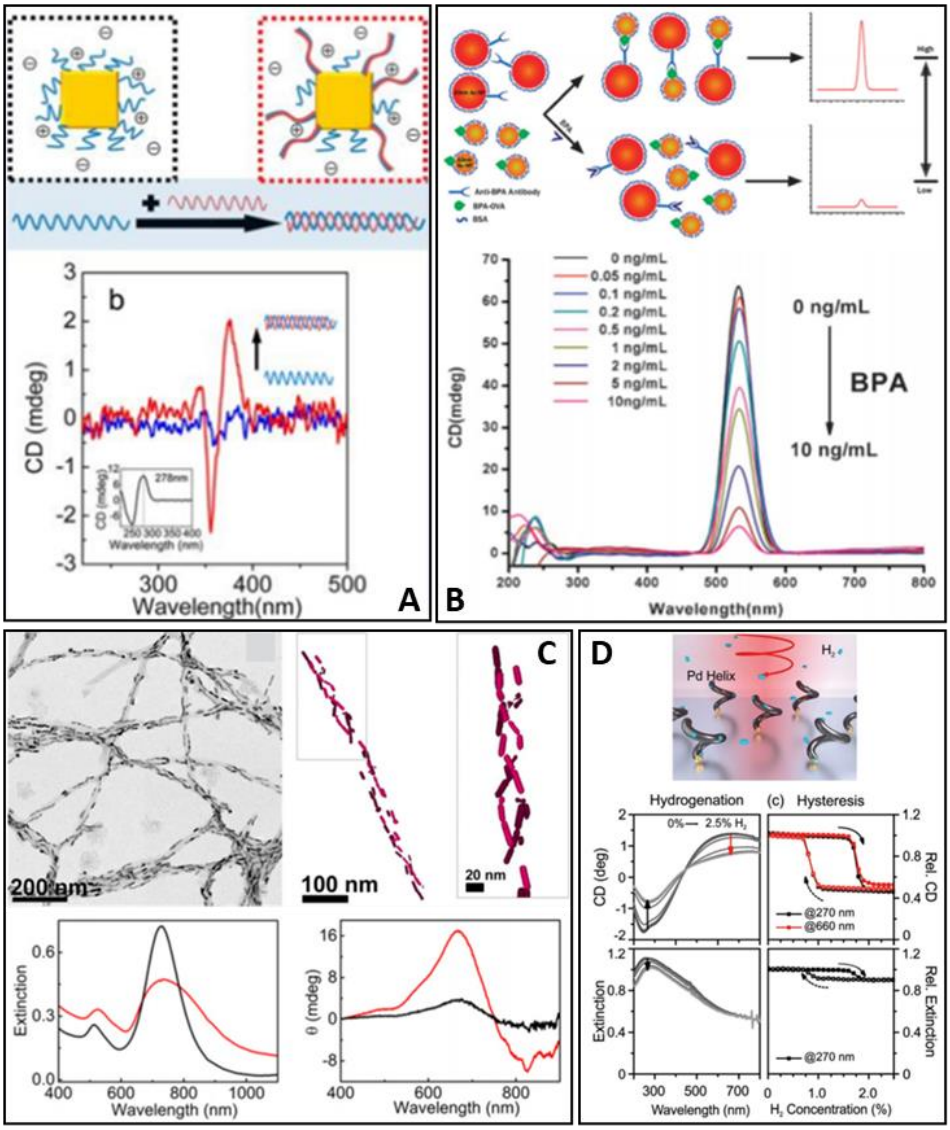

Figure 17. (A) Single-stranded DNA (ssDNA, balck-dotted frame) on a Ag nanocube was exchanged for double-stranded DNA (dsDNA, red-dotted frame) by hybridization (top), and their CD spectra change from no signal (ssDNA, blue curve) to detectable CD signal (dsDNA, red curve).[82] (B) The recognition reaction between an anti-bisphenol A (anti-BPA) antibody attached on a 20 nm Au NP and an antigen coating (BPA-OVA) on a 10 nm Au NP leads to the formation of an asymmetric plasmonic dimer, giving rise to CD signals. The disturbance of this reaction and tailoring of CD intensity by BPA molecules in the medium allows for the detection of BPA concentration with a sensitivity of 0.02 ng/ml.[85] (C) TEM image and Cryo-TEM tomography reconstruction image of Au NRs arranged on chiral α-synuclein fibrils and extinction and CD spectra of Au NRs monitored 30 min after the addition of 30 µL of purified brain homogenates from healthy (black traces) and Parkinson's disease patients (red traces).[86] (D) Chiral Pd helix for hydrogen detection.[87]

I.4.2. Enantio-separation

Given the importance of chirality stated in the previous sections, it has been a major task for chemists to separate and obtain pure enantiomers, especially for pharmacological use. The most commonly used enantio-separation and analysis technique at present is chromatography. However, this technique relies on trial-and-error tests for a given analyte, and thus is expensive and time-consuming when applied to new chiral compounds[89]. It is therefore attractive to develop novel effective and versatile techniques for enantio-separation and analysis.[90] Chiral plasmonic nanostructures, in particular achiral nanoparticle cores protected by chiral molecules / ligands (belonging to catalog I.2.3), have been proven to be an efficient tool to separate enantiomers.[91] For instance, some functionalized metal nanoparticles were found to aggregate with the presence of one enantiomer of a racemate, but not with the other one. As metal nanoparticles have often characteristic colors, the aggregation process is usually accompanied with a color change, which allows for colorimetric recognition of enantiomers by naked eyes, and furthermore enantio-separation by centrifugation. UTP (uridine triphosphate) capped Ag NPs were reported to aggregate with the presence of L-cysteine but not D-cysteine[92] (***Figure 18A***). Chiral N-acetyl-L-cysteine capped Au NPs were used to separate D- and L-tyrosine[93], while ZnTPPS (sulfonated-substituted zinc tetraphenylporphyrin) capped Ag NPs were used for the separation of chiral amino acids[94]. Selective adsorption of a plasmid DNA molecule (pcDNA3) on N-isobutyryl-l(d)-cysteine (NIBC) modified gold nanorods surfaces was also reported.[95]

Interestingly, metal nanoparticles protected by achiral molecules were also found to be effective for enantio-separation. For example, CTAB capped Au NRs were reported to aggregate and precipitate in the presence of D-Gln (glutamine), but do not with L-Gln[96] (***Figure 18B***). The effect was even reported for “unmodified” nanoparticles, while the authors assign it to the “inherent chirality” of “unmodified” (citrate capped) Au NPs[97] (***Figure 18C***). This “inherent chirality” is assumed to be based on the “terrace-ledge-kink” model of the intrinsic chiral metal

surface[98,99]. This intrinsic chirality, arising from the asymmetrical arrangement of atoms on the surface of metal crystals, has also been used for enantio-selective applications[100] (***Figure 18E***). However, metal crystals with symmetrical surfaces have also shown enantio-separation properties. A. Kuhnle et al. found that, on a (110) gold surface, L(D)–cysteine enantiomers tended to form homochiral dimers composed of two cysteine molecules of the same chirality, when a racemic mixture of them was deposited on the gold surface[101] (***Figure 18D***).

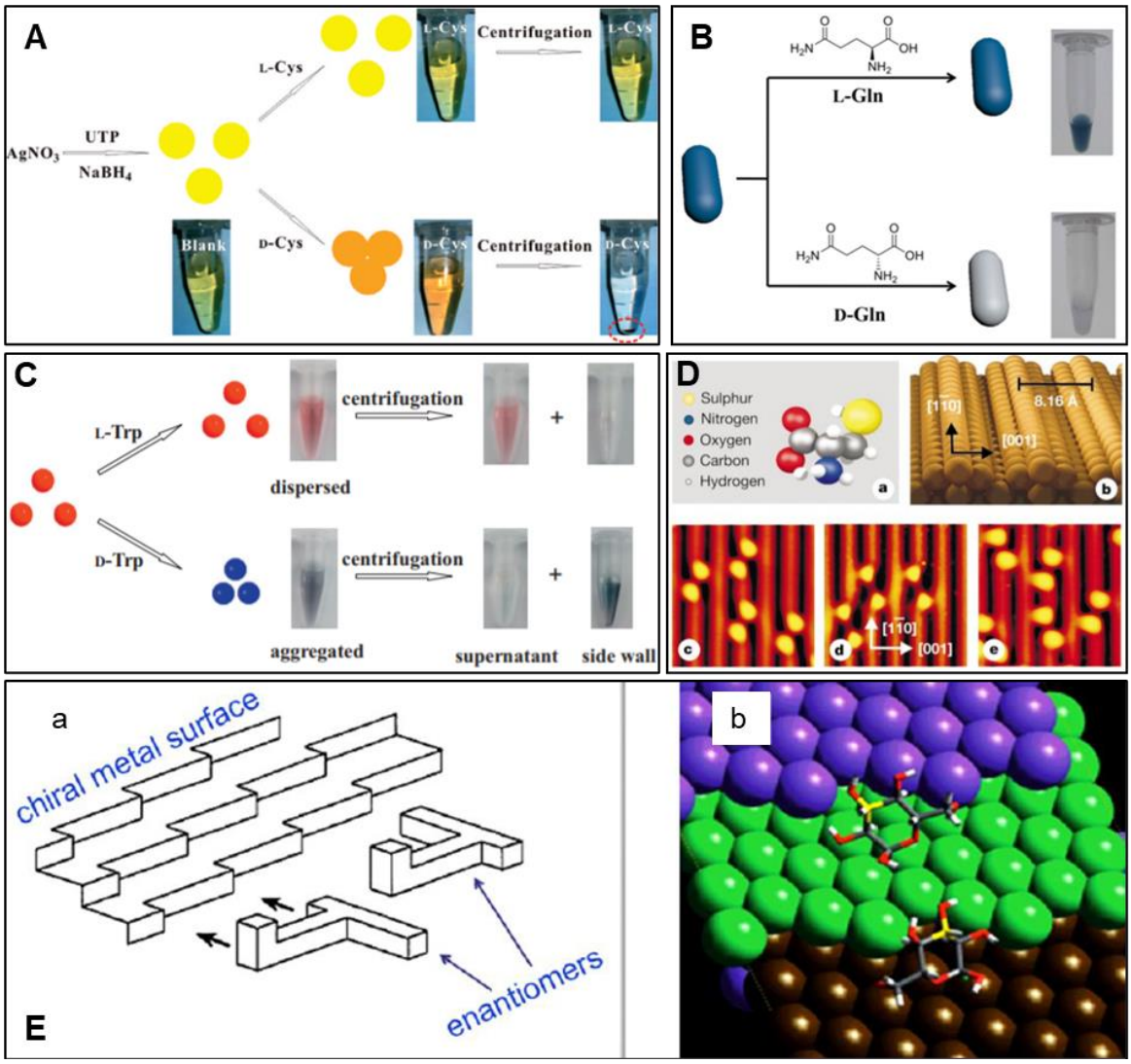

Figure 18. (A) UTP capped Ag NPs for separation of D- and L-Cysteine[92].(B) Discolouration effect of CTAB capped Au NRs with L(D)-Gln.[96] (C) Enantio-separation of D- and L-Tryptophan by Au NPs. The Au NPs were synthesized by the reaction between sodium citrate solution and $HAuCl_4$ and were used for enantio-separation without further modification[97]. (D) Homochiral dimers of cysteine enantiomers formed on gold surface. a) Schematic drawing of a cysteine molecule; b) Ball model of the Au (110) surface; c) STM image of L-cysteine pairs; d) D-cysteine pairs rotated anticlockwise (same size); e) Molecular pairs formed from DL-cysteine (same size).[101] (E) Schematics of interactions of enantiomers with intrinsically chiral metal surfaces possessing "terrace-ledge-kink" structure.[91]

I.4.3. Chiral catalysis

Noble metal nanoparticles are very often used for catalysis thanks to their high efficiency and versatility. In addition, metal nanoparticles are easy to immobilize on solid substrate, which makes them good candidate for recoverable and reusable heterogenous catalysts. On the other hand, asymmetric catalysis by conventional molecular catalysts remains a challenge due to their low efficiency. It is thus desirable to develop plasmonic nanostructures for chiral catalysis. Comparing to biosensing, chiral catalysis, using chiral plasmonic nanostructure to assist asymmetric and / or enantioselective reactions, is a relatively new and developing field, where the chiral surface ligands (see section **I.2.3**) play a primary role.[102,103] In 1979, Orito and co-workers (***Figure 19A***) reported the asymmetric hydrogenation of methyl pyruvate or methyl benzoylformate catalyzed by cinchonidine-modified Pt on carbon[104], and Pd nanoparticle-catalyzed asymmetric allylic alkylations (***Figure 19***A) were reported as first examples of chiral metal nanoparticle-catalyzed asymmetric C−C bond forming reactions in the early 2000s[105,106]. Functionalized chiral Au NPs[107] have been frequently used in this aspect. Enantioselective catalysis was achieved by using chiral ligands modified Au NPs[108] (***Figure 19***D). More recently, E. Gross et al. reported the catalysis of asymmetric cyclopropanation reactions by Au NPs embedded in chiral self-assembled monolayer (SAM) immobilized on mesoporous SiO_2 support (***Figure 19***B).[109] Another recent example is the asymmetric catalysis using copper with a prolinol-phosphine chiral ligand (***Figure 19***C).[110], Ir[111], Pd[112] and Fe_3O_4[113] nanoparticles were also found to be effective in asymmetric catalysis.

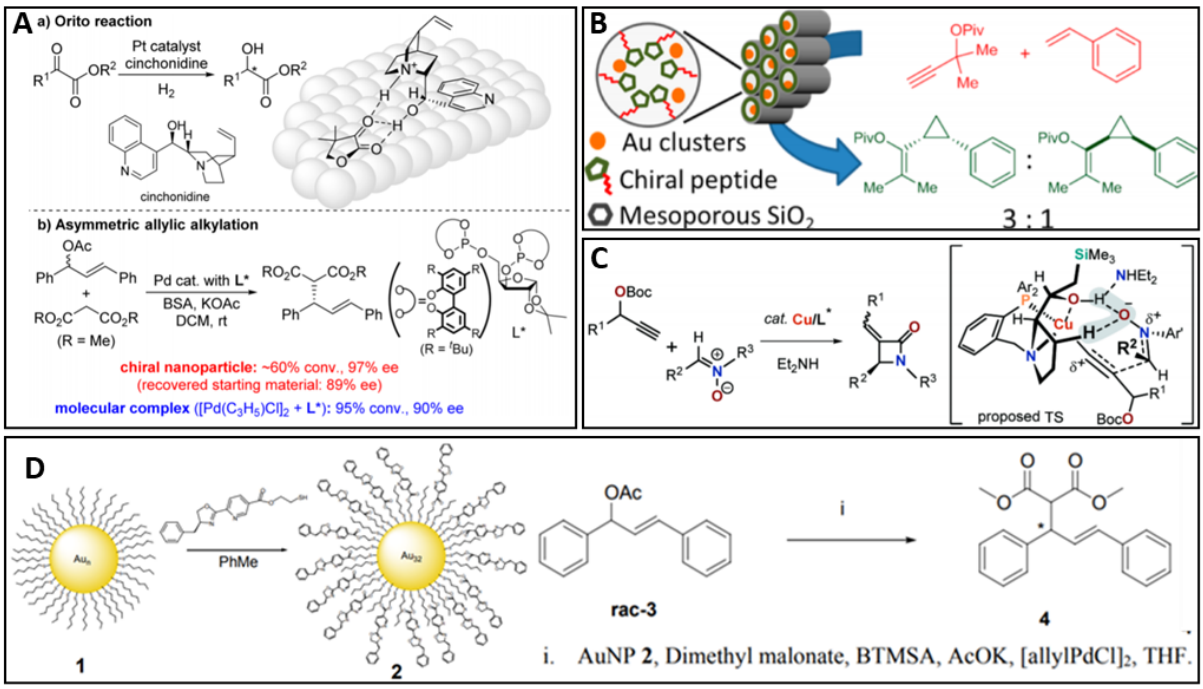

Figure 19. (A) Early example of chiral nanoparticle catalysis: a) Orito reaction: asymmetric catalysis by cinchonidine-modified Pt;[104] b) Pd nanoparticle-catalyzed asymmetric allylic alkylations.[105,106] (B) Catalysis of asymmetric cyclopropanation reactions by Au@SAM/MCF.[109] (C) Asymmetric Synthesis of α-Alkylidene-β-Lactams with prolinol-phosphine chiral ligand modified copper as catalyst.[110] (D) Chiral modification of the surface of Au NP (left) and its enantioselective catalysis of alkylation of chalconol acetate 3 with dimethyl malonate (right), which has a selectivity better than a tradition polystyrene bound catalyst.[108]

I.4.4. Chiroptical effects and light-matter interaction

The electric field lines of a chiral electromagnetic field wrap around its propagation axis. This geometrical picture is embodied by the quantity optical chirality[114]:

$$C \equiv \frac{\varepsilon_0}{2} \boldsymbol{E} \cdot \nabla \times \boldsymbol{E} + \frac{1}{2\mu_0} \boldsymbol{B} \cdot \nabla \times \boldsymbol{B} \qquad (42)$$

The degree of chirality of matter is determined by its dissymmetry factor:

$$g \equiv \frac{2(A^+ - A^-)}{(A^+ + A^-)} = \frac{\Delta A}{A} \qquad (43)$$

where A^+ and A^- are absorbance for left circularly polarized (LCP) light and right circularly polarized (RCP) light. $\Delta A = A^+ - A^-$ is defined as the circular dichroism of the matter and $A =$

$(A^+ + A^-)/2$ is its absorbance for non-polarized light. One is therefore capable to calculate g-factor of a sample from its CD spectroscopy and absorption spectroscopy.

In addition, the dissymmetry factor is associated with the electric polarizability $\alpha = \alpha' + i\alpha''$, the isotropic mixed electric-magnetic dipole polarizability $G = \alpha G' + iG''$ and the optical chirality C by[115]:

$$g = -\left(\frac{G''}{\alpha''}\right)\left(\frac{2C}{\omega U_e}\right) \quad \textbf{(44)}$$

Generally, we talk about the g-factor for circularly polarized light, for which $C = \pm 2U_e \frac{\omega}{c}$, and therefore $g = -\frac{4G''}{c\alpha''}$. Thus, the conventional dissymmetry factor g of a material appears to be an intrinsic property of this material.

The dissymmetry factor of chiral plasmonic nanostructures can be several orders of magnitude higher than that of molecules. This is because of the localized chiral field enhancement by plasmonic nanostructures, known as the "superchiral" field. Hence, the interaction of chiral plasmonic nanostructures and electromagnetic fields lead to remarkable chiroptical effects[116], especially circular birefringence (CB) and circular dichroism (CD). CB is defined as the different phase delay for LCP and RCP, which is related to the difference in the real part of the refractive index. This phase delay causes a rotation of the polarization plane, also known as optical rotation (OR) or optical rotatory dispersion (ORD) when conducted as a function of wavelength. CD is defined as the differential absorption for LCP and RCP, corresponding to the difference in the imaginary part of the refractive index. CD maximum could be found generally at λ_{max} of absorption. Besides CD and CB, asymmetric transmission[117] and / or reflection[118] is another chiroptical effect, which is found in chiral plasmonic nanostructures.

For a chiral compound that has no chromophore in the considered spectral range, its ORD spectrum is a plain curve increasing or decreasing with wavelength (normal ORD curve, ***Figure 20A***). However, for a chiral compound with a chromophore, its ORD spectrum displays a bisignate shape (anomalous ORD curve, ***Figure 20A***) which changes sign at the absorption

wavelength (λ_{max}). This is the so-called Cotton effect, which is divided into positive and negative one depending on the signs of ORD on both sides of λ_{max}. In such cases, the CD spectrum shows a single peak at λ_{max} ***(Figure 20B)***.[119] For compounds containing two or more similar highly absorbing chromophores, the Cotton effect occurs in the CD spectra and the exciton coupling theory[120] may be applied to explain this phenomenon. Upon looking through the center of the two dipoles of a molecule containing two chromophores, a negative Cotton effect in CD is obtained when an anticlockwise rotation by an acute angle brings the dipole in the front onto that in the back, and a positive Cotton effect when the rotation is clockwise ***(Figure 20C)***.[121] ORD spectra are dispersive whereas CD spectra are absorptive. CD is measured in or near the absorption bands, while ORD can be measured far from these bands. CD is apparent in the data analysis. Structural elements are more clearly distinguished since their recorded bands do not overlap extensively at particular wavelengths as they do in ORD. Therefore, CD spectra are more commonly used than ORD spectra in analysis of chiral media, although these two measurements can be interconverted through Kramers–Kronig transform[122].

CD spectra of chiral plasmonic nanostructures have typically bisignate shapes. Different theoretical models, including Born-Kuhn model[123], have been developed for interpretation of the spectra, regarding plasmonic modes as coupled oscillators.

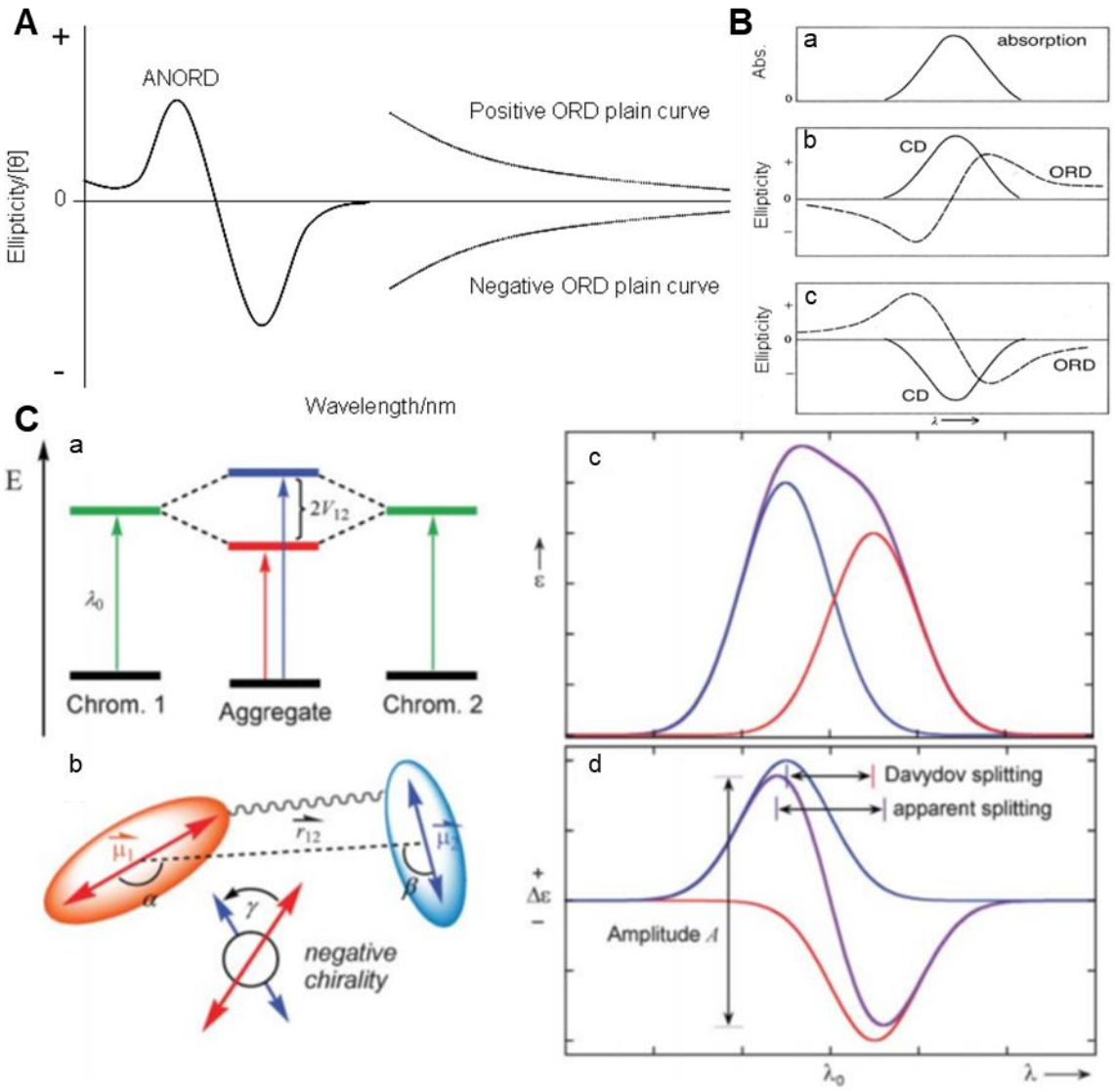

Figure 20. (A) An anomalous ORD curve (ANORD) and positive / negative ORD plain curves.[124] (B) Absorption (a), CD spectra and ORD curves of positive Cotton effect (b) and negative Cotton effect (c).[124] (C) Splitting of excited states (a) of a chiral compound generated by exciton coupling of its two chromophores (b). $2V_{12}$ is called Davydov splitting. The rotation of the dipoles is anticlockwise (b) and the CD spectrum shows thus a negative cotton effect (d), that is, negative CD in longer wavelength, positive CD in lower wavelength, and change sign around absorption (c) wavelength. Component spectra are red / blue lines and resultant spectra are in violet.[121]

The fascinating chiroptical effects of chiral plasmonic nanostructures lead to various optical application[125], such as broadband circular polarizer (***Figure 21A***), manipulation of chiral optical forces (***Figure 21D***), chirality switching devices (***Figure 21C***), chiral mirrors (***Figure 21D***) etc.

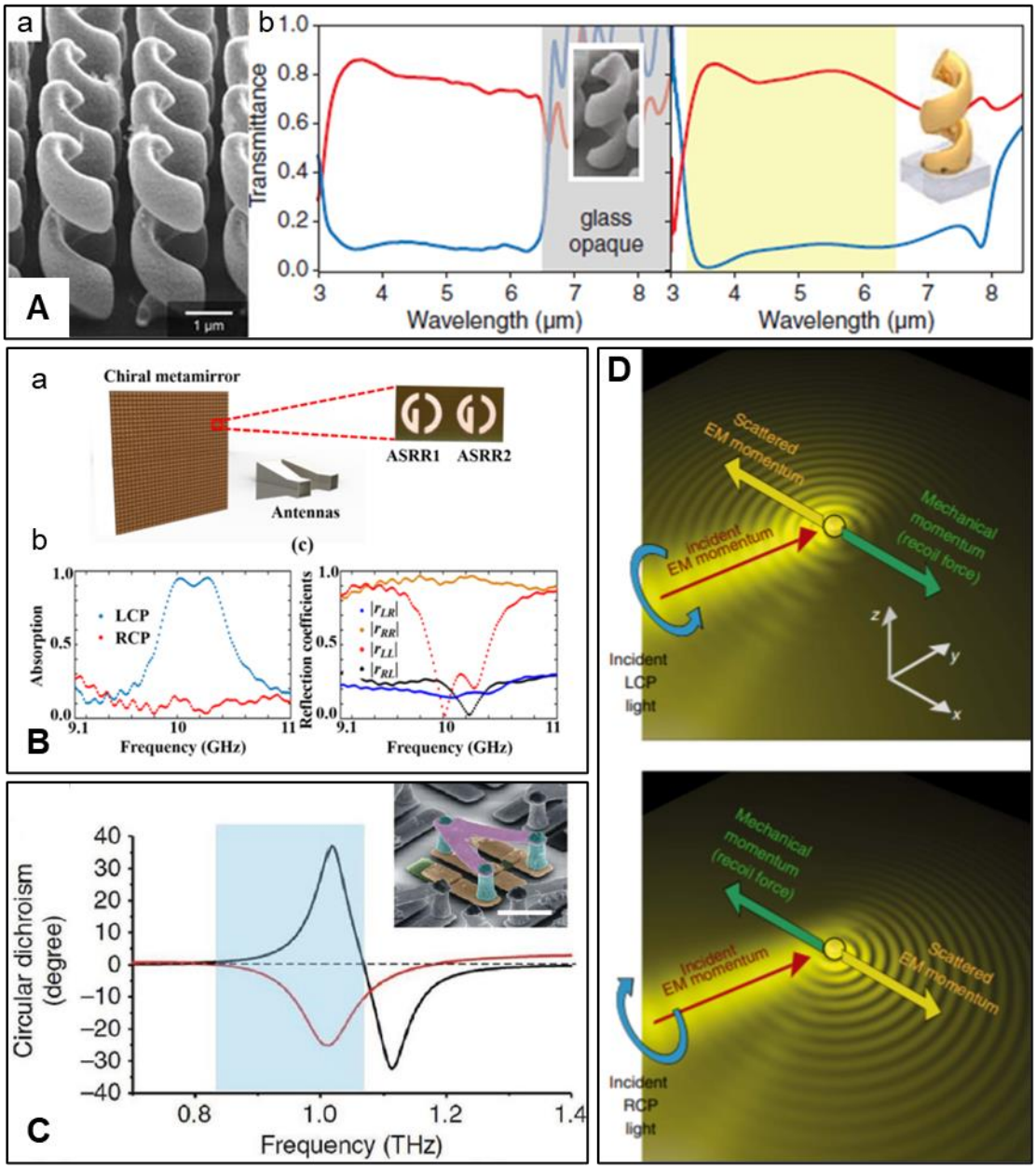

Figure 21. (A) (a) Chiral gold helix arrays. See fabrication process in section I.5.1. (b) Experimental (left panel) and simulated (right panel) transmittance of the chiral gold helix for LCP (red lines) and RCP (blue lines).[126] (B) (a) Metallic mirror with asymmetric split-ring resonators (ASRRs), and (b) chiral absorption and (c) reflection of the chiral mirror.[127] (C) CD of the chirality switching device (inset) with (red line) and without (black line) photoexcitation. The CD is reversed in the range between 0.9 and 1.14 THz without any structural reconfiguration.[128] (D) Nanoparticle moves towards different directions when illuminated by LCP and RCP.[129] Polarized illumination of a nanoparticle over a surface supporting guided modes results in unidirectional excitation of guided modes and a corresponding polarization-dependent recoil force on the particle.

Not only chiral plasmonic nanostructures can interact with electromagnetic fields, but also light-matter interaction occurs when an active molecule is brought close to the superchiral field of the plasmonic nanostructures. More specifically, surface plasmon polaritons, as presented

section I.3.2, are evanescently confined electromagnetic wave propagating at the interface of a dielectric and a metal, resulting from the coupling (with an external stimulus) of the incident electromagnetic waves with the surface plasmons of the metal. This confined electromagnetic field can apparently interact with active molecules and materials in its vicinity. On the other hand, localized surface plasmon resonance, resonant modes of the plasma oscillation of metallic nanoparticles in response to incident electromagnetic waves, leads to localized enhancement of the electromagnetic fields. The LSPR can thus also interact with active molecules and materials in its proximity.

In physics, light-matter interaction can be divided into either weak or strong coupling regimes[130,131]. Take exciton-photon coupling as an example: in the weak coupling regime, the spontaneous emission rate can be modified but exciton dynamics (emission frequency) are barely altered, while in the strong coupling regime, strongly modified exciton dynamics leads to formation of novel hybrid energy states,[132–134] separated by the Rabi splitting energy (***Figure 22A,B***). Since the observation of strong coupling of light and molecules by D. G. Lidzey et al.[132], optical cavities with organic molecules have been extensively studied[131,135] as a classical model for exciton-photon strong coupling. If the light-matter coupling were to be explained using the paradigm model of two coupled harmonic oscillators[136], as it usually is, the extension to exciton-plasmon coupling[137–139], with exciton and plasmon acting as the two oscillators, is straightforward. In fact, thanks to nano-fabrication technologies and physical understanding of their light interacting properties, the exciton-plasmon coupling has attracted wide attention recently and is loosely referred to the term “strong coupling” by some while others call the formed quasiparticle a plexciton[140–142].

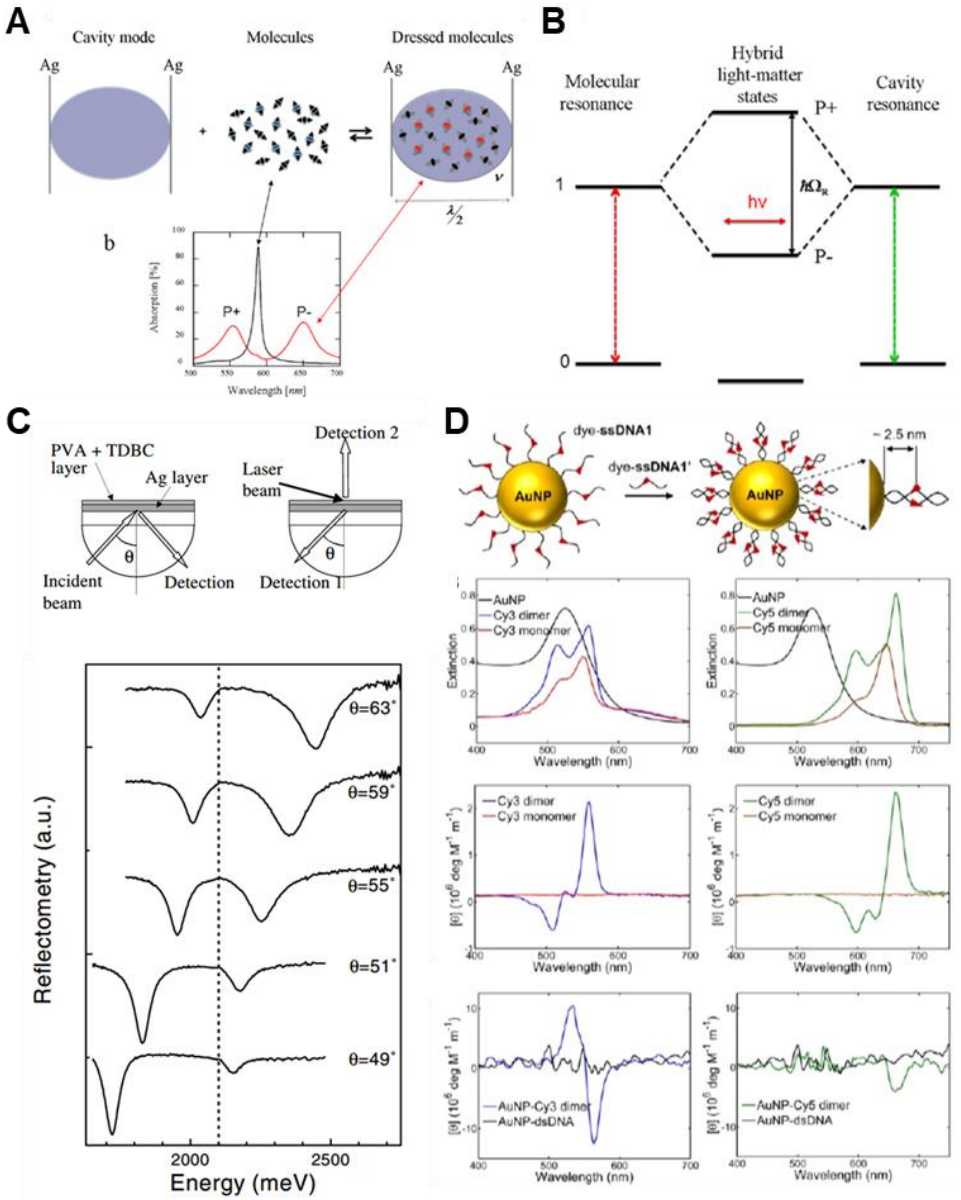

Figure 22. (A) Strong coupling of a molecular transition to the resonant light wave confined in an optical cavity composed of two Ag mirrors, giving rise to Rabi splitting in extinction spectrum of the molecule.[131] (B) Representation of strong coupling in terms of energy.[131] (C) Strong coupling of TDBC with surface plasmon polariton.[143] (D) LSPR enhanced CD.[144]

Whatsoever, the optical phenomena and theories associated with the coupling between LSPR modes and excitons of all kinds, especially the J-aggregates of dye molecules and quantum dots have been considerably studied. In particular, the surface plasmon enhanced spectroscopy[145,146], including surface enhanced absorption[147,148] scattering[149] and fluorescence[150] as well as the surface plasmon enhanced chirality of chiral molecules[144] have been widely known. Many works have also shown the modification of the optical properties of plasmonic nanostructures

by approaching molecules. However, the modification of the chiroptical properties of an achiral molecule by a chiral plasmonic environment seems to be less studied. One of the objectives of this manuscript is to discuss the coupling of LSPR of chiral plasmonic superstructures with excitons of J-aggregates of cyanine dyes, and in particular, the precise tuning of induced chiroptical performance of the hybrid systems, including modified circular dichroism effects and eventually polarized emissions.

I.5. Methods to build chiral plasmonic nanostructures

The fabrication strategies for chiral plasmonic nanostructures can be divided into top-down methods, bottom-up methods (including self-assembly methods). Self-assembly approaches belong to the bottom-up category, yet its importance and abundance are worth an independent section.

I.5.1. Top-down methods

The top-down approach involves the elimination of local materials from a larger object or film in order to obtain the desired shape, order and properties, using technologies such as direct laser writing, focused ion beam etching and lithography. Nanofabrication of chiral plasmonic helices, typically gold and silver, is one classical example for this. J. K. Gansel et al.[126] developed gold helix arrays fabricated by direct laser writing (DLW), which show selective transmittance for left circularly polarized (LCP) light and right circularly polarized (RCP) light in mid-infrared regime (***Figure 23***.A). They spin-coated first a positive photoresist on a glass substrate covered by an indium-tin oxide (ITO) film. The regions sufficiently exposed to light were then removed and pores with a helical shape were formed after 3D DLW and development. The structure was afterwards put into an electrochemical cell, where gold infiltration was monitored by the current density and growth time. Finally, the polymer template was removed by plasma etching. Another example of direct laser writing is combining with electroless silver plating. A. Radke and coworkers[151] fabricated “bichiral” silvered crystals (bichiral refers to crystals composed of

helices of two kinds of handedness, aligned in two kinds of arrangement, namely again left and right, with regard to the helix axes[152]). The direct laser writing process is similar to conventional ones as presented above in Ref[126]. (***Figure 23***.B).

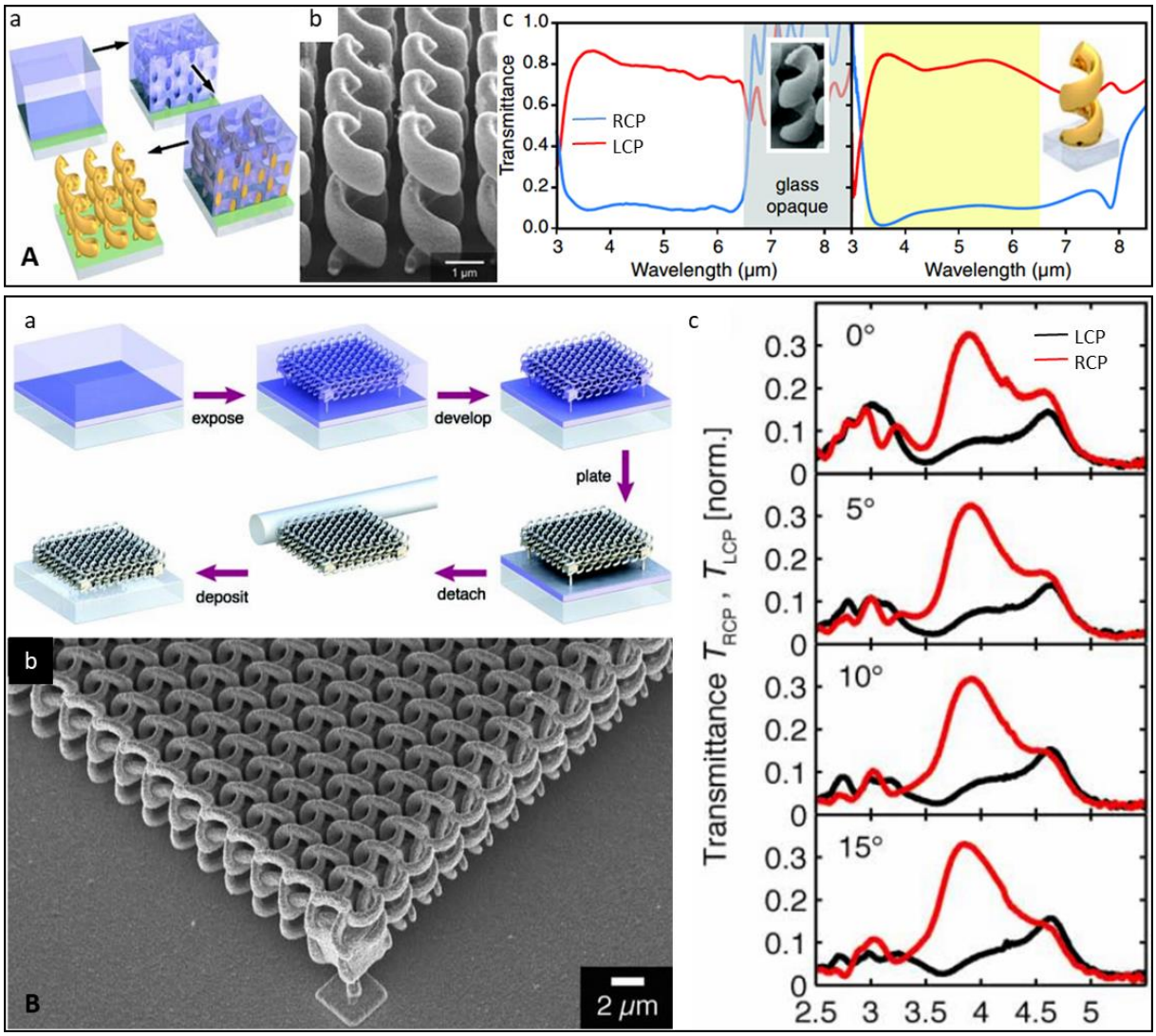

Figure 23. (A) a) Laser writing process. b) Oblique view of an array of left-handed helices. c) Experimental and theoretical transmittance spectra of right-handed helices for LCP and RCP.[126] (B) a) Laser writing combined with electroless silver plating. b) Oblique view of a bichiral crystal with right-handed corners and right-handed helices. c) Transmittance spectra of a bichiral crystal with left-handed corners and left-handed helices for LCP and RCP at different incident angles.[151]

Lithography is another widely used top-down approach, which includes various techniques such as electron beam lithography (EBL)[153,154], photolithography[155], and focused ion beam lithography[156], to name a few. Recently, Dietrich et al.[157] fabricated chiral nanomaterial arrays by on-edge electron beam lithography (***Figure 24***A). A film of electron beam resist was spin-

coated on a pre-structured template with periodic nanoscale arrays. The resist was exposed by electron beam in such a way that the shaped enclosures are placed above the edge of the arrays on the template, before a layer of gold was finally evaporated through the mask. The transmittance of LCP and RCP were then characterized for these structures, which reveals its strong handedness. DNA origami has been recently reported as lithography mask to fabricate chiral plasmonic nanostructures[158] (***Figure 24***B). The advantages of using DNA origami as the mask compared to conventional lithography techniques are its structural versatility and its high productivity, giving rise to improved effectiveness of nanofabrication on large area.

Twisted optical metamaterials composed of multilayer of gold nanorods were developed recently by Y. Zhao and coworkers[56] as already mentioned in above sections using lithography (***Figure 24***C). A 100 nm thick film of silicon dioxide was deposited on a glass substrate, and then 55-nm-deep trenches were pre-structured via reactive ion etching, with the help of the e-beam resist mask. An e-beam resist pattern with gold alignment marks was written using a e-beam aligner and transferred to the silicon dioxide film. A 5 nm titanium adhesion layer and 50 nm gold were sequentially deposited onto the sample using an e-beam evaporator. Lift-off process was afterwards realized to complete the first layer structure. The process can be repeated for multilayer structures. Impressive are the reproducibility and robustness of the optical properties of the obtained multilayer structure and its rich possibility to tune the structural parameters and thus the optical responses. Another newly emerging nanofabrication technique is colloidal lithography[159,160] (***Figure 25***A), where self-assembled colloidal crystals, such as polystyrene and SiO_2 nanospheres, serve as lithographic masks. Z. Wu et al.[161] reported recently chiral nanostructures with multilayered gold plates as building blocks, realized by colloidal lithography and photolithography (***Figure 25***B).

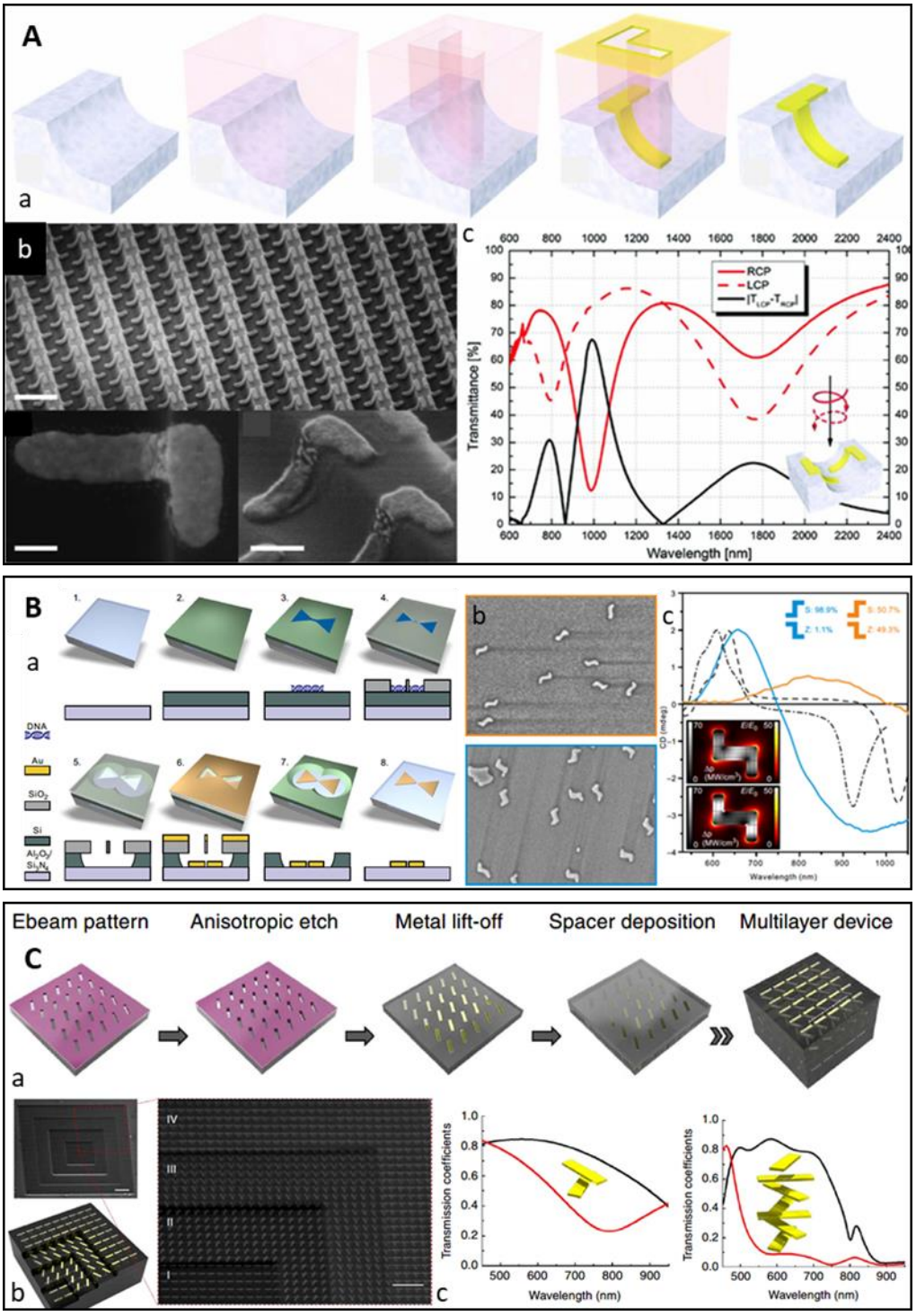

Figure 24. (A) a) Lithography process, see details in text above. b) SEM images of fabricated chiral nanomaterial array. c) Simulated transmittance spectra of a 3D-L particle array for RCP and LCP and their intensity difference.[157] (B) a) Lithography process with DNA origami. b) SEM images of a sample containing 50:50 distribution of S- and Z-shaped (top) and ~99% S-configuration chiral nanoparticles (bottom). c) Measured CD spectra from the samples shown in b) and simulated CD response for a symmetric (dashed) and slightly asymmetric (dash-dotted) S-shaped chiral nanoparticles.[158] (C) a) Lithographic fabrication of multilayered chiral nanostructure. b) SEM images of a four-layer device. d) Transmittance spectra of a two-layer and a four-layer devices for LCP and RCP.[56]

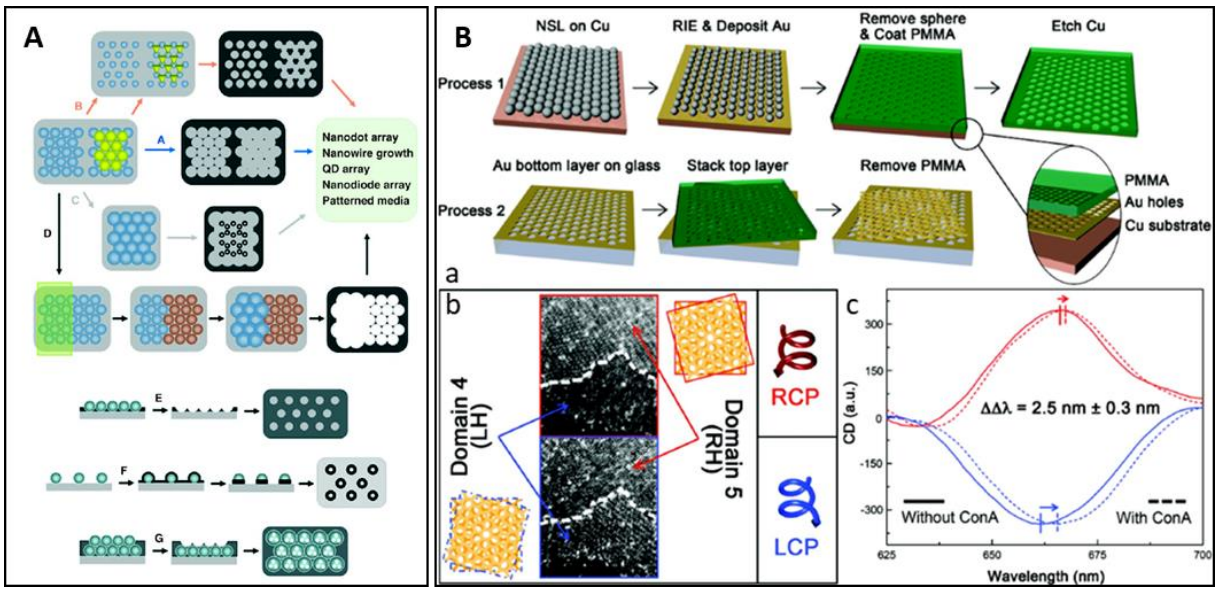

Figure 25. (A) Typical nanofabrication routes of colloidal lithography. Route A shows the simplest colloidal lithography of nanodots by depositing metal through a colloidal mask. Route B and C illustrate the colloidal lithography deposited at a tilted angle and the masks are modified via reactive ion etching and annealing of the colloids. Route D is photocurable colloids as hierarchical patterns. Route E demonstrates a templating of organic and inorganic materials with a hexagonally packed structure. Route F shows the formation of nanorings. Route G shows the formation of regular holes in colloidal lithography. [159] (B) a) Top panels: Schematic illustration of process 1, including nanosphere lithography for Au nanohole arrays and subsequent release and transfer of the Au layer onto a sacrificing polymer layer. Bottom panels: Schematic illustration of process 2 for stacking two layers of Au nanohole array on a glass substrate to form moiré chiral metamaterials (MCMs), with the assistance of the sacrificial polymer layer. b) Gray-scale optical images at the boundary of two enantiomers (indicated by 4 and 5) with opposite structural handedness (i.e., θ = -15° vs 15°, respectively) under LCP and RCP illuminations. c) CD spectra of two enantiomers of the MCMs) with θ of-15° (blue curves) and 15° (red curves). The solid and dashed curves are obtained before and after the adsorption of canacalin A (ConA).

I.5.2. Bottom-up methods

The bottom-up methods, as opposed to top-down methods, attempt to arrange small components into more sophisticated structures with desired properties, e.g. chirality as concerned herein, using techniques such as chemical synthesis, glancing-angle deposition, focused ion beam, electron beam induced deposition (FIBID / FEBID) and self-assembly. The top-down methods are accurate and effective in fabricating certain nanostructures such as arrays and layered plates, but non-scalable for size above 100 nm, time-consuming and normally costly, whereas bottom-up methods are often faster, less expensive and more adaptable for arbitrary structural geometries in a larger range of scales.[162]

Focused ion beam and electron beam induced deposition (FIBID /FEBID) represent a pair of classical example of bottom-up methods.[163,164] The FIBID / FEBID consist in depositing materials contained in a vaporized precursor molecule decomposed by an ion- / electron beam (***Figure 26***A). M Esposito et al.[165] realized chiral platinum nanohelices which exhibit chiroptical effects in the optical regime, employing and comparing both FIBID and FEBID (***Figure 26***A). Vacuum evaporation can be an alternative approach for top-down fabrication of chiral nanostructures. B. Yeom and coworkers fabricated chiral gold shells by depositing gold on ZnO nanopillars with a tilted angle of 45° (***Figure 26***B).[166] By rotating the sample for the second layer deposition in a direction different from the direction of first deposition, left- and right-handed chiral plasmonic nanostructures were obtained. Another similar approach to fabricate chiral (helical) nanostructures is known as the glancing angle deposition[167,168] (***Figure 26***C,D). The idea is to deposit and grow materials onto the seeds (e.g. Au nanodots) pre-located on the substrate by vapor spraying at a grazing angle and / or rotating the substrate.

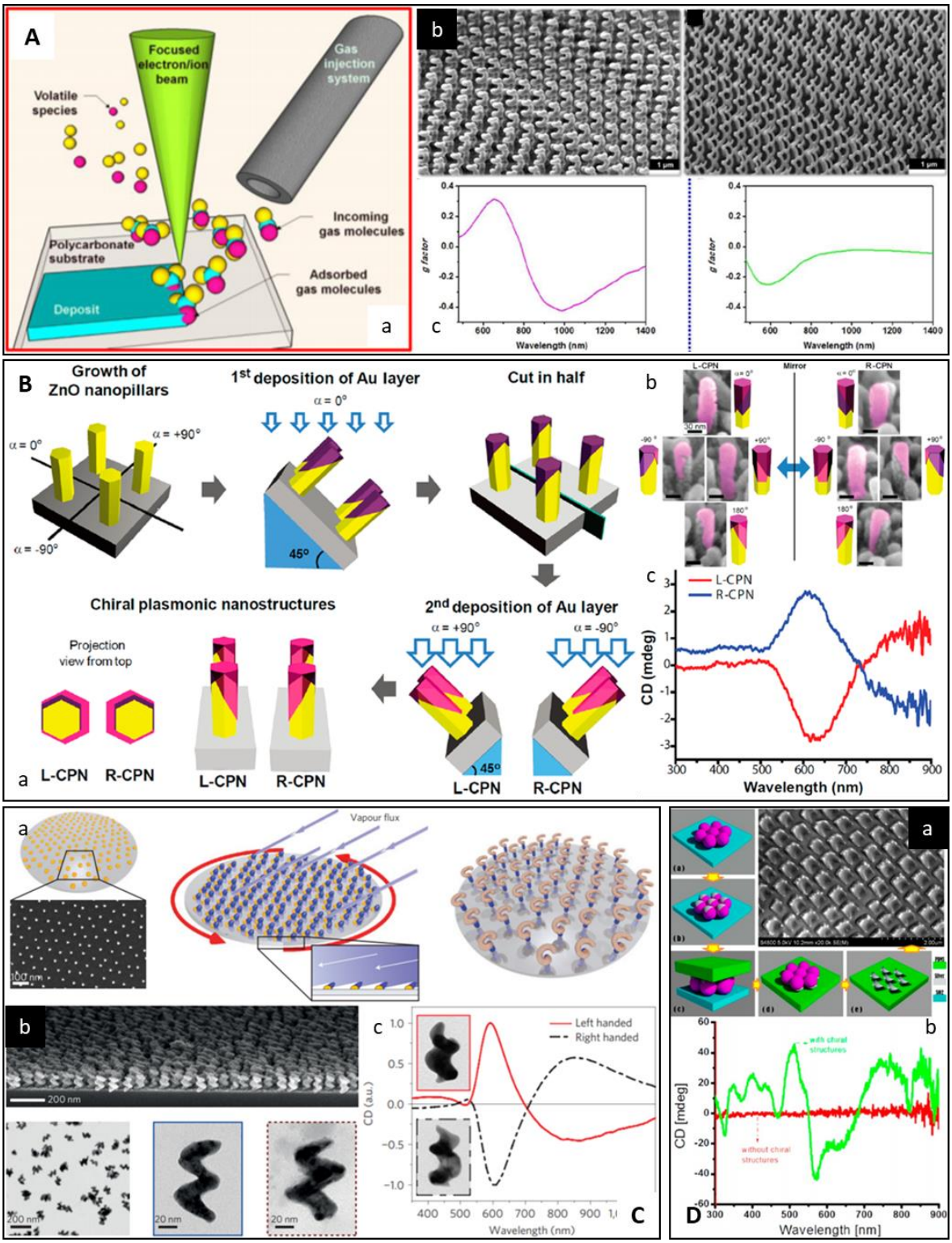

Figure 26. (A) a) Schematic of FIBID / FEBID.[169] b) Arrays of chiral platinum nanohelices with different pitches fabricated by FIBID (left) and right and c) their experimental CD spectra.[165] (B) a) Fabrication schematics of chiral plasmonic nanoshells by vaccum evaporation. b) SEM images of left- and right-handed nanostructures in different angles, Au layers were colored for clarity, and c) their CD spectra.[166] (C) a) Schematics of glancing angle deposition (GLAD). b) SEM imgaes of Au nanohelices fabricated by GLAD. c) CD spectra of obtained helices.[168] (D) a) Chiral plasmonic nanostructures fabricated by GLAD on polystyrene spheres and their SEM image. b) CD spectra.[167]

I.5.3. Self-assembly

Self-assembly[170,171] of nanoobjects into functional superstructures including those with chiroptical effects has been a dynamic field of research in recent years. Many examples of structures that can be obtained were already given in I.2, while we focus here on their fabrication process. Self-assembly of nanoparticles can take place in colloidal dispersions or at interfaces. An efficient way to assemble plasmonic units, such as nanospheres and nanorods, into chiral superstructures is the use of (chiral) templates. Conventional templates include polymers[172], nanofibers[51], DNA[41,49,57,173,174] and other biomolecules[40,175]. In some cases, the chirality originates from the plasmon-molecule interaction between the plasmonic building blocks and the chiral templates[40,41] (see section I.2.3), while more frequently the chiral configuration generates the chirality of the assembly via the plasmon-plasmon interaction[49,51] (see section I.2.4).

Figure 27A illustrates the case of chiral exciton-plasmon interaction.[144] Non-chiral chromophores were hybridized with double stranded DNA, which induced bisignated CD signals at the absorbance band of the chromophore. Interestingly, when coupled to a plasmonic resonance mode of Au nanorods, the CD signals were reversed, and the magnitude enhanced by a factor of 10. Isotropic nanoparticles such as plasmonic nanospheres can be assembled into chiral configurations like helices. C. Song et al.[176] prepared enantiomeric gold nanoparticles double helices by using peptides, while W. Ma et al.[177] assembled Au nanorods in a twisted conformations by polymerase chain reaction. Chiral self-assemblies of suspensions of plasmonic nanorods were also achieved by using chiral nanofibers[51] and cellulose as templates[175].

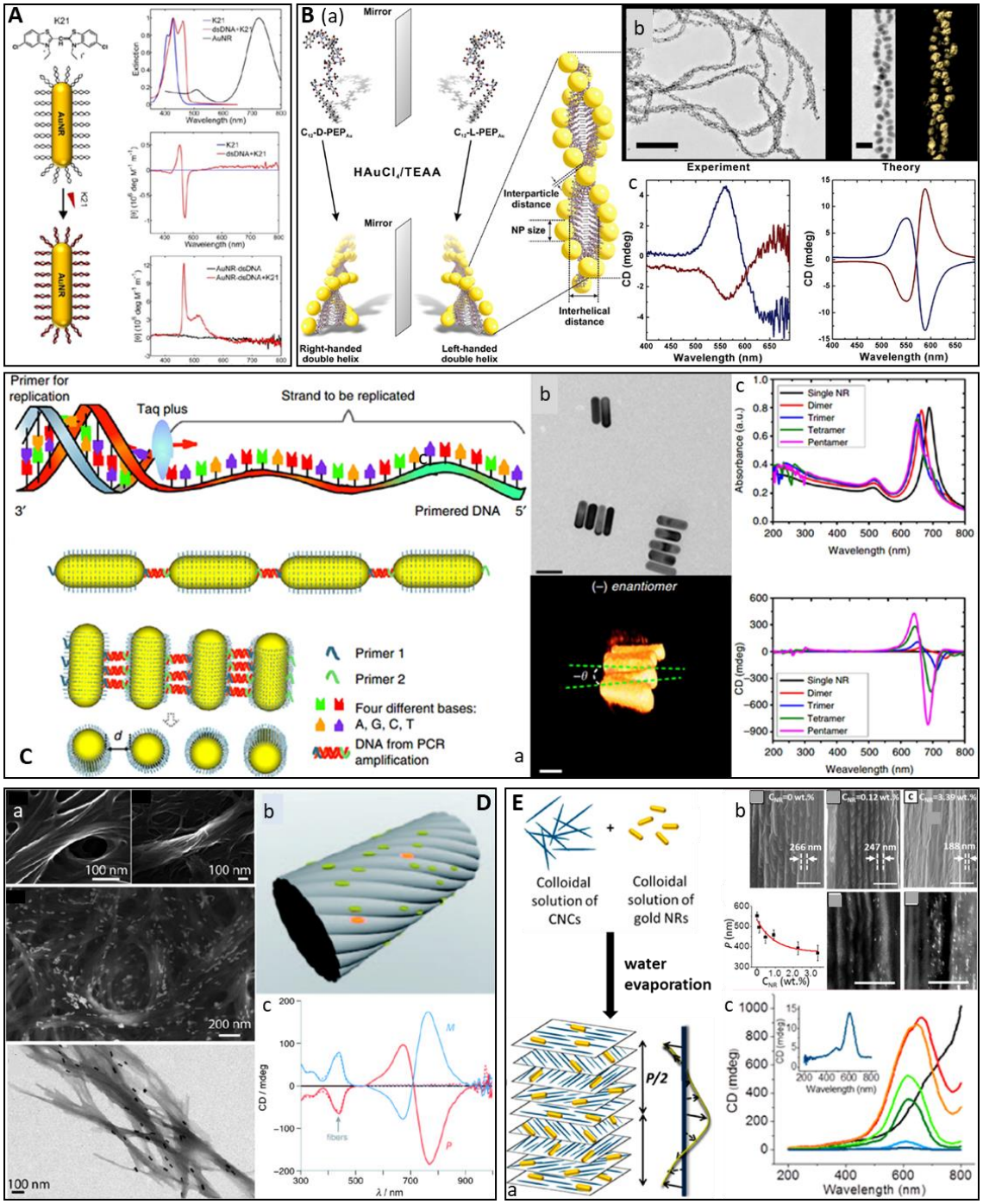

Figure 27. (A) Non chiral chromophore K21 displayed collective chiral excitons when self-assembled with DNA template. This chirality was reversed and enhanced by a magnitude of 10 by binding DNA to plasmonic An nanorods.[144] (B) By mixing the pre-designed synthetized peptide conjugate molecules (C_{12}-D-PEP_{Au} and C_{12}-L-PEP_{Au}) and gold precursor solution, the Au NPs self-assembled into double helix with left or right handedness, which was revealed by the SEM images and the CD spectra.[176] (C) Chiral assembly of Au nanorods was realized using the polymerase chain reaction (PCR), which allows for the controlled assembly of nanorods connected by DNA in small oligomers with a tunable number and complexity. By end-site modifications with regard to the PCR primers, the end-to-end or side-by-side growth modes of nanorods were favored or suppressed. Attributing to twisted conformation of side-by-side assemblies, CD signals appeared with its intensity highly depending on the

number of nanorods connected. The preference for one enantiomer as opposed to another is related to symmetry breaking of the parallel NR due to twisting of the connected DNA bridges and the general preference of non-parallel orientation of charged nanoscale rods as the conformation with minimal energy.[177] (D) NRs adsorbed onto a scaffold of supramolecular fibers with chiral morphology through specific non-covalent interactions.[51] a) SEM images of twisted fibers with right- (P) and left-handedness (M) with / without absorbed nanorods. b) Schematic of the nanocomposite system. c) Two CD peaks are present corresponding to the chirality of the nanofiber (~450 nm) and the LSPR of Au nanorods (~780 nm). (E) Upon slow evaporation of water in the mixture of aqueous suspension of cellulose nanocrystals (CNCs) and gold nanorods, the CNCs formed a left-handed liquid crystalline cholesteric phase, and Au nanorods loaded in the cholesteric solid film align with the cellulose orientation. The CD responses varied depending on the nanorods concentration in the films (see c)).[175]

An increasingly popular template for chiral plasmonic self-assembly is DNA origami[178,179], which involves the folding of long DNA into 2D and 3D nanostructures by hybridizing with so called staple oligonucleotides. The staple oligonucleotides are connected with DNA through Watson–Crick base pairing, and their positions are predetermined. Therefore, the DNA origami structures can be designed. The DNA origami, when used as template for self-assembly of chiral plasmonic nanostructures[162], fulfills a dual purpose, first as scaffold arranging the nanoparticles and second as an origin of chirality. For example, DNA origami with 24 bundles which offers nine attachment sites for single-stranded DNA coated AuNPs were made from hybridization of long DNA with hundreds of designed staple oligonucleotides. Left-handed and right-handed self-assembled gold helices were thus obtained (***Figure 28A***). L. M. Kneer et al. prepared a two-layer sheet (2LS) DNA-origami, supporting single-stranded DNA coated gold nanospheres or nanorods. Chirality transfer occurred from the DNA origami located in the hotspots to the nanoparticles, leading to enhanced CD signals at the plasmonic resonances (***Figure 28B***). In addition, thanks to the reversable binding of the DNA strand, actively tunable chiral plasmonic nanostructures are feasible using DNA origami templates. For instance, A. Kuzyk et al. prepared gold nanorod dimers supported and attached by two DNA bundles. By adding specific DNA strands connecting or disconnecting the four arms of the two DNA bundles, it is possible to tune the relative angle between the gold nanorods dimers, and thus the handedness of the structure (***Figure 28C***). C. Zhou et al. have shown that the CD of nanorod dimer could be altered through directional, progressive and reverse nanoscale “walking” of a nanorod on the two-layer sheet DNA origami (***Figure 28D***).

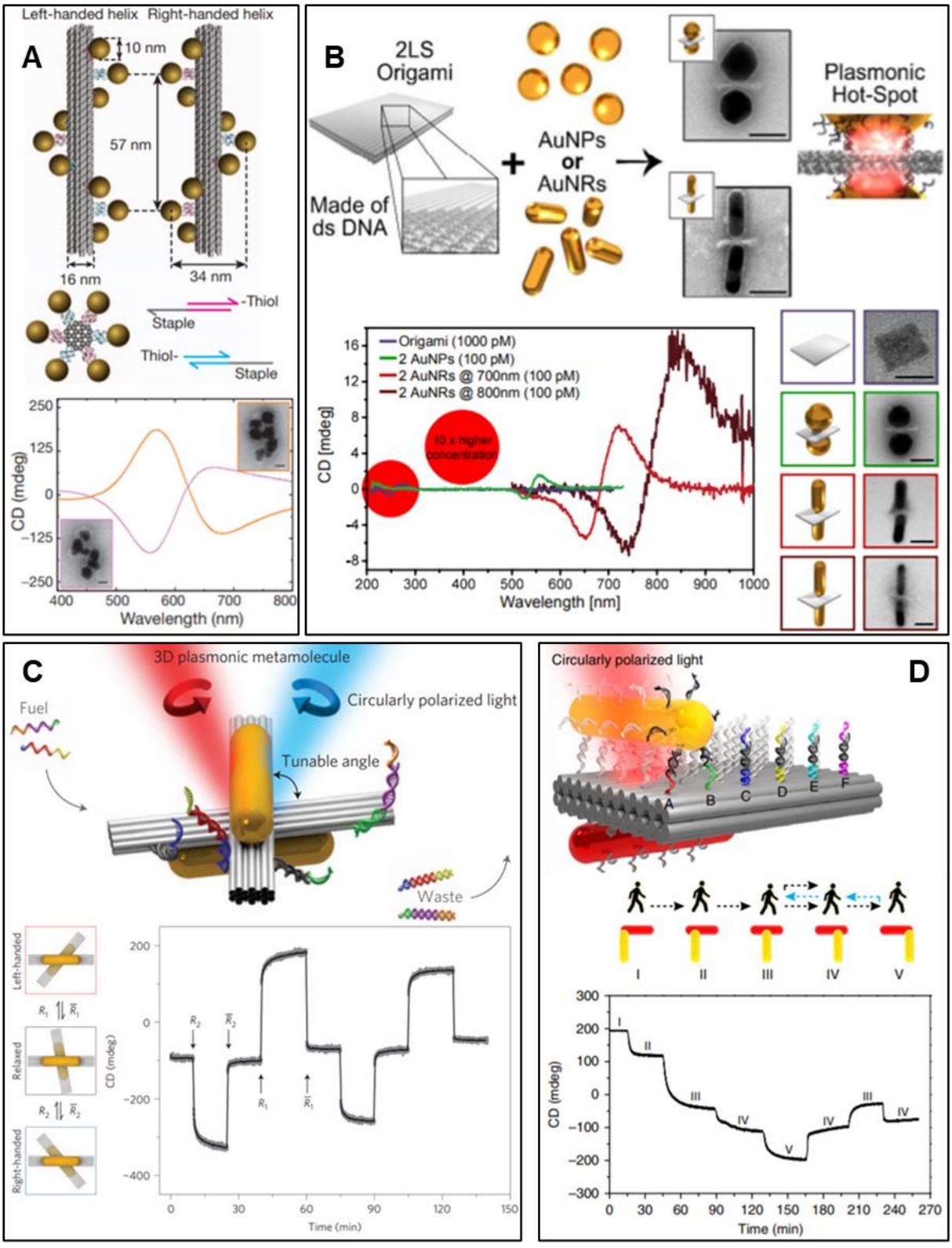

Figure 28. (A) Left-handed and right-handed gold helices assembled on DNA bundles and their CD spectra.[174] (B) Gold nanospheres and nanorods supported by two-layer sheet DNA origami with tailored CD.[180] (C) Gold nanorod dimer attached on two DNA bundles with tunable angle. The CD of the structure is tunable by adding specific DNA strands and changing the angle between the two nanorods.[181] (D) Directional, progressive and reverse nanoscale "walking" of nanorod on the DNA sheet leads to change in CD of the nanorod dimer.[182]

I.6. Introduction to Grazing Incidence Spraying and Layer-by-Layer assembly

To date, most fabrication strategies targeting chiral plasmonic nanostructures, including but not limited to those introduced above, are often expensive and time-consuming. Especially when it concerns the assembly of a large array of nano-elements, instead of individual nanoparticles, and / or over large surfaces, it turns out to be challenging in terms of efficiency and hierarchical organization of the nanoscale building blocks. In this context, conceiving new methods to assemble one-dimensional nanomaterials into two- or three-dimensional structures with well-controlled location, orientation, and spacing across multiple length scales has attracted interest in the nanoscience community, and our group has recently introduced the preparation of chiral plasmonic nanostructures by Grazing Incidence Spraying (GIS) and Layer-by-Layer (LbL) assembly.

I.6.1. Grazing Incidence Spraying

As previously described, one approach to fabricate 3D chiral plasmonic nanostructures is to arrange in-plane aligned 1D nanoobjects into asymmetric hierarchical organization (***Figure 24*C** for example). Besides lithography used in this example, there exist many other methods for in-plane alignment of 1D nanoobjects[183]. These alignment methods rely on different forces such as external electronic / magnetic field, mechanical force, chemical interactions, etc. Some of these methods are only suitable for monolayer deposition of aligned nanoobjects, while the others are effective to realize multilayered architectures. The latter is indispensable for implantation of 3D chiral nanostructures.

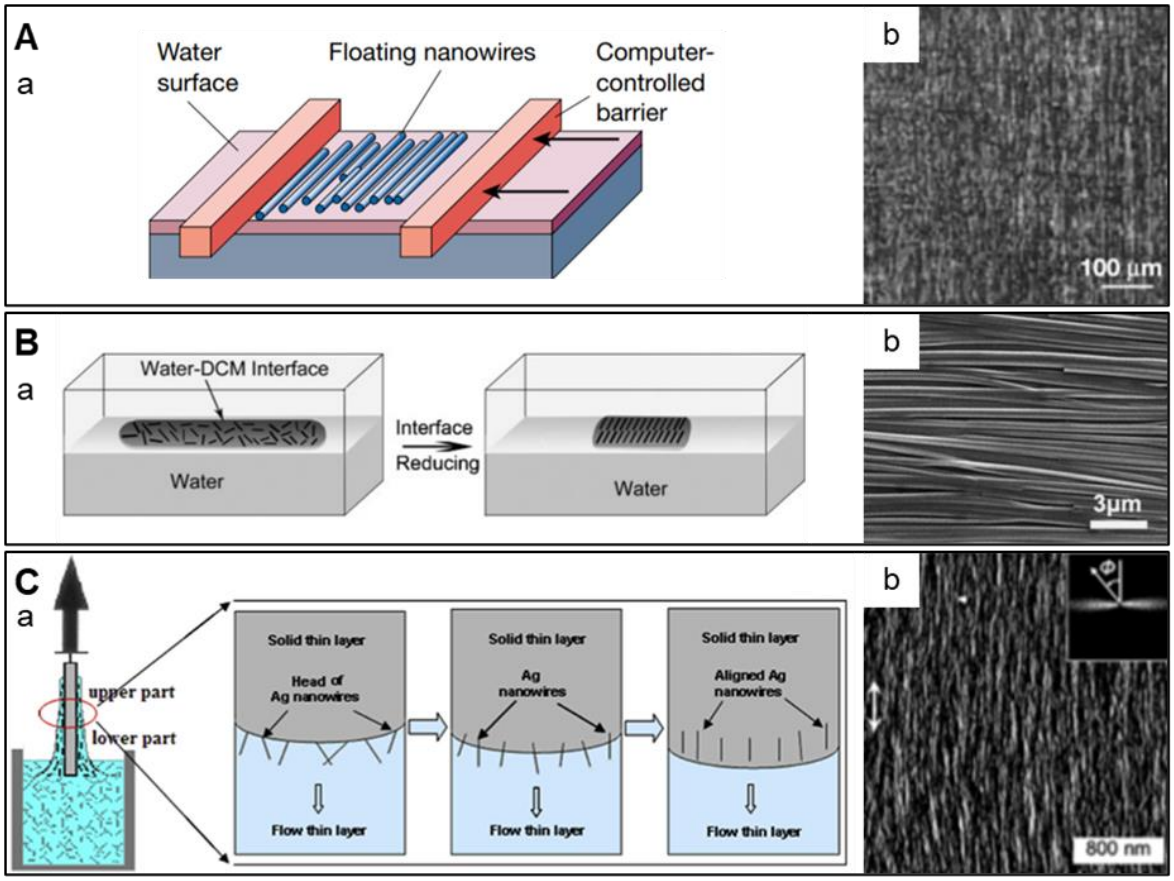

Figure 29. (A) Schematic representation of Langmuir–Blodgett technique[191] (a), and SEM image of silicon nanowires aligned by this technique[192] (b). (B) Schematic representation of evaporation induced assembly (a), and SEM image of a squaraine dye (2,4-bis[4-(N,Ndimethylamino)phenyl]squaraine) nanowires aligned by this technique (b).[193] (C) Schematic representation of dip-coating induced alignment[194] (a), and AFM image and the corresponding FFT image (inset) of aligned thin film of a combination of $V_2O_5 \cdot nH_2O$ nanowires and CNCs (cellulose nanocrystals) nanorods by this technique[195] (b).

Langmuir–Blodgett technique[184] (***Figure 29A***) is one of the most classical methods among them. This technique was initially used to make monolayer of molecules and has been extended to assemble nanoobjects in recent years. The nanoobjects, for instance silver nanowires (AgNWs), are dispersed in a volatile organic solvent and then spread onto a subphase (usually water). As the organic solvent is evaporated, a barrier compresses the AgNWs floating at the air-water interface at a given speed and with a controlled surface pressure. The AgNWs are thus close-packed and aligned along their longitudinal axis perpendicular to the compression direction. The aligned monolayer of Langmuir–Blodgett film can be transferred to a solid substrate. 1D nanoobjects can also be aligned by evaporation induced assembly[185] (***Figure 29B***).

A droplet of nanoobject suspension is spread on a substrate or a liquid / liquid interface. During the evaporation of the solvent, the 1D nanoobjects tend to pack along the longitudinal axis and the thus are aligned. The physical mechanism of the method is rather complicated, but it has been proven to be effective for alignment of a variety of 1D nanoobjects. Another simple alignment method at the solid–liquid interface is dip-coating[186] (***Figure 29C***). The 1D nanoobjects are aligned by directly pulling out the substrate from the nanoobject suspension. Many other methods which allow for in plane alignment of 1D nanoobjects and meanwhile the development into multilayered architectures can be listed, such as bubble blowing extrusion[187], contact printing[188], assembly at liquid–liquid interfaces[189], and electrospinning[190], to name a few.

However, all these methods have drawbacks of one kind or another. They require either expensive equipment and / or precise control of experimental parameters. Some methods are suitable for certain nanoobjects but not others, and most of these methods are time-consuming. In this context, a versatile and efficient alignment method is desirable.

Our group developed several years ago a novel alignment method for 1D nanoobjects, the Grazing Incidence Spraying (GIS). It is a spray-assisted shear-induced assembly method that relies on the low-angle (10° - 15°) spraying of a nanorod / nanowire suspension on a substrate. Using this approach, monolayer thin films of metallic nanorods or nanowires (namely AgNWs in this manuscript) in which all the nanowires are pointing in the same in-plane direction over >cm^2 areas are obtained[196]. The anisotropic optical

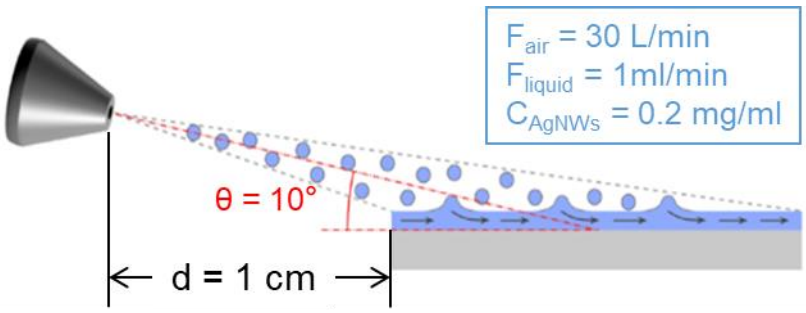

Figure 30. Schematic representation of the GIS method. The nozzle is connected to a fluid inlet and an air inlet, whose flow rates are regulated by a valve and a pump, respectively. During a GIS process, a suspension of AgNWs is sprayed on the substrate by air flow and the AgNWs are aligned by the shear force of the flowing liquid, and adsorbed on the substrate by electrostatic interactions. The distance d and angle θ between the sample and the nozzle can be easily adjusted.

and conductive properties of the oriented monolayer thin films were investigated[197], and multilayer films with oriented cellulose were also reported[198]. It was also shown that multilayer thin films containing AgNWs as building blocks can be built by combining GIS with the Layer-by-Layer (LbL) assembly.

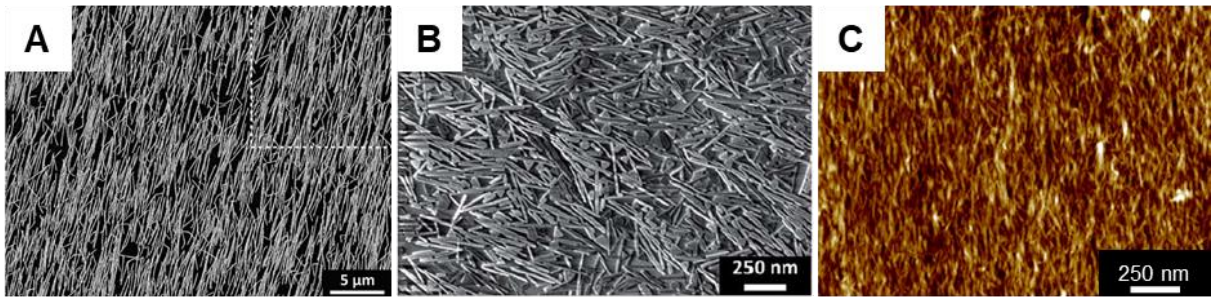

Figure 31. SEM images of one layer of oriented (A) AgNWs[196] and (B) gold nanorods[197]; and (C) AFM image of one layer of oriented nanofibrils[198]. All three samples were prepared by GIS.

The GIS technique is very easy to implement and a monolayer of oriented nanoobjects can be obtained in a few minutes. Meanwhile, the GIS requires no costly equipment nor complicated sample preparation, compared to other alignment techniques.

I.6.2. Layer-by-layer assembly

While the GIS allows for the in-plane orientation of AgNWs, the LbL-assembly[199] leads to multilayer structures. It involves the alternated deposition of oppositely charged materials, in particular polyelectrolytes, by dipping, spraying or spin coating, on a charged substrate. The stratified arrangement of the multilayer structure of LbL-films can give rise to novel materials with fascinating properties drastically different from the individual constituents, and the versatility of the technique allows to functionalize all kinds of charged surfaces with a reduced roughness and a well-defined thickness which depends on the number of polyelectrolyte layers.

The first report on LbL-assembly dates from 1966 by R. K. Iler[200] with colloidal particles. However, the technique has long been unrecognized thereafter, while the field of thin organic films was overwhelmingly dominated by the Langmuir-Blodgett technique[201–203] and self-assembled monolayers[204,205] at that time. The concept of "Layer-by-Layer" was re-introduced

in the early 1990s when G. Decher[206] and coworkers extended its applicability to a wide range of polyelectrolytes starting with bola-shaped amphiphiles[207,208].

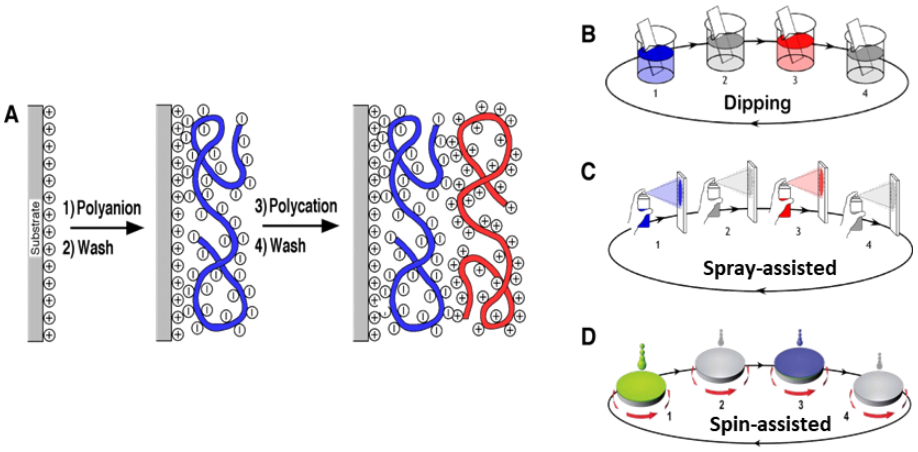

Figure 32. (A) Principle of LbL-assembly and (B) dipping method[206] (C) spray-assisted method and (C) spin-assisted method.

Since then, the technique has seen a vigorous development with various kinds of building blocks, from functional macromolecules including proteins or DNA[209,210], to biological nanoparticles[211] and inorganic nanoparticles[212,213], including magnetic[214] and gold[215] nanoparticles. The layers can be constructed by dipping the substrate in the solution, enabling the process to functionalize surfaces regardless of their size and topology. In fact, the takeoff of the field has been so rapid that already in late 1990s and early 2000s, polyelectrolyte multilayers functionalized macro-[216] / nano-particles[217,218] were reported, which led to objects with interesting surface properties[219,220]. On the other hand, the driving force for the multilayer build-up was not limited to the conventional electrostatic interaction, but has been proven to have many choices[221], including covalent bonds[222,223], hydrogen bonds[224–226], halogen bonds[227], van der Waals force[228,229], metal coordination interaction[230,231] and other specific recognitions.

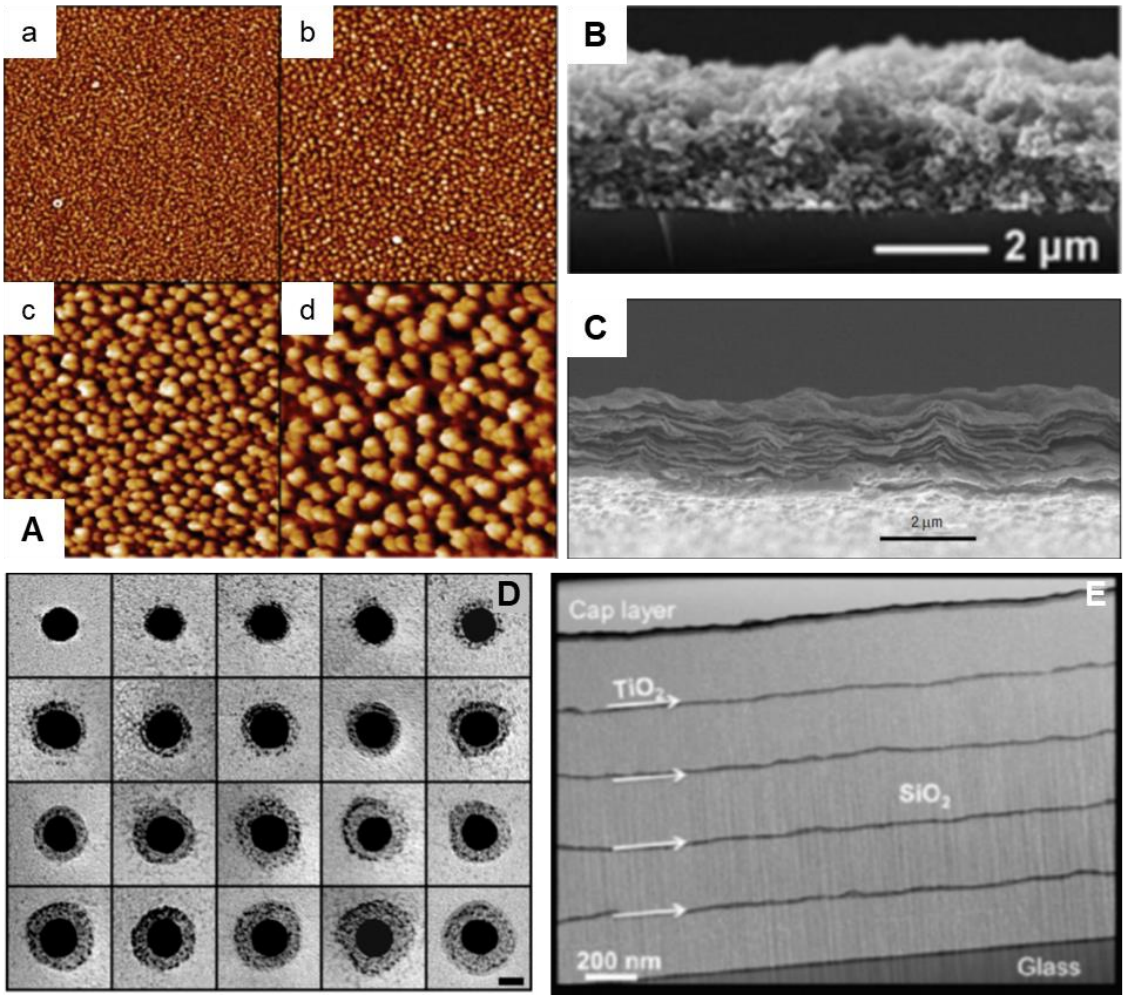

Figure 33. (A) AFM images (2 µm × 2 µm) of PEM films containing 6 (a), 20 (b), 60 (c), 110 (d) layer pairs of PSP/PAH (poly(sodium phosphate) and poly(allylamine hydrochloride)). The roughness of the film increases with the number of layer pairs.[247] (B) Cross-sectional SEM image of a $(PAA\text{-}DAR/DAR\text{-}PSS)_{20}$ coating, PAA-DAR being the complexes of poly(acrylic acid) and diazoresin, and DAR-PSS being the complexes of diazoresin and poly(sodium 4-styrenesulfonate).[248] (C) SEM image of an edge of a multilayer film containing 100 layer pairs of PDDA (poly(diallydimethylammonium) chloride) and montmorillonite clay platelets.[249] (D) TEM images of individual gold colloids stabilized by sodium citrate only (upper left corner) and PEM films composed of alternating PSS and PAH with increasing layer number of polyelectrolyte (up to 19 layers for lower right corner). The bar in the lower right corner corresponds to 10 nm.[250] (E) Cross-sectional TEM image of an 11-stack reflector made of alternating layers of TiO2 (dark gray) and SiO2 (light gray) nanoparticles assembled via spray-assisted LbL.[251]

Furthermore, more preparation methods for LbL-assembly are nowadays available[221]. Whereas the primary dipping method remains a frequently used technique, J. B. Schlenoff et al. established the spray-assisted method in 2000[232], which is much more time-saving. Only one year later, the spin-assisted method[233] was reported by P. A. Chiarelli et al., who prepared LbL-assembled PEM (polyelectrolyte multilayer) films using a spin-coater. The authors proved that

the average thickness of each layer pair of the PEM film was thicker than conventional dipping method yet its roughness was reduced[234]. Other unconventional methods also came forth in recent years, such as electrodepositing[235], magnetic assembly[236] and fluidics[237], to name a few.

To date, the LbL-assembly exhibits many applications in various fields, namely surface modifications[238,239], photonics[240], optics[241,242], electronics[243], solar cells[244], field effect transistors[245], and especially biomedicine[246].

In this manuscript, LbL-assembled PEM films will be used as a spacer in the hierarchical chiral plasmonic superstructures, separating the layers of AgNWs aligned in different direction. We use here one major interest of LbL, namely that the PEM thickness can be precisely controlled by the number of layer pairs of polyelectrolytes while the roughness is maintained at an extremely low level.

I I . Materials and methods

II.1. Materials

Poly(ethyleneimine) (PEI, M_w = 750,000; Lupasol PS, 33 wt% PEI in water) was purchased from BASF (Germany). Poly(sodium 4-styrene sulfonate) (PSS, M_w = 70,000; ref number: 243051), poly(allylamine hydrochloride) (PAH, M_w = 15,000; ref number: 283215), poly(diallyldimethylammonium chloride) (PDDA, M_w = 400,000-500,000; ref number: 409030, 20wt% in water), poly(methyl methacrylate) (PMMA, M_w = 120,000; ref number: 182230) and sodium chloride (NaCl) were purchased from Sigma-Aldrich (Germany). Silver nanowires (ref number: NWAG03E1) were purchased from ACS Material (USA). The organic dyes, including 5,6-Dichloro-2-[[5,6-dichloro-1-ethyl-3-(4-sulfobutyl)-benzimidazol-2-ylidene]-propenyl]-1-ethyl-3-(4-sulfobutyl)-benzimidazolium hydroxide, inner salt, sodium salt (TDBC; ref number: S 0046), 2-[3-[3,3-Dimethyl-1-(4-sulfobutyl)-1,3-dihydro-indol-2-ylidene]-propenyl]-3,3-dimethyl-1-(4-sulfobutyl)-3H-indolium hydroxide, inner salt, sodium salt (ref number: S 2165), 5-Chloro-2-[2-[5-chloro-3-(4-sulfobutyl)-3H-benzothiazol-2-ylidenemethyl]-but-1-enyl]-3-(4-sulfobutyl)-benzothiazol-3-ium hydroxide, inner salt, triethylammonium salt (ref number: S 2284) and 5-Chloro-2-[2-[5-chloro-3-(4-sulfobutyl)-3H-benzothiazol-2-ylidenemethyl]-but-1-enyl]-3-(4-sulfobutyl)-benzothiazol-3-ium hydroxide, inner salt, triethylammonium salt (ref number: S 2275) were purchased from Few Chemicals (Germany). Absolute ethanol was purchased from Fisher Scientific (USA), toluene was purchased from Sigma-Aldrich (USA) and chloroform was purchased from Carlo Erba (Italy). Hellmanex III solution used for rinsing the substrates was purchased from Hellma GmbH & Co. KG (Germany). All the chemicals were used without further purification, unless otherwise specified.

Silicon wafers were purchased from WaferNet Inc. (USA) and glass slides from Thermo Fisher Scientific (USA). Ultrapure water with a resistivity of 18.2 MΩ·cm was obtained from the Milli-Q Direct Water Purification System (Millipore, France) and was used directly after production.

The 1/4J SS air atomizing nozzles and accessories used for spraying AgNWs were purchased from Spraying Synstems Co. (USA), alternative nozzles Mod.970/0 were purchased from Schlick (Germany). The A480L nozzles used for the automated spraying robot for polyelectrolytes were purchased from Aztek (USA).

II.2. Experimental

II.2.1. Preparation of solutions

PEI solutions were prepared by dissolution of 2.5 mg/mL of the polymer in milli-Q water. PSS solutions were prepared in NaCl solution (0.5 M) at concentration of 0.616 mg/mL. PAH solutions were prepared in NaCl solution (0.5 M) at concentration of 0.0765 mg/mL. PDDA solutions were prepared in milli-Q water at concentration of 0.05 mg/ml. PMMA solutions were prepared in a mixed solvent chloroforme / toluene (1 / 1) at a mass fraction of 10%.

AgNWs solutions were prepared at a concentration of 0.2 mg/ml by diluting 50 times the commercial solution (originally in ethanol at 10 mg/ml) in milli-Q water. Solutions of TDBC and other cyanine dyes were freshly prepared by dissolution in milli-Q water at a concentration of 0.1 mg/ml.

II.2.2. Preparation of substrates

The silicon wafers and glass (or quartz) slides were immersed in absolute ethanol and then in a Hellmanex solution for several minutes under ultrasound, rinsed with milli-Q water and dried with compressed air.

The rinsed substrates were then treated by a plasma cleaner from Harrick Plasma (model PDC-002, USA). Plasma cleaning leads to the removal of impurities and contaminants from surfaces through the use of an energetic plasma or dielectric barrier discharge (DBD) plasma created from gaseous species. The surface cleaning is a multi-step process consisting of the generation

of the active (cleaning) species, their transport to the surface, the "reaction(s)" on the surface, and the ultimate removal of the reaction products from the surface. In the case of plasma cleaning, electrons, ions and radicals are generated in plasma. Their interaction with the solid surface causes mainly three basic phenomena that lead to surface cleaning: heating, sputtering and etching. Through the plasma cleaning treatment, the hydrophilicity and wettability of the substrate are also improved. In addition, as a result of the interaction with the electrons, ions and radicals, the surface of the substrate is negatively charged, which favors the deposition and adhesion of the first layer of PEI and the following LbL-assembly of PEM.

II.2.3. Grazing Incidence Spraying

The aligned deposition of AgNWs was realized by GIS. A suspension of commercial AgNWs was fed to a liquid handling Pump (*M50 Syringe-Free Liquid Handling Pump* model CP-CM1-P, Valco Instruments Co.) by a tube in fluorinated ethylene propylene (FEP, Interchim), which allows to precisely control the liquid flow (1 mL/min) of the AgNWs suspension. The pump was connected to a spraying nozzle (Spraying Systems), which is also connected to a gas flow controller fed by compressed air. The compressed air flow (30 L/min) was monitored by a flowmeter (Vögtlin Instruments GmbH, model GSP-C5SA-BB12), which allows to precisely control the flow by a valve. A polyelectrolyte multilayer PEI/PSS/PAH/PSS/PEI is deposited on a substrate treated as described in section II.2.2 by either dipping or spray-assisted LbL (see II.2.4). The substrate was then main by vacuum suction to the a motorized xy-theta sample holder perpendicular to the spraying direction of AgNWs, with a small angle $\alpha = 10° - 15°$ and distance d = 1 cm between the nozzle and the substrate. The suspension of AgNWs was sprayed through the nozzle by starting simultaneously the fluid and air flow during a given time (200 seconds unless otherwise specified), followed by a rinsing step for 10 seconds by spraying milli-Q water to the surface with a "air-boy" spraying bottle. The substrate was then dried with compressed air. The sample holder is motorized and can thus be precisely rotated to a certain angle, which allows depositing a second AgNW layer in a different direction. The setting of the spraying parameters, including the fluid flow, the air flow and the spraying time were controlled

by a home-made Labview software, while the movements (translation and rotation) of the sample holder were controlled by the software.

II.2.4. Layer-by-Layer assembly

II.2.3.1) Dipping-assisted LbL-assembly

The LbL-assembly of the PEM can be realized by dipping the substrate in the polymer solutions. The negatively charged substrate (silicon wafer, glass or quartz) was immersed in a PEI solution for 15 min, followed by rinsing 3 times by immersing it in milli-Q water for 3 minutes. The rinsing steps were necessary to remove weakly adsorbed polyelectrolyte. The substrate was then dried with compressed air. By repeating the same procedure for the other polyelectrolytes, alternating layer pairs of polyanion / polycation (mainly PSS/PAH in this manuscript) were deposited, which led to PEM films with the desired thickness.

The LbL-assembly of TDBC and other cyanine dyes involved in this manuscript was also realized by the dipping method, while the dipping time has been increased to 1 hour due to the different adsorption kinetics of the J-aggregates of the dyes compared to the polyelectrolyte chains (see details in section III.2.2).

The whole dipping process can be realized by an automated dipping robot in the lab in which the sequence of beakers and dipping time in each solution can be chosen. Such a robot has been used in this thesis for the thicker films when more than 200 layer pairs had to be deposited.

II.2.3.2) Spray-assisted LbL-assembly

The deposition of PEM can also be carried out by spray-assisted assembly. Instead of immersing the substrate in the polyelectrolyte solutions as in the case of the dipping approach, the spray-assisted method consists in spraying the polyelectrolyte solutions to the charged substrate for 6 seconds and then rinsing it for 10 seconds by spraying milli-Q water to the surface. For this

purpose, pneumatic spray cans (the so-called "air-boy" spray bottle, Carl Roth GmbH, Germany) have been used, which produce a cloud of low-velocity droplets. The advantage of spraying is that the time necessary to build a monolayer is drastically reduced compared to dipping.

The alternated spraying of polyanion / polycation can also be realized by an automated spraying robot in the lab. The same setup as for Grazing Incidence Spraying has been used, with different nozzles (Aztek), a lower gas flow (10 L/min) and a higher liquid flow (25 mL/min). The spray nozzles were placed orthogonally and at a larger distance from the substrate in order to wet the surface without applying the high shear force characteristic of GIS. The spraying robot was used used in this thesis when more than 15 layer pairs had to be deposited.

II.2.3.3) Spin-assisted LbL-assembly

The PMMA layers, with a typical thickness up to microns, were deposited by spin-coating, using a spin-coater from Laurell Technologies Corporation (USA, model WS-650HZ-8NPP). 100 µL of a PMMA solution was dropped on a PEI-coated substrate, placed in the spin coater, which then spun during 60 seconds at a maximum rotation speed of 8000 rpm and an acceleration of 200 rpm/s. A layer of PMMA of about 1 µm was deposited, followed by another layer of PEI by dipping or spraying.

II.3. Characterization techniques

II.3.1. Ellipsometry

Ellipsometry is a polarimetry technique for thin films and interfaces, which is based on the measurement of the change of polarization state of polarized light after reflection from a flat surface. This change of polarization is dependent on the refractive index and thickness of the thin film, and thus it is knowing the refractive index of a film it is possible to trace back to its thickness and vice versa. It is a non-destructive technique that allows to rapidly characterize the thickness of a thin film and its homogeneity over a flat reflective surface.

The thickness of the PEM films deposited on a silicon wafer can be measured using an ellipsometer purchased from PLASMOS (model SD 2300), operating at a single wavelength (632.8 nm) and at a constant angle of 70° with respect to the normal of the film, noted "Φ" in ***Figure 34***.

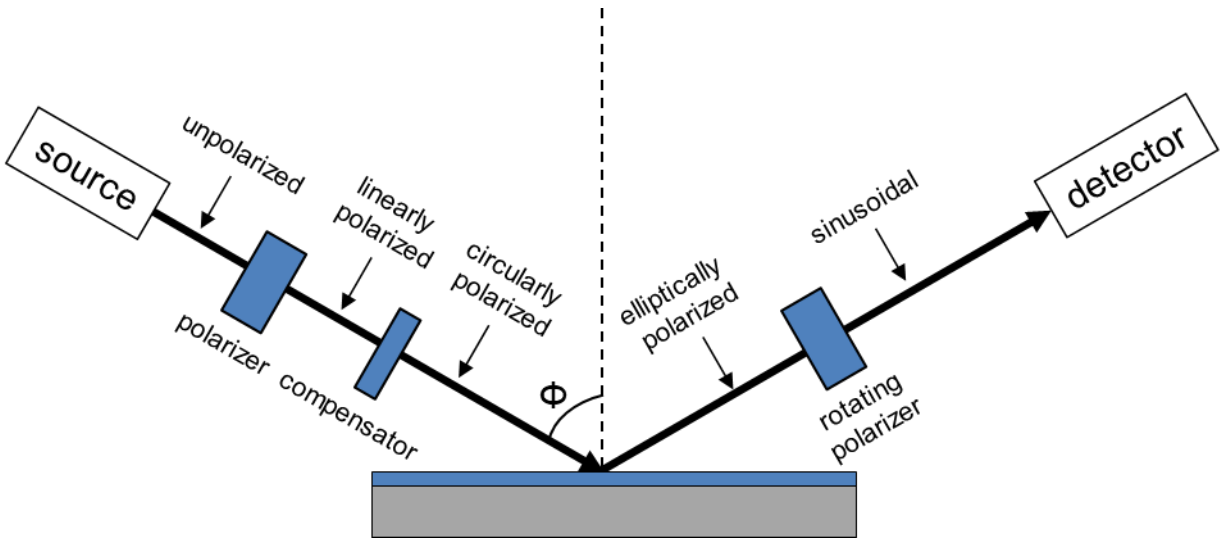

Figure 34. Schematic representation of a single-wavelength ellipsometer with rotating analyzer.

A light beam is emitted from the light source and is linearly polarized by a polarizer fixed at an azimuth of 45°. The linearly polarized light then passes through a quarter-wave plate, the compensator, to get a circularly polarized light. This light reaches the sample at a defined incidence angle at 70°. The polarization state of the light is changed after the reflection from the sample. The light passes through then a continuously rotating linear polarizer which results in sinusoidal signals. The signals are sent to the system computer by the photodetector where the thickness or the refraction index of the sample is calculated.

In this manuscript, the thickness of the PEM films deposited on silicon wafers were followed by ellipsometry, for which a constant refractive index was used (n = 1.465, value of the silicon oxide layer which is close to the refractive indices of the polymers). Despite this approximation, this technique enabled the quick characterization of the thickness of the PEM films, and its

accuracy was confirmed to be fairly good by the electron microscopy of the cross-section of the PEM films. (see section III.3.5)

For each sample, 9 points chosen at a random position all over the surface were measured, from which we considered the average thickness and the standard deviation.

II.3.2. Ultraviolet-Visible spectroscopy

The ultraviolet-visible-near infrared spectroscopy in this manuscript was measured with the Carry 5000 spectrometer from Agilent, which allowed to characterize the extinction of solutions and films in a spectral range from 180 nm to 3300 nm. In the process of a measurement, a beam is emitted from the light source, which passes through a monochromator and is then separated into two beams by a beam splitter. One goes to the sample to be characterized, and the other to the reference. The samples were fixed on a sample holder with a circular opening of 5 mm in diameter, and an identical sample holder was placed on the light path of the reference beam. The detector collects alternatively the light intensity from the refence I_0 and that from the sample I. The absorbance of the sample is thus given by:

$$A = -log\frac{I}{I_0} \quad \textbf{(45)}$$

Since the source beam of the Carry 5000 was slightly polarized due to the monochromator and that samples based on aligned AgNWs are very sensitive to the polarization, it was necessary to use a depolarizer when characterizing the extinction of the AgNW films. For this, a Hanle wedge depolarizer (B. Halle) was placed in front of the sample.

It is also possible to measure the extinction of the films with linearly polarized light at different angles using a motorized Glan-Taylor linear polarizer.

II.3.3. Circular dichroism spectroscopy

Circular dichroism spectroscopy is measured by alternately irradiating the sample with left and right circularly polarized light and measuring the difference in absorption between the two polarization states. Unpolarized light is passed through a linear polarizer and then a photoelastic modulator which allows to generate alternatively left circularly polarized (LCP) light and right circularly polarized (RCP) light. After light is passed through the sample, its intensity is measured by a photomultiplier tube (180-800 nm) or an InGaAs detector (800-1600 nm and 1600-2500 nm). This leads to the difference in absorbance between LCP and RCP, which is the circular dichroism of the sample.

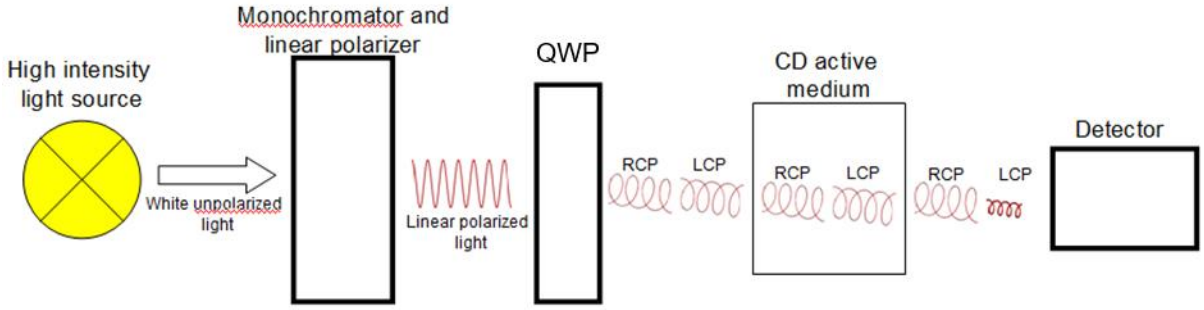

Figure 35. Schematic representation of a CD spectrometer.[252]

$$\Delta A = A_{LCP} - A_{RCP} \qquad (46)$$

where A_{LCP} and A_{RCP} correspond respectively to the absorbance of left and right circularly polarized light. From ΔA, it is possible to deduce the ellipticity θ given by:

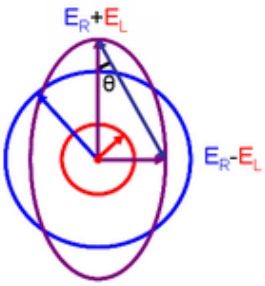

Figure 36. Elliptically polarized light (purple) is the superposition of LCP (red) and RCP (blue) light. θ is the angle between the magnitude of the electric field vector at its maximum and its minimum.

$$\tan\theta = \frac{E_l - E_r}{E_l + E_r} \qquad (47)$$

Thus, we have:

$$\theta\ (\text{radian}) = \frac{ln10}{4}\,\Delta A \qquad \textit{(48)}$$

The CD of a real sample has normally small ΔA values and θ is therefore usually expressed in millidegree (mdeg) unit.

$$\theta\ (\text{mdeg}) = \frac{ln10 * 180 * 1000}{4\pi}\,\Delta A \qquad \textit{(49)}$$

The CD in this manuscript was measured by a spectrometer from Jasco (model J-1700). The sample holder had a circular opening of 5 mm in diameter, allowing the characterization of the central area of the sample. It must be noted that the linear birefringence and the linear dichroism may have a strong influence on the CD measured on a commercial J1700 spectrometer, and thus the CD spectra measured by the Jasco spectrometer were regularly compared with those measured by the Mueller Matrix Polarimetry for the same samples.

II.3.4. Mueller matrix polarimetry

The state of polarization of light can be described by its Stokes vector **S**,

$$\boldsymbol{S} = [S_0\ S_1\ S_2\ S_3]^t \qquad \textit{(50)}$$

where the parameters are defined as follows:

$$S_0 = \langle I_x \rangle + \langle I_y \rangle = \langle I_{x'} \rangle + \langle I_{y'} \rangle = \langle I_{LC} \rangle + \langle I_{RC} \rangle \qquad \textit{(51.a)}$$

$$S_1 = \langle I_x \rangle - \langle I_y \rangle \qquad \textit{(51.b)}$$

$$S_2 = \langle I_{x'} \rangle - \langle I_{y'} \rangle \qquad \textit{(51.c)}$$

$$S_3 = \langle I_{LC} \rangle - \langle I_{RC} \rangle \qquad \textit{(51.d)}$$

S_0 is thus related to the total intensity of the light beam, while the other 3 coordinates are related to the polarization degree of the light propagating along the z axis perpendicular to the (xy) plane. I_x and I_y are the linear polarizations with respect to the Cartesian coordinate system along

x and y axis; $I_{x'}$ and $I_{y'}$ are the linear polarizations referring to the Cartesian coordinate system rotated by 45° with respect to x and y, and I_{LC} and I_{RC} are left-handed circularly polarization (LC) and right-handed circularly polarization (RC).

The stokes vector **S** can also be reduced to a three-dimensional vector by normalizing to the total intensity S_0:

$$\boldsymbol{s} = [s_1\ s_2\ s_3\ ] = \ [S_1/S_0\ \ S_2/S_0\ \ S_3/S_0] \qquad \textit{(52)}$$

We obtain thus the degree of polarization of the light:

$$P = |\boldsymbol{s}| = \sqrt{s_1^2 + s_2^2 + s_2^2} \qquad \textit{(53)}$$

with $0 \leq P \leq 1$. In the s_1, s_2, s_3 space, the unit sphere P = 1, named the Poincaré sphere, represents the states of perfectly polarized light, while its center P = 0 ($s_1 = s_2 = s_3 = 0$) represents unpolarized light. Inside the sphere, where $0 < P < 1$, there are all the partially polarized states, which can be regarded as a superposition of a totally polarized state and a unpolarized component.

When interacting with an optical element (transmission, reflection or scattering), the state of polarization of the incident light can be modified. This process can be mathematically expressed as the transformation of the original Stokes vector **S** into a new vector **S′**, by multiplying to the Mueller matrix **M**. This 4×4 matrix named after Hans Mueller represents the effect of the sample on the polarization and is a function of the frequency of light. In the absence of depolarization from the sample, its Mueller matrix can be written in the following form, which consists of seven elements, including the circular dichroism (CD), the circular birefringence (CB), the linear dichroism (LD) and the linear birefringence (LB).

$$\mathbf{M} = \exp\begin{pmatrix} A & -LD & -LD' & CD \\ -LD & A & CB & LB' \\ -LD' & -CB & A & -LB \\ CD & -LB' & LB & A \end{pmatrix} \qquad \textit{(54)}$$

where LD and LB correspond to linear dichroism and the linear birefringence at 0°, and LD' and LB' correspond to those at 45°.

Mueller matrix polarimetry makes it possible to measure the different elements of the Mueller matrix. The polarimetry involves passing depolarized light through a polarization state generator (PSG), which consist of a linear polarizer and a rotating quarter wave plate (retarder). It will produce light with defined and time varying states of polarization. The light then passes through (or is reflected from) the sample, which may change the polarization states of the light beam. The light then passes through a polarization state analyzer (PSA), which also consist of a quarter wave plate and linear polarizer. This analyzer measures the various defined polarization states which vary over time. As the generator and the analyzer vary their polarization states at different frequencies, it is possible to retrieve each transmitted polarization state for each incident polarization state. The parameters of the Mueller matrix can thus be calculated and are normalized according to the parameter M_{11}.

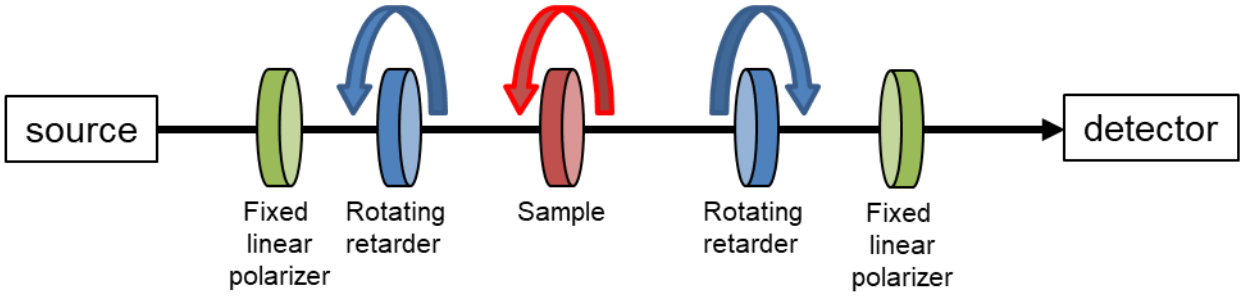

Figure 37. Schematic representation of a dual-rotating compensator polarimeter.

The normalized values of the elements of the Mueller matrix are comprised between -1 and 1. To compare the results of circular dichroism measured in the Mueller matrix polarimetry (CD_{MMP}) and the results of circular dichroism measured by circular dichroism spectrometer (CD_S), it is necessary to convert the values obtained by the normalized Mueller matrices to millidegrees through the following equation.

$$CD_s = \frac{180000 * ln10 * CD_{MMP}}{4\pi} \quad \textbf{(55)}$$

The Mueller Matrix of this manuscript were measured by Yann Battie at the University of Lorraine. Two kinds of polarimeter were used, one is the dual-rotating compensator polarimeter described above, which allows for the measurement of all the elements of the Mueller Matrix; the other is a polarimeter without the rotating retarder in the polarization state generator, which

allows for the measurements of the first three rows of the Mueller Matrix. Considering the symmetry of the Mueller Matrix, both polarimeters can provide full scale information of the Mueller Matrix.

II.3.5. Fluorescence spectroscopy

Fluorescence is the emission of a photon by an excited molecule, atom or nanostructure, through its relaxation to a lower energy state (possibly the ground state). It may have been excited from the ground state by absorption of a photon. The excited state undergoes rapid thermal energy loss to the environment through vibrations, and then a photon is emitted from the lowest-lying singlet excited state (***Figure 38***). The emitted photon has normally lower energy than the absorbed photon, and thus has a longer wavelength.

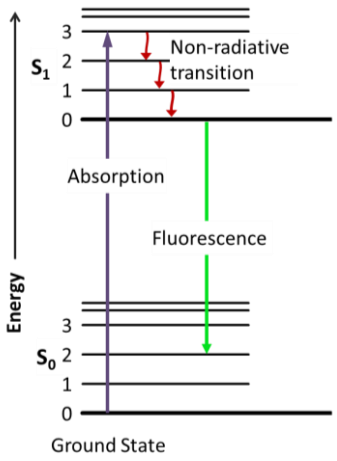

Figure 38. Jablonski diagram that illustrates the electronic states of a molecule and the transitions between them.

Fluorescence spectroscopy is the spectroscopy that analyze the fluorescence of a sample. There are two types of fluorescence spectroscopy, the emission spectrum and the excitation spectrum. An emission spectrum is the fluorescence emission intensity as a function of emission wavelength when the excitation wavelength is fixed. An excitation spectrum is when the emission wavelength is fixed and the excitation monochromator wavelength is scanned. The excitation spectrum gives information about the wavelengths at which a sample will absorb so as to emit at the chosen emission wavelength.

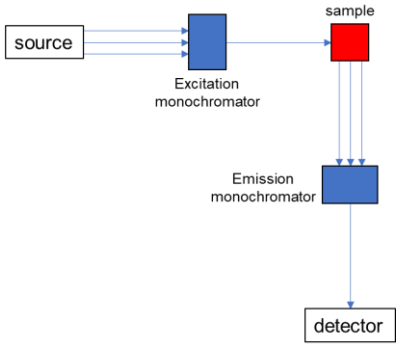

Figure 39. Schematic representation of a fluorometer.

The instrument allowing for the fluorescence spectroscopy is a fluorometer (***Figure 39***). Light is emitted from the light source and then filtered by the excitation monochromator. The sample is excited by the filtered light with a selected narrow band of wavelengths and emits afterwards a fluorescence photon. The emission light is filtered by the emission monochromator and then analyzed by the detector.

The fluorescence of the films containing TDBC was measured by a Fluoromax-4 spectrometer from Horiba (Japon).

II.3.6. Scanning electron microscopy

Scanning electron microscopy (SEM) is a technique that produces images of the surface of a sample by probing it with a focused electron beam. A Scanning electron microscope consists of an electron optical column, several electron detectors, a vacuum system, electronics and software. The primary electrons emitted by the electron gun of the microscope can interact with atoms of the sample, as the electron beam penetrates the surface of the sample into a certain volume called the "interaction pear". The producing signals that can be detected and that contain information about the sample's surface morphology and composition include secondary electrons, reflected or back-scattered electrons, characteristic X-rays and transmitted electrons.

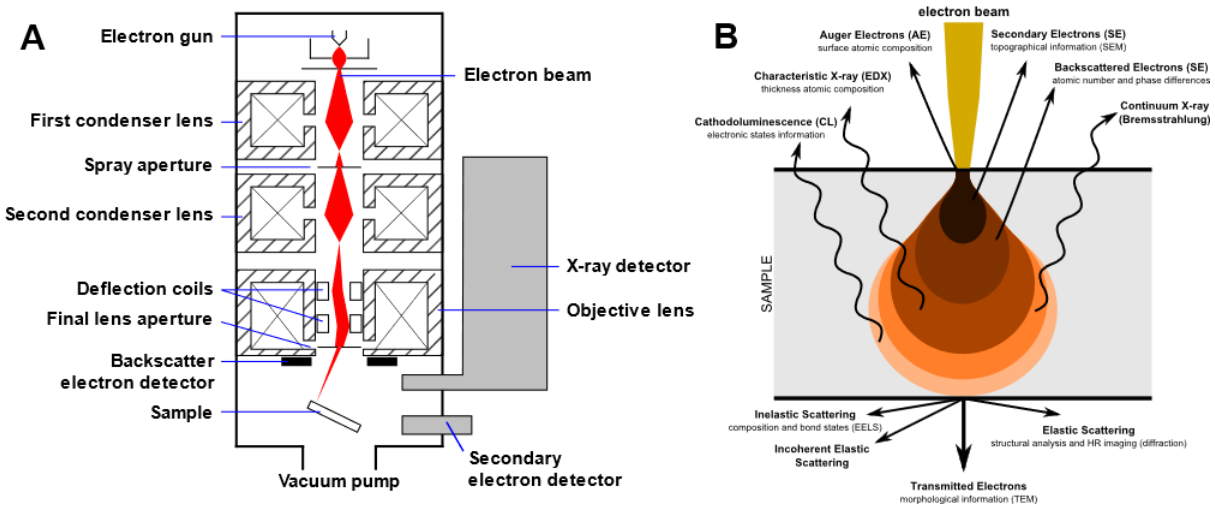

Figure 40. (A) Schematic representation of a SEM.[255] (B) Interaction pear showing the different interactions between the electrons and the sample.[256]

The most widely used detector is the secondary electron detector. As the primary electrons encounter the atoms of the sample and lose some of their energy during the collision, secondary electrons are emitted, which are collected and analyzed by the detector. Due to their low energy on the order of 50 eV, the secondary electrons tend to be emitted from a highly localized volume at the point of impact of the primary electron beam, making it possible to collect images of the sample surface with a resolution below 1 nm.

The primary electrons can also collide with the sample in an elastic way with a weak loss in energy, in this case we speak of back-scattered electrons, for which the detector is placed close to the axis of the primary electron beam. Atoms with a high atomic number have a nucleus with a higher positive charge than lighter elements and generate more back-scattered electrons. Therefore, a significant contrast will be observed between the zones of atoms with high and low atomic numbers. Image acquisition using the back-scattered electron detector thus provides compositional contrast between, for example, metallic and organic components.

Characteristic X-rays are emitted when the electron beam removes an inner shell electron from the sample, causing a higher-energy electron to fill the shell and release energy. The energy or wavelength of these characteristic X-rays can be measured by Energy-dispersive X-ray

spectroscopy and be used to identify and measure the abundance of elements in the sample and map their distribution.

The scanning electron microscope used in this manuscript is an SU8010 electron microscope from Hitachi (Japan) using the secondary electron detector. AgNWs thin films are highly conductive and thus convenient for SEM imaging. It was possible to take micrographs of the samples with the microscope, not only from the top view, but also from their cross section. In order to do so, the samples were firstly cut in two parts at a given region of interest, the cross section was then milled with a focused Ar^+ ion beam, using an ion milling system from Hitachi (Japan, model IM4000plus).

II.3.7. Atomic force microscopy

Atomic force microscopy (AFM) is a scanning probe microscopy (SPM) with nanoscale resolution. Unlike electron microscopy, AFM collects information of a surface by "touching" it with a mechanical probe. Therefore, AFM is rather a topographic imaging technique, which allows to analyze the topography of the surface and to calculate its roughness. The interaction of the probe and the surface also reveals information on the surface mechanical properties.

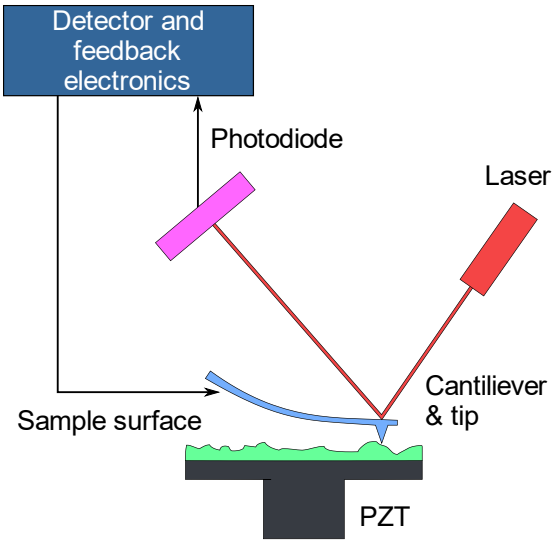

Figure 41. Schematic representation of an Atomic Force Microscope.

As illustrated in ***Figure 41***, the sample surface is scanned by a sharp tip placed on a cantilever. When the distance between the tip and the surface is reduced, the cantilever is deflected, which is detected by the movement of the reflection spot of a laser reflected by the cantilever to a

photodiode. A feedback electronic circuit follows these changes and leads to the formation of height profiles of the sample.

There exist two scanning modes of AFM: the contact mode and the tapping mode. In the contact mode, the tip is always in contact with the sample during the surface scanning. In the tapping mode, the tip oscillates very closely to the surface instead of contacting the surface. The Van der Waals force between the tip and the surface modifies the resonance frequency of the tip and therefore the cantilever. The tapping mode is usually used for fragile samples or when high resolution images are required.

The Atomic Force Microscope used in this manuscript is AFM multimode 8 (Bruker, USA) in tapping mode.

II.4. Simulation of the optical properties

The numerical simulations of the Mueller Matrix of our samples were carried out by Y. Battie from the Université de Lorraine using the Berreman formalism[253]. It is a 4x4-matrix method that describes the electromagnetic wave propagation in multilayer media, including multiple birefringent layers, crystals, chiral coatings and other complex optical configurations with many birefringent layers of arbitrary optical axis orientation.

Each sample is considered as a stack of layers. The refraction index of the glass substrate is taken from the literature[254]. The refraction index of the polymer, TDBC and the AgNW layer are measured by ellipsometry. Each layer of nanowires is considered as a uniaxial linearly birefringent and linearly dichroic medium, and thus 2 complex indices are necessary. The so-called ordinary and extraordinary indices measured on a typical AgNW oriented layer were considered for the simulation. The simulations are carried out at normal incidence, in transmission at azimuth 0 with respect to the bottom layer of nanowires.

The propagation of light in the structure is modeled using the Berreman formalism. This matrix formalism links the amplitudes of the incident field A to those of the reflected field B and of the field transmitted C by the structure.

$$\begin{pmatrix} A_s \\ B_s \\ A_p \\ B_p \end{pmatrix} = T \begin{pmatrix} C_s \\ 0 \\ C_p \\ 0 \end{pmatrix} \quad \textbf{(56)}$$

The indices p and s denote a polarization of p (TM polarization) and s (TE polarization) type. T is a (4×4) transfer matrix which represents the sample. It is obtained by calculating the product of the transfer matrices of each layer.

$$T = L_a^{-1} \prod_{i=1}^{N} T_i(-d_i)\, L_t \quad \textbf{(57)}$$

The transfer matrix $T_i(d_i)$ of the layer i of thickness d_i is given by:

$$T_i(d_i) = e^{-jk\Delta_i d_i} \quad \textbf{(58)}$$

where $k = \frac{2\pi}{\lambda}$ and $\Delta_i = \begin{pmatrix} 0 & 0 & 0 & 1 \\ 0 & 0 & -1 & 0 \\ -\varepsilon_{21,i} & -\varepsilon_{22,i} & 0 & 0 \\ \varepsilon_{11,i} & \varepsilon_{12,i} & 0 & 0 \end{pmatrix}$. This matrix is simplified because we are interested in the transmittance at normal incidence and in the case of a uniaxial medium.

The input matrix is defined by

$$L_a^{-1} = 0.5 \begin{pmatrix} 0 & 1 & -1 & 0 \\ 0 & 1 & 1 & 0 \\ 1 & 0 & 0 & 1 \\ -1 & 0 & 0 & 1 \end{pmatrix} \quad \textbf{(59)}$$

The output matrix is defined by

$$L_t = \begin{pmatrix} 0 & 0 & 1 & 0 \\ 1 & 0 & 0 & 0 \\ -n_s & 0 & 0 & 0 \\ 0 & 0 & n_s & 0 \end{pmatrix} \quad \textbf{(60)}$$

With n_s the refractive index of the substrate (glass slide).

The Fresnel coefficients of the sample are then calculated from the matrix T.

$$t_{ss} = \frac{T_{33}}{T_{11}T_{33} - T_{13}T_{31}} \quad \textbf{(61.a)}$$

$$t_{sp} = \frac{-T_{31}}{T_{11}T_{33} - T_{13}T_{31}} \quad \textbf{(61.b)}$$

$$t_{pp} = \frac{T_{11}}{T_{11}T_{33} - T_{13}T_{31}} \quad \textbf{(61.c)}$$

$$t_{ps} = \frac{-T_{13}}{T_{11}T_{33} - T_{13}T_{31}} \quad \textbf{(61.d)}$$

We can then build the Jones matrix in transmission:

$$J = \begin{pmatrix} t_{pp} & t_{ps} \\ t_{sp} & t_{ss} \end{pmatrix} \quad \textbf{(62)}$$

The Mueller matrix is thus: $M = A(J \otimes J^*)A^{-1}$ with $A = \begin{pmatrix} 1 & 0 & 0 & 1 \\ 0 & 0 & 0 & -1 \\ 0 & 1 & 1 & 0 \\ 0 & i & -i & 0 \end{pmatrix}$.

I I I . Plasmonic assemblies: from a single layer to chiral superstructures

Many efforts have been devoted to the fabrication of chiral plasmonic nanostructures, using various techniques (I.5). In this chapter, we will introduce the fabrication of chiral plasmonic superstructures with oriented AgNWs as building blocks, using Grazing Incidence Spraying (GIS) and Layer-by-Layer (LbL) assembly. Structures containing a single layer of aligned AgNWs (achiral structure), two layers and three or more layers of AgNWs (both left- and right-handed structures) will be presented. Their optical properties will be discussed, including CD spectroscopy, extinction spectroscopy and Mueller matrix polarimetry. The optical properties will also be compared to numerical simulations. In particular, the influence of different structural parameters on the chiroptical properties of the two-layer structures will be discussed. This chapter is divided in the following sections:

III.1. Single layer of aligned AgNWs

III.2. Layer-by-layer assembly of polyelectrolytes

III.3. Chiral superstructures containing two layers of AgNWs

III.4. Chiral superstructures containing three and more layers of AgNWs

III.5. Conclusion

III.1. Single layer of aligned AgNWs

The key prerequisite to fabricate a 3D multilayer chiral nanostructure is first of all the controlled alignment of AgNWs on a substrate. By using the GIS method described in the previous chapter, we obtain a dense film of AgNWs with the nanowires well-oriented along the spraying direction. In this section, the orientation distribution in a single layer of aligned AgNWs will be analyzed, and its optical properties (linearly polarized extinction spectroscopy and Mueller Matrix Polarimetry) will be studied.

III.1.1. Orientation distribution

Grazing Incidence Spraying (GIS) is a method allowing for the orientation of 1D anisotropic nanoobjects by spraying a suspension of the 1D nanoobjects on a pre-treated substrate at a small incidence angle. The nanoobjects are oriented along the flow direction during their adsorption due to the shear force of the flowing liquid. ***Figure 42***A shows a sketch and an optical photograph of the AgNW film deposited on a glass slide by GIS. ***Figure 42***B is the extinction spectrum of a monolayer of aligned AgNWs, illuminated by non-polarized light.

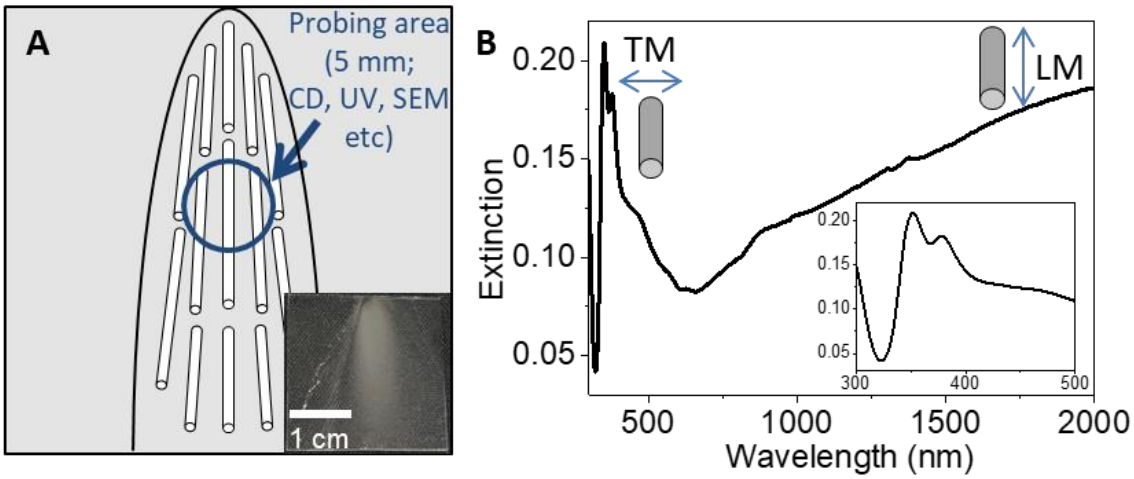

Figure 42. (A) Sketch of a layer of AgNWs aligned on a glass substrate deposited by GIS (inset: optical photograph of a sample). The area in which the spectroscopic measurements and microscopy imaging are carried out is a circle with a diameter of 5 mm in the center of the sample. The substrate is 25 mm × 25 mm. (B) Typical extinction spectrum of a layer of aligned AgNWs under non-polarized light. The double peak at 350 and 380 nm (inset) corresponds to the transverse modes of the LSPR of the AgNWs, while the broad band starting from 600 nm corresponds to the longitudinal modes of the LSPR.

Unlike isotropic plasmonic nanoparticles, such as gold nanospheres, which have a single LSPR mode depending on criteria discussed in section I.3.3 (**Figure 16**), anisotropic plasmonic nanoobjects display several LSPR modes. For example, in ***Figure 42***B, we see a double peak in the UV-Vis range corresponding to the transverse modes (TMs) of the LSPR of our AgNWs with a pentagonal cross-section. When the section of a nanowire / nanorod has a round shape, a single peak is often observed for the transverse mode. We also notice a broad band extending in the NIR, corresponding to the longitudinal modes of the LSPR. This broad extinction band is due to the superposition of several longitudinal modes that arise at different wavelength due

to the large length distribution of the AgNWs. Indeed, the exact shape and intensity of the extinction spectra of the AgNW films depend strongly on the AgNW aspect ratio, orientation distribution, density of the film etc, and thus may have slight differences from sample to sample. However, the main features are always present, which allows to compare the spectra obtained under different experimental conditions.

The alignment of the AgNWs was confirmed both from a microscopic and a spectroscopic point of view. As we can see in the SEM image (***Figure 43***), the AgNWs are well aligned.

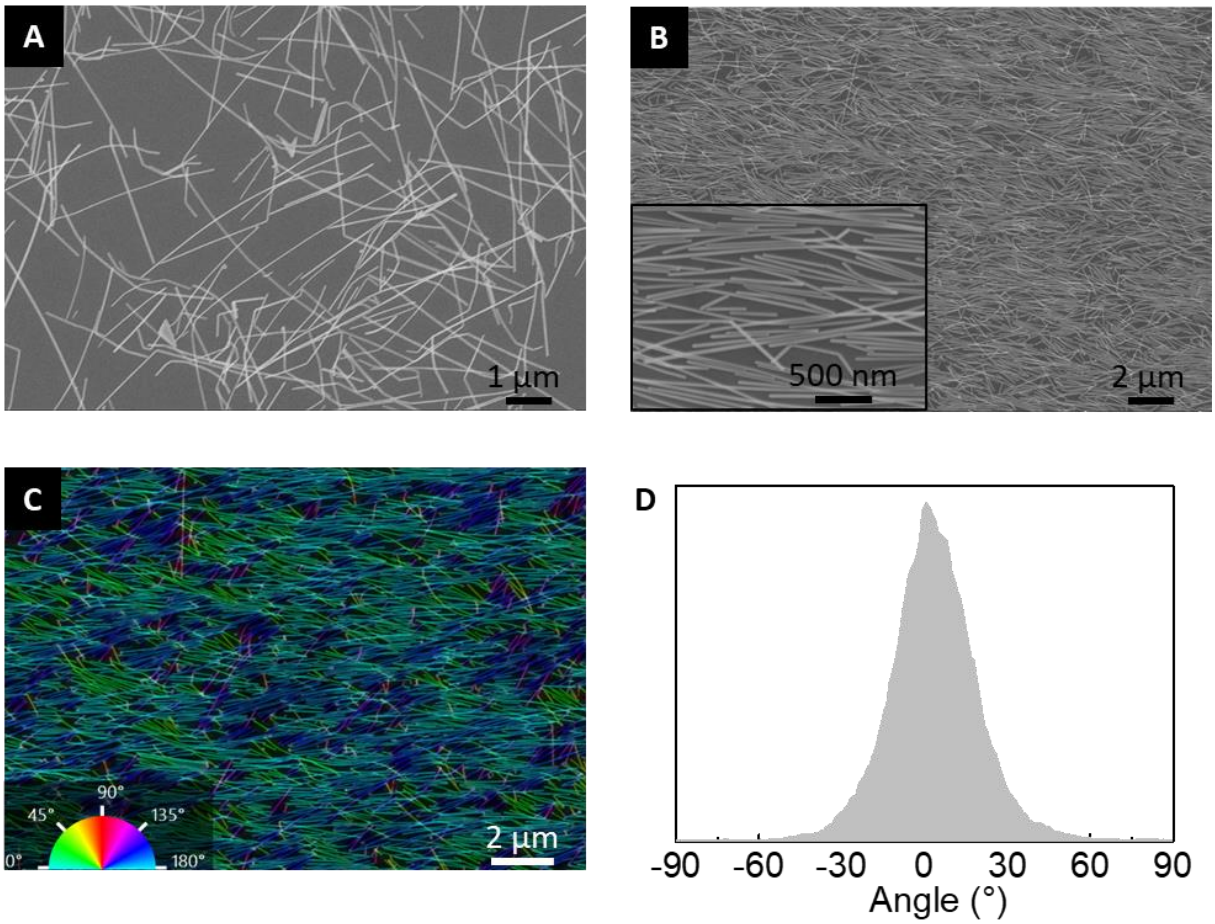

Figure 43. (A) SEM image of a non-oriented AgNWs film by dip coating. The diameter of the AgNWs is around 60 nm, and their length is several microns. (B) SEM image of a monolayer thin film of AgNWs aligned by GIS. (C) same image as in B) colored depending on its absolute orientation using OrientationJ, a plugin for Image-J. The inset shows the color scale (D) Orientation distribution of the AgNWs with respect to the main orientation.

The orientation analysis was realized with OrientationJ, a plugin for ImageJ, which computes the local orientation for each pixel in the image by comparing the gray level of one pixel to the

neighboring pixels. The distribution of orientation can be built, counting the numbers of pixels with identical deviation with respect to the main direction defined as θ = 0°. The nematic order parameter S_{2D} can thus be calculated and can be used to quantify the degree of alignment as function of the angular deviation θ with respect to the main orientation. This parameter is equal to zero when the orientation of the AgNWs is totally random and is equal to 1 when all the AgNWs have the same orientation angle.

$$S_{2D} = < 2cos^2\theta - 1 > \quad \textbf{(63)}$$

We obtain an order parameter S_{2D} = 0.85, which means 80% of the AgNWs are aligned within ±20°.

Considering that the AgNWs display a LSPR with orientation-dependent modes (TM and LM), one can expect that the extinction spectrum of a film of oriented AgNWs will depend on the direction of polarization if the spectra are measured with linearly polarized lights. The LMs of the LSPR should be excited when the incident light is polarized at 0° (the electric field of the light is parallel to the orientation of the AgNWs), while TMs should be excited when the incident light is polarized at 90° (the electric field of the light is perpendicular to the orientation of the AgNWs). Light polarized at an angle α between 0° and 90° would lead to a spectrum intermediate between those measured at 0° and 90°. In order to confirm this, we varied α from 0° to 90° with a step of 10° (***Figure 44***A). The extinction between 600 nm and 2000 nm (corresponding to the LM) increases with α while the extinction between 320 nm and 450 nm decreases with α (***Figure 44***B). One can observe that the extinction is highly polarization-dependent, as the extinction at 2000 nm varies from 0.75 (α = 0°) to 0.1 (α = 90°). This confirms the excellent alignment of the AgNWs and that the optical properties are highly anisotropic at the macroscopic scale.

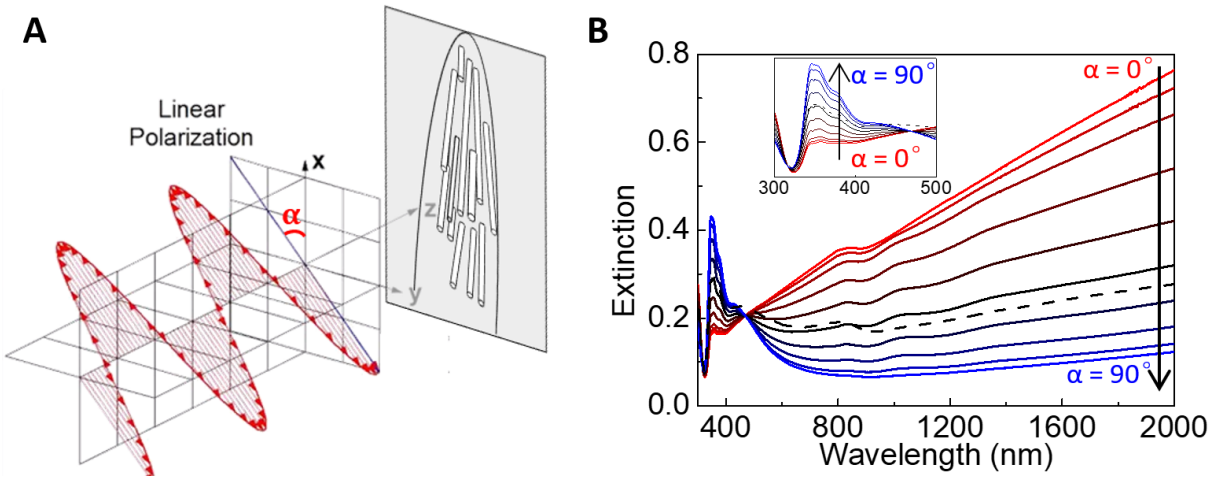

Figure 44. (A) Schematic illustration of extinction spectroscopy with light linearly polarized at angle α with respect to the direction of orientation of the AgNWs. (B) Polarized extinction spectra of a monolayer of aligned AgNWs measured with linearly polarized light. The angle α was varied from 0° - 90° with 10° steps. The dashed line is the extinction spectrum measured with a depolarizer. The features around 900 nm are an artefact of the spectrometer.

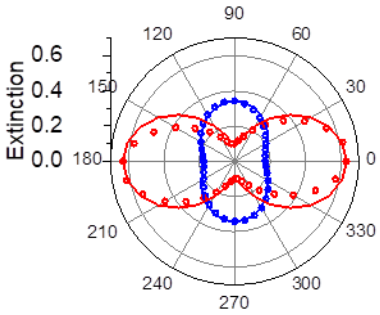

Figure 45. Polar plot of the measured (circles) and simulated (lines) extinction at 380 nm (blue) and 1500 nm (red) of a layer of aligned AgNWs as a function of polarization angle α.

Furthermore, the extinction of a layer of aligned AgNWs at two fixed wavelengths (380 nm and 1500 nm, corresponding to the transverse and longitudinal modes respectively) can be measured as function of the angle of the linearly polarized light (every 10° from 0° to 360°). The experimental results and modeling are given in the polar plot (***Figure 45***). We observed an extinction maximum for the transverse mode at 90° and an extinction maximum for the longitudinal mode at 0°, which shows the anisotropic response of the oriented thin film to linearly polarized light.

The variation of the extinction with the polarization can be fitted by a cosine square (or sine square) variation between a maximum and minimum value:

$$A_{long} = (A_{long\,max} - A_{long\,min})cos^2(\alpha) + A_{long\,min} \quad \textbf{(64.a)}$$

$$A_{trans} = (A_{trans\,max} - A_{trans\,min})sin^2(\alpha) + A_{trans\,min} \quad \textbf{(64.b)}$$

where A_{trans} and A_{long} correspond respectively to the extinctions at 380 nm and 1500 nm, A_{max} and A_{min} represent maximum and minimum extinctions at corresponding wavelengths, and α the polarization angle.

III.1.2. Influence of spraying time on the AgNW density

One major advantage of GIS is that the density of the deposited AgNW thin film can easily be tuned by varying the spraying time of the AgNW suspension. We varied the spraying time from 30 s to 800 s, and measured the extinction spectrum for each sample (***Figure 46***A).

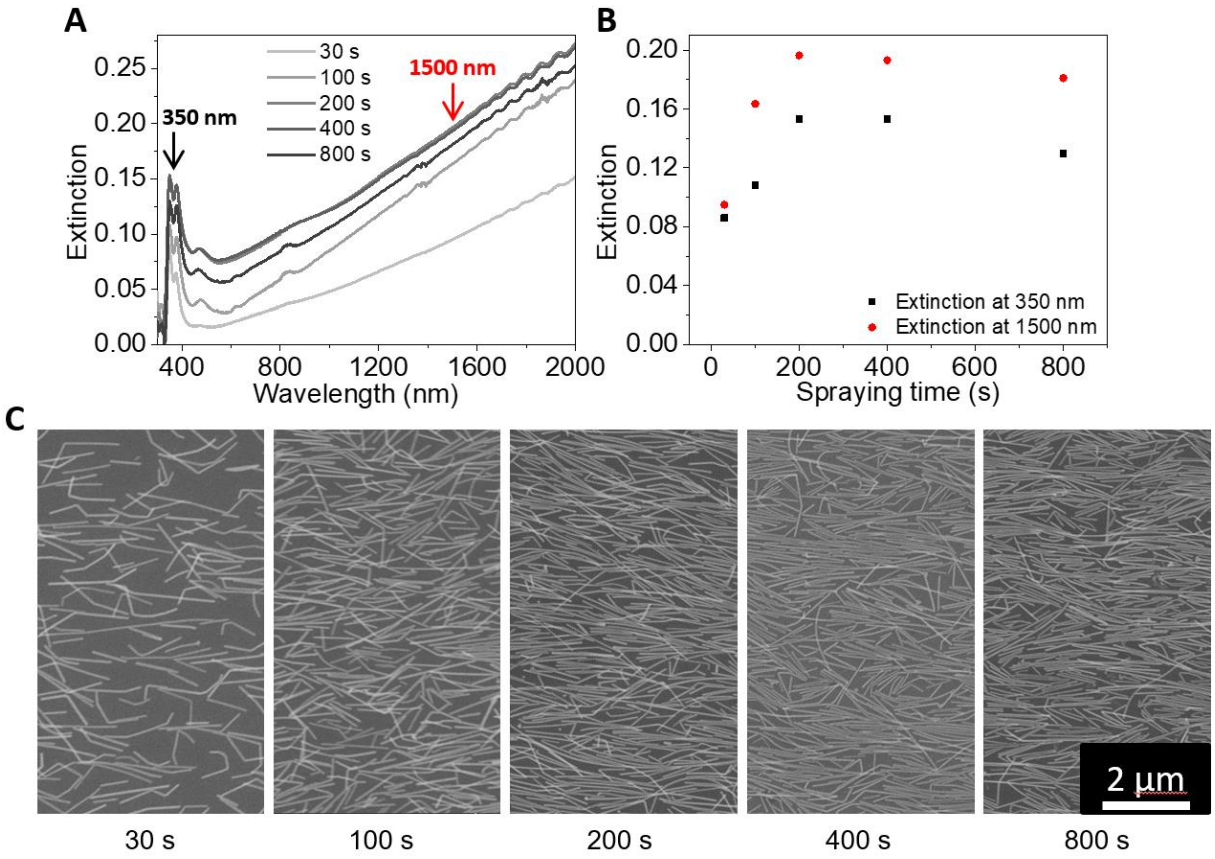

Figure 46. (A) UV-Vis-NIR extinction spectra of a layer of AgNWs deposited by GIS at different spraying time. (B) Extinctions at 350 nm and 1500 nm as a function of the spraying time. (C) SEM images of one layer of AgNWs with a spraying time of 30 s, 100 s, 200 s, 400 s and 800 s (form left to right).

We extracted the values of the extinction at 350 nm (TM) and 1500 nm (LM) and plotted them as a function of the spraying time (***Figure 46***B). The extinction increases with the spraying time until reaching its maximum for 200 s, which means that a saturated AgNW monolayer has been formed on the surface. Interestingly, the extinction decreases when increasing the spraying time from 400 s to 800 s, probably because weakly adsorbed AgNWs are desorbed from the substrate by the continuous shear force applied during spraying for a long time. Therefore, in order to obtain dense films of AgNWs and maximize the optical anisotropy, the optimal spraying time of 200 s will be used for the rest of this thesis unless otherwise specified.

III.1.3. Mueller Matrix Polarimetry

The Mueller Matrix Polarimetry (MMP) of a layer of aligned AgNWs was measured by Yann Battie from the Université de Lorraine. MMP provides a comprehensive description of the polarization properties of the sample, and can be compared to the results from other optical characterization methods. It is indeed well-known that the LD/LB of thin films with strong linear anisotropies can induce large artifacts on the CD measured with a commercial CD spectrometer, whereas all the contribution to the polarimetry (LD, LB, CD and CB) can be measured accurately with MMP. The linear properties are the difference between the x component and the y component, while x corresponds to the longitudinal direction of the AgNWs, and y corresponds to the transversal direction of the AgNWs. The circular properties are the difference between the left circularly polarized (LCP) light and right circularly polarized (RCP) light.

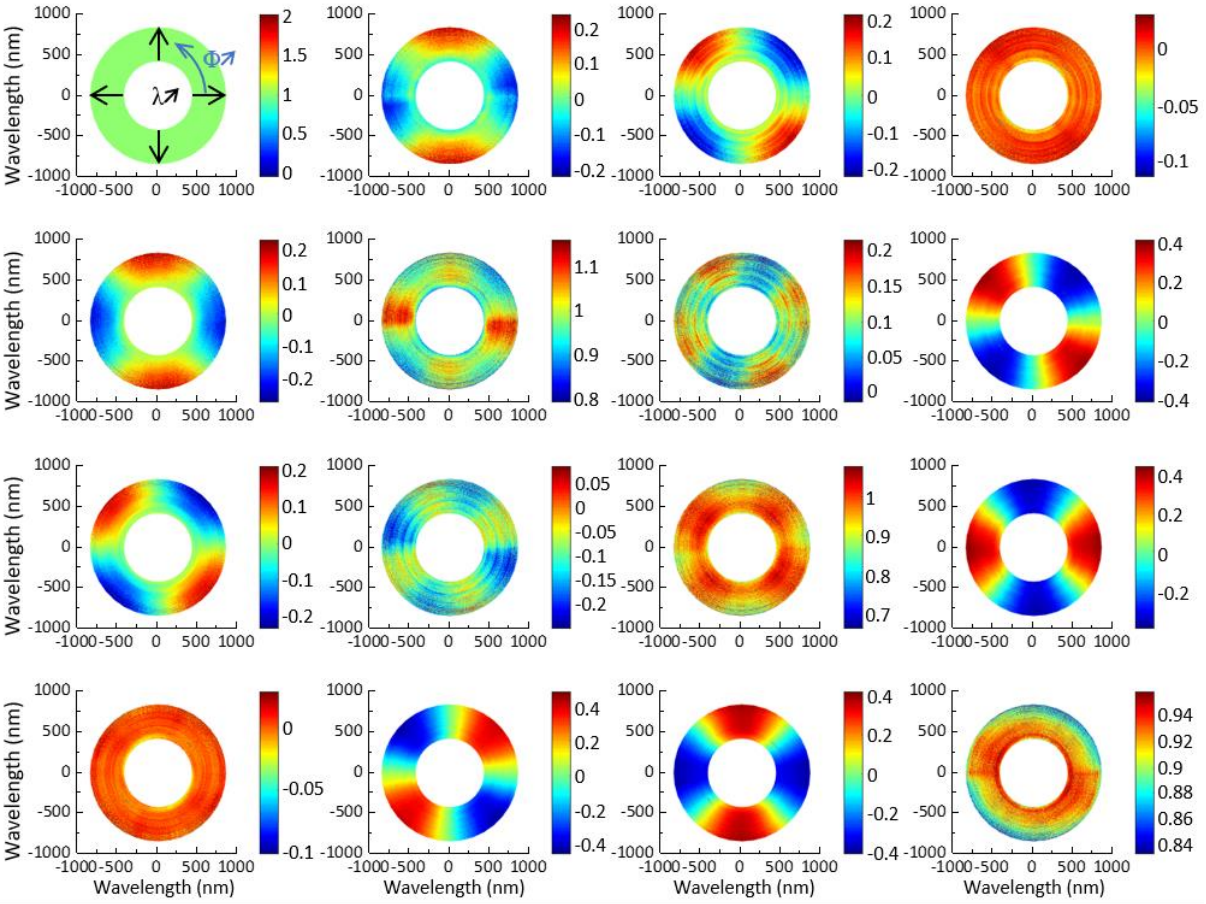

Figure 47. Mueller Matrix of a layer of aligned AgNWs as function of the azimuth angle (Φ) and wavelength (λ), measured by MMP. The radial coordinate is the wavelength (λ), the angular coordinate is the azimuth angle (Φ) and the color-code represent the amplitude of the different elements of the Mueller Matrix.

The measurements were performed in a spectral range from 382 nm to 842 nm, for different azimuth angle Φ, i.e. for different orientations of the AgNW thin films with respect to the polarization of the incident light. Φ = 0° when the incident light is polarized in the longitudinal direction of the AgNWs, and Φ = 90° when the incident light is polarized in the transverse direction of the AgNWs. The spectra have then been extrapolated to plot the polar graphs shown in ***Figure 47***, in which the wavelength is along the radius and the angle correspond to the azimuth of the sample, while the value of each element of the Mueller Matrix is color-coded. With the Mueller Matrix of the sample, which can be written in the following form ***(65)***, one is able to extract the important optical properties of the sample, including the circular dichroism

(CD), circular birefringence (CB), linear dichroism (LD) and linear birefringence (LB), given that the depolarization is negligible.

$$\mathbf{M} = \exp\begin{pmatrix} A & -LD & -LD' & CD \\ -LD & A & CB & LB' \\ -LD' & -CB & A & -LB \\ CD & -LB' & LB & A \end{pmatrix} \quad \textbf{(65)}$$

The depolarization d_p of a medium is given by the following equation:

$$d_p = \sqrt{\left(\left(tr(\boldsymbol{M}^t * \boldsymbol{M})\right) - 1\right)/3} \quad \textbf{(66)}$$

where **M** represents the Mueller Matrix and $\mathbf{M}^t$ represents the transposed matrix of the Mueller Matrix. When $d_p = 0$ the medium is considered as an ideal depolarizer and when $d_p = 1$, the medium is considered as non-depolarizing.

The depolarization of a layer of aligned AgNWs was calculated from its Mueller Matrix and the result is given in ***Figure 48***. This measurement allows to demonstrate that for all azimuth angles and over the entire measured spectral range, the d_p is close to 1 and thus the AgNWs can be considered as a non-depolarizing medium. LB, CB, LD and CD of the sample can thus be extracted from its Mueller Matrix (***Figure 49***).

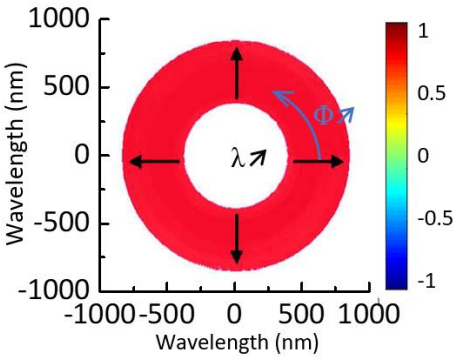

Figure 48. Depolarization values (color) as a function of the wavelength (radius) and the azimuth (angle) of the sample with respect to the polarization of the incident light.

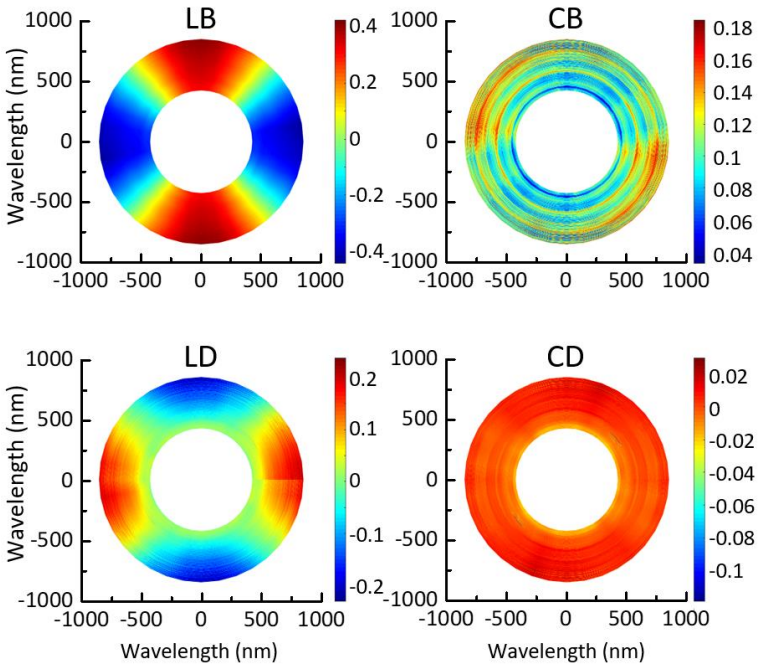

Figure 49. LB, LD, CB and CD of the single layer of aligned AgNWs as a function of the azimuthal angle (Φ) and wavelength (λ), extracted from the Mueller Matrix.

Simulations of the Mueller Matrix of the single layer of aligned AgNWs were also carried out, using the method described in section II.4. The simulated LB, LD, CB and CD are illustrated in ***Figure 50***, while the complete Mueller Matrix can be found in the appendix.

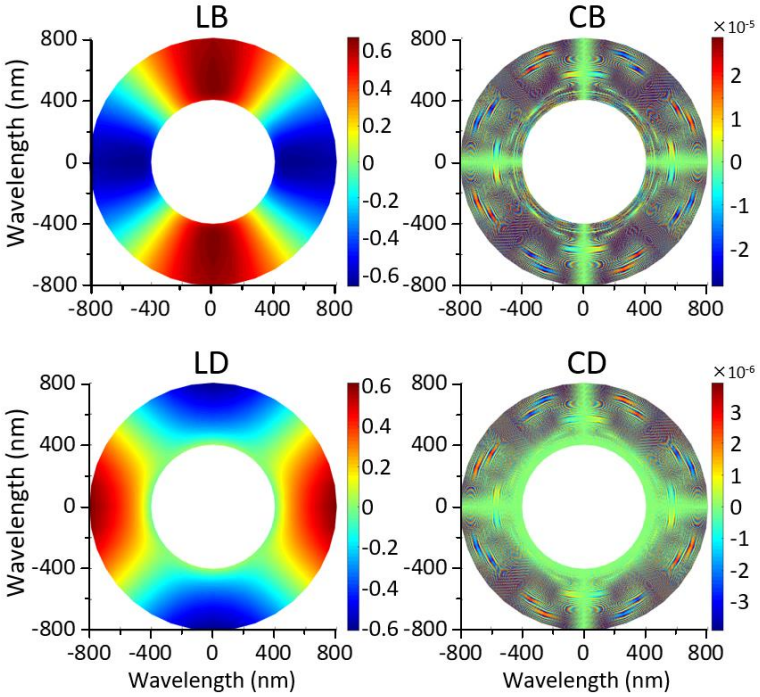

Figure 50. Simulated LB, LD, CB and CD of the single layer of aligned AgNWs as a function of the azimuthal angle (Φ) and wavelength (λ).

In both the measured (***Figure 49***) and simulated (***Figure 50***) MMP, we can see that the circular components (CD and CB) of a single layer of aligned AgNWs are independent of the azimuth angle. In particular the CD (both measured and simulated) of a layer of aligned AgNWs is close to 0 in the entire spectral range, which in other words means that the sample is non-chiral. The CB also has very small values compared to the linear components (LB and LD). On the other hand, the LB and LD have much higher values compared to the CB and CD, and are highly dependent on the azimuthal angle and the wavelength (for LD). Indeed, the symmetry of the MMP fits well what can be expected for a uniaxial medium such as an aligned monolayer of nanowires, i.e. high linear polarization properties (dependent on the azimuth angle), but no circular polarization properties. This is consistent with the (polarized) UV-Vis extinction spectra of the one-layer sample discussed in the previous sections. Despite the important dependence of LB and LD on the azimuth angle, the central interest of this manuscript is the chiroptical properties (CD) of the plasmonic nanostructures, which are actually independent of the azimuth angle. Measuring at different azimuth also increases a lot the measurement time and data treatment complexity. Thus, most of the measurements and simulations will be realized at only one azimuth ($\Phi = 0°$, that is, the orientation of the first layer of AgNWs is parallel to the polarization direction of the incident light) in the following sections.

III.2. Layer-by-layer assembly of polyelectrolytes

Now that we have shown that well-aligned AgNW thin films with highly anisotropic properties can be prepared by GIS, it is desirable to fabricate 3D superstructures containing several AgNWs layers, which are eventually chiral as long as the orientation of each layer of AgNWs is chosen to be different from each other. Both left- and right-handed superstructures were prepared, depending on the rotation direction of the AgNWs orientations. The interlayer spacer separating adjacent layers of AgNWs is a LbL-assembled polyelectrolyte multilayer film, consisting of alternated polyanion and polycation layers. In our case poly(sodium styrene

sulfonate) (PSS) has been used as the polyanion and poly(ethylene imine) (PEI) and poly(allylamine hydrochloride) (PAH) as the polycations.

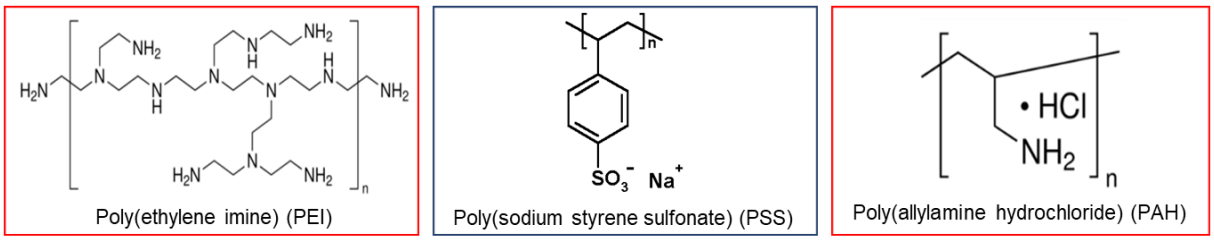

Figure 51. Chemical structure of the polyelectrolytes.

As a result, the structure of our chiral plasmonic superstructure containing two layers of AgNWs can be described as following: PEI/PSS/PAH/PSS/PEI/$Ag_{@0°}$/PEI/$(PSS/PAH)_n$/PSS/PEI/$Ag_{@\alpha}$ (***Figure 52***).

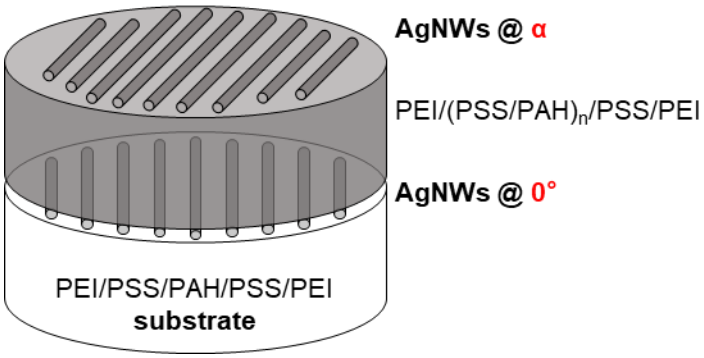

Figure 52. Schematic of a chiral superstructure consisting of two layers of AgNWs, the relative angle between the two directions of orientation is defined as α. The two AgNWs layers are separated by a multilayer polyelectrolyte thin film deposited by LbL-assembly.

An oligolayer assembly of (PEI/PSS/PAH/PSS/PEI) was deposited on the substrate, following its activation by plasma. Afterwards the first layer of AgNWs was spray-oriented by GIS on the polymer coated substrate. Before the spray-deposition of the second layer of AgNWs, a polyelectrolyte multilayer film acting as the interlayer spacing was deposited. It consisted of the classical polyelectrolyte sequence PEI/$(PSS/PAH)_n$/PSS/PEI, which has been established since two decades and has been widely used until now. It starts and ends with a layer of PEI, which has a very strong stickiness towards the substrate and the AgNWs. The repeating $(PSS/PAH)_n$ layer pairs lead to smooth and robust thin films with determined and tunable thickness by varying the layer pair number n, thanks to their high charge densities and their long chain structures compared to the dendritically branched structure of PEI. This section aims to introduce the two frequently used LbL-assembly methods (dipping and spray-assisted methods), and their precise control of the thickness of the polyelectrolyte multilayer films up to very large number of layers.

There are typically three LbL-assembly strategies: dipping, spray-assisted and spin-assisted LbL-assemblies. This manuscript includes mainly the dipping and spray-assisted methods. We prepared several LbL films of PEI/(PSS/PAH)$_5$ by the dipping methods, with different dipping time per layer varying from 0.2 to 30 min.

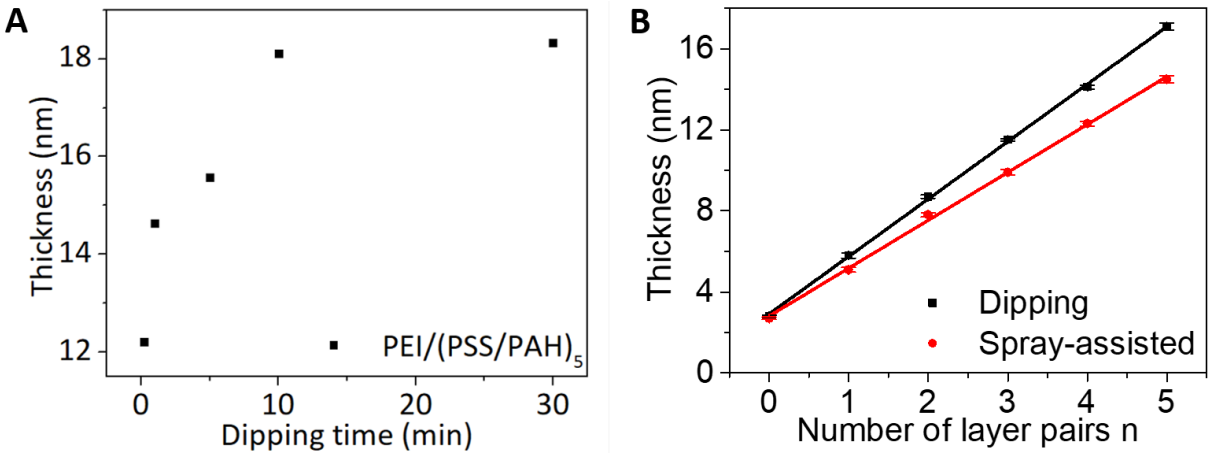

Figure 53. (A) Thickness of a PEI/(PSS/PAH)$_5$ film obtained by the dipping method with different dipping time from 0.2 – 30 min per layer. (B) Thickness of a PEI/(PSS/PAH)$_n$ measured by ellipsometry as a function of n, the number of (PSS/PAH) layer pairs. The thickness at n = 0 of about 2.5 nm is that of the PEI layer and the oxidized layer of the substrate resulting from plasma cleaning.

As we plot the total thicknesses as function to the dipping time per layer, we observe that the thickness increases with the dipping time and reaches a maximum at 15 min (***Figure 53***A), which is the saturation of the deposition, while this saturation is reached after a few seconds via the spray-assisted method.

We produced a multilayer polyelectrolyte film with a structure of PEI/(PSS/PAH)$_n$ ($0 < n < 5$) via the dipping and spray-assisted methods, and its thickness was followed by ellipsometric measurements for each n, i.e. after the deposition of PEI and each layer pair of PSS/PAH. As demonstrated in ***Figure 53***B, the thickness of a LbL-assembled polyelectrolyte film increases linearly as the number of layer pairs of PSS/PAH is growing. LbL films obtained by the dipping method have a slightly larger thickness in our experimental conditions. Dipping is more time-consuming than spraying as the dipping time is typically several minutes vs. several seconds for spraying. It is also more economical in terms of chemical products, as the same beaker can be re-used for the dipping of a large number of layers.

In order to reach higher interlayer spacings of several tens or hundreds of nanometers, a large number of polyelectrolyte layers have to be deposited (we used samples with up to 100 layer pairs of PSS/PAH in this thesis). Luckily, we could use a dipping robot and a spraying robot, which allow for the automated fabrication of LbL films, and the linear growth of the multilayer with the number of layers was maintained (***Figure 54***).

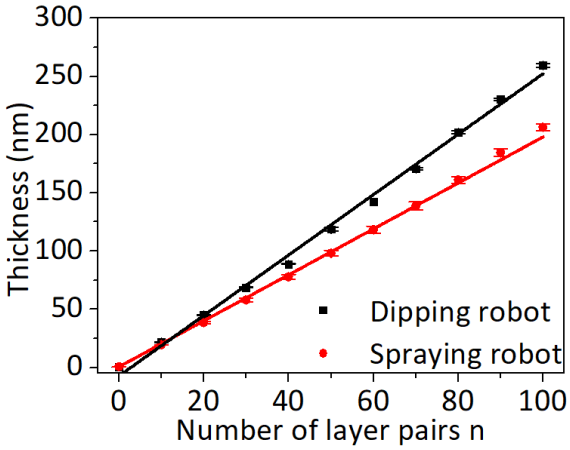

Figure 54. Thickness of LbL polyeletrolyte multilayer thin films with up to 100 PSS/PAH layer pairs prepared by an automated dipping robot or spraying robot.

The thicknesses in ***Figure 53*** and ***Figure 54*** were measured by ellipsometry, and the samples thus had to be prepared on silicon wafers instead of glass slides because a reflective substrate is required. We measured for each sample nine different spots and calculated the average thickness. Error bars, which represent the standard deviation of the thickness over the different measurement points, were smaller than the data points in ***Figure 54***, which reveals the excellent homogeneity of the film. The reliability of the ellipsometric thickness measurement and the reproducibility of identical LbL films on silicon wafers and glass slides were confirmed later by SEM imaging of cross sections of samples on glass slides (see section III.3.4).

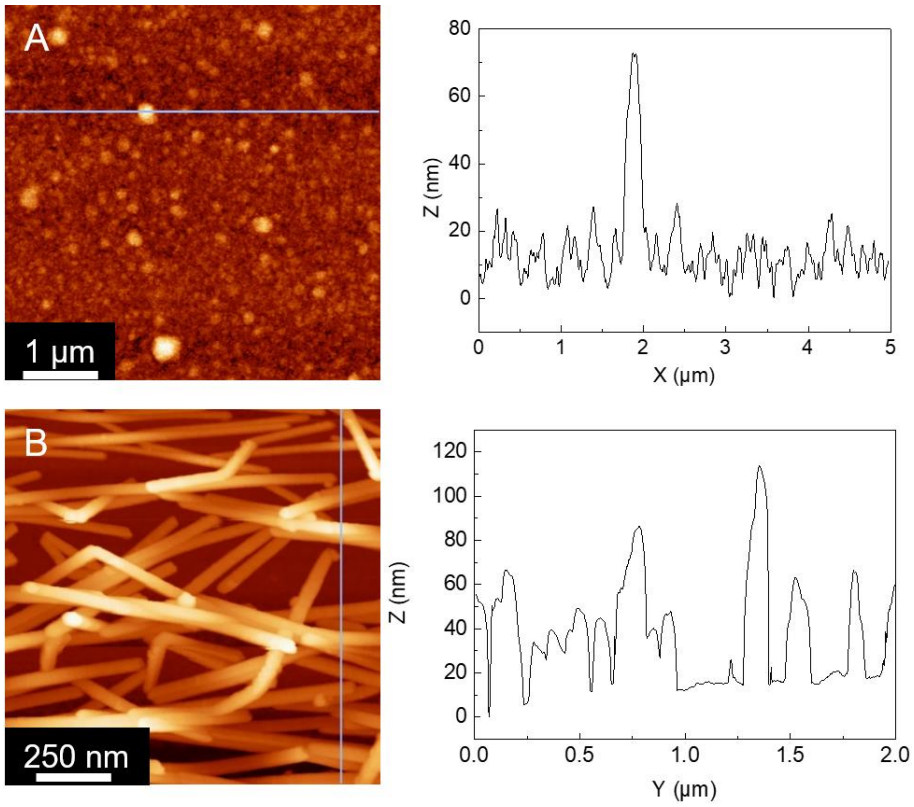

Figure 55. (A) AFM image of a PEM (PEI/(PSS/PAH)$_{100}$) thin films consisting of 100 layer pairs of PSS/PAH and the line profile analysis across the surface. The surface is relatively smooth with some islands distributed over the surface (for example z (x = 2 µm) = 80 nm in the line profile analysis). (B) AFM image of a single layer of aligned AgNWs and the line profile analysis. z = 60 nm is the approximate height of an AgNW monolayer (corresponding to the diameter of the AgNWs) and z = 120 nm corresponds to the crossing of two AgNWs.

Figure 55A is an AFM image and a line profile on a polyelectrolyte multilayer (PEM) thin film consisting of 100 layer pairs.Small islands can be observed on the surface (bright spots in the AFM image) over the surface, while its overall roughness remains at a very low level. The root mean squared roughness R_q = 6.9 nm, which is small compared to the total thickness (d ≈ 200 nm). ***Figure 55***B is an AFM image of a single layer of aligned AgNWs and its line profile. We can see in the line profile analysis the diameter of the AgNWs (z ≈ 60 nm) and its double (z ≈ 120 nm) when two AgNWs are crossing each other.

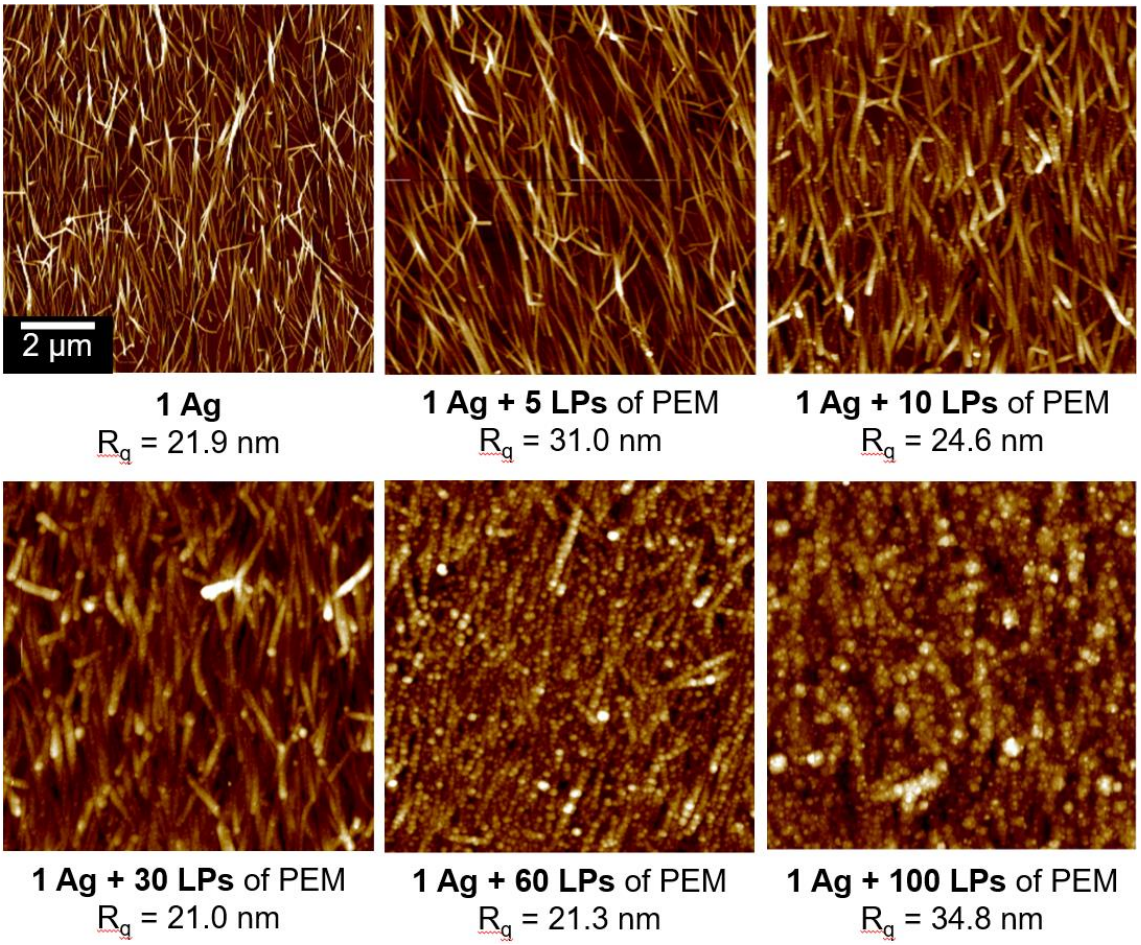

Figure 56. AFM images of films consisting of a single layer of aligned AgNWs coated by PEM films of increasing thickness. The structure of the films is denoted as $(PEI/AgNWs/PEI/(PSS/PAH)_n)$.

Figure 56 shows AFM images of films consisting of a single layer of aligned AgNWs coated by PEM films of increasing thickness. We observe that the roughness of the film remains at a relatively low level independent of the number of layers in the PEM. The AgNWs layer has a certain roughness due to the fact that it consists of a sub-monolayer of nano-objects with a diameter of 60 nm. The PEM film can reduce the roughness of the AgNWs layer by filling the "valleys" between the AgNWs, which makes that the topography of the AgNWs is less obvious on the images of the films with 60 and 100 layer pairs. On the other hand, the PEM films may lead to an additional roughness due to the small islands evidenced in ***Figure 55***A and which are also visible in the films with the thicker PEM. Consequently, the root mean squared roughness of the surfaces with different number of layers deposited on a single layer of AgNWs are in the same range (R_q =21 – 35 nm).

In conclusion, we have shown that the Layer-by-Layer assembly allows building homogeneous polyelectrolyte films on top of AgNWs with a relatively low roughness, and whose thickness can be easily and finely tuned at the nm level by changing the number of deposited polymer layers.

III.3. Chiral superstructures containing two layers of AgNWs

By combining the orientation of AgNWs by GIS and the LbL-assembly of polyelectrolytes described above, multilayer superstructures containing several layers of AgNWs can be fabricated by the repeated deposition of PEM films and AgNWs (***Figure 57***).

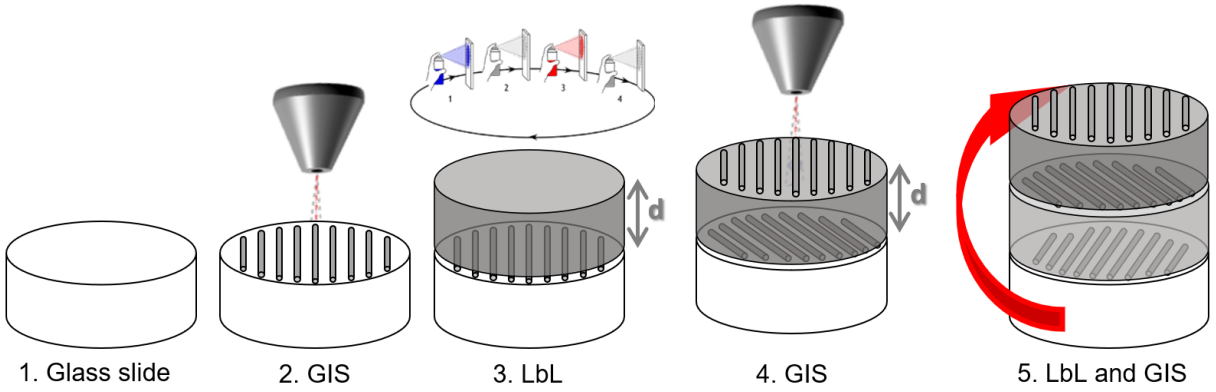

Figure 57. Schematic representation of the fabrication process of chiral plasmonic superstructures containing several layers of AgNWs oriented in different directions, combining the GIS and LbL-assembly: 1. A glass slide is functionalized by a polyelectrolyte multilayer film (PEI/PSS/PAH/PSS/PEI) with a thickness of approximately 5 nm. 2. The first layer of AgNWs oriented at 0° is deposited by GIS. 3. A polyelectrolyte multilayer film (PEI/$(PSS/PAH)_n$/PSS/PEI) of variable thickness is deposited by LbL. 4. The sample is rotated to deposit by GIS the second layer of AgNWs oriented at an angle α . This gives a chiral structure (left- or right-handed, depending on $\alpha > 0$ or $\alpha < 0$). 5. By repeating the process, chiral superstructures with a controlled architecture containing multiple layers of AgNWs can be obtained.

We focus in this manuscript on two- and three-layered superstructures, considering the fact that the spectroscopic studies turn to be technically difficult for samples with more than 3 AgNW layers as the extinction of the thin films is getting too large to allow a reliable measurement of the optical properties. This section aims to present the optical properties of the chiral superstructures containing two layers of AgNWs, both left- and right-handed, and to study the

structural parameters which influence the optical properties of the sample, namely the angle between the two layers AgNWs and the interlayer spacing between them.

Figure 58 shows top-view and cross-section SEM images of left- and right-handed 2-layer thin films of oriented AgNWs.

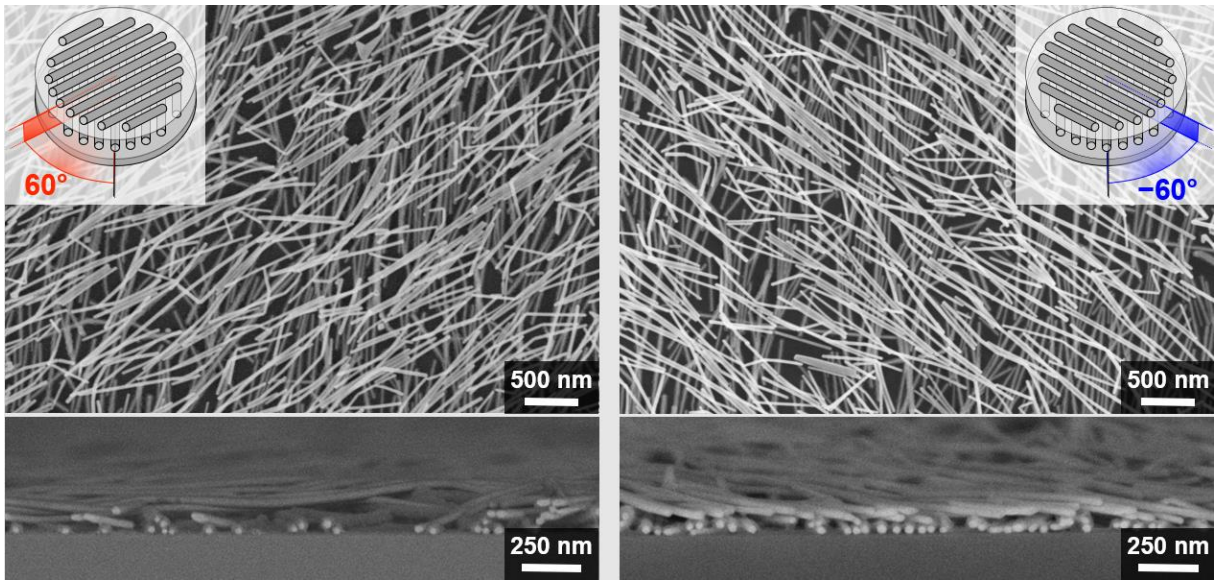

Figure 58. SEM images of left-handed and right-handed structures containing two layers of AgNWs from top view and from the cross section.

The two layers of AgNWs can be easily identified in the top-view SEM images (***Figure 58***), and the angle between the AgNW layers is well defined (±60° for left- and right-handed structures). The samples were cut and prepared according to the procedure described in the section II.3.6, and the samples were tilted by 8° for the SEM imaging of the cross-section so that the orientation of the upper layer can be seen. The distance between the two layers of AgNWs were measured to be 13 nm, which is consistent with the ellipsometric measurements.

III.3.1. Chiral optical properties of the two-layer superstructures

CD and extinction spectra as well as the g-factor spectra of a one-layer sample of oriented AgNWs and left- and right-handed two-layer superstructures are given in ***Figure 59***.

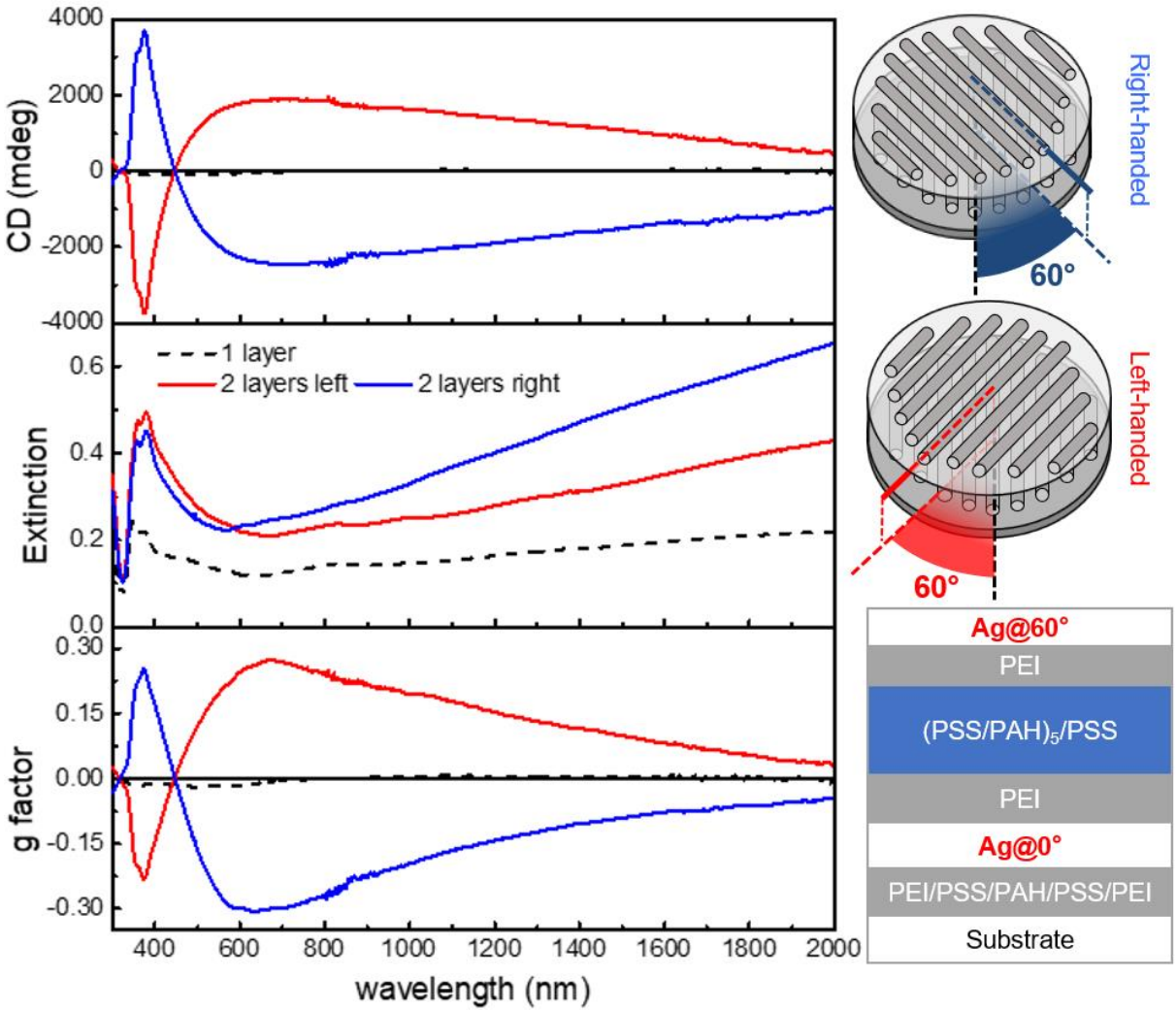

Figure 59. Left panel: CD, extinction and g-factor spectra of samples composed of a single layer (dashed lines) of aligned AgNWs (non-chiral), and 2 layers (solid lines) of AgNWs with both left (red) and right (blue) handedness. Right panel: Schematics of left- and right-handed superstructures containing 2 layers of AgNWs and the layer-by-layer composition of a two-layer structure (from top to bottom). The angle between two adjacent layers of AgNWs was 60°, the PEM between them was PEI/$(PSS/PAH)_5$/PSS/PEI (~13 nm). The difference of extinction between the left- and right- handed structures in the near infrared is probably due to the depolarizer which only partially depolarizes the incoming beam of the spectrometer.

The one-layer structure is by definition not chiral, and hence it has a CD and g-factor close to 0, which indicates that the linear dichroism doesn't affect too much our CD measurements. The two-layer superstructures show a strikingly high CD (up to ±4000 mdeg) and g-factors (up to ±0.3), which was not yet reported for similar self-assembled chiral plasmonic superstructures. Furthermore, the CD and g-factors of the left- and right-handed structures are perfectly symmetric. These chiral superstructures displayed chiral optical properties over a broad spectral range from UV to near infrared, which is promising for various optical applications. In addition,

the efficiency and ease of operation of the fabrication process over large surfaces by combining GIS and LbL-assembly is also promising towards the possibility to scale up the process towards the production of large-scale functional devices.

We also measured the extinction spectra for the two-layer superstructures with linearly polarized light at different angles (every 10° from 0° to 360°) at two selected wavelengths, 380 nm and 1500 nm corresponding to the transversal modes and longitudinal modes of the LSPR of the AgNWs (***Figure 60)***.

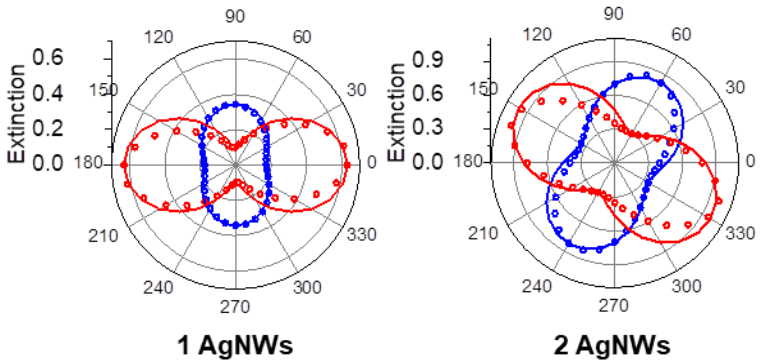

Figure 60. Polar plots of the extinction at 380 nm (blue) and 1500 nm (red) of one and two layers of AgNWs with an angle α = 60° as a function of the polarization angle of the incident light. Dots are experimental results, and solid lines are simulations.

Compared to the one-layer structure, we observe that the extinction of the transverse mode is maximum at 70°, and that the extinction of the longitudinal mode is maximum around 160°, while the maximum is expected at 60° and 150°. This small difference may be due to the misalignment of the sample with respect to the polarizer or a lower density for the second layer. The difference between the maximum and the minimum of the extinction at both wavelength decreases. The simulation of the extinction as the sum of two cosine-square (or sine-square) shifted by 60° ***(67.a)*** matches the measured variation with a reasonably good agreement.

$$A_{long} = (A_{long\,max} - A_{long\,min})\left(cos^2(\alpha) + cos^2(\alpha - 60°)\right) + A_{long\,min} \qquad \textbf{(67.a)}$$

$$A_{trans} = (A_{trans\,max} - A_{trans\,min})\left(sin^2(\alpha) + sin^2(\alpha + 60°)\right) + A_{trans\,min} \qquad \textbf{(68.b)}$$

where A_{trans} and A_{long} correspond respectively to the extinction at 380 nm and 1500 nm, A_{max} and A_{min} represent maximum and minimum extinctions at corresponding wavelengths, and α the polarization angle.

III.3.2. Mueller Matrix Polarimetry and simulations

The Mueller Matrix of the same samples were measured using MMP and simulated by Yann Battie from the Université de Lorraine. We remind here the physical meaning of the different elements of Mueller Matrix ***(68)***. The Mueller Matrix gives us a complete understanding of the linear and circular polarization properties of the sample, from which we can extract the LD, LB, CD and CB of the sample.

$$\mathbf{M} = \exp\begin{pmatrix} A & -LD & -LD' & CD \\ -LD & A & CB & LB' \\ -LD' & -CB & A & -LB \\ CD & -LB' & LB & A \end{pmatrix} \qquad \textbf{(68)}$$

Figure 61 and ***Figure 62*** show the measured and simulated LD, LB, CD and CB, respectively.

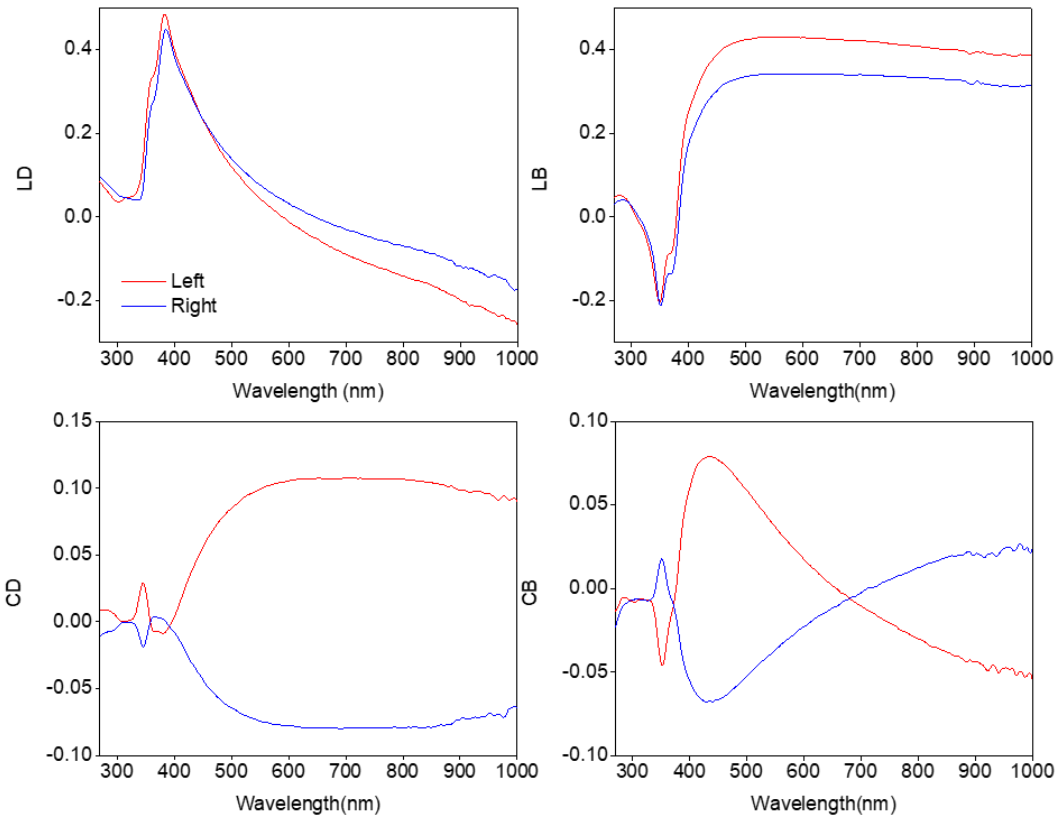

Figure 61. LD, LB, CD and CB measured by Mueller Matrix Polarimetry for left- (red) and right-handed (blue) two-layer structures.

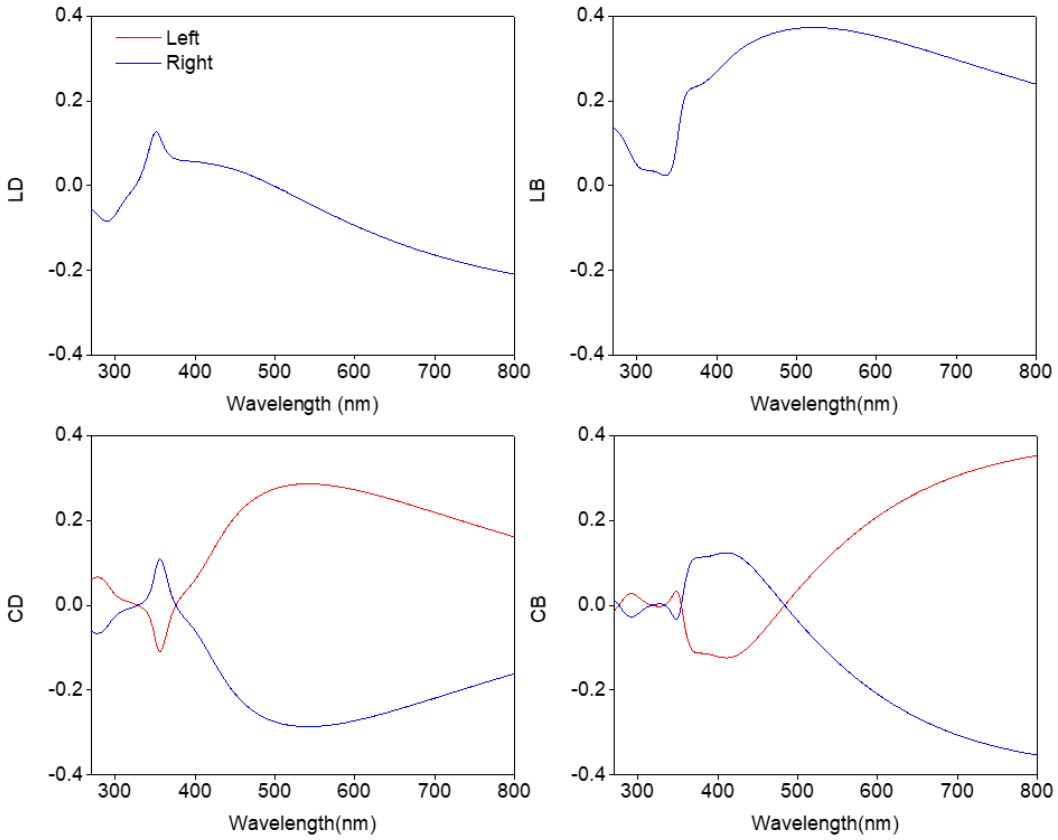

Figure 62. Simulated LD, LB, CD and CB for left- (red) and right-handed (blue) two-layer structures.

We can see in ***Figure 61*** (MMP measurements) and ***Figure 62*** (simulations) that the linear terms are similar for LH and RH samples, which is expected for 2 enantiomorphs which are linearly symmetric for an azimuth of 0°. The circular terms are mirror-symmetric, which is also expected for two enantiomorphs.

We have strong linear polarization (LD and LB) for the two-layer structures, which may influence the measurements of CD by commercial CD spectroscopy (***Figure 59***). However, the MMP allows measuring the CD of the sample without artifacts. The MMP measurements and the simulations show that we have effectively important CD for the two-layer structures, which has opposite signs over the spectral range. These results proved the chirality of the structures. ***Figure 63*** thus compares the CD of the left and right-handed structures made of two layers of AgNWs measured by Jasco CD spectrometer, MMP and simulations. The results of the MMP and simulations were converted in millidegree using equation ***(55)***.

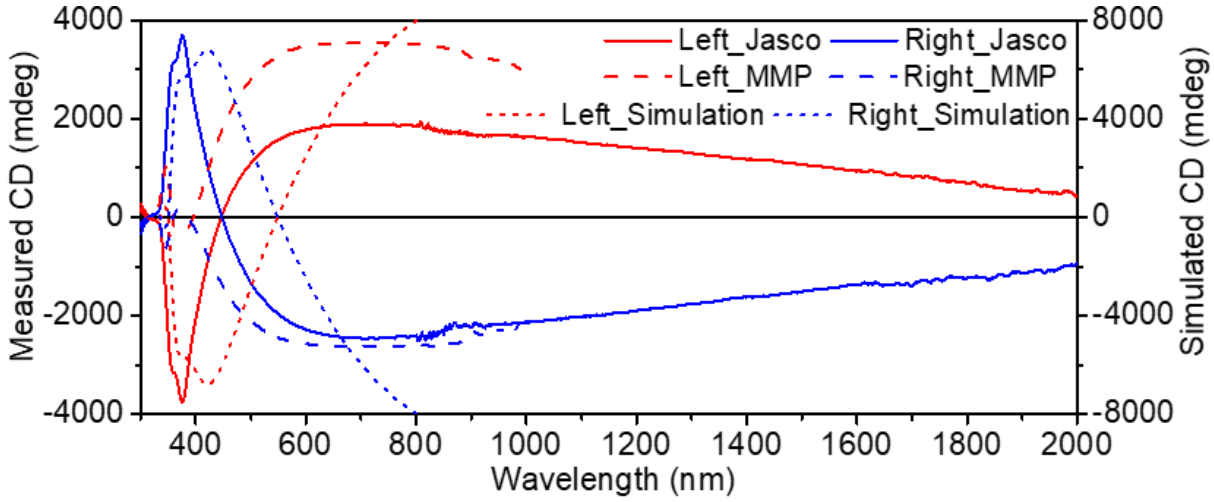

Figure 63. Comparison of CD measured on a Jasco CD spectrometer (solid lines), MMP (dashed lines) and from simulations (dotted lines) for left-handed (red) and right-handed (blue) two-layer structures. The CD scale is different for the measured spectra (left scale) and for the simulated spectra (right scale).

The CD measured by CD spectroscopy and by MMP are relatively similar. The simulated CD is larger than the measured CD (it has been plotted with a different scale two times larger than for the measured spectra in ***Figure 63***), and the simulated spectra are red-shifted in wavelength compared to measured ones. This may be because 1. ideal structures were considered in simulations; 2. possible coupling between the LSPR of the two layers of AgNWs were not taken into account in the simulations. However, the main features of the simulated spectra are similar to the measured ones, and the symmetry for left- and right-handed structures is well-reproduced. Thus, the simple model used for the simulation is effective to explain the CD effects of the films. These results thus confirmed not only the circular dichroism effects and handedness of the samples, but also the reliability of the CD spectroscopy.

III.3.3. Influence of the angle between two layers of AgNWs

In the model of the simulations, the layers of AgNWs are considered as independent “slabs” interacting with the electromagnetic fields. The transmission through the multilayer structure can be explained by stacking several independent monolayers twisted at a certain angle and with a certain spacing. The coupling between the LSPR of the two layers of AgNWs may also influence the CD effects of the films. This coupling occurs in the evanescent field of the LSPR,

leading to the enhancement of the local electromagnetic fields. The coupling strength and the induced chiroptical properties are therefore related to the angle between the orientation direction of the two layers of AgNWs and the distance between them. In both cases, the chiroptical properties of the two-layer structures are sensitive to the angle and distance between the two layers of AgNWs.

In order to investigate the influence of the angle α, we varied it from 0° to 90° (one sample every 15°; and a sample with α = -45° to make a comparison right-handed / left-handed with α = ±45°), while keeping the spacing between the two layers of AgNWs fixed at 13 nm by maintaining the PEI/(PSS/PAH)$_5$/PSS/PEI interlayer PEM structure.

We measured the CD and extinction spectra (***Figure 64***) for each sample and calculated their g-factor (***Figure 65***).

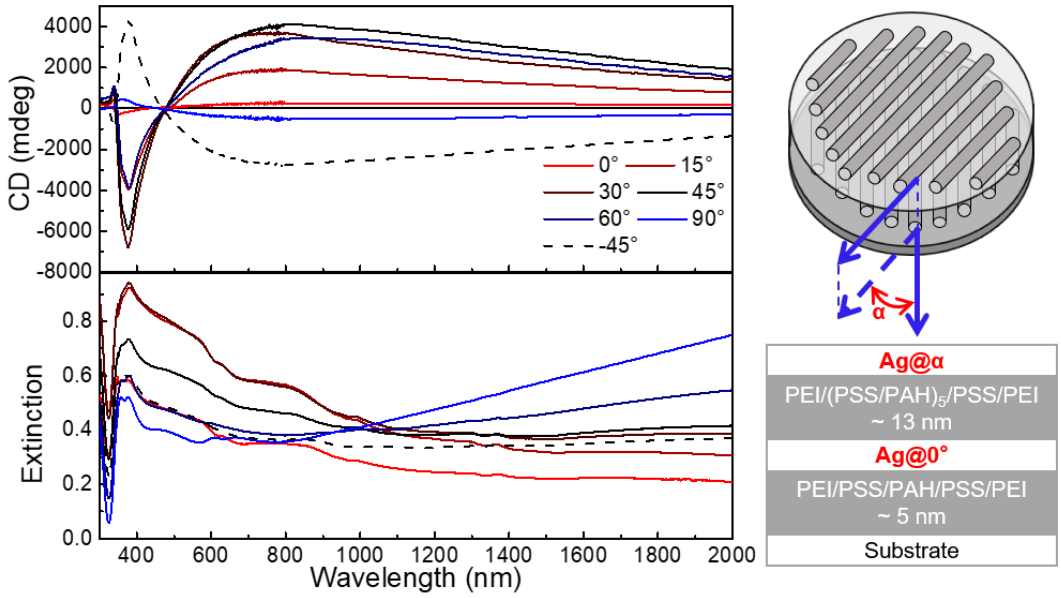

Figure 64. CD and extinction spectra of samples composed of two layers of AgNWs with angles between them varying from 0° to 90°. The distance between the AgNW layers was fixed at 13 nm. The extinction spectra were measured with a depolarizer. The differences of the extinction in the NIR range was probably due to the depolarizer which only partially depolarizes the incoming beam of the spectrometer.

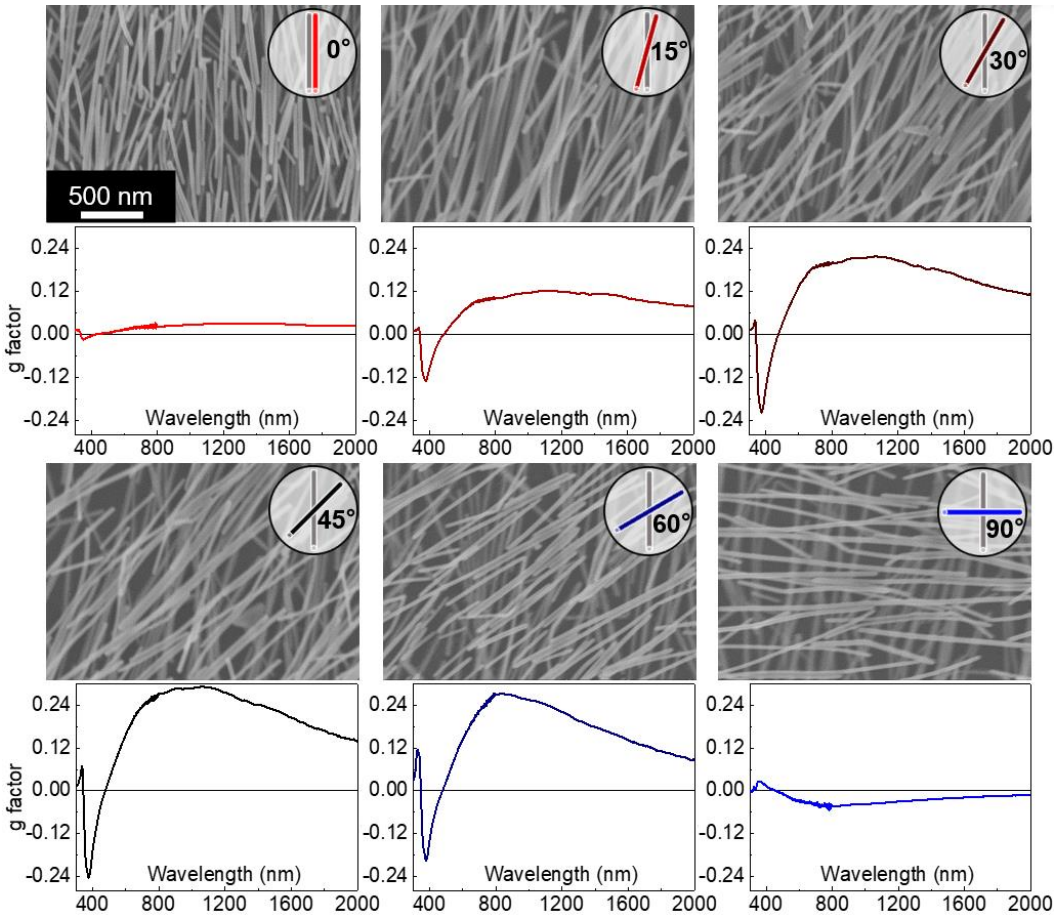

Figure 65. g-factors for each sample with a different angle α between the two layers of AgNWs and corresponding SEM images.

Samples with α = 0° or 90° have a CD and g-factor close to 0, which is consistent with the fact that they are actually achiral structures. On the other hand, the CD and g-factors increase with α between α = 0° and 45° and reaches a maximum at α = 45°, which is the most chiral superstructure, and decreases from α = 45° to 90° (***Figure 66***). α = 45° has thus been used for most of the samples in the rest of this manuscript.

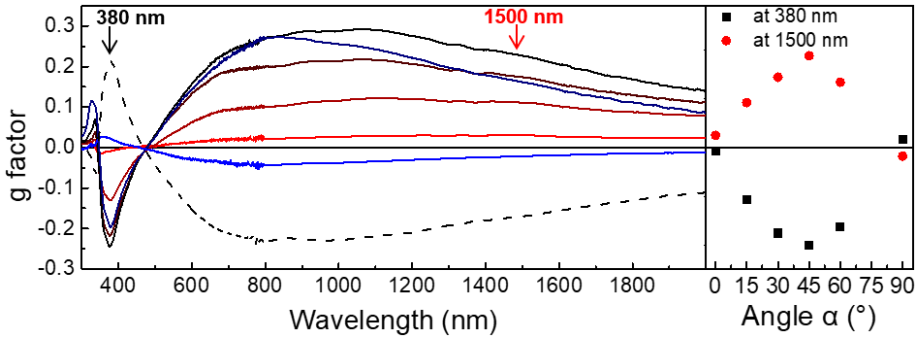

Figure 66. g-factor spectra of samples with a different angle α between the two AgNW layers and g-factors at 380 nm and 1500 nm plotted as a function of α.

Another series of samples, varying the angle between the two layers of AgNWs, were carried out with a larger interlayer spacing of 1 µm obtained by spin coating a layer of PMMA in place of the PEM multilayer between the two AgNW layers. Due to the oscillations of the CD, which is going to be discussed in details in the following section III.3.2, it is hard to do a quantitative comparison of the variation of CD with the angle α, but the evolution of the amplitude of CD at 380 nm is similar to that of the samples with a 13 nm spacing ***(Figure 67)***.

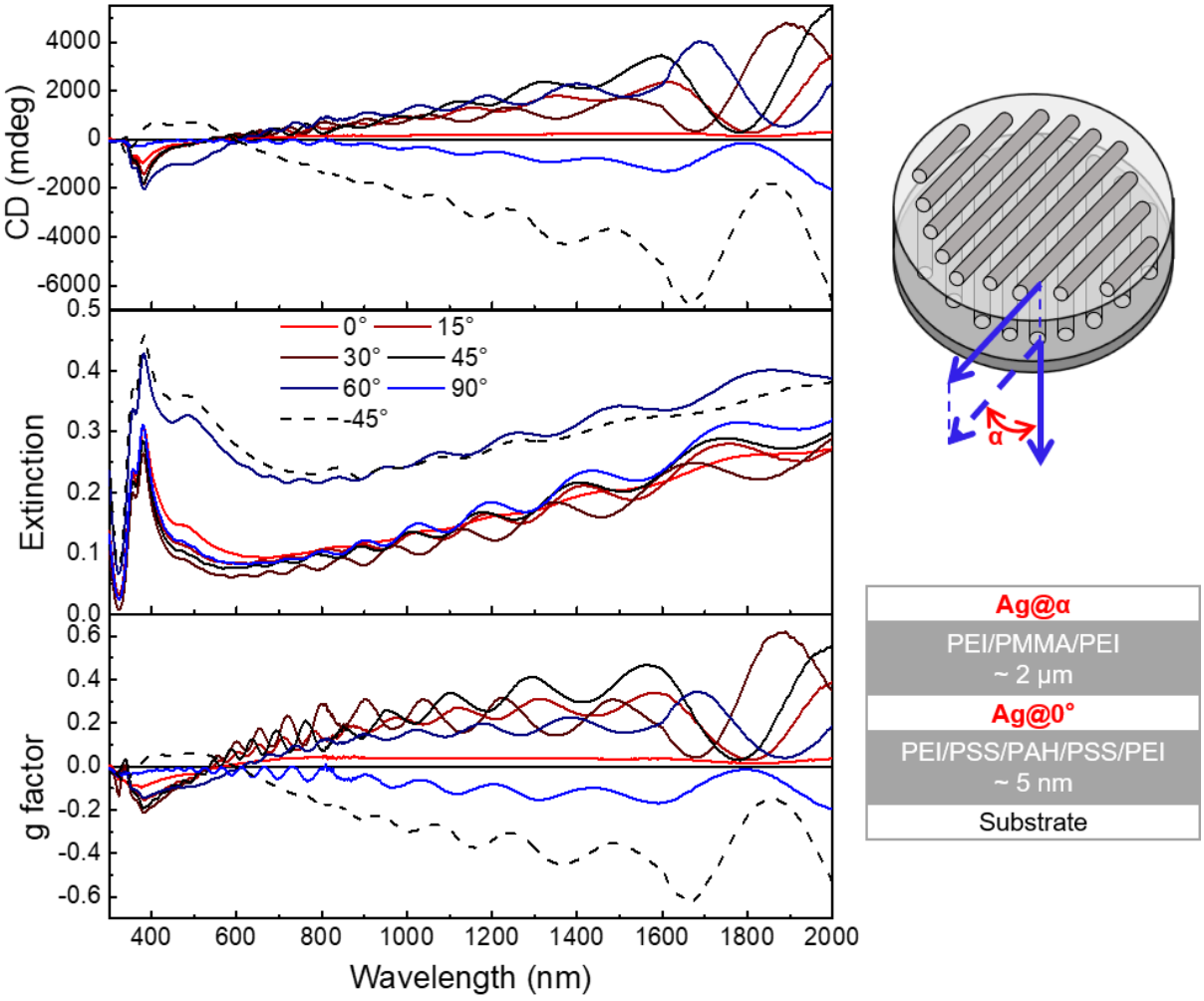

Figure 67. CD, extinction and g-factor spectra of samples composed of two layers of AgNWs with a different angle α between the two layers of AgNWs varied from 0° to 90°. The distance between the AgNW layers was fixed at 1 µm.

Simulations for two-layer structures with a different angle α were performed for two different interlayer spacings (13 nm and 130 nm) by Yann Battie from University of Lorraine (***Figure 68*** and ***Figure 69)***.

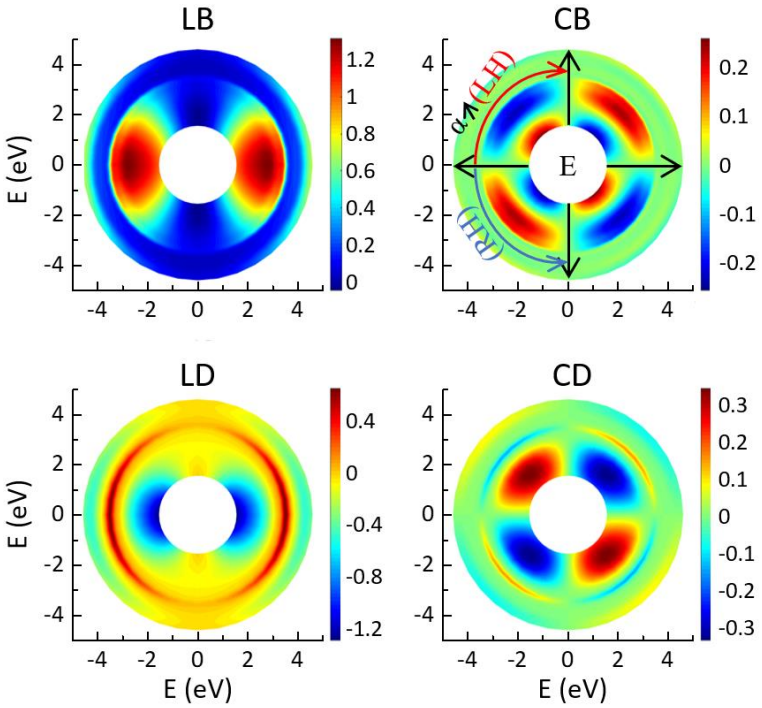

Figure 68. Simulated LB, LD, CB and CD for two-layer structures with a different angle α between the AgNW layers with the interlayer spacing fixed at 13 nm, as a function of the photon energy (E). The radius corresponds to the photon energy (in eV), the color to the intensity of the different elements, and the angular coordinate to the angle α between the two AgNW layers.

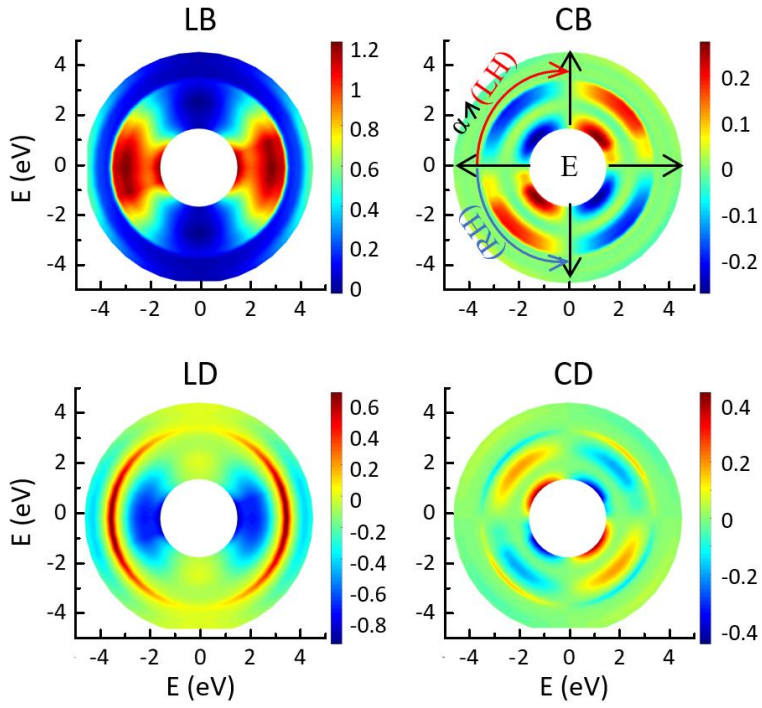

Figure 69. Simulated LB, LD, CB and CD for two-layer structures with a different angle α between the AgNW layers with the interlayer spacing fixed at 130 nm, as a function of the photon energy (E). The radius corresponds to the photon energy (in eV), the color to the intensity of the different elements, and the angular coordinate to the angle α between the two AgNW layers.

These simulations were carried out with one single azimuth angle (Φ = 0) by keeping the orientation of the lower layer of AgNWs parallel to that of the polarization of the incident light. The radius corresponds to the photon energy (in eV), the color to the intensity of the different elements, while the angular coordinate corresponds to the angle α between the two AgNW layers.

We have again a high LB and LD for the two-layer structures, which are highly dependent on the angle α. When α = 0° (the two layers of the AgNWs are aligned in the same direction), the LB and LD tend to be the highest. When α = 90° (the two layers of the AgNWs are perpendicular to each other), the LB and LD have the lowest values. Regarding the chiroptical properties, the samples with α = 0° and 90° have a CD and CB close to 0, and the intensity of CD and CB are maximum at α = 45° and -45° with opposite signs (different handedness). This confirms our results above measured by commercial CD spectroscopy. All the four polar color-maps are centrosymmetric, because angle α and angle α+180° are actually identical. The spectra with a spacing between the AgNW layers equal to 13 nm or 130 nm have the same symmetry and share the same trends, although the spectra have maxima and minima at a different wavelength (energy), as it will be discussed in the following section.

III.3.4. Influence of the spacing between two layers of AgNWs

Another parameter which has an influence on the chiroptical properties of the two-layer chiral superstructure is the interlayer spacing. The LbL-assembly approach allows us to tune the PEM thickness between two layers of AgNWs with a nanoscale precision. We thus varied the number of polyelectrolyte layers pairs between two layers of AgNWs from n = 5 up to n = 100 in order to tune the interlayer spacing (from d = 13 nm to 213 nm), while keeping the angle between the orientation of the two AgNW layers constant at 60° and 45°.

We first prepared a series of samples composed of two layers of AgNWs, with an angle α fixed at 60°, while the interlayer spacing varied from 13 nm to 213 nm by changing the number of layer pairs of (PSS/PAH), n, from 5 to 100. We cut the samples in the central area where the spectroscopic measurements are done and the cross-section was polished with a low-energy Ar^+ ion beam. The sample were subsequently images by SEM through their cross-section, which allows measuring the LbL PEM. The thickness of the PEM multilayer measured by SEM could thus be compared with the thickness determined by ellipsometry. We measured the distance between the two layers of AgNWs at 10–20 different positions in the SEM of the cross-section and plotted the average as function of the interlayer spacing, and compared with the thicknesses obtained by ellipsometry (***Figure 70***). It turns out that the thickness determined by the two methods are very close. Furthermore, the low standard deviation indicates that the PEM roughness is low and that the thickness is homogeneous over large areas, even on a substrate with pre-deposited AgNWs.

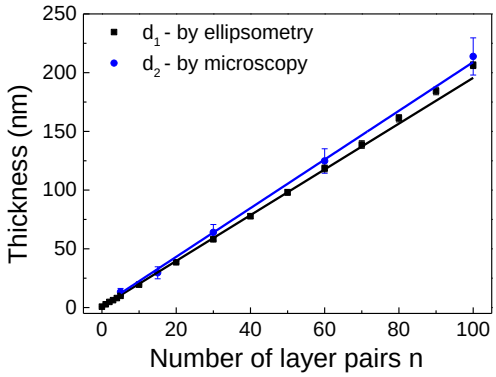

Figure 70. Thicknesses of the LbL-assembled PEM measured by ellipsometry and microscopy. The samples measured by ellipsometry were prepared on silicon wafers without AgNWs, while the sample by microscopy were prepared on silicon wafers with the presence of two layers of AgNWs.

The CD and extinction were measured (***Figure 71***) and the g-factors were calculated (***Figure 72***) for the samples with different interlayer spacing.

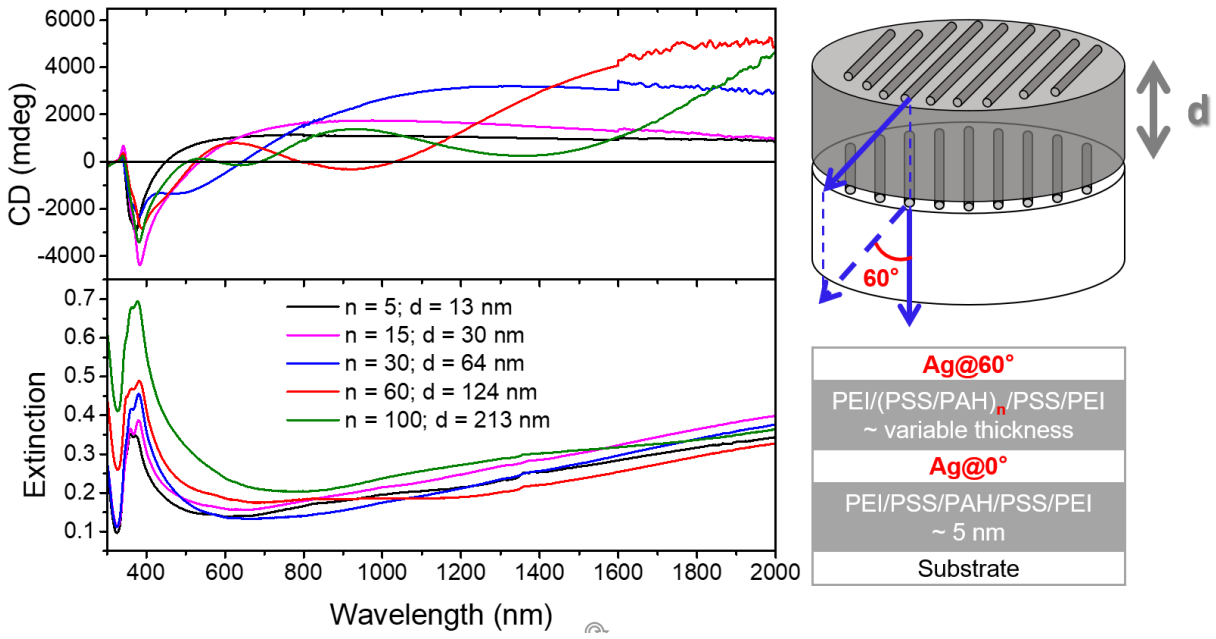

Figure 71. CD and extinction spectra of samples composed of two layers of AgNWs with the interlayer spacing varying from 13 nm to 213 nm, while the angle between the AgNW orientation direction is fixed at 60°.

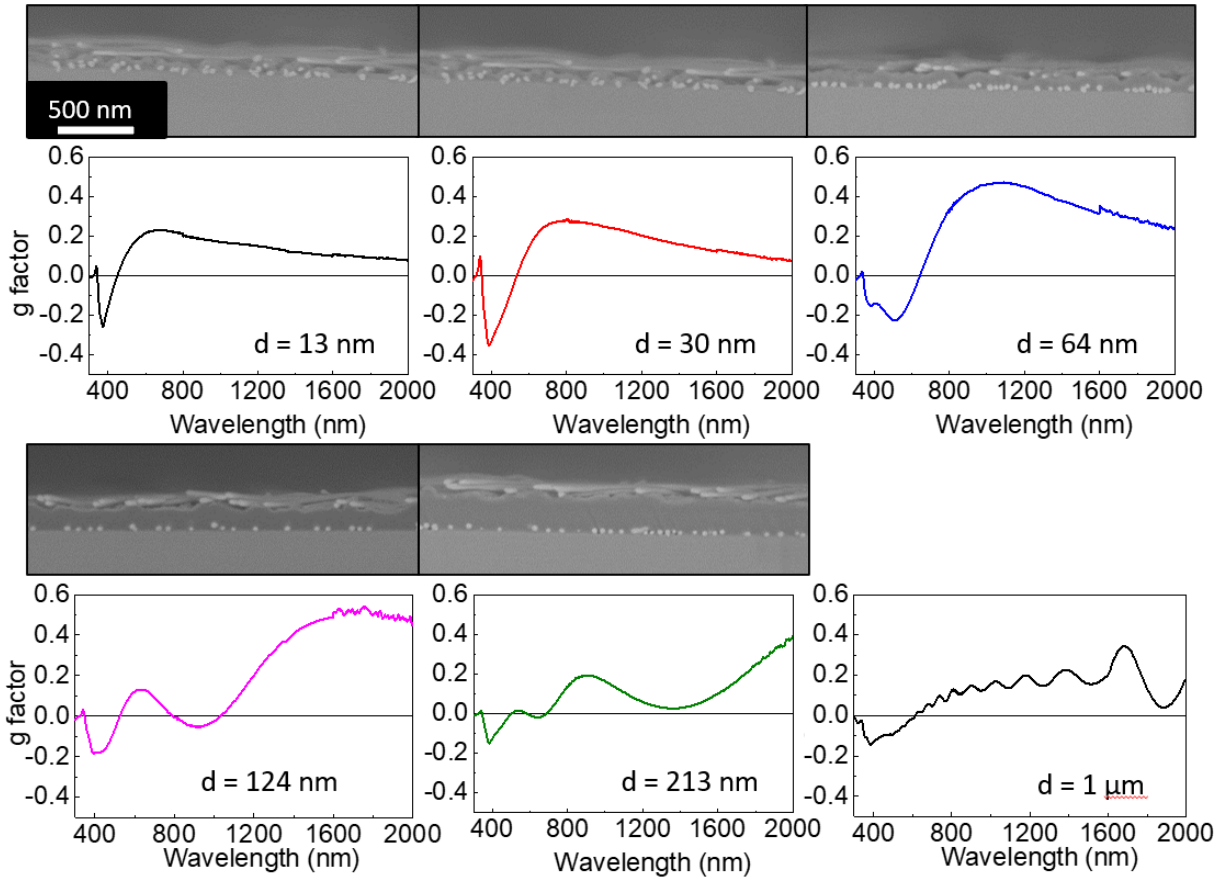

Figure 72. g-factors of samples with different interlayer spacing d and an angle between the AgNW orientation direction fixed at 60° and corresponding cross-section SEM images.

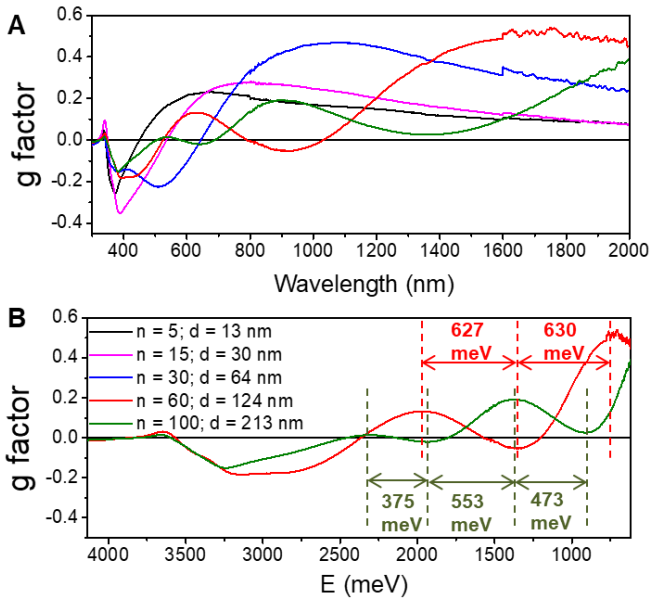

Figure 73. g-factors of two-layer chiral superstructure with different interlayer spacing as a function of wavelength (A) and energy (B).

The tremendous impact of the interlayer spacing on the chiroptical properties of the two-layer chiral plasmonic superstructures is evidenced by plotting the g-factor of the samples with different interlayer spacings on the same graph (***Figure 73***A).

We observed that the shape and intensity of the g-factor spectra are extremely dependent on the interlayer spacing: the spectra are red-shifted as the interlayer spacing increases. If we extract the wavelengths of the maximum, minimum and intercept on x-axis for each g-factor spectrum and plot them as a function of the corresponding interlayer spacing, we have a somewhat linear tendency (***Figure 74***).

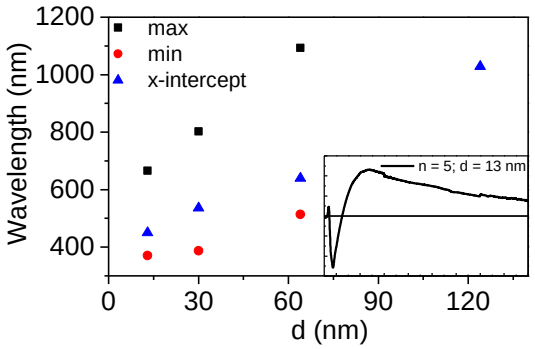

Figure 74. The wavelengths of maximum, minimum and x-intercept of g-factor curves plotted as a function of the interlayer spacing.

Furthermore, for interlayer spacings above 124 nm, we observed oscillations in the g-factor spectra that resemble the oscillations that are observed in the transmittance of Fabry-Perot cavities arising from the interferences of light between the two interfaces of the cavity. As the Fabry-Perot oscillations happen with a period that scales with the energy of the light beam, we plotted the g-factors as a function of energy (***Figure 73***B) instead of the wavelength, the oscillation of the curves shows that they appear with a more or less regular period. The number of oscillations is however too small to draw a definite conclusion on this point.

We prepared another series of two-layer samples with an angle α = 45° (left-handed structures). As the exact thickness of the PEM between two layers of AgNWs were confirmed by ellipsometry and microscopy, for this series we did not choose round numbers for the number n of PSS/PAH layer pairs in the PEM multilayer, but rather round number for the interlayer spacing (30 nm, 60 nm, 100 nm, 150 nm and 200 nm, corresponding to n = 15, 28, 48, 72 and 96 layer pairs respectively). A sample with an angle α = -45° (right-handed structure) and interlayer spacing d = 30 nm, and a sample with an angle α = 45° and interlayer spacing d = 1µm were also prepared for comparison (***Figure 75***). The 1 µm thick interlayer spacing was obtained by spin coating a PMMA layer on the first AgNW layer. This thickness was measured by FIB-SEM by a former PhD student of the group, Vincent Lemaire.[257]

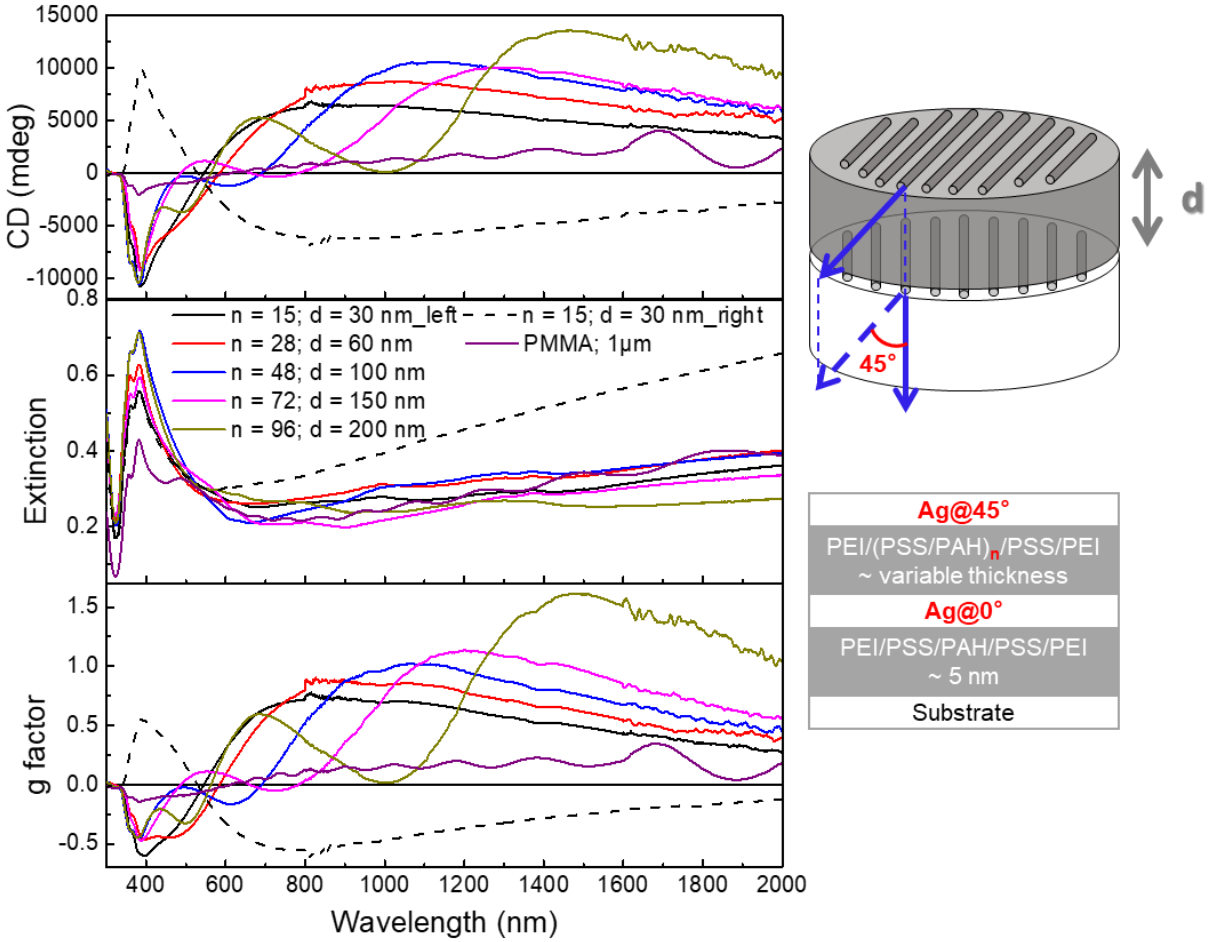

Figure 75. CD, extinction and g-factors of samples composed of two layers of AgNWs with the interlayer spacing varied from 30 nm to 200 nm, while the angle between the AgNW orientation of each layer is fixed at 45°.

Similar trends as for the samples with an angle α fixed at 60° were observed. The g-factor spectra observed for the sample with a 1 μm thick interlayer spacing showed oscillations with a much shorter period than the samples obtained with a PEM spacing, in accordance with the larger spacing between the AgNW layers. In particular, we obtained a g-factor up to 1.6 for the structure with d = 200nm. This is the highest g-factor reported to date for similar nanostructures to the best of our knowledge.

The Mueller Matrix of the samples were measured using MMP and simulated by Yann Battie from the Université de Lorraine, from which we obtained the measured (***Figure 76***) and simulated (***Figure 77***) LD LB, CD and CB of the samples.

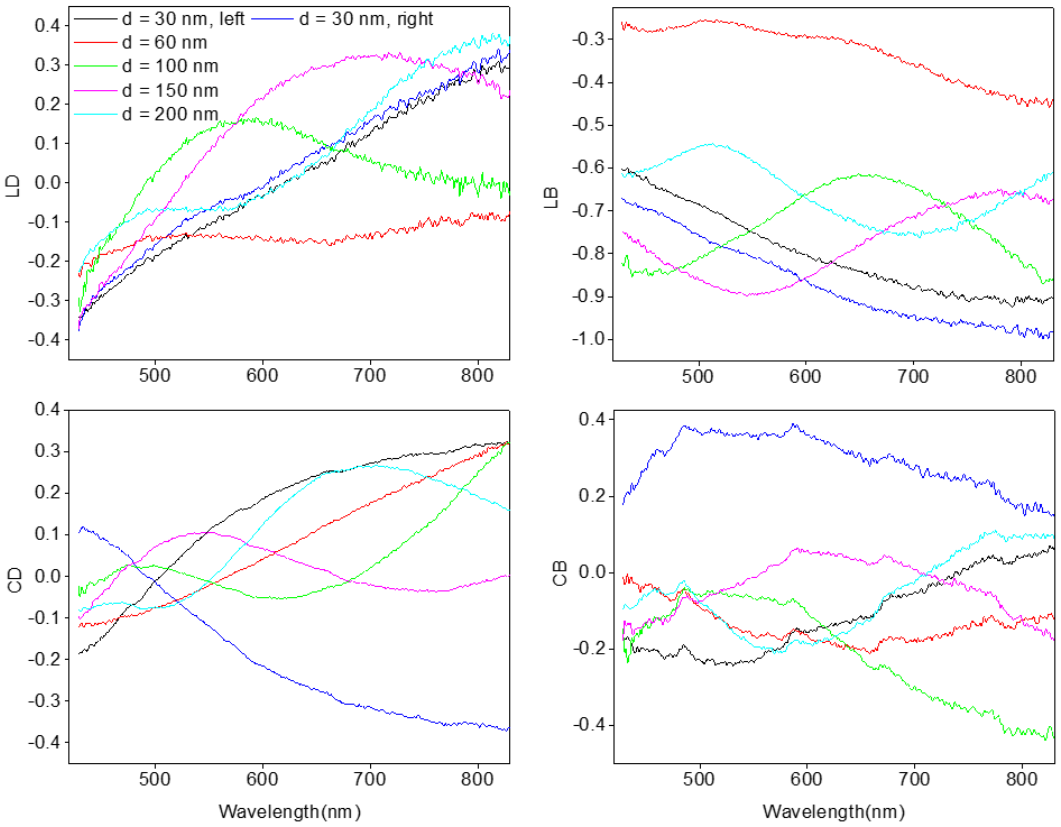

Figure 76. Measured LD, LB, CD and CB of the samples containing two layers of AgNWs, with the angle α fixed at 45° and the interlayer spacing varying from 13 nm to 195 nm.

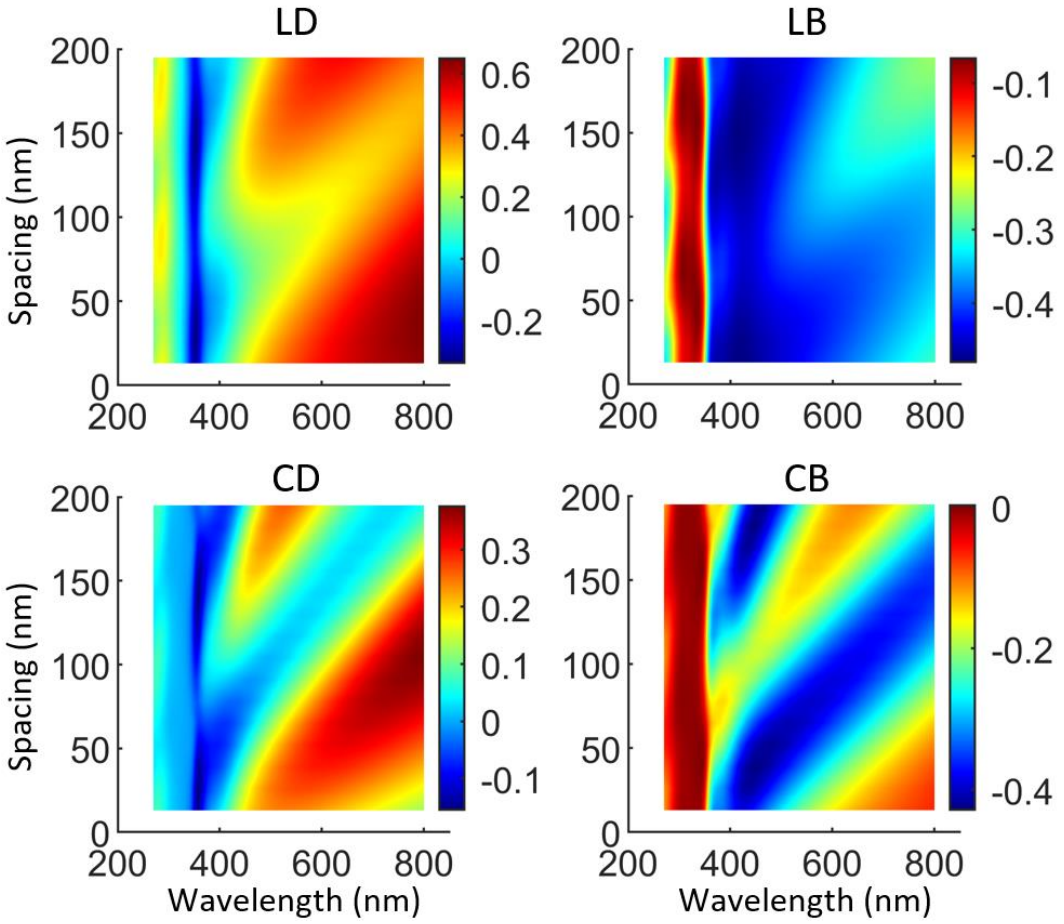

Figure 77. Simulated LD, LB, CD and CB of the samples containing two layers of AgNWs, with the angle α fixed at 45° and the interlayer spacing varying from 13 nm to 195 nm. The x-axis corresponds to the spectral range, the y-axis corresponds to the interlayer spacing and the colors represents the intensity of the different elements.

The drastic influence of the spacing on the optical properties is clear. In particular, the trend observed on the measured CD (***Figure 75***) is confirmed, in which the oscillations of the CD for the larger interlayer spacings are well-reproduced. The measured and simulated results also reveal that the interlayer spacing has influence on not only the circular polarization properties (CB and CD) of the sample but also the linear ones (LB and LD). Similar oscillations as in the CD can be observed in the other terms with the increase of the interlayer spacing. In addition, we confirmed in the measurements once again, that corresponding structures with opposite handedness have comparable linear polarization properties and symmetrical circular polarization properties.

The CD measured by CD spectroscopy (solid lines) and MMP (dashed lines) are compared with the simulations (short dashed lines) in ***Figure 78***. The spectra are arranged along the Y axis depending on the interlayer spacing, while the scale for each spectrum is identical.

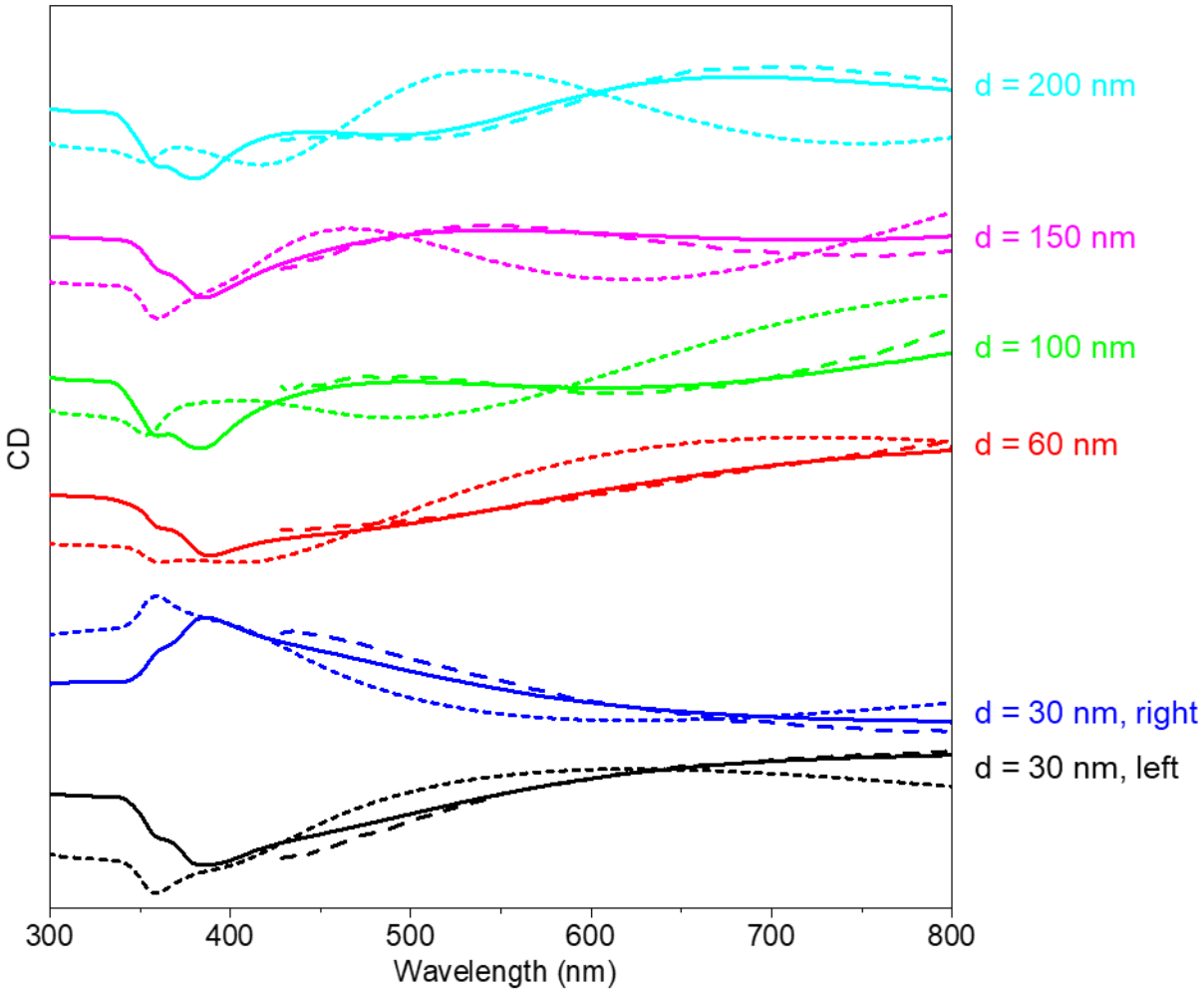

Figure 78. CD measured by CD spectroscopy (solid lines), MMP (dashed lines) and by simulations (short dashed lines), for two-layer structures with the angle α fixed at 45°, and the interlayer spacing varying from 30 nm to 200 nm.

The CD measured by CD spectroscopy and MMP are consistent, both in terms of position of the peaks and CD scale. However, the simulated results are slightly different from the measurements. The main trends are reproduced (handedness of the structure, positive or negative sign of the bands, appearance of the oscillations for the largest spacings), but the exact wavelength at which the peaks appear and the amplitude vary between the simulations and measurements. The possible reasons are the following: 1. ideal structures were considered in

simulations; 2. possible coupling between the LSPR of the two layers of AgNWs were not taken into account in simulations; 3. the simulations have taken theoretical thicknesses for the interlayer spacing, while the actual thicknesses in measured sample could be slightly different. Although this error is believed to be very small thanks to the precision of the LbL-assembly as demonstrated in section III.2, the CD of a sample is extremely sensitive to the spacing between the AgNW layers, and only a small difference of a few % in the PEM thickness can alter significantly the wavelength of the main features of the CD curve. Whatsoever, the trend of the simulated CD was also comparable to the results by CD spectroscopy as shown in ***Figure 78***. The red-shifting and increasing oscillations in the CD spectra with the increase of the interlayer spacing are obvious, which matches well the conclusion drawn from the measurements.

Moreover, one could eventually increase the interlayer spacing to macroscopic scales (~ mm) by playing with two layers of AgNWs sprayed on two separate glass slide and sticking them together for CD measurements. As the thickness of a glass slide is 1 mm, the interlayer spacing can be chosen to be close to 0 mm (by sticking the sides with AgNWs face to face), 1 mm and 2 mm. Surprisingly, two layers of AgNWs deposited on two separate glass slides can generate equally very important CD, when the glass slides are placed such as the distance between the AgNW layers is on the mm scale. Oscillations of the CD spectra were observed and their frequencies and amplitudes were highly dependent on the distance (***Figure 79***A). High CD was observed for an angle $\alpha = 45°$ but not for 0° nor 90° (***Figure 79***B).

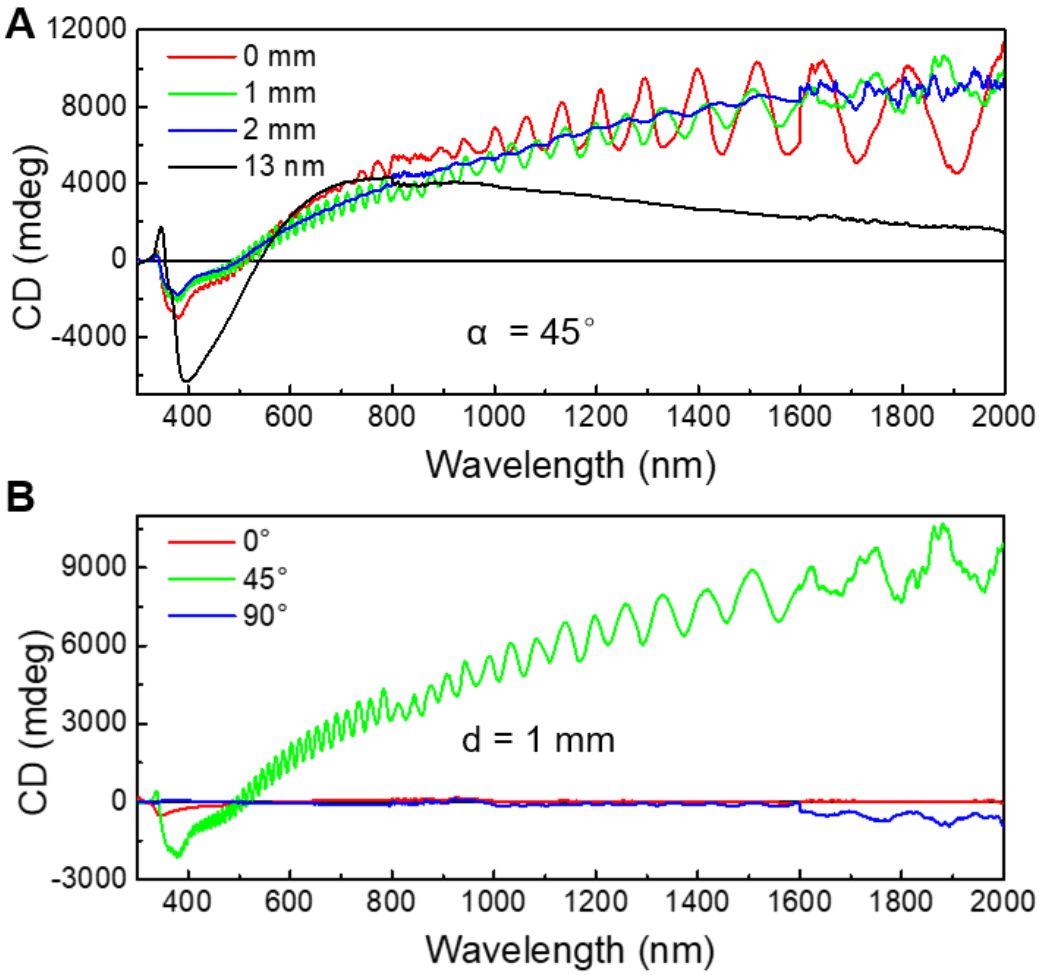

Figure 79. CD spectra of samples consisting of 2 layers of AgNWs sprayed on two separate 1 mm-thick glass slides placed in different configurations: (A) the distance between the two layers of AgNWs was varied from 0 mm, 1 mm to 2 mm, by sticking the AgNWs sides face to face, face to back or back to back, respectively, while the angle between the AgNW layers was fixed at 45°. The results are compared with a sample composed of 2 layers of AgNWs on a single glass slide with a PEM interlayer of 13 nm. (B) The distance between the two layers of AgNWs was fixed at 1 mm by sticking the AgNWs monolayer samples face to back, while the angle between them was varied from 0°, 45° to 90°.

There is certainly no coupling between the two layers of AgNWs as the distance between them goes beyond mm. These results reveal that coupling between the LSPR of the two layers of AgNWs is not a prerequisite to generate high CD, as it is often claimed in the literature. Indeed, we show here that placing two linear dichroic and birefringent layers in line with a certain angle is enough to generate CD. However, coupling between the plasmon modes is surely present, when the two layers of AgNWs are close enough to each other (for example 13 nm), and this coupling may have an influence on the CD. For example, a possible reason for the difference

of the CD intensity around 400 nm and beyond 1000 nm between the sample “0 mm” and “13 nm” in ***Figure 79***A could be an effect of the coupling. Modeling approaches, which consider the coupling between the plasmon modes, such as FDTD, would be necessary to distinguish between the CD that arises from coupling and the CD that is due to the transmission between two twisted birefringent and dichroic layers.

III.4. Chiral superstructures containing three and more layers of AgNWs

By repeating the LbL-assembly of PEM and GIS of AgNWs on a two-layer superstructure, three-layer superstructures can be obtained as illustrated in ***Figure 57***. The three layers of AgNWs aligned in different directions can be evidently observed in the SEM images (***Figure 80***) of the left- and right-handed structures from the top-view and from the cross section. The interlayer spacing between adjacent layers is 13 nm. The diameter of the AgNWs is around 60nm. Thus, the AgNWs layers are actually tightly stacked.

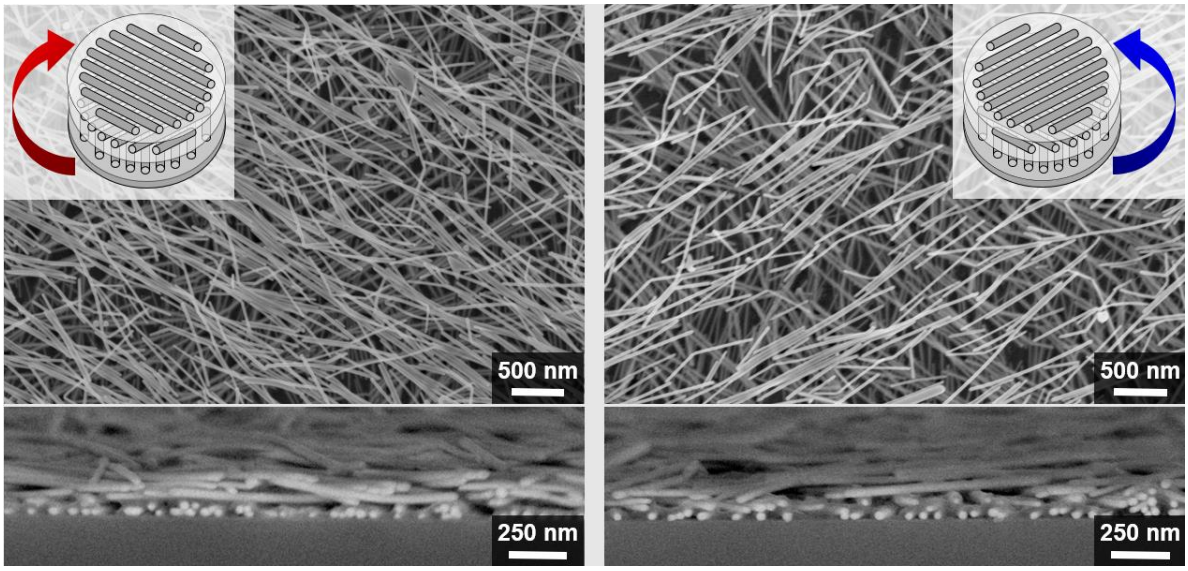

Figure 80. Top view and cross section SEM images of left-handed and right-handed structures containing three layers of AgNWs.

The extinction spectra of the three-layer structures have a similar shape but with an increased intensity. The left- and right-handed structures show again impressive symmetry in CD and g-factor (***Figure 81***).

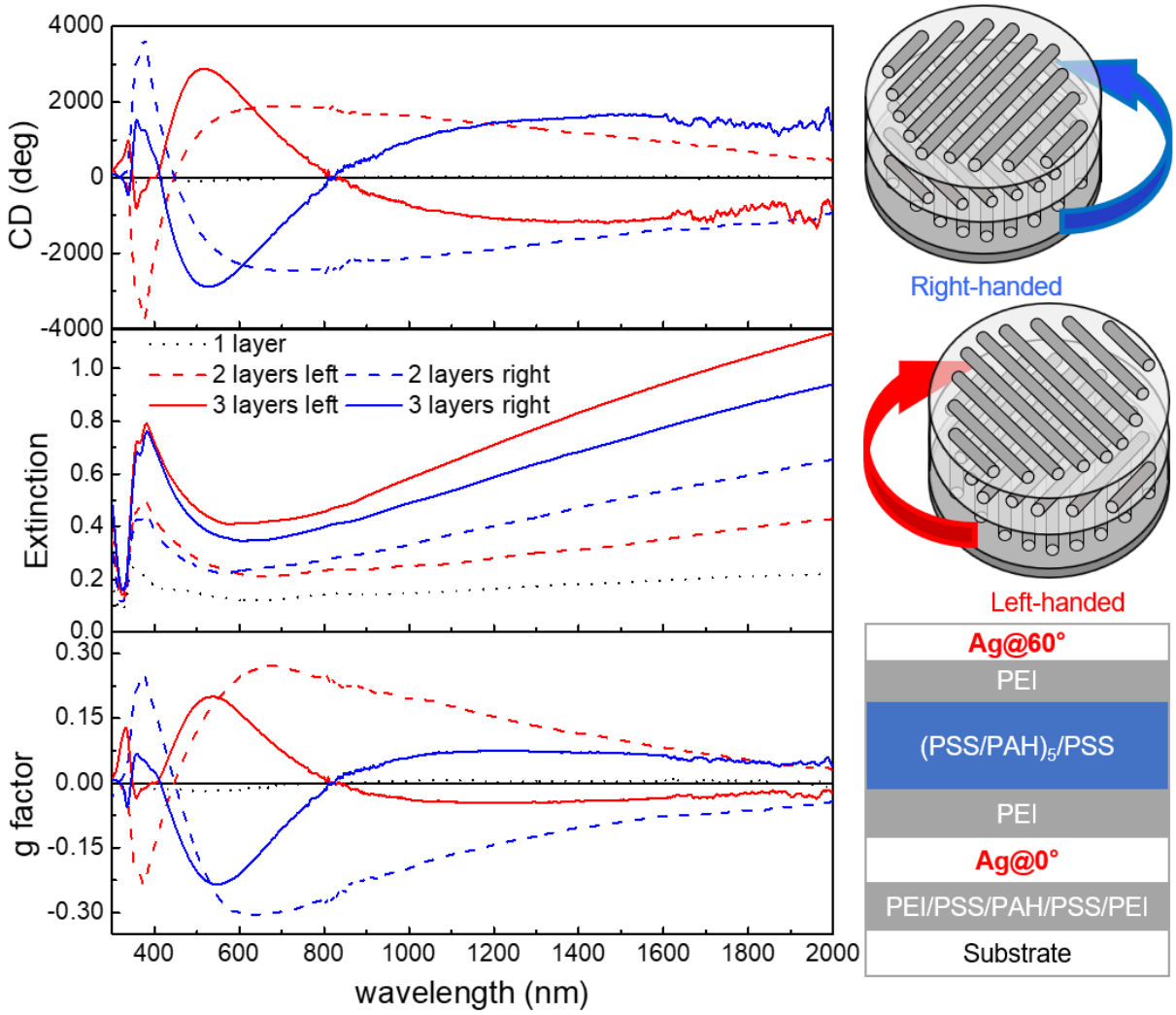

Figure 81. Left panel: CD, extinction and g-factor spectra of samples composed of one layer (dotted lines) of aligned AgNWs (non chiral), 2 layers (dashed lines) and 3 layers (solid lines) of AgNWs with left (red) and right (blue) handedness. Right panel: Schematics of left- and right-handed superstructures containing 3 layers of AgNWs and the layer-by-layer composition of a two-layer structure (from top to bottom). The angle between two adjacent layers of AgNWs is 60°, and the PEM between them is PEI/$(PSS/PAH)_5$/PSS/PEI (~13 nm).

It could have been expected that the three-layer structures have a stronger CD than the two-layer structures, but actually the CD is slightly weaker by comparing the maxima and minima of the CD. Given their much stronger extinction, the g-factors of the three-layer structures turn out to be smaller than for the two-layer structures. In addition, the shape of the CD spectra of the three-layer superstructures are significantly different from those of the two-layer

superstructures. Additional positive and negative peaks are observed, and the CD changes more often its signs, similarly to the so-called Cotton effect. The CD and g-factor peak around 380 nm is reduced, while another smaller peak around 320 nm can be observed. The latter was actually already present in two-layer structure but at a very small intensity. At around 800 nm, the CD and g-factor curves cross the x-axis, which was not the case for two-layer structure.

We measured again the extinction spectra for the three-layer superstructures with linearly polarized light at different angles (every 10° from 0° to 360°) and plotted the polar plots at two selected wavelengths, 380 nm and 1500 nm corresponding to the transversal modes and longitudinal modes of the LSPR of the AgNWs (***Figure 82***).

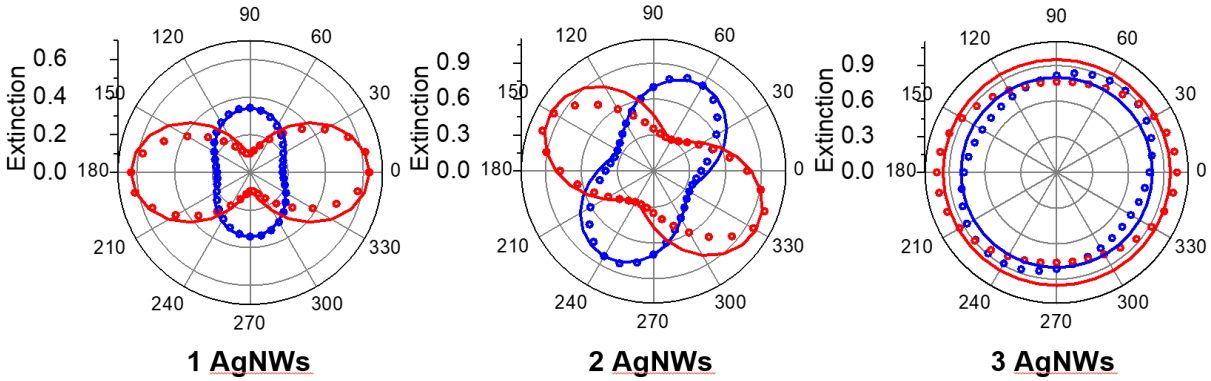

Figure 82. Polar plots of the extinction at 380 nm (blue) and 1500 nm (red) of samples consisting of one, two and three layers of AgNWs with an angle α = 60° as a function of the polarization angle of the incident light. Dots are experimental results, and solid lines are simulations.

Comparing to the one-layer and two-layer structures, we observed that the transverse mode and the longitudinal mode varied only slightly with respect to the polarization angle, as expected by summing 3 cosine-square or sine-square functions twisted by an angle of 60° each. The 3-layer superstructure with 3 layers oriented at an angle of 60° thus have a negligible linear dichroism but a high circular dichroism.

The Mueller Matrix of the three-layer structures were simulated and measured by Yann Battie from the University of Lorraine, from which we obtained the measured (***Figure 83***) and the simulated (***Figure 84***) LD, LB, CD and CB.

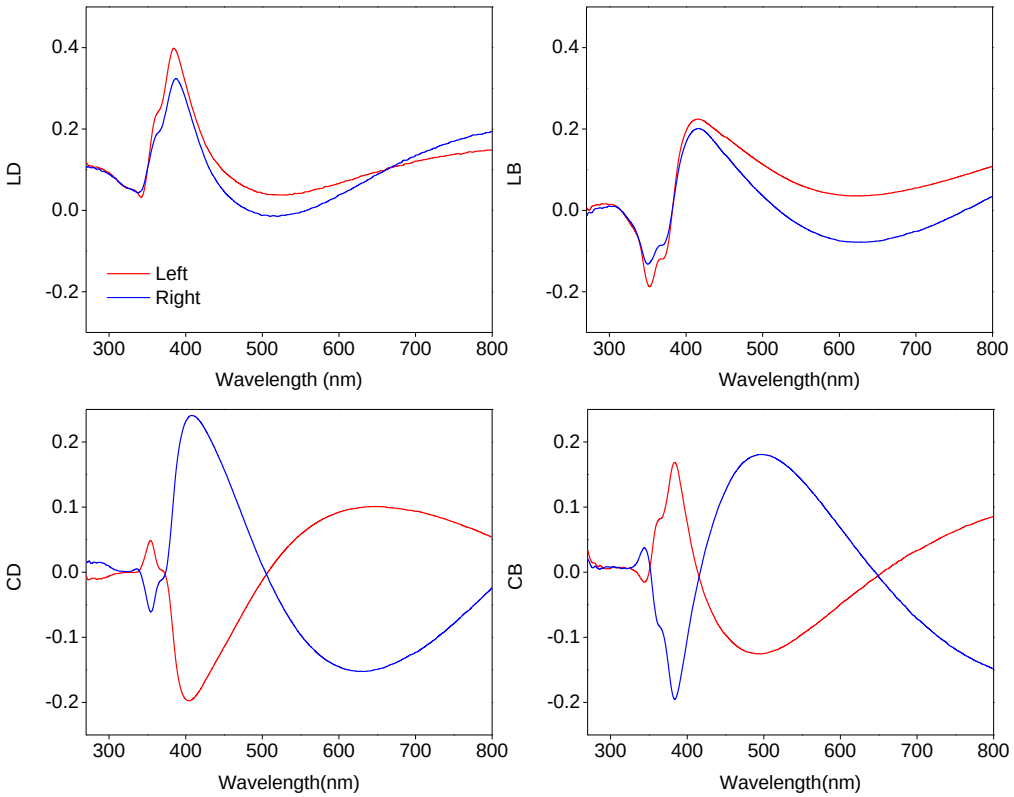

Figure 83. LD, LB, CD and CB measured by MMP on samples consisting of three layers of AgNWs oriented at 60° from each other with a 13 nm interlayer spacing.

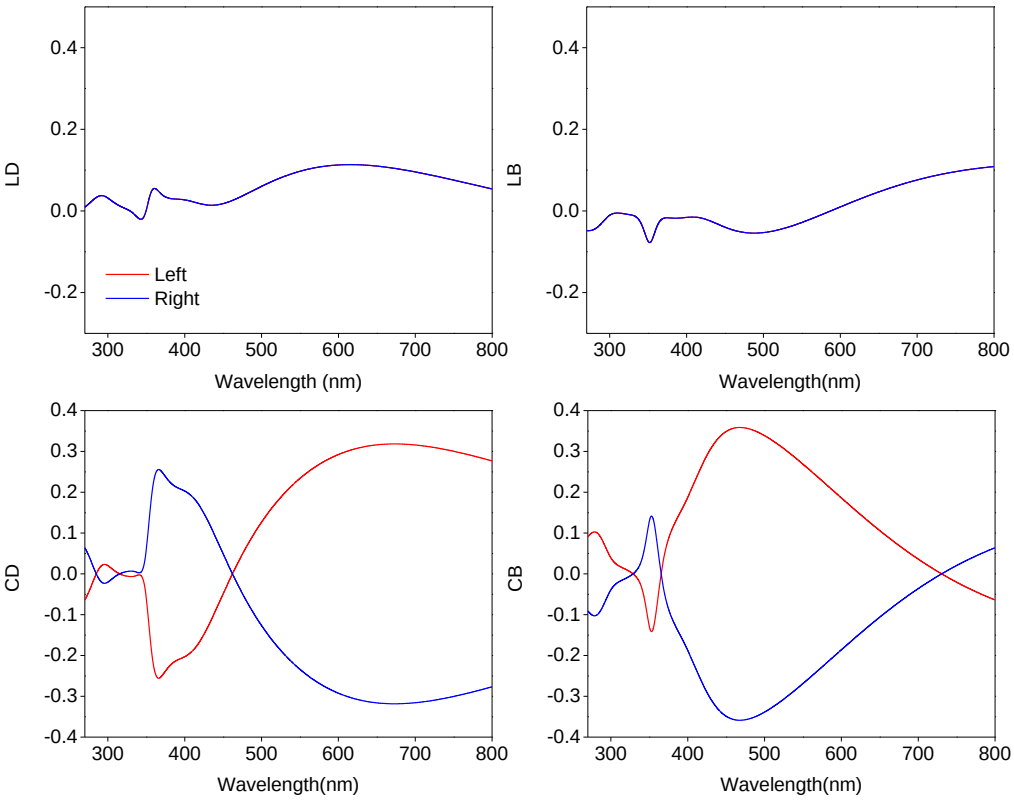

Figure 84. LD, LB, CD and CB calculated from the simulated MMP on structures consisting of three layers of AgNWs oriented at 60° from each other with a 13 nm interlayer spacing.

It is clear that the three-layer structures still have linear polarization (LD and LB), and in both simulations and measurements, the LB and LD of left- and right-handed structures are comparable. However, the measured values are much higher than simulated ones. In fact, a three-layer structure, left- or right-handed, has a linear symmetry, thus should have relatively small LB and LD as shown in the simulations. The high LD and LB in the measurements arise from the imperfection of the samples, especially the fact that the density of AgNWs in each layer is not constant.

The simulated and measured CD were compared with the CD measured by the commercial CD spectrometer (***Figure 85***).

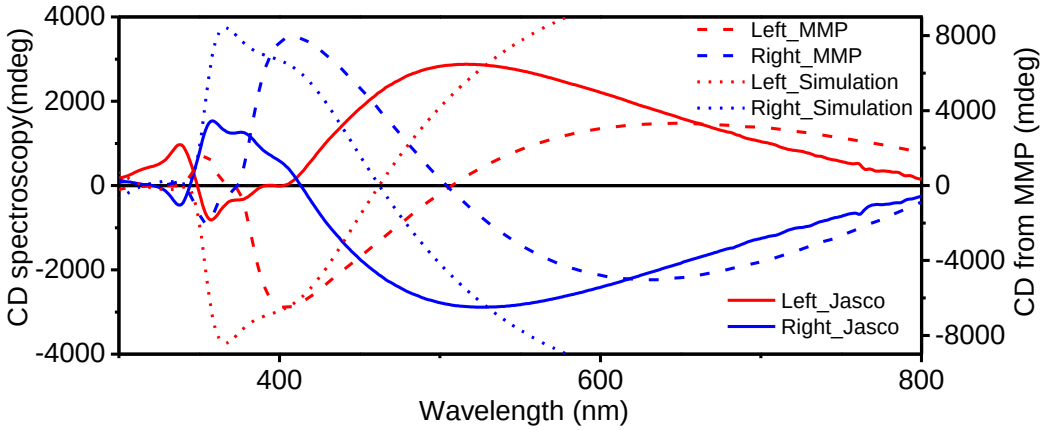

Figure 85. Comparison of CD by Jasco CD spectrometer (solid lines, left scale), MMP (dashed lines, right scale) and simulations (dotted lines, right scale) for left-handed (red) and right-handed (blue) two-layer structures.

The measured CD are quite similar to the simulated ones. The main features are well reproduced, although the simulated spectra are red-shifted compared to the experimental spectra, as it was already observed for the 2-layer structures. The CD and CB for left- and right-handed structures are perfectly symmetric in both simulations and measurements. The measurements by MMP and the simulations have two times higher values than the measurements by the commercial spectrometer. However, the shape of CD spectrum is similar and the symmetry of the left- and right-handed structures is preserved.

We prepared furthermore multilayer chiral superstructures with different angles. The CD of the sample was measured after the deposition of each AgNW layer (***Figure 86***).

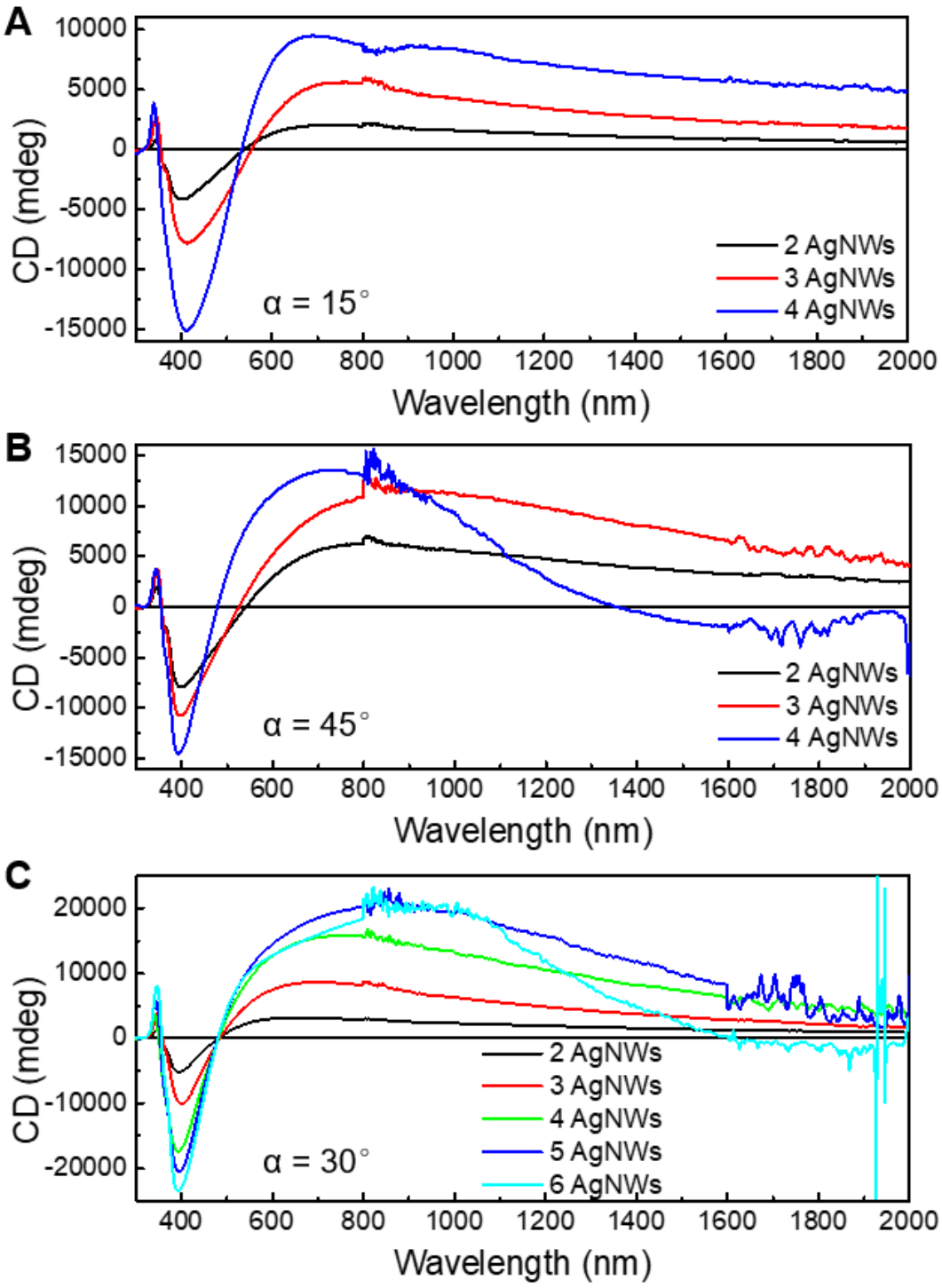

Figure 86. CD of left-handed plasmonic superstructures containing 4 or 6 layers of AgNWs with the angle α between two adjacent layers of AgNWs equal to 15°, 45° and 30°. The noise above 1600 nm increases for the samples with more than 4 AgNW layers due to the high extinction of those samples and the limited sensitivity of the detector.

We observe that the CD increases with the number of AgNW layers (n) for each angle α, except for the samples for which n × α = 180°. The shape of all spectra is more or less similar, except for the samples for which n × α = 180°, for which CD crosses the x-axis in the NIR, similarly to what was observed for the three-layer structure with α = 60° (3 × 60° = 180°) (***Figure 81***).

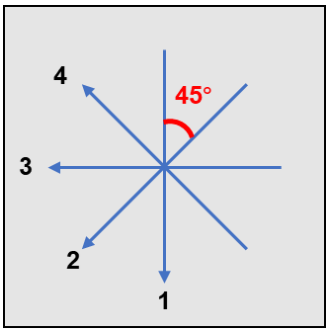

Figure 87. n = 4 and α = 45°. A "full turn" is obtained for n × α = 180°.

III.5. Conclusion

We have shown that it is possible to obtain well aligned AgNWs on a substrate using grazing incidence spraying, and to obtain multilayer chiral plasmonic superstructures with very high CD and g-factors by combining GIS with the LbL-assembly. The hierarchical parameters of the superstructures can be precisely controlled and the influence of the structural parameters on the chiroptical properties have been investigated. The helix-like multilayer superstructures present strong linear polarization properties (LB and LD), and more importantly strong chiroptical properties (CD and CB).

There are three effects which we believe are responsible for the chiroptical properties:

1. The light beam interact independently and successively with each layer of AgNWs. Each AgNW layer acts as a linearly polarizing filter (exhibiting both linear dichroism and birefringence), and the combination of those layers induces circular birefringence and dichroism. This is exactly what is included in the proposed model, which nicely reproduces the trend observed, including the effect of the distance and angle between the two layers of AgNWs. This model also explains why CD is observed for distances between the two layers of AgNWs much larger than optical wavelength (from micrometers up to several millimeters), going thus well beyond the typical length required for coupling of plasmon modes.

2. When the two layers of AgNWs are close enough to each other (below 100 nm), a coupling may occur between their LSPR, which may also contribute to the CD and CB of the film and

could be the cause of the observed difference of the shape of the CD curve for interlayer spacing smaller and larger than 100 nm. Furthermore, as for multilayer chiral superstructures containing more than three layers of AgNWs, the chiroptical properties increase with the number of AgNW layers. In addition, the CD curve crosses the x-axis in NIR when $n \times \alpha = 180°$ (n is the layer number of AgNWs, α is the angle between two adjacent layers of AgNWs), i.e. when the projection of the n layers of AgNWs form a symmetric structure.

3. For interlayer spacing larger than 100 nm, another effect may get involved and may be responsible for the oscillations observed in the CD spectra, that is the interference of light between the semi-reflective AgNWs layers. This could be the reason why the "frequency" of the oscillations is highly dependent on the distance between the layers of AgNWs and why the oscillations were not observed for small interlayer spacing (below 60 nm).

Based on these three effects, the structural parameters, namely the number of AgNW layers, the angle and the spacing between two layers of AgNWs, are studied and have been proven to have a critical influence on the chiroptical properties of the structure. For superstructures containing two layers of AgNWs at a fixed interlayer spacing, the most chiral structure is obtained when the angle α between the orientation of the two layers of AgNWs is 45°, while $\alpha = 0°$ or 90° are achiral structures. For a fixed angle α ($\alpha \neq 0°$ or 90°), the interlayer spacing modifies significantly the chiroptical properties of the film. The peaks of CD spectra red-shift with the increase of the interlayer spacing and oscillations of the curves have been observed for large interlayer spacing (> 100 nm).

The simulations performed are based on a model which considers a stack of non-interacting layers, and the optical properties are simulated thanks to the Berreman formalism (transmission matrix through a sequence of layers) taking into account the measured effective optical properties of an oriented layer of AgNWs. The main features of the spectra are reproduced, and the effect of the structure are well reproduced (effect of number of layers, spacing and angle between the AgNW layers). Some differences between the measurement and simulations exist, which may be due to small differences in the interlayer spacing, to the non-ideal character of

the samples compared to simulations and to the fact that no coupling of the plasmon modes is considered in the simulations.

In conclusion, we have introduced in this chapiter an easy way to make chiral nanostructures from non-chiral commercially available products, and using simple equipment and a simple concept. The same strategy can be used with other nano-objects such as AuNRs or cellulose nanofibers for other properties (mechanical, magnetic, electronic, etc.). This new approach allows fabricating nanostructures that are (almost) as powerful as structures made by lithography, but on much larger surfaces and at much lower cost. Furthermore, the chiral superstructures have a huge broadband CD that can be easily tuned over the entire UV, Visible and NIR range with simple geometric parameters, which is not the case for most self-assembly approaches which rely on a template whose structure cannot be modified at will. The proposed approach also allows making more complex nanostructures in which a functional molecule can be placed at a well-controlled position within the assembly, which is what will be presented in the following chapter.

IV. Coupling of achiral dyes to chiral superstructures

The LSPR in metallic nanoobjects gives rise to the enhancement of the electromagnetic field in the vicinity of the nanoobject. This enhanced electromagnetic field thus modifies the local environment and may couple to molecules and materials placed close to the nanoobject. In particular, plasmon-exciton coupling in both weak coupling and strong coupling regimes have recently raised interest. Most researches up to date focus on the effect of the plasmon-exciton coupling on the absorption and / or scattering, such as surface plasmon enhanced absorption and scattering, and to the Rabi splitting appearing in the absorption band in the strong coupling regime. The interaction of exciton modes to a LSPR with a chiral geometry is however less studied. We will show here that it is possible to modify the optical properties of an achiral organic dye by putting it within a chiral plasmonic nanostructure made from aligned AgNWs. The organic dye we used here is TDBC, which is a frequently used molecule to study plasmon-exciton coupling because it spontaneously forms a J-aggregate in aqueous solution which gives rise to a narrow and intense absorbance peak in the visible range. In addition, it is a charged molecule which makes it easy to integrate within the polyelectrolyte multilayer by LbL-assembly. This chapter aims to study the modification of the chiroptical properties of TDBC and other materials when embedded in the chiral plasmonic superstructures, and to study how the optical properties can be tuned by the geometrical parameters of the superstructure.

IV.1. Layer-by-Layer assembly of TDBC

TDBC is an organic dye molecule which forms spontaneously J-aggregates in aqueous solution. Although a sheet-like structure was once observed using cryo-TEM[258], the exact conformation of the J-aggregates is not yet clear. In any case, the formation of J-aggregates gives rise to a strong transition dipole moment and an intense narrow absorption peak in the visible range (589 nm) (***Figure 88***). Furthermore, the high charge density of the J-aggregates favors the adsorption

to oppositely charged surfaces and understandably the LbL-assembly. This is actually the reason why it has been the most frequently chosen molecule in the studies of photon-exciton and exciton-plasmon couplings. In this manuscript, the integration of TDBC into the chiral plasmonic superstructure was realized by LbL-assembly via the dipping method. This section aims to determine the optimal experimental conditions for TDBC deposition.

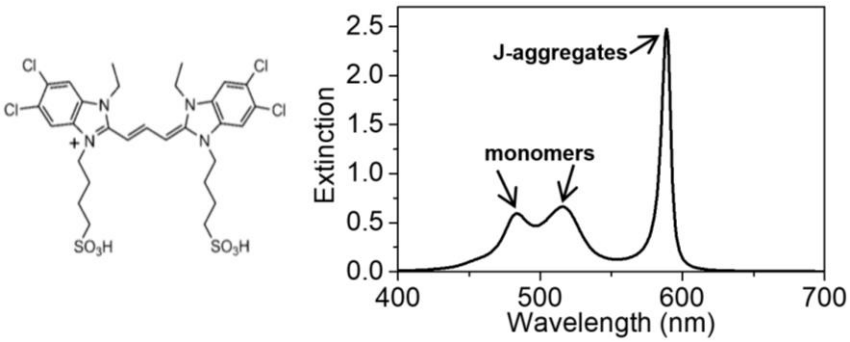

Figure 88. Chemical structure of TDBC and the extinction spectrum of its solution in water at a concentration of 0.1 mg/ml.

First, we simply replaced one PSS layer in a PEI/(PSS/PAH)$_n$/PSS/PEI structure with TDBC, since the latter is negatively charged as the PSS polyanion. Hence, on a glass slide, we prepared the following LbL structure: PEI/(PSS/PAH)$_5$/TDBC/PAH/PSS. The polyelectrolyte layers were deposited by spray-assisted method using polyelectrolyte solutions prepared as described in section II.2.4. The TDBC layer was deposited by dipping the sample in a 0.1 mg/ml TDBC aqueous solution during 15 min. We found out that, 1. the extinction of the TDBC layer is rather low (~ 0.18); 2. the TDBC layer is not stable in this structure since more than half of it (~ 55%) was desorbed from the film after the deposition of the following PAH/PSS layer pair (***Figure 89***).

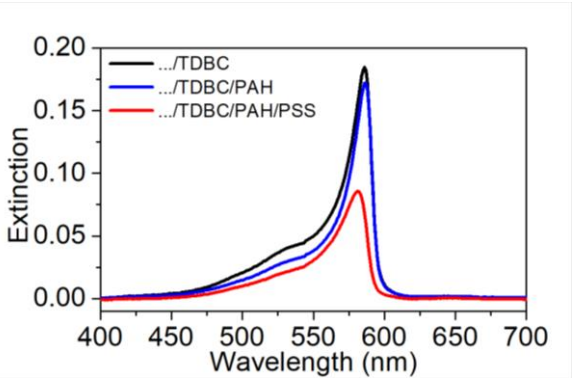

Figure 89. Extinction spectra of the LbL film PEI/(PSS/PAH)$_5$/TDBC/PAH/PSS, after the deposition of the TDBC layer (black), the PAH layer (blue) and the PSS layer (red) following TDBC.

It was reported that the composition of the polyelectrolyte solutions (pH, concentration of salt, dispersity of the polymers), especially the PSS solution, was critical for the attachment of TDBC on the LbL film[259]. Therefore, we repeated the same experiments with pre-treated

solutions of PSS and PAH. The solutions were first dialyzed using a membrane with a molecular weight cut-off of 5000 Da in order to remove the short polymer chains, we did not add any NaCl to the polymer solution (the NaCl concentration was 0.5 mol/L in the previous polyelectrolyte solutions) and the pH was adjusted to 8.5 with 0.1 M NaOH.

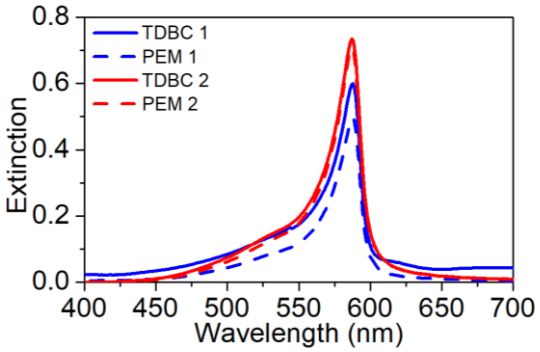

Figure 90. Extinction spectra of the LbL film TDBC 1/PEM 1/TDBC 2/PEM 2, after the deposition of corresponding layers.

With the pre-treated polyelectrolyte solutions, we prepared a LbL film containing two layers of TDBC: PEI/$(PSS/PAH)_5$/TDBC/$(PAH/PSS)_5$/PAH/TDBC/PAH/$(PSS/PAH)_5$. The same structure is written as PEM 0/TDBC 1/PEM 1/TDBC 2/PEM 2, for which an extinction spectrum was measured after the deposition of each "TDBC", "PEM 1" and "PEM 2" (***Figure 90***). By comparing the extinction spectra, we conclude that, 1. the amount of TDBC included in the multilayer was significantly increased, as the extinction increases from 0.18 to 0.6 for one layer of TDBC; 2.the stability of TDBC in the multilayer was improved but not perfect (~ 10% of the TDBC layer was desorbed by the following PAH/PSS layer pair); 3. the extinction of two layers of TDBC deposited was not exactly twice that of the one-layer sample. In addition, the necessity to modify the polyelectrolyte solutions for each deposition is tedious (in particular the dialysis which takes a few days).

We thus tested other LbL multilayer structures keeping non-treated polyelectrolyte solutions with 0.5 M NaCl. We tried to replace PAH with PDDA (PEI/$(PSS/PDDA)_5$/TDBC), which turned to be inefficient since the adsorption of TDBC on PDDA was extremely weak. We tried also the $[PEI/(PSS/PEI)_5/TDBC]_3$ structure, which worked relatively well, in the sense that the loss of TDBC during the adsorption of the following polyelectrolyte layers was avoided and the density of the first layer of TDBC reached a comparatively high level (Abs ≈ 0.6). However, the deposition of the 2nd and 3rd layers of TDBC was not as effective as for the first layer.

Finally, the multilayer structure PEI/(PSS/PAH)$_4$/PSS/PEI/[TDBC/PEI/PSS/(PAH/PSS)$_4$/PEI]$_3$ in which TDBC is sandwiched between 2 layers of PEI is the most effective one. The same structure is written as PEM 0/TDBC 1/PEM 1/TDBC 2/PEM 2/ TDBC 3/PEM 3, for which an extinction spectrum was measured after the deposition of each "TDBC", "PEM 1", "PEM 2" and "PEM 3" (***Figure 91***A). This structure leads to extremely homogeneous TDBC film (the standard deviation of the absorbance obtained by measuring 9 spots dispersed on the entire glass slide is around 2% for 3 layers of TDBC), negligible desorption of TDBC due to the following polyelectrolyte deposition, and linear increase of the extinction by adding more layers of TDBC. Furthermore, we found out that for all the LbL structures studied above, the J-aggregates are preferentially adsorbed into the LbL films than the monomers (***Figure 91***B).

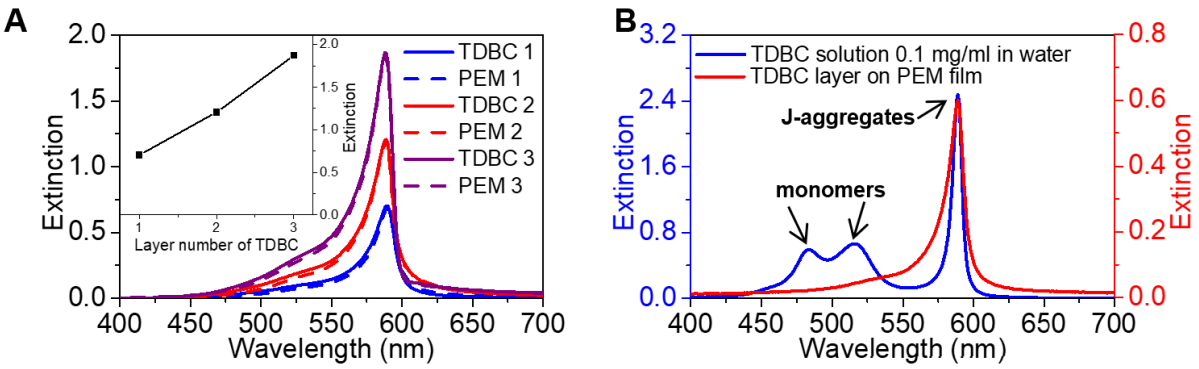

Figure 91. (A) Extinction spectra of the LbL film TDBC 1/PEM 1/TDBC 2/PEM 2/ TDBC 3/PEM 3, after the deposition of corresponding layers. The inset is the maximum extinction as a function of the layer number of TDBC. (B) Extinction spectra of TDBC solution and film.

The adsorption kinetics of TDBC on PEI might be different from the kinetics for PSS or PAH, which we studied in the previous section (the adsorption by dipping reached a plateau after 15 min). We thus did similar experiments for TDBC and we show that the dipping time required for a saturated deposition of a TDBC layer on the PEI/(PSS/PAH)$_4$/PSS/PEI multilayer is 1 hour (***Figure 92***).

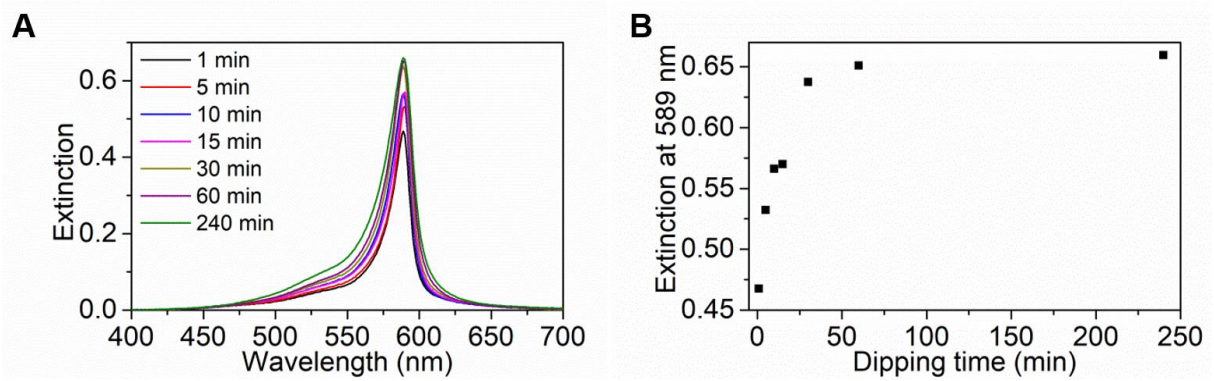

Figure 92. (A) Extinction spectra of the LbL films with one layer of TDBC for different dipping times of TDBC from 1 min to 240 min. (B) Extinction at 589 nm as function of the dipping time, which saturates at 60 min.

Furthermore, TDBC may adsorb differently to a polyelectrolyte multilayer compared to PAH and PSS. In particular, it may be possible that the TDBC J-aggregates can diffuse into the underlying polyelectrolyte multilayer and not only adsorb on top of the outmost layer. In order to investigate this, we prepared several samples with a structure of PEI/$(PSS/PAH)_n$/PSS/PEI/TDBC (n = 2, 7, 14, 29, 49) in which the TDBC is adsorbed on polyelectrolyte multilayer films with increasing thickness. The fact that the extinction spectra are identical confirmed that the amount of TDBC which is adsorbed doesn't depend on the thickness of the PEM film and thus that it probably doesn’t diffuse into the polymer film (***Figure 93***).

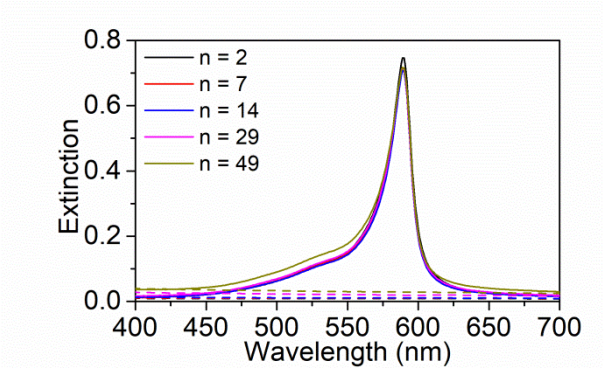

Figure 93. Absorption of LbL films with one layer of TDBC deposited on different numbers of layer pairs PSS/PAH. Dashed lines are corresponding absorptions of LbL films before the deposition of TDBC.

In conclusion, we have presented the fabrication of PEM films by LbL-assembly with precisely controlled thickness and well understood the LbL deposition of TDBC in a PEM film. It is difficult to determine the thickness of the TDBC layer by ellipsometry since it is intensely colored and highly absorbing at the wavelength of the laser. We will thus compare the thickness measured by electron microscopy on PEM films with and without TDBC. This will be done in section IV.5.

IV.2. Optical properties of a TDBC monolayer film

The TDBC and its aggregate are known to be achiral in solution. The TDBC film exhibits no polarization properties either, which was confirmed by the measurement of the Mueller Matrix of a single layer of TDBC LbL-assembled in a PEM film (***Figure 94***).

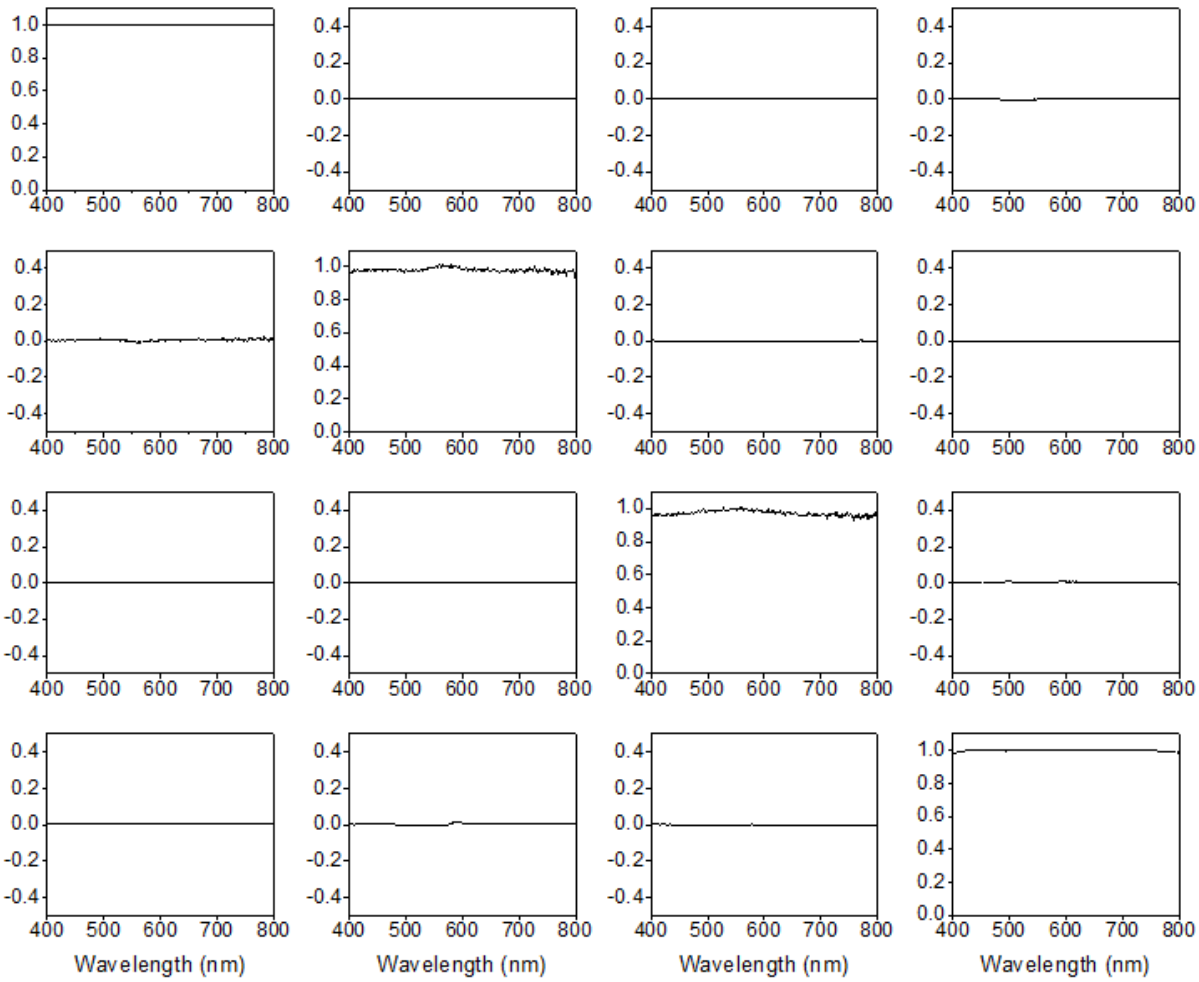

Figure 94. Mueller Matrix of a layer of TDBC deposited on a PEM film measured by MMP.

The Mueller Matrix of a single layer of TDBC is an identity matrix, in which the diagonal elements are equal to 1 and the off-diagonal elements equal to 0. This reveals that the TDBC film has neither linear nor circular polarization properties and the film is isotropic.

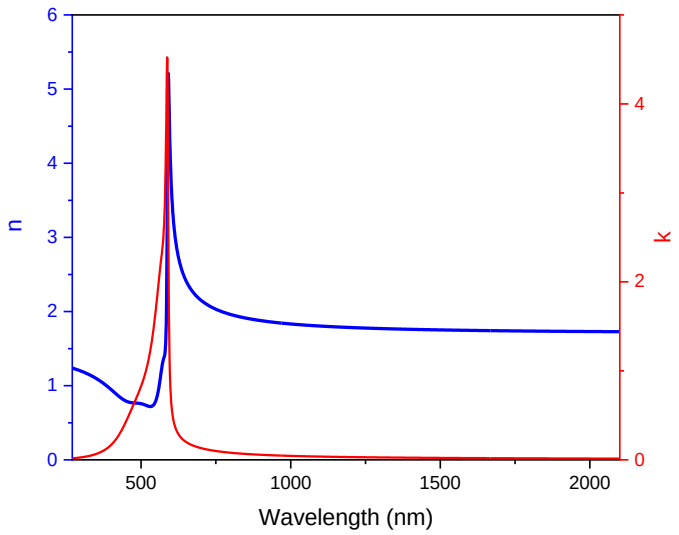

Figure 95. Real part (n) and imaginary part (κ) of the refractive index of the TDBC film measured by ellipsometry.

The complex refractive index of the TDBC film, $\tilde{n}(\omega) = n(\omega) + i\kappa(\omega)$, was measured using ellipsometry by Yann Battie (***Figure 95***). The dielectric function of the film, $\varepsilon(\omega) = \tilde{n}(\omega)^2$, was then used in the following simulations.

IV.3. Chiroptical properties of hybrid TDBC-AgNW chiral nanostructures

Thanks to the versatility of the LbL-assembly and the high charge density of the J-aggregates of the cyanine dye, we are able to fabricate hybrid nanostructures containing TDBC placed at a precise position within the chiral plasmonic nanostructure to study the optical properties of the hybrid film.

We developed chiral plasmonic superstructures containing two layers of AgNWs with one layer of TDBC between them. The fabrication process of the chiral plasmonic superstructures using GIS and LbL-assembly was presented in the previous chapter. The introduction of the TDBC layer was realized by using LbL-assembly under the optimized conditions presented in section IV.1. The structure can be described as PEI/PSS/PAH/PSS/PEI/Ag/PEI/PSS/PAH/PSS/PEI/TDBC/PEI/PSS/PAH/PSS/PEI/Ag. An

achiral structure was prepared for comparison, consisting of one single layer of aligned AgNWs and one layer of (PEI/PSS/PAH/PSS/PEI/Ag/PEI/PSS/PAH/PSS/PEI/TDBC).

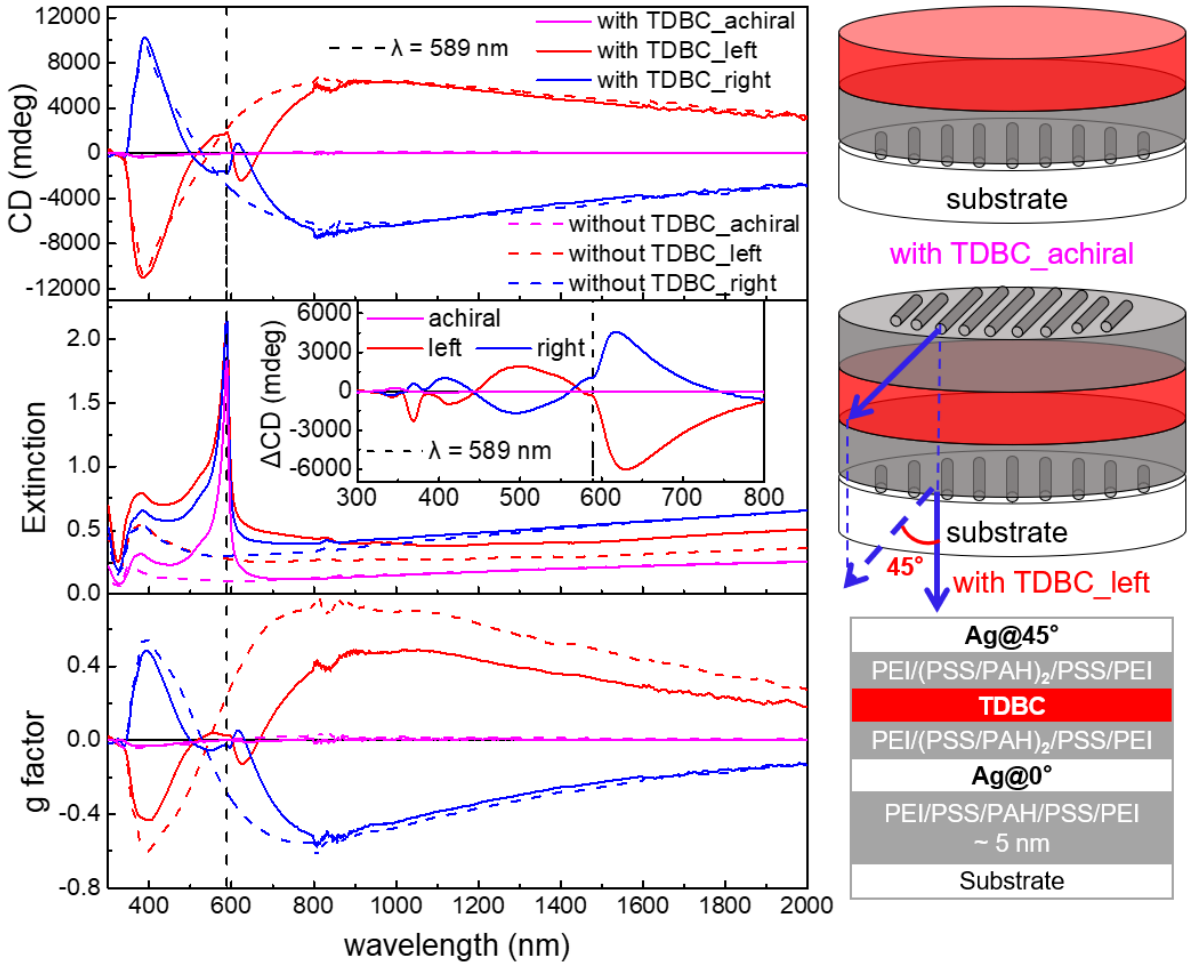

Figure 96. Left panel: CD, extinction and g-factor spectra of samples consisting of two layers of AgNWs with one layer of TDBC between them (solid lines) and a control sample (achiral) consisting of one layer of AgNWs with one layer of TDBC. The corresponding structures without TDBC (dashed lines) are those with identical interlayer spacing and angle. Both left- (red) and right-handed (blue) structures are presented. The inset shows Δ CD, which is the difference between the CD of the structures with and without TDBC. Right panel: schematic of the superstructures (top) and its composition (bottom).

The chiroptical response (CD, UV and g-factors) are similar to the properties of the chiral AgNW superstructures discussed in the previous section with an additional feature: a sharp dip in the CD spectrum appears at the absorption wavelength of the TDBC J-aggregates, and the dip remains symmetrical for the left- and right-handed structures. The chirality transfer from chiral molecules to achiral nanostructures is a phenomenon widely studied (see section I.2.3). However, the modification of the chiroptical properties of an achiral molecule by chiral

plasmonic nanostructures is relatively rare. Here, we realize this modification with a remarkable change in the CD spectrum in a tunable and reproducible way. By plotting ΔCD, the difference between the CD of the structures with and without TDBC, we highlight the modification of the CD due to the TDBC layer as a function of wavelength (inset of ***Figure 96***). The ΔCD related to the TDBC layer has a bisignate shape as the CD spectrum of many chiral molecules, while TDBC itself is achiral. This bisignate ΔCD exhibits negative / positive Cotton effect around the absorption wavelength of TDBC for left- / right-handed structures respectively. In addition, the ΔCD has extremely high values (up to a few thousands millidegrees) compared to classical chiral molecules, which have typically a CD of dozens of millidegrees. The extinction of the film turns out to be the addition of the extinction spectra of the AgNWs layers and the TDBC layers, while the extinction intensity of the TDBC J-aggregates is significantly enhanced. The achiral structure (one layer of AgNWs + TDBC) displays no CD and of course no modification of CD, but the enhancement of the TDBC absorption is also observed.

The Mueller Matrix of the one- and two-layer structures with one layer of TDBC was simulated and measured by Yann Battie from University of Lorraine. The measured and simulated LD, LB, CD and CB are shown in ***Figure 97*** and ***Figure 98*** respectively.

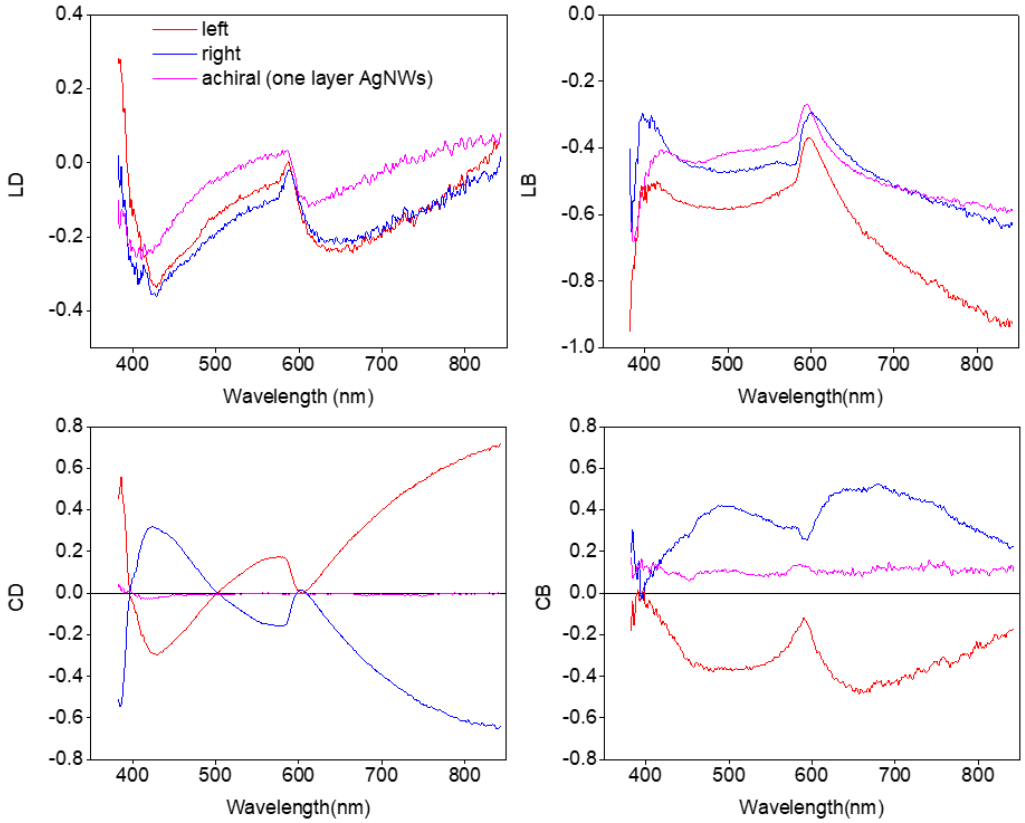

Figure 97. LD, LB, CD and CB of the one- and two-layer structures (left and right-handed) with TDBC measured. by MMP.

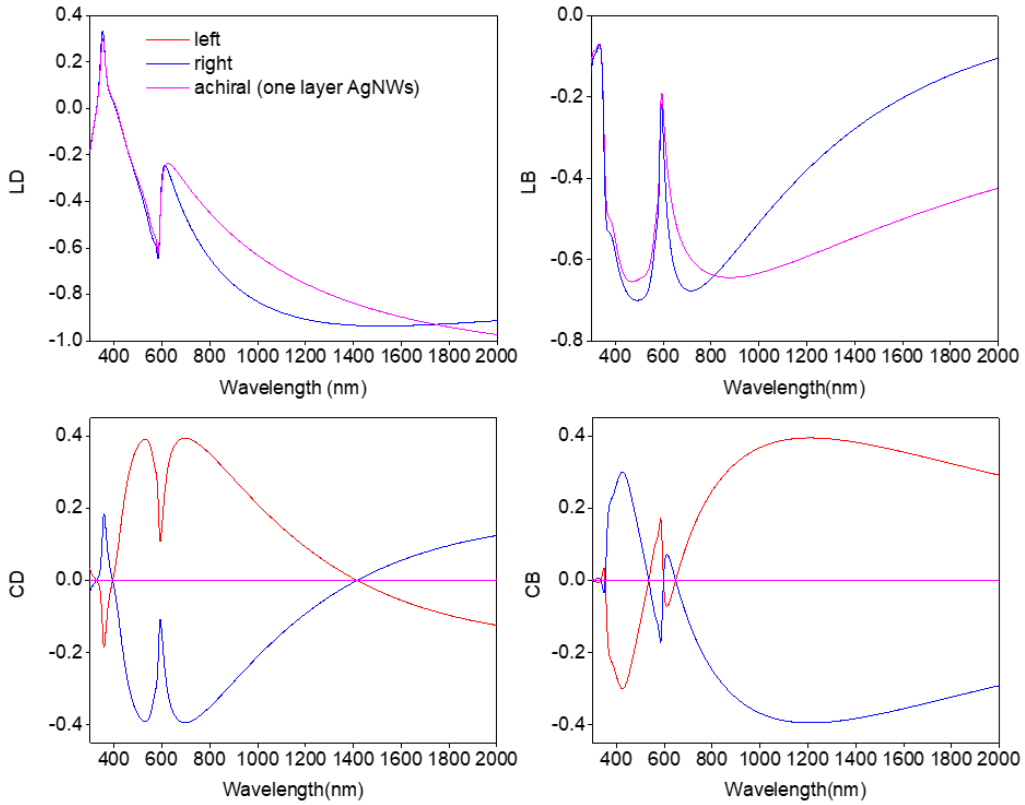

Figure 98. Simulated LD, LB, CD and CB of the one-layer and two-layer structures (left and right-handed) with TDBC.

Modifications of CD as well as CB similar to the CD measured by commercial spectrometer discussed above (***Figure 96***) are observed in the MMP measurements and the simulations. Interestingly, the linear polarization properties (LB and LD) of the structures (both achiral and chiral ones) have also seen a modification due to the TDBC layer: a peak near the maximum absorption wavelength of TDBC J-aggregates is shown in the LB and LD, in both MMP measurements and simulations. However, the linear modifications seem to be independent of the handedness and the number of layers of AgNWs.

The CD measured by the Jasco CD spectrometer and by MMP are compared with the simulations in ***Figure 99***.

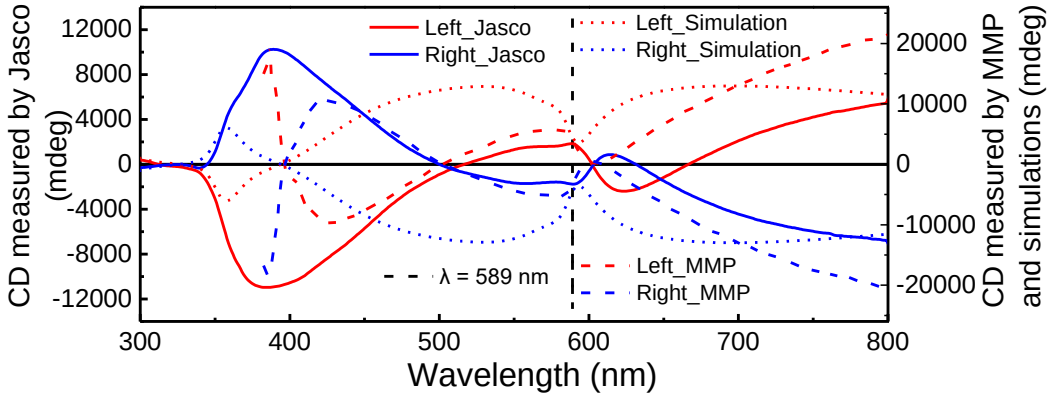

Figure 99. CD spectra measured by the Jasco CD spectrometer (solid lines, left scale), MMP (dashed lines, right scale) and simulations (short dashed lines, right scale) for left-handed (red) and right-handed (blue) two-layer structures with one layer of TDBC.

The spectra measured by CD spectroscopy and MMP are close to each other in the visible range, in particular close to the TDBC absorption wavelength, while they are quite different in the UV range. The simulations are not fully consistent with the measurements. However, the modification of CD is quite well reproduced in the simulations, although the “dip” in the CD spectrum due to TDBC is red-shifted in the measured spectra compared to the simulations, in which the “dip” appears very close to the absorption wavelength of TDBC. This means that the simple model considering the LbL-assembled superstructures as independent layers stacked together is able to partly reproduce the change in CD induced by the TDBC. However, the details of the modification are not well simulated, and thusit may be possible that coupling

between the LSPR of the AgNWs and the TDBC layer also contributes to the CD modification, wich was not taken into account in the simulations.

IV.4. Surface plasmon enhanced absorption and emission

As mentioned above, the absorption of the TDBC J-aggregates is enhanced when the TDBC layer is in vicinity of the AgNWs layer(s). The enhanced absorption can reach the double or even the triple of its typical absorption (0.6 – 0.7) in a PEM film without AgNWs. This phenomenon is known as the surface plasmon enhanced absorption.

In order to study this phenomenon and its dependence on the distance between the TDBC layer and the AgNWs layer(s), we prepared a series of samples with one layer of TDBC deposited on a layer of aligned AgNWs, separated by a LbL-assembled PEM film (***Figure 100***A).

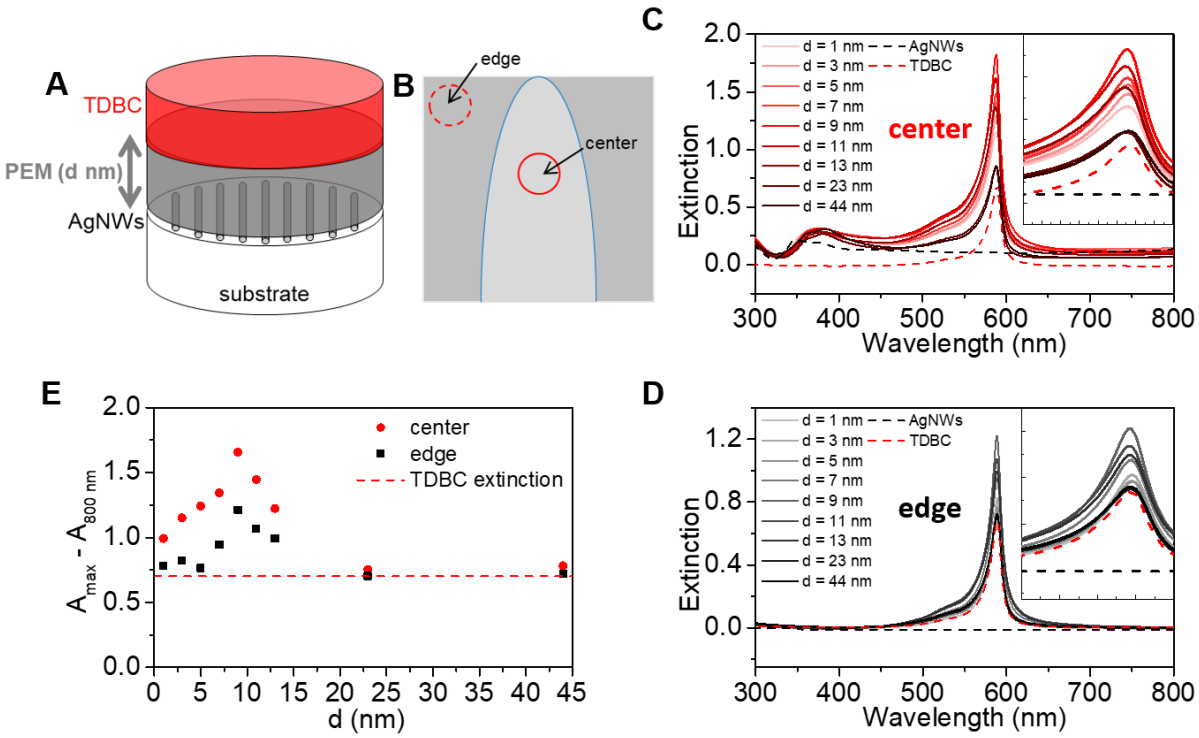

Figure 100. (A) Sketch of the structure: a layer of TDBC deposited on a layer of aligned AgNWs, separated by a PEM film of a certain thickness d. (B) The extinction spectra were measured in the central area of the samples and at the edge, where TDBC is present but no AgNWs are deposited. (C) Extinction spectra of the central area for different d. (D) Extinction spectra at the edge for different d. (E) Difference between the maximum extinction and the extinction at 800 nm $A_{max} – A_{800\ nm}$ as a function of d. The horizonal dashed red line is the extinction of TDBC without AgNWs.

The structure can be written as following: PEI/PSS/PAH/PSS/PEI/AgNWs/PEI/$(PSS/PAH)_n$/PSS/PEI/TDBC ($-1 \leq n \leq 20$ corresponding to 1 nm $\leq n \leq$ 44 nm; n = -1 for only one layer of PEI between TDBC and AgNWs). We measured the extinction spectra of the sample in its central area, where TDBC, polymers and the AgNW layer are present; and on its edge, where only the TDBC layer and the polymer layers with the same structure are present without AgNWs (***Figure 100***B). The extinction spectrum of one layer of AgNWs and the extinction spectrum of one layer of TDBC were measured for comparison. The single layer of AgNWs and that of TDBC were both deposited on PEI/PSS/PAH/PSS/PEI The difference of the maximum extinction and the extinction at 800 nm ($A_{max} - A_{800\ nm}$) was calculated and was considered as the (enhanced) extinction of TDBC (***Figure 100***E). We observed that, in the central area, the absorption of the TDBC J-aggregates (589 nm) was significantly enhanced. This enhancement increases from d = 1 nm to d = 9 nm, reaching a maximum at d = 9 nm, and then decreases from d = 9 nm to d = 23 nm. Starting from d = 23 nm, we observed no more the enhancement phenomenon. This enhancement of the absorption of organic dyes adjacent to the localized surface plasmon is called surface plasmon enhanced absorption. This phenomenon has been extensively studied and has many applications. Surprisingly, we also observed an enhancement of the absorption of TDBC on the edge of the sample (***Figure 100***E). This enhancement is much weaker than that in the center yet noticeable. As the homogeneity and reproducibility of the LbL-deposition of TDBC was confirmed in the previous section, we believe that this weak enhancement is due to the very small amount of AgNWs residing on the edge. This is inevitable by doing the GIS of AgNWs. The surface plasmon enhanced absorption is an evidence of the plasmon-exciton interaction between the AgNWs and the TDBC J-aggregates.

We studied furthermore the surface enhanced absorption of the TDBC layer placed in the middle of the gap between two AgNW layers oriented at 45° (left-handed). The structure can be written as PEI/PSS/PAH/PSS/PEI/AgNWs/PEI/$(PSS/PAH)_m$/PSS/PEI/TDBC/PEI/$(PSS/PAH)_m$PSS/PEI/

AgNWs, with m varied from 0 to 15 corresponding to d from 3 nm to 34 nm. The extinction spectra were measured on the same sample after the deposition of the TDBC layer and the deposition of the second layer of AgNWs (***Figure 101***B). A two-layer film without TDBC was also prepared for comparison (***Figure 101***A).

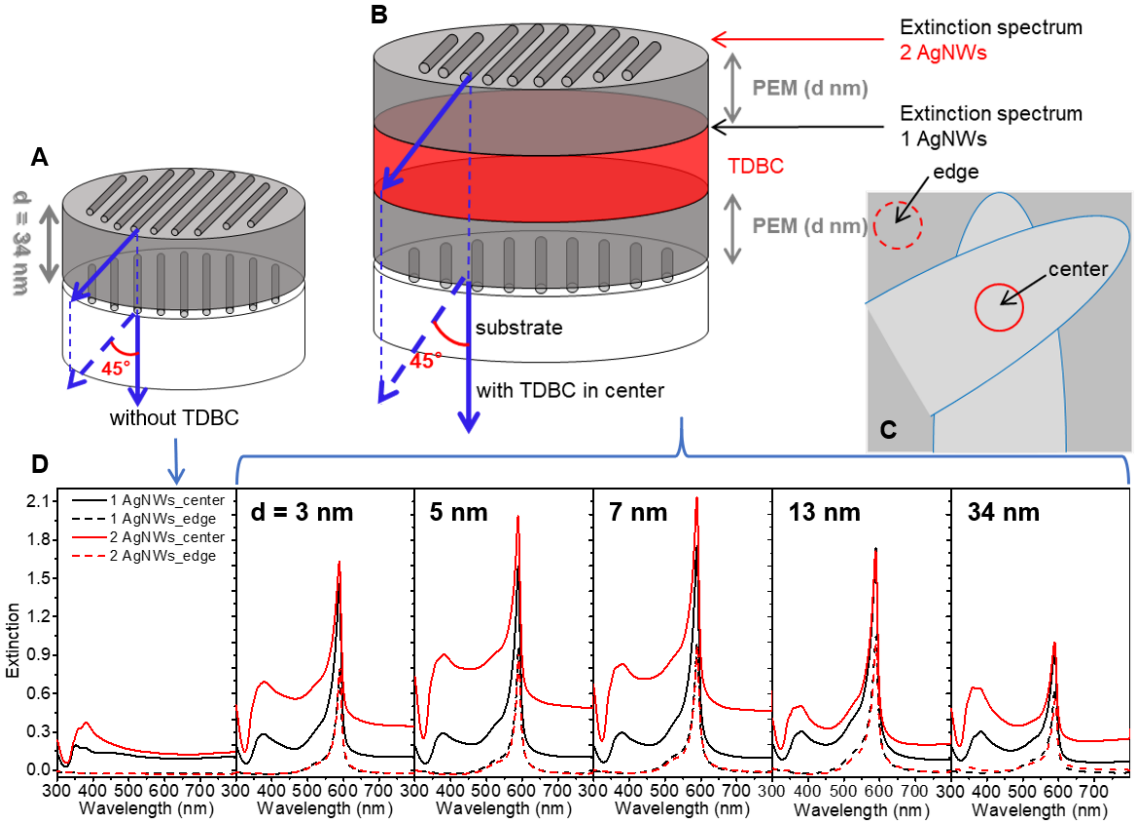

Figure 101. (A) Sketch of the structure without TDBC. (B) Sketch of the structure with TDBC: a layer of TDBC placed in the middle of two layers of AgNWs, the distance between the TDBC layer and each layer of AgNWs is d. (C) The extinction spectra were measured in the central area of the samples and on their edge. (D) Extinction spectra were measured after the deposition of the TDBC layer (black) and after the deposition of the second layer of AgNWs (red) in the central area (solid lines) and on the edge (dashed lines). From left to right: extinction spectra for structure without TDBC and those with TDBC with increasing d.

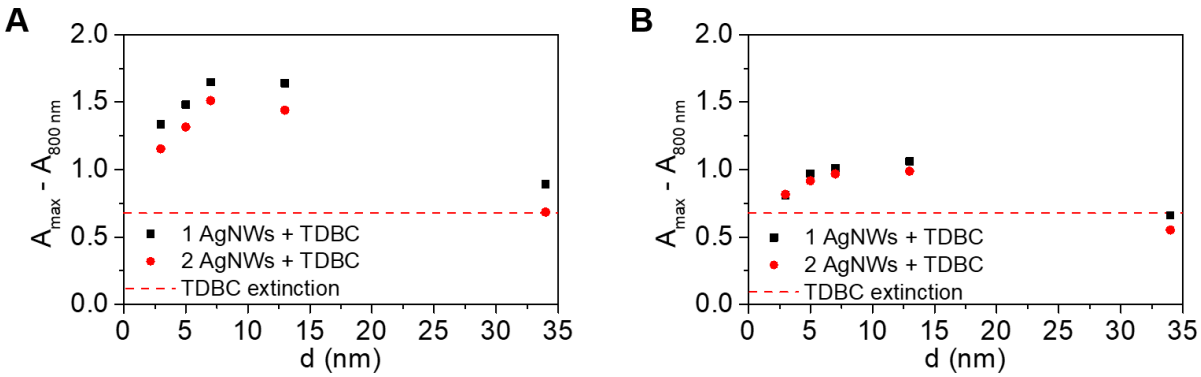

Figure 102. $A_{max} - A_{800\ nm}$ as a function of d in the center (A) and on the edge (B). The horizonal dashed red line is TDBC extinction without AgNWs.

Similar conclusion can be made by plotting $A_{max} - A_{800\ nm}$ as a function of d (***Figure 102***) for the two-AgNW-layer structure as for the structure containing only one layer of AgNW discussed above. The enhancement increases with d from d = 3 nm to d = 7 nm and decreases for d > 7 nm. The enhancement was negligible for d = 34 nm (***Figure 102***). In addition, the change occurred also in transversal mode of the LSPR of AgNWs at around 380 nm for the two-layer structures, but this is more likely due to the change of the interlayer spacing between the two layers of AgNWs as demonstrated in section III.3.4, since it was not the case for the one-layer structures (extinction spectra after the deposition of TDBC layer). Again, the enhancement was observed in both the center (***Figure 102***A) and edge (***Figure 102***B) of the samples, although it is much more important in the central area.

In order to reduce the influence of the change of interlayer spacing, we prepared a series of samples in which the TDBC layer is deposited at a varying distance above 2 layers of AgNWs oriented at 45° and separated by a constant spacing of 13 nm. The structure can be described as:

PEI/PSS/PAH/PSS/PEI/AgNWs/PEI/$(PSS/PAH)_5$/PSS/PEI/AgNWs/PEI/$(PSS/PAH)_n$/PSS/PEI / TDBC ($1 \leq n \leq 47$, corresponding to 5 nm ≤ d ≤ 100 nm, ***Figure 103***A). The effect of the distance on the enhancement of the absorption of TDBC is very clear in this case (***Figure 103***E): when the TDBC layer is very close to the two layers of AgNWs (≤ 10nm), its absorption is enhanced by a factor of almost 3. Above a spacing of 20 nm, we observed almost no enhancement, the absorption of the TDBC layer being similar to that of a TDBC layer in a PEM film without AgNWs. The transverse mode of LSPR of AgNWs at 380 nm was not much influenced here, compared to two layers of AgNWs without TDBC. Only a small change can be observed which could arise from the change of refractive index of the surrounding due to increasing number of PEM layer.

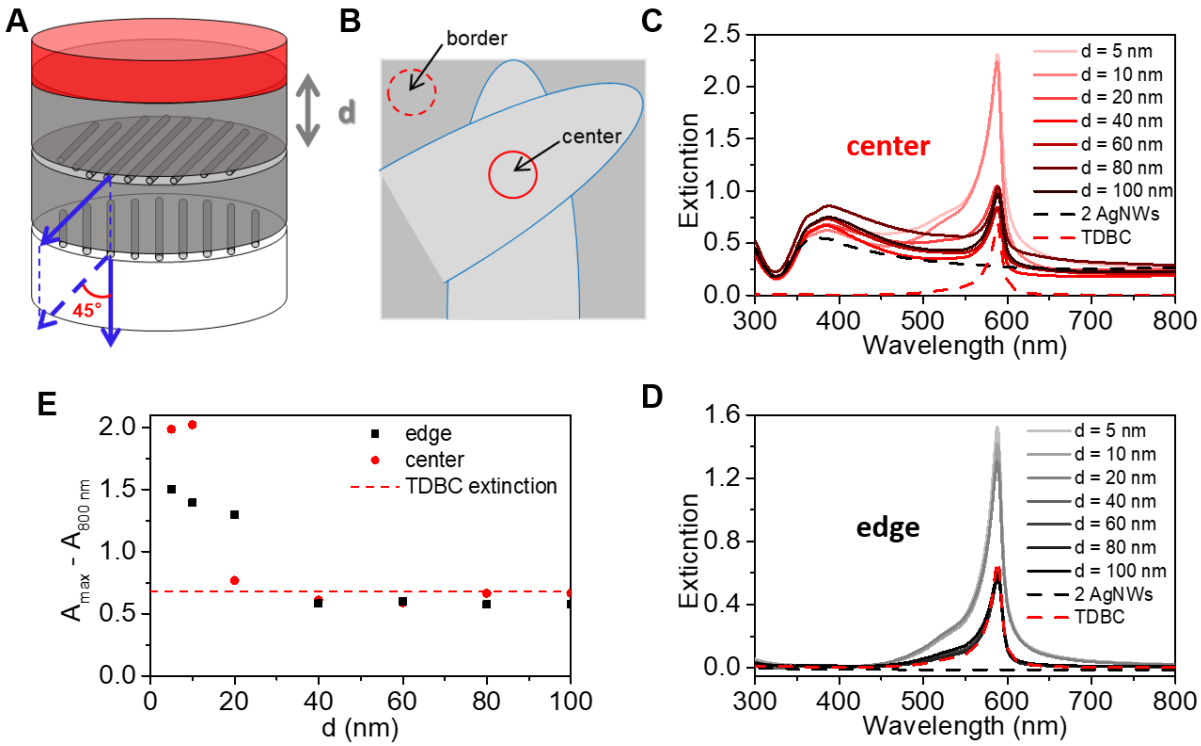

Figure 103. (A) Sketch of the structure: a layer of TDBC deposited on top of two layers of aligned AgNWs, separated by a PEM film of a thickness of d. (B) The extinction spectra were measured in the central area of the samples and on their edge. (C) Extinction spectra measured in the central area for different spacing d. (D) Extinction spectra of the edge for different spacing d. (E) $A_{max} - A_{800\,nm}$ (intensity of TDBC extinction) as a function of d. The horizonal dashed red line is TDBC extinction without AgNWs.

Furthermore, we measured fluorescence spectra for this series of samples.

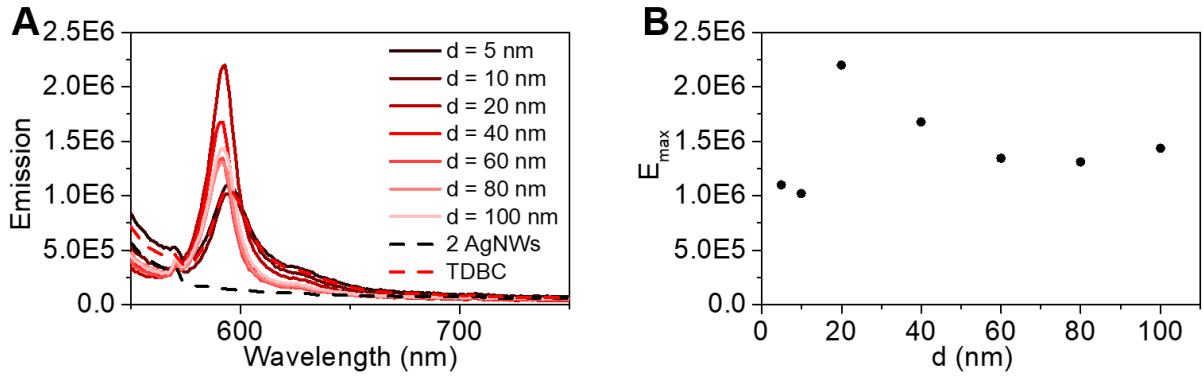

Figure 104. (A) Fluorescence emission spectra of a layer of TDBC deposited on two layers of AgNWs, the distance between the TDBC layer and the AgNWs changed from 5 nm to 100 nm. (B) Maximum emission intensity as a function of distance d. The excitation wavelength is 520 nm.

As we can see in ***Figure 104***, the emission intensity of the TDBC layer depends on the distance between TDBC and the two layers of AgNWs. Contrary to the surface plasmon enhanced

absorption, the emission for very close distance (d = 5 nm and 10 nm) is not enhanced. It is well-known that the fluorescence can be quenched close to plasmonic particles. The emission is only enhanced above d = 20 nm and the enhancement then decreases with d as the absorption was shown to decrease with increasing d.[219]

Not only the intensity of the fluorescence of TDBC is modified by the AgNWs, preliminary experiments indicate that the polarization of the emitted light can also be modified by the chiral plasmonic superstructures. When excited by non-polarized light, the fluorescence light emitted by a layer of TDBC embedded in a PEM film is non-polarized, while the fluorescence light emitted by a layer of TDBC placed between two layers of AgNWs with a chiral superstructure (left-handed) is circularly polarized ($E_{left} - E_{right} \approx 10$ mdeg) (***Figure 105***). This is the so called circularly polarized luminescence (CPL). The CPL was measured by the group of Prof. Reiko Oda from University of Bordeaux. This is a preliminary result and more experiments should be done.

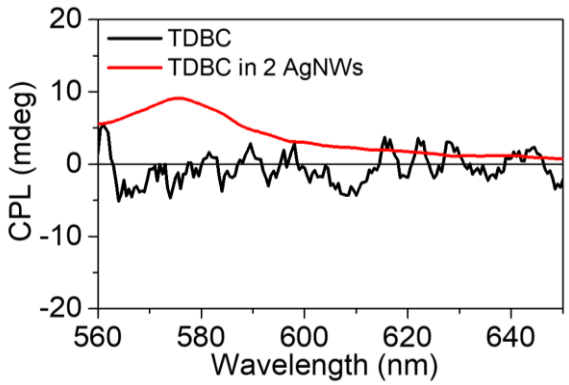

Figure 105. CPL of a layer of TDBC embedded in a PEM film (black) and in a left-handed chiral plasmonic superstructure containing two layers of AgNWs (red). The TDBC layer shows no CPL when embedded in an achiral polymeric environment whereas a CPL signal can be detected when it is embedded in a chiral plasmonic environment.

IV.5. Influence of the spacing between two layers of AgNWs

As it has been shown previously that the interlayer spacing has a major influence on the chiroptical properties of a two-layer superstructure without TDBC, and as we have shown in the last section that the chiroptical properties are strongly modified when TDBC is embedded in the chiral plasmonic superstructure, we will investigate here how the chiroptical properties of a hybrid superstructure containing TDBC placed between 2 AgNW layers oriented at 45° depend on the spacing between the AgNW layers.

Before doing so, it is however necessary to determine precisely the thickness of the TDBC layer in the PEM film. Indeed, we have shown that the distance between the AgNW has a huge influence on the spectroscopic properties and it is thus necessary to very precisely control this distance with and without TDBC. As noted earlier, it is technically difficult to determine the thickness of the TDBC layer by ellipsometry, so we used electron microscopy to measure the cross-section.

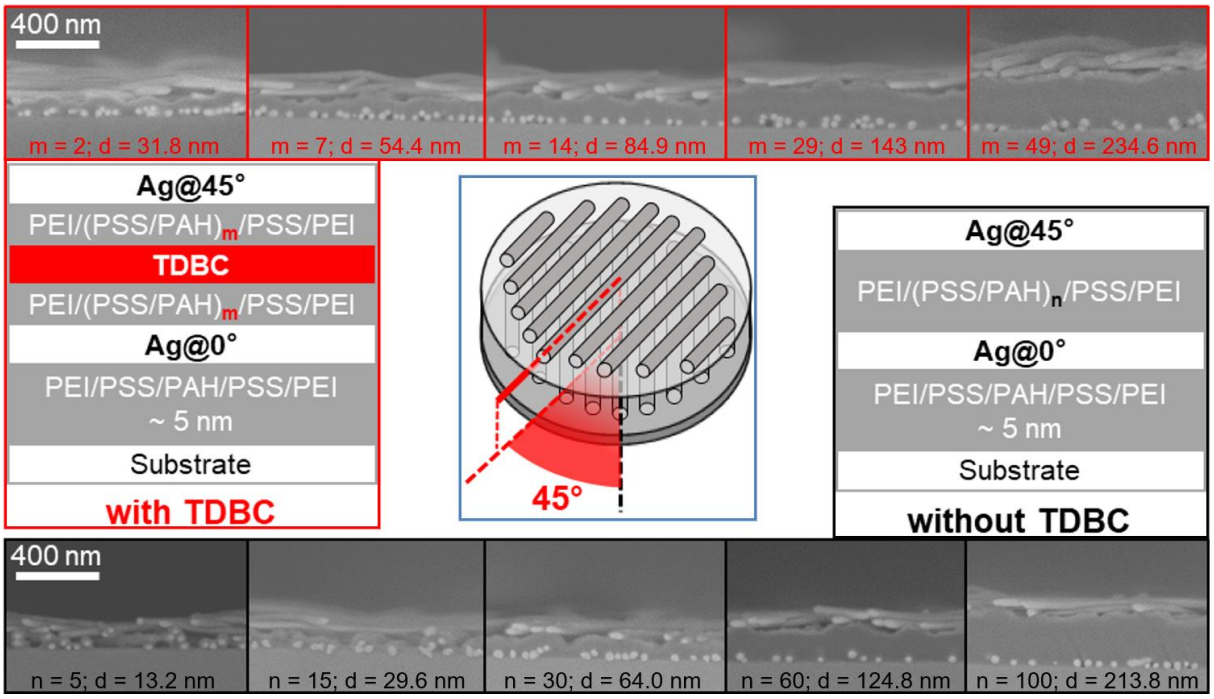

Figure 106. Blue frame: the microscopy measurements of the interlayer PEM thickness were carried out on two-layer superstructures with an angle α = 45°. Red frame: Cross-section SEM images of samples with one layer of TDBC, whose structure is describe as PEI/PSS/PAH/PSS/PEI/Ag/PEI/$(PSS/PAH)_m$/PSS/PEI/TDBC/PEI/$(PSS/PAH)_m$/PSS/PEI/Ag (m = 2, 7, 14, 29 and 49). Black frame: Samples without TDBC, whose structure is PEI/PSS/PAH/PSS/PEI/Ag/PEI/$(PSS/PAH)_n$/PSS/PEI/Ag (n = 5, 15, 30, 60 and 100). The thicknesses are the average distance between the two layers of AgNWs measured at different positions. m and n for each pair of samples correspond to the same total number of layers, when n = 2(m+1), between the AgNW layers.

We prepared a series of samples with two layers of AgNWs oriented at 45° from each other, and the interlayer film consisted of one layer of TDBC placed between two identical PEM films whose thickness is varied by changing the number m of PSS/PAH layer pairs from 2 to 49: PEI/PSS/PAH/PSS/PEI/Ag/PEI/(PSS/PAH)m/PSS/PEI/TDBC/PEI/(PSS/PAH)m/PSS/PEI/Ag (m = 2, 7, 14, 29 and 49). We cut the sample and polished the cross-section in order to take

microscopy images, measured the total thickness and compared it with structures without TDBC: PEI/PSS/PAH/PSS/PEI/Ag/PEI/(PSS/PAH)n/PSS/PEI/Ag (n = 5, 15, 30, 60 and 100).

The thickness as a function of m was plotted and compared with the thickness of PEM without TDBC (***Figure 107***). The thickness of PEM film with a layer of TDBC increased perfectly linearly as the layer number of PEM increased. For an identical total number of layers between the AgNWs, the spacing between the AgNW layers of a film with TDBC is ~20 nm larger than without TDBC. This observation is not sufficient to conclude that a layer of the J-aggregates is 20 nm thick, as it could also be possible that the deposition of TDBC changes slightly the structures of the surrounding polyelectrolyte layers to a certain extent. Although the exact morphology and conformation of the TDBC layer on a PEM is unknown as well as that of the J-aggregates in aqueous solution itself, we can safely conclude that the insertion of a layer of TDBC in a PEM structure increases its total thickness by 20 nm. This increase is independent of the thickness of the PEM films below and above TDBC. This information is however sufficient to build thin films with and without TDBC having an identical spacing between the AgNW layers to investigate their chiroptical properties.

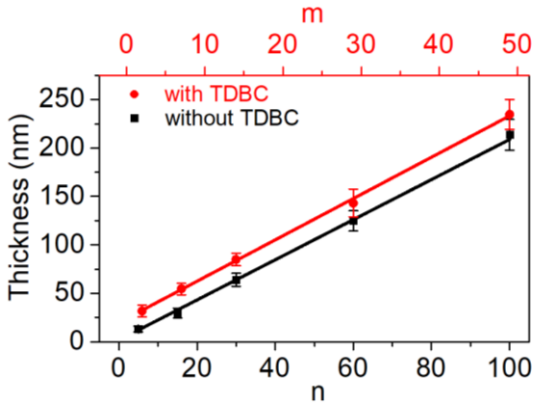

Figure 107. Thicknesses of PEM films containing one or no TDBC layer as a function of m and n, respectively.

As we had a good control on the thicknesses of PEM films with and without the TDBC layer, we prepared a series of samples of two AgNW layers oriented at 45° with a TDBC layer in the center varying the interlayer spacing between the two layers of AgNWs, and compared their chiroptical properties with the structures with identical interlayer spacing but without the TDBC layer. For a given interlayer spacing d (d = 30, 60, 100, 150 and 200nm), we used the corresponding m (m = 2, 8, 18, 30 and 42) and n (n = 15, 28, 48, 72 and 96) derived from ***Figure 107*** for two-layer superstructures with and without TDBC respectively.

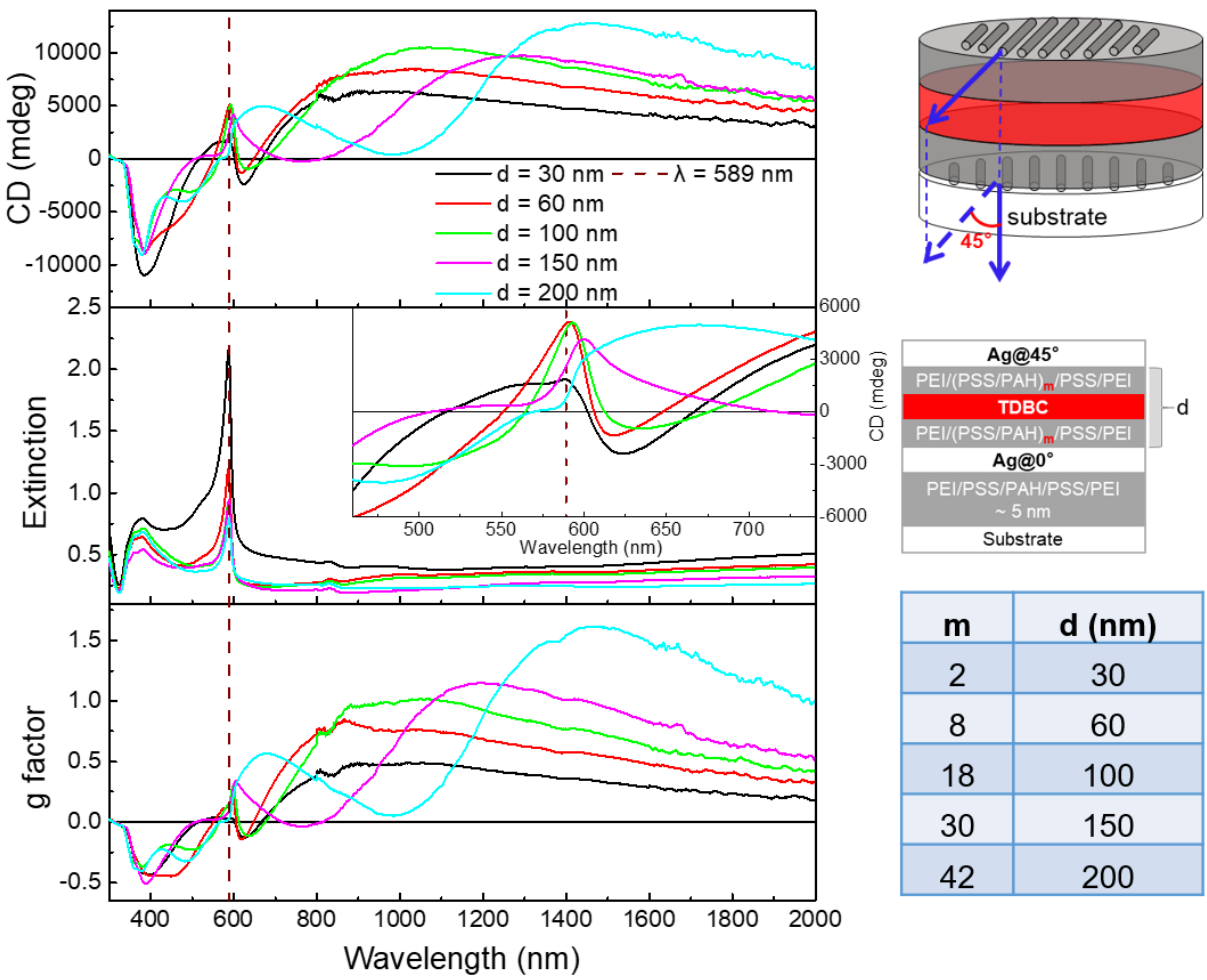

m	d (nm)
2	30
8	60
18	100
30	150
42	200

Figure 108. Left panel: CD, extinction and g-factor spectra of samples composed of two layers of AgNWs with the interlayer spacing varied from 30 nm to 200 nm, containing a layer of TDBC in the center and keeping the angle α fixed at 45°, the inset is a zoom in CD spectra. Right panel: schematics of the structure.

The CD and extinction spectra of the samples with TDBC are given in ***Figure 108*** and those of the samples without TDBC were presented in **Figure 75**, and they are compared for each interlayer spacing in ***Figure 109*** together with ΔCD, the difference in CD for samples with an identical spacing between the AgNW layers with and without TDBC.

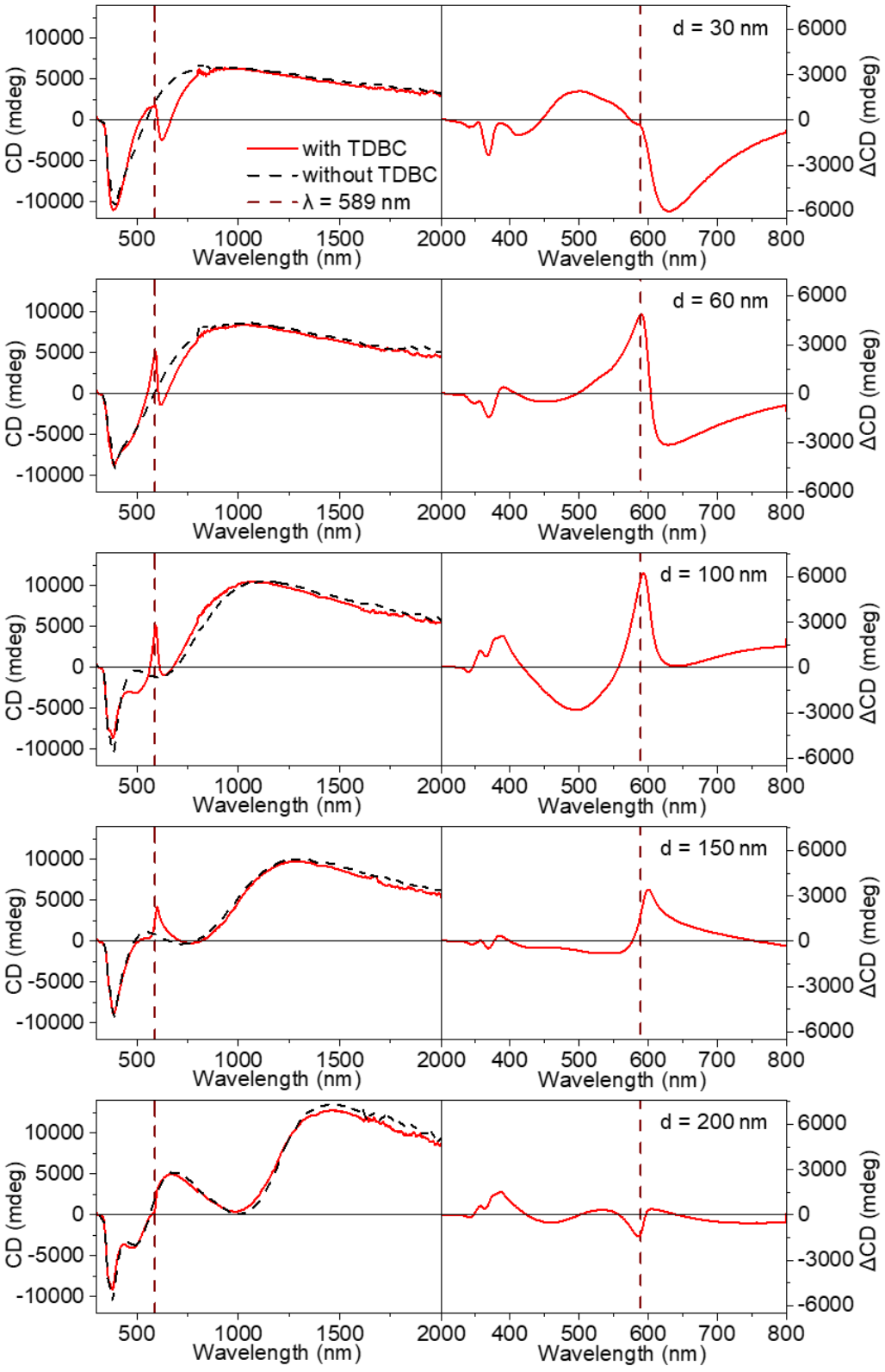

Figure 109. Left column: comparison of CD spectra of samples with and without TDBC, with identical interlayer spacing from d = 30 nm (corresponding to m = 2 for structure with TDBC and n = 15 for structures without TDBC), 60 nm (m = 8, n = 28), 100 nm (m = 18, n = 48), 150 nm (m = 30, n = 72) and 200 nm (m = 42, n = 96). Right column: spectra of ΔCD, the difference in CD for samples with an identical spacing between the AgNW layers with and without TDBC.

We observed an excellent reproducibility (***Figure 109***) of the CD spectra for samples of identical interlayer spacing with and without the TDBC layer, which confirms the good control on the spacing presented previously, knowing that the CD spectra are extremely sensitive to the interlayer spacing and that the samples need up to over 200 deposition steps for the n = 100 or m = 49 samples. The dependence of the CD spectra over the entire spectral range due to the variation of the interlayer spacing (similar to ***Figure 75***) is confirmed (***Figure 108***), besides the modification of the CD spectra at the maximum absorption wavelength of the TDBC J-aggregates. In addition, the surface plasmon enhanced absorption of TDBC is confirmed for the smaller interlayer spacing (d = 30 nm, i.e. 5 nm from the TDBC layer to each of the AgNWs layers).

We calculated ΔCD by subtracting the CD of corresponding structure without TDBC from that with TDBC (***Figure 109)***. The ΔCD can be considered as the CD modification due to the introduction of the TDBC layer. The ΔCD has a bisignate shape. The spacing between the layers of AgNWs has a strong influence on the change of CD due to TDBC, although it is not easy to identify a clear trend. In these left-handed structures, for small interlayer spacing (d = 30 nm and 60 nm), it seems that the ΔCD shows a negative Cotton effect, red-shifting with the increase of d. For d = 100 nm and 150 nm, the ΔCD displays a positive Cotton effect, red-shifting with the increase of d and intensity decreasing with d. For d = 200 nm, the ΔCD has "double Cotton effect" around 589 nm with decreased intensity: a positive Cotton effect on the right of λ = 589 nm and a negative one on the left of λ = 589 nm.

The Mueller Matrix of these samples were measured and simulated by Yann Battie from the University of Lorraine, from which we obtained the measured (***Figure 110***) and the simulated (***Figure 111***) LD, LB, CD and CB.

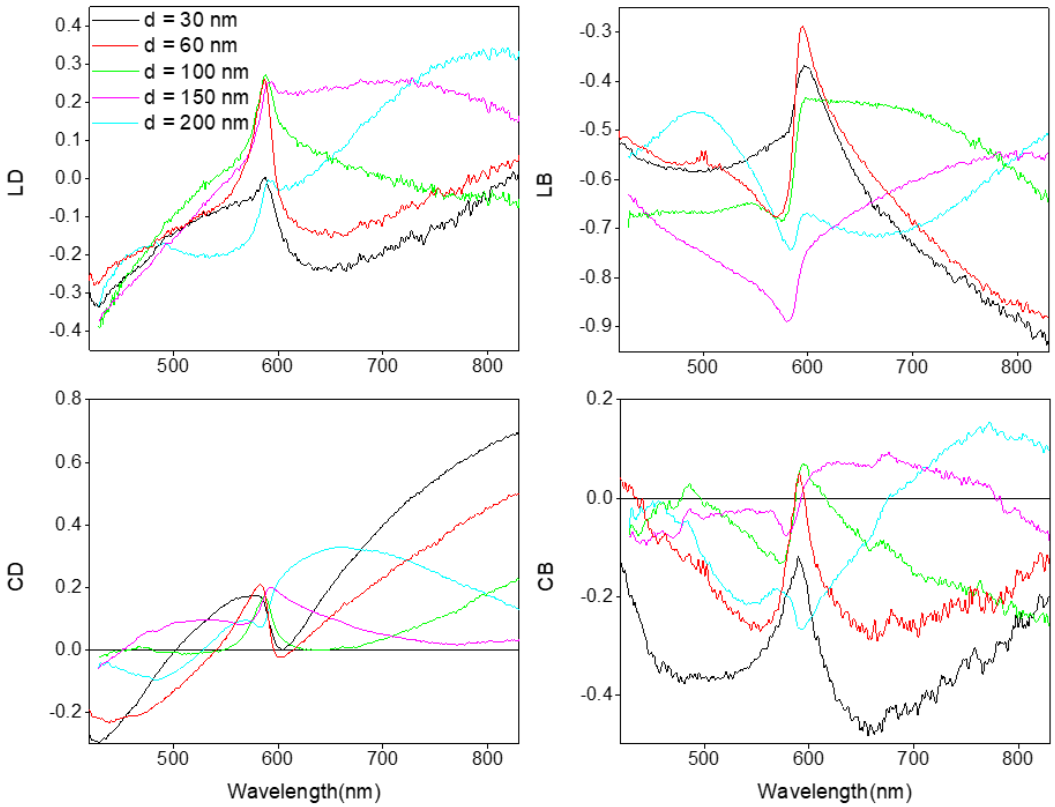

Figure 110. LD, LB, CD and CB measured by MMP for different interlayer spacing with a layer of TDBC in the middle.

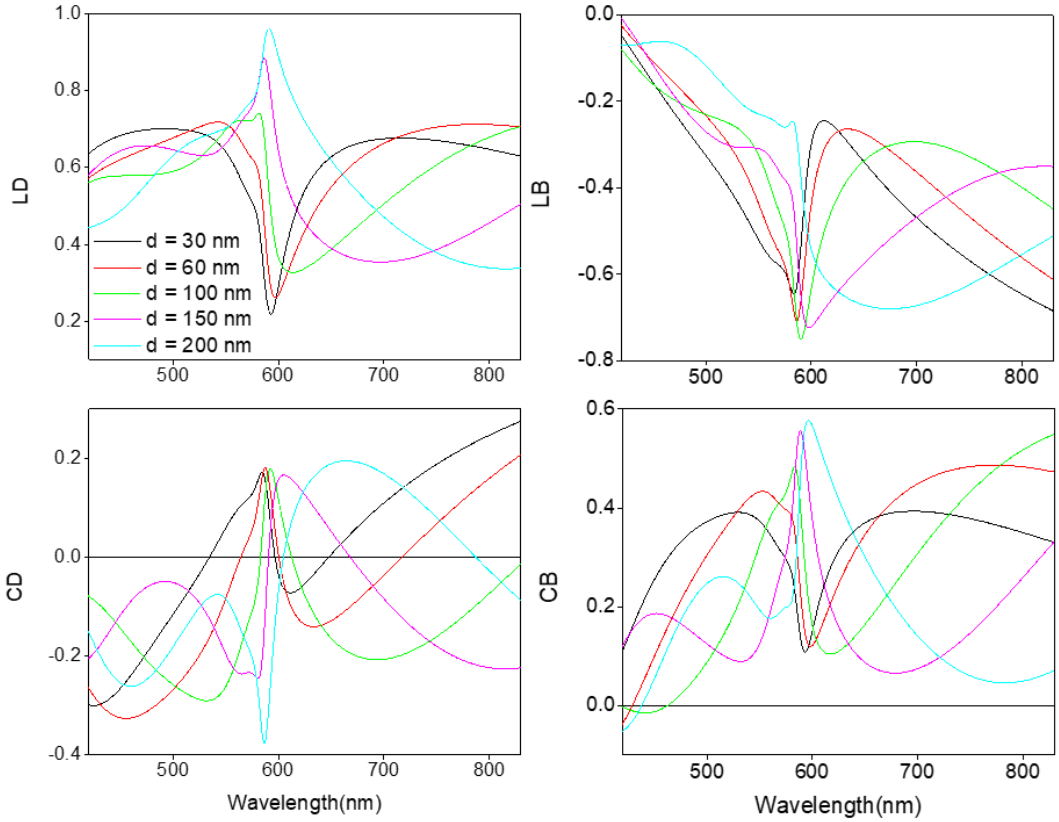

Figure 111. Simulated LD, LB, CD and CB for different interlayer spacing with a layer of TDBC in the middle.

We can see in the results by MMP and in the simulations that the linear polarization properties are modified as much as the circular polarization properties by introducing the TDBC layer in the chiral plasmonic superstructures. In addition, the modification of the LD and the LB is also highly dependent on the interlayer spacing. Important changes in CD and CB as function of the interlayer spacing are noticed. Similarly, we calculated the ΔCD between the CD of corresponding structures with and without TDBC, using results by MMP and by simulations (***Figure 112***). We found out that in both measurements by MMP and simulations, the transformation of ΔCD from a negative Cotton effect form a positive one is reproduced with the increase of interlayer spacing.

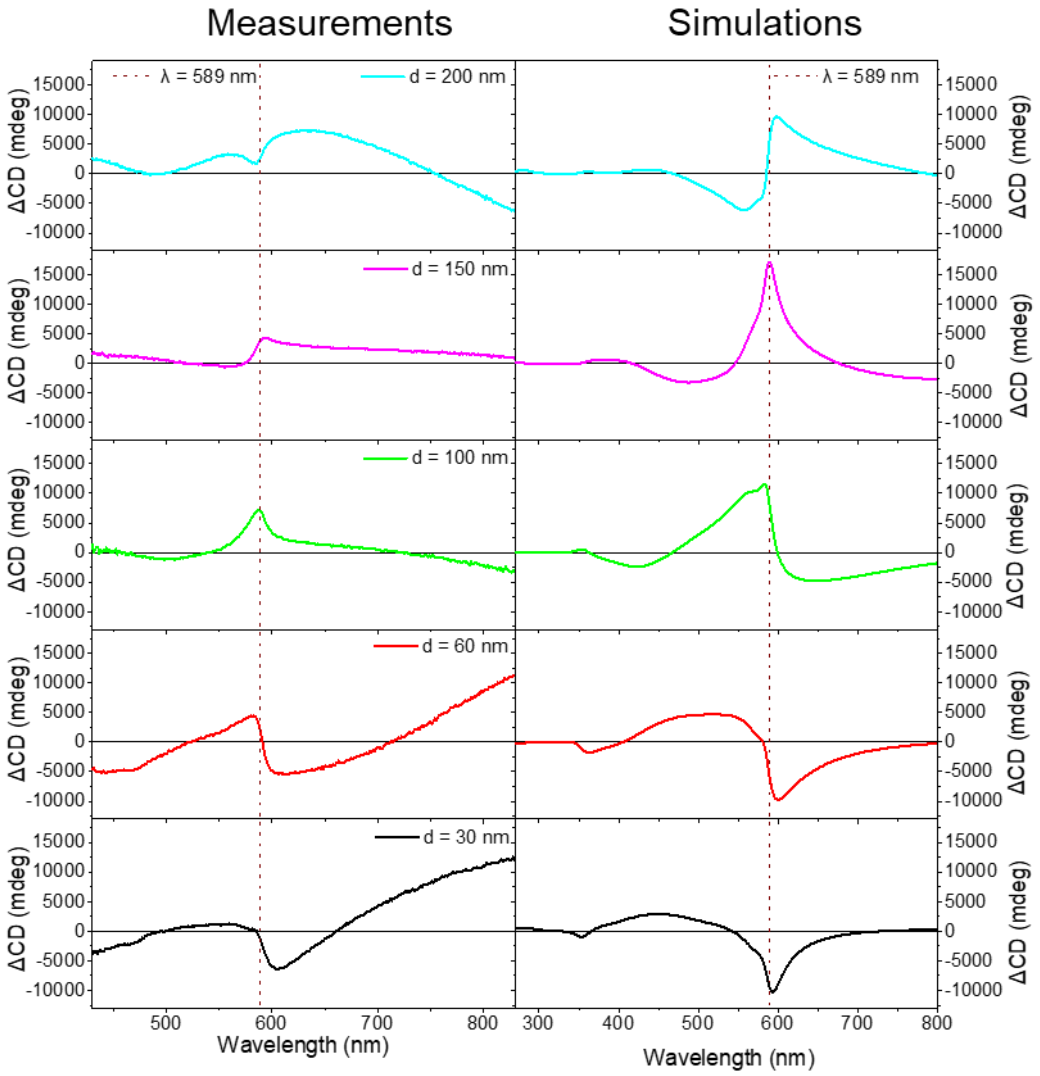

Figure 112. Spectra of ΔCD, the difference in CD for samples with an identical spacing between the AgNW layers with and without TDBC, for measured (left panel) and simulated (right panel) results.

The CD measured by MMP and Jasco are compared together with the simulations in ***Figure 113***.

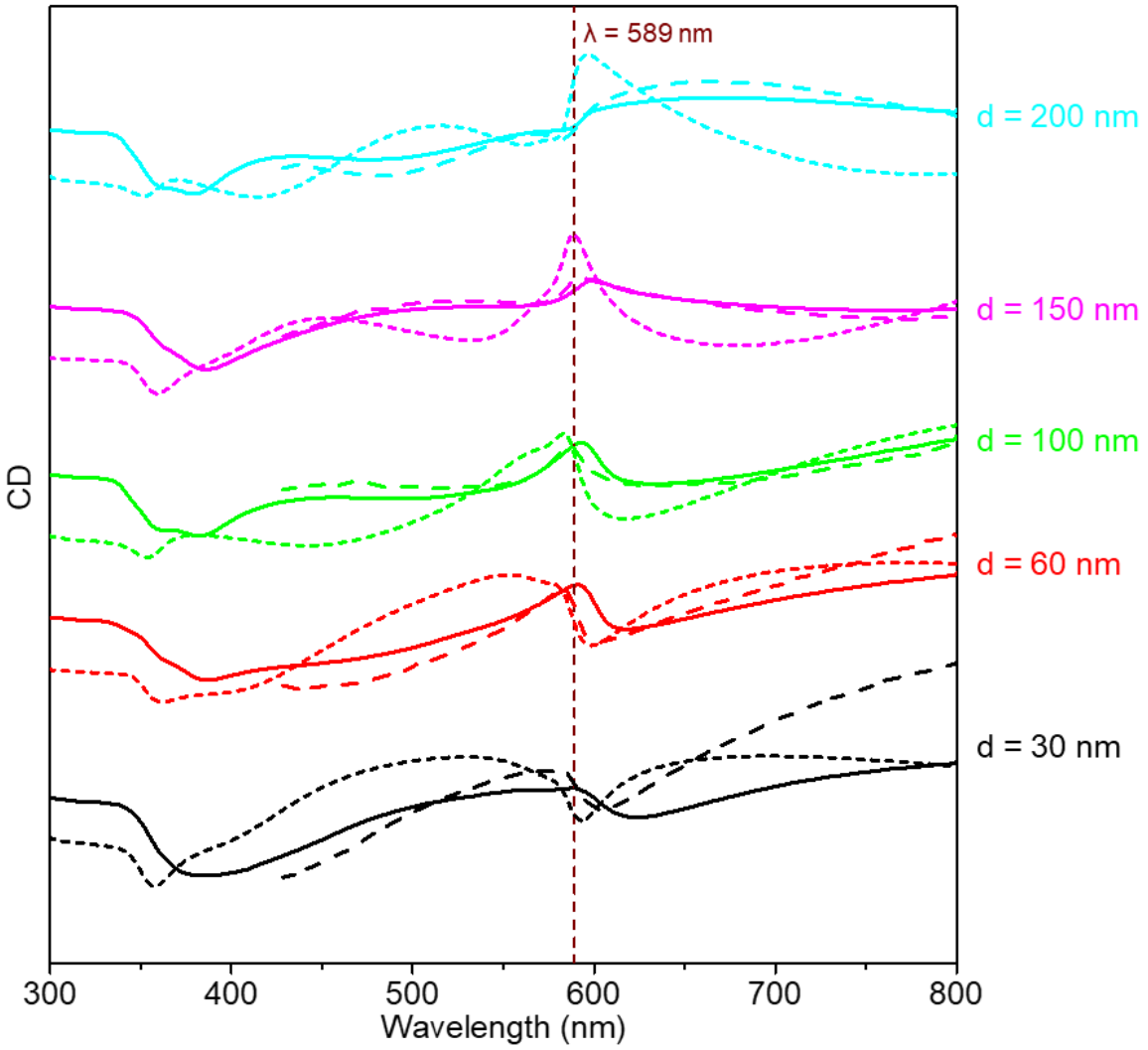

Figure 113. CD by Jasco CD spectroscopy (solid lines), MMP (dashed lines) and simulations (short dashed lines) for different interlayer spacing d with TDBC.

The agreement between CD determined by both measurement techniques is impressively good. The simulations are again less consistent, possible reasons were given in previous sections: the simple model is effective to reproduce the CD modification effect, but not capable to simulate the details of the modification as possible coupling are not considered.

IV.6. Influence of the position of the TDBC layer in the superstructure

Since the CD of the hybrid film is so much affected by the distance between the TDBC layer and the AgNWs, we aim to study the influence of the position of the TDBC layer between two layers of AgNWs at a fixed distance on the chiroptical properties. We made a series of samples, whose structure is described as PEI/PSS/PAH/PSS/PEI/Ag/PEI/(PSS/PAH)$_{\mathbf{m1}}$/PSS/PEI/TDBC/PEI/(PSS/PAH)$_{\mathbf{m2}}$/PSS/PEI/Ag (m_1 = 9, 19, 29, 39 and 49; TDBC layer is in the middle when m_1 = 29). By keeping the total number of polyelectrolyte and TDBC layers between the two layers of AgNWs constant, we maintain a constant interlayer spacing of d = 147 nm. Considering the semi-reflective property of the AgNWs, a standing wave and / or interferences of a specific wavelength related to the width of the "cavity" may arise. We chose here d = 147 nm and later d = 294 nm, because they are the $\lambda/4$ and $\lambda/2$ of the maximum absorption wavelength of TDBC J-aggregates (589 nm). Through the variation of m, we are able to modify the position of the TDBC layer with respect to the two layers of AgNWs, which is considered to have confined electromagnetic field of different strength.

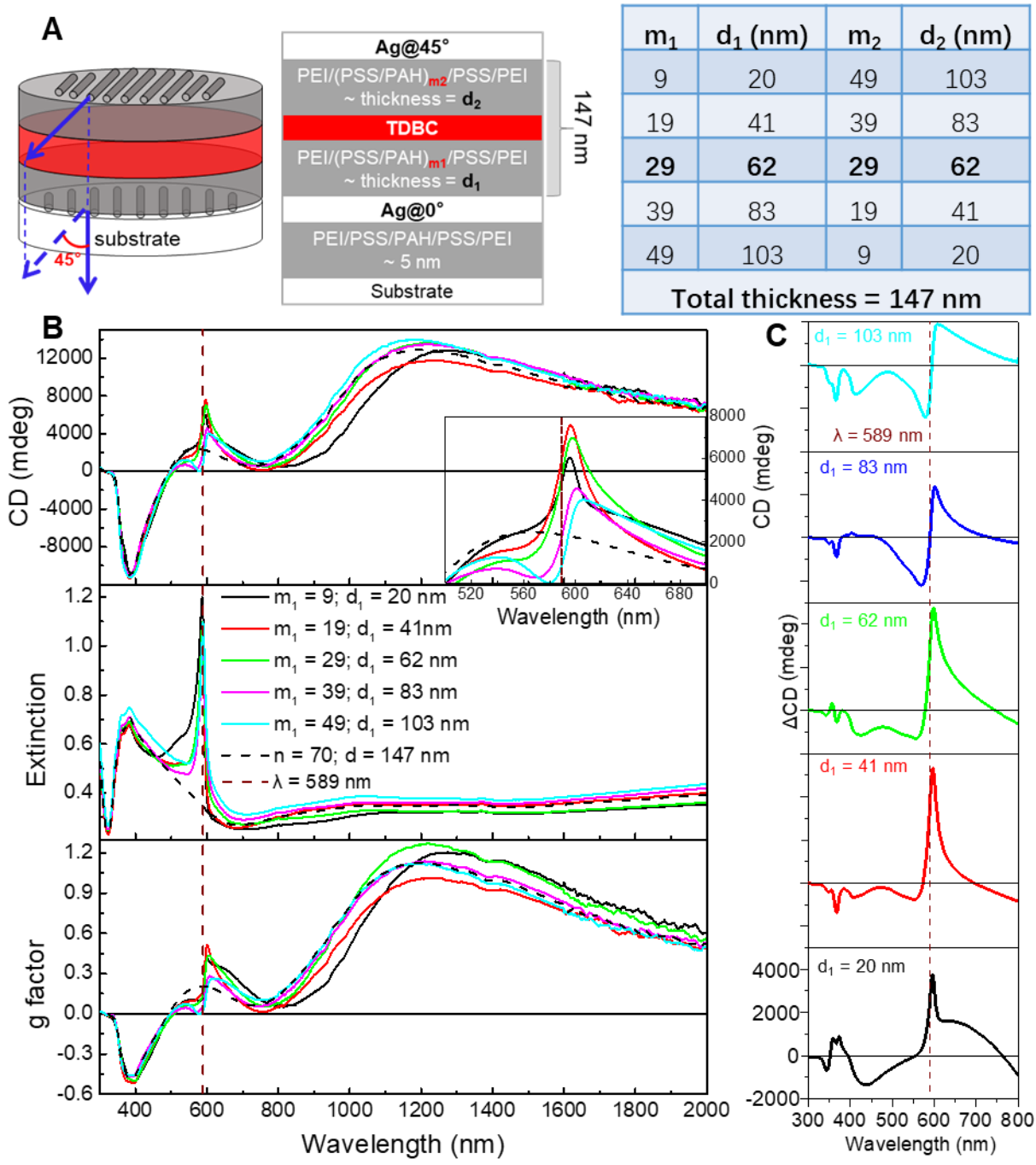

m_1	d_1 (nm)	m_2	d_2 (nm)
9	20	49	103
19	41	39	83
29	**62**	**29**	**62**
39	83	19	41
49	103	9	20
Total thickness = 147 nm			

Figure 114. (A) Sketch of the structures. The total distance between the two layers of AgNWs is fixed at 147 nm. The position of the TDBC layer is varied by changing d_1 (distance from the TDBC layer to the lower layer of AgNWs) and d_2 (distance from the TDBC layer to the top layer of AgNWs). When the TDBC layer is in the middle of the structure, $d_1 = d_2 = 62$ nm. (B) CD, extinction and g-factor spectra of the superstructures for different TDBC layer position (d_1). (C) Δ CD for different TDBC position (d_1), the scale for all the spectra is the same.

CD and extinction spectra were measured as well as g-factors calculated for each sample. The overall shape of the CD spectrum is not much changed and is comparable to a structure with the same interlayer spacing but without the TDBC layer, while the CD spectrum around the

absorption wavelength of TDBC J-aggregates were shown to depend strongly on the position of TDBC. ΔCD is calculated by subtracting the CD of the structure without TDBC (interlayer spacing is also 147 nm) from the CD of the structures with TDBC for different TDBC position (d_1) (***Figure 114***C). The ΔCD for all d_1 has a positive Cotton effect with slightly shifted peak positions and slightly varied intensities. This observation matches the conclusion of the previous section: a negative Cotton effect in ΔCD is only observed for small AgNW-TDBC distance (< 20 nm), while a positive Cotton effect is observed for larger AgNW-TDBC distances.

The Mueller Matrix of these samples were measured and simulated by Yann Battie from the University of Lorraine, from which we obtained the measured (***Figure 115***) and the simulated (***Figure 116***) LD, LB, CD and CB.

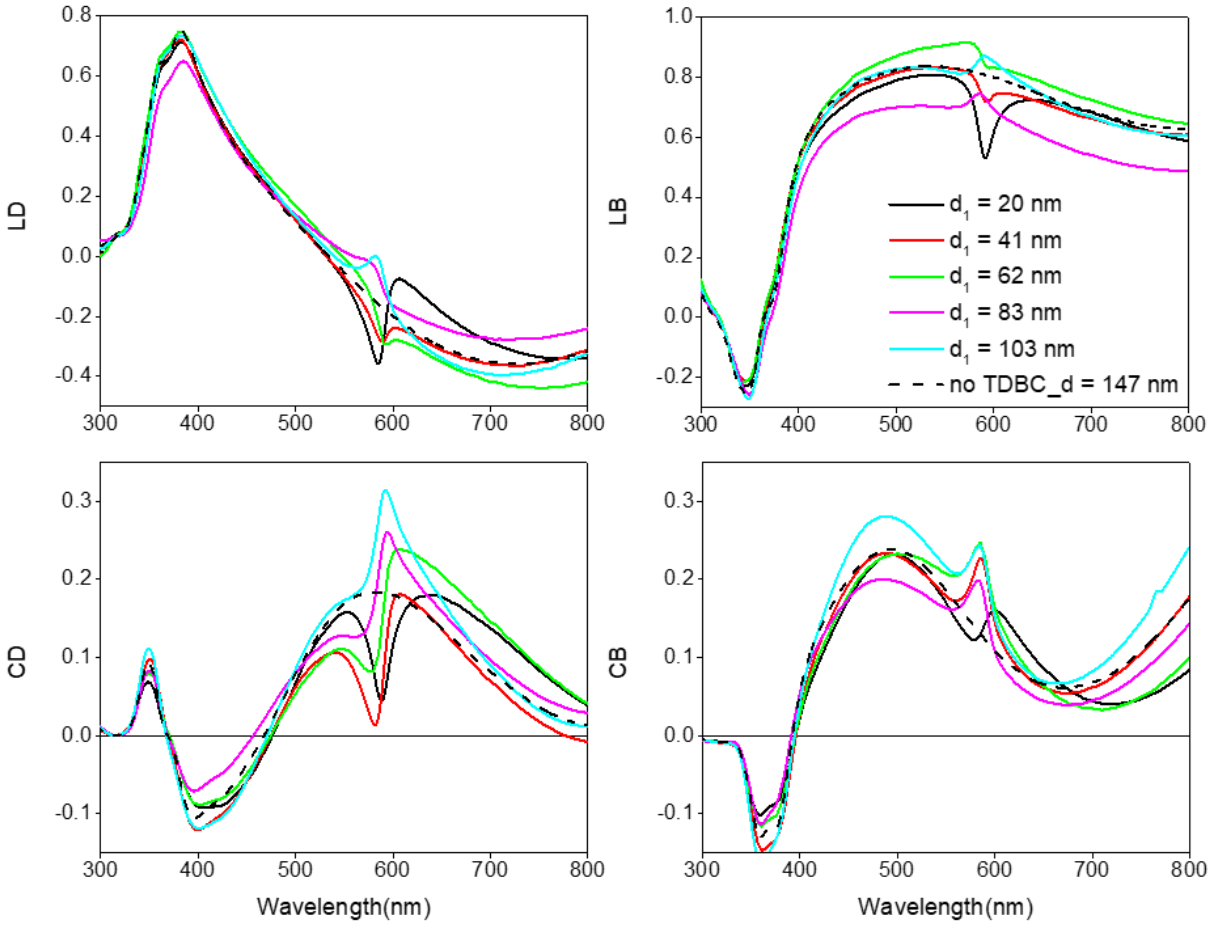

Figure 115. LD, LB, CD and CB measured by MMP for two layers of AgNWs with a fixed interlayer spacing (147 nm) containing a layer of TDBC between them while the position of the TDBC layer (d_1) varies.

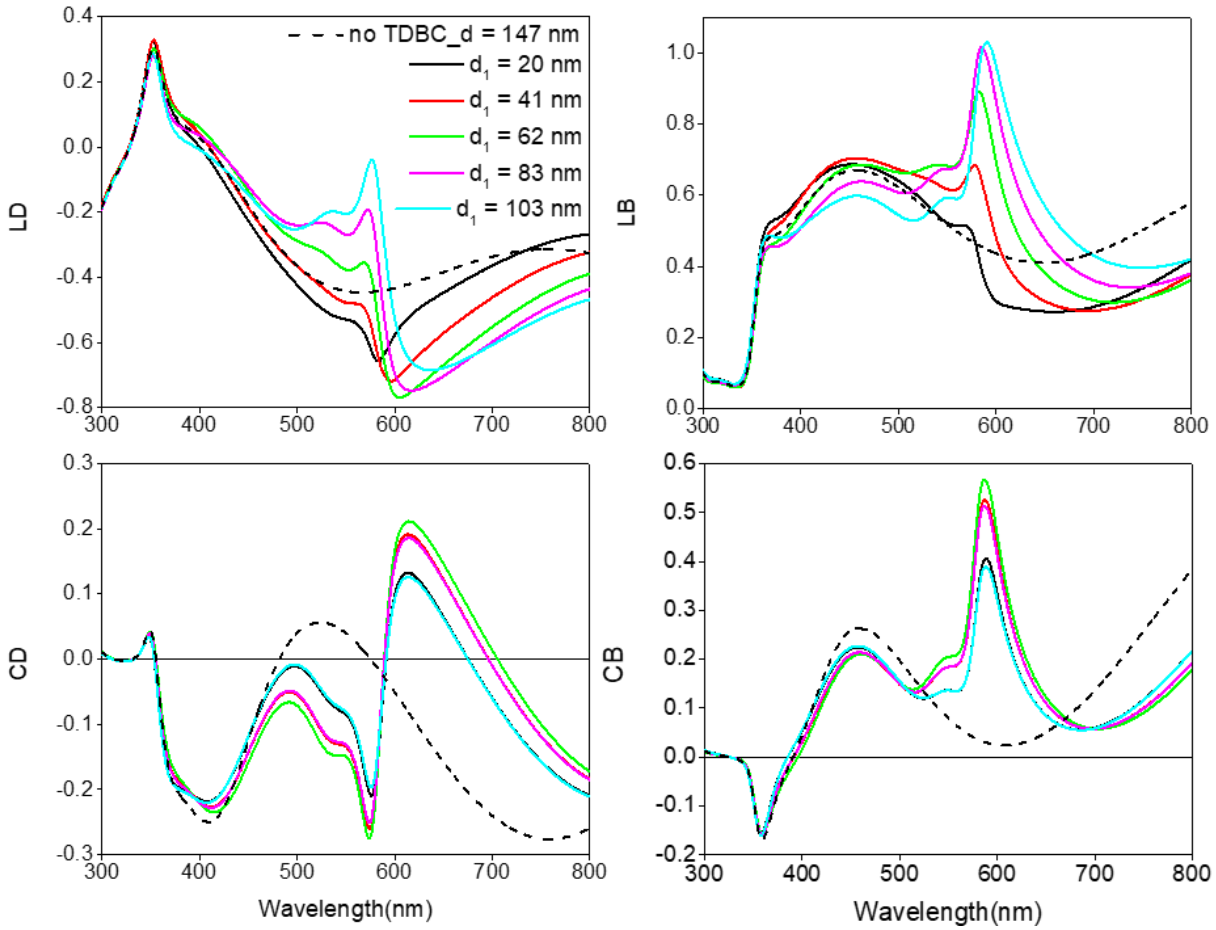

Figure 116. Simulated LD, LB, CD and CB for two layers of AgNWs with a fixed interlayer spacing (147 nm) containing a layer of TDBC between them while the position of the TDBC layer (d_1) varies.

We observed that in both measurements and simulations, all the LD, LB, CD and CB terms depend on the position of the TDBC. In the simulations, ideal structures were considered, thus the CD and CB with symmetric d_1 are identical (i.e. same results are obtained for $d_1 = x$ and $d_1 = 147 - x$). This is not the case for the measurements, because 1. the structures are imperfect; 2. the measurements were carried out with one azimuth angle, which may have an influence on the results. However, the simulated CD and CB show only small variations depending on the position of TDBC, while the measured CD and CB are much more sensitive to this parameter.

The results by MMP and simulations are compared with the measurements made on the Jasco CD spectrometer in ***Figure 117***. The agreement between the two measurements are as good as for the other ones. The simulations are not fully consistent with the measurements, especially for the smaller spacings wbhere the effect of near-field coupling may be the highest.

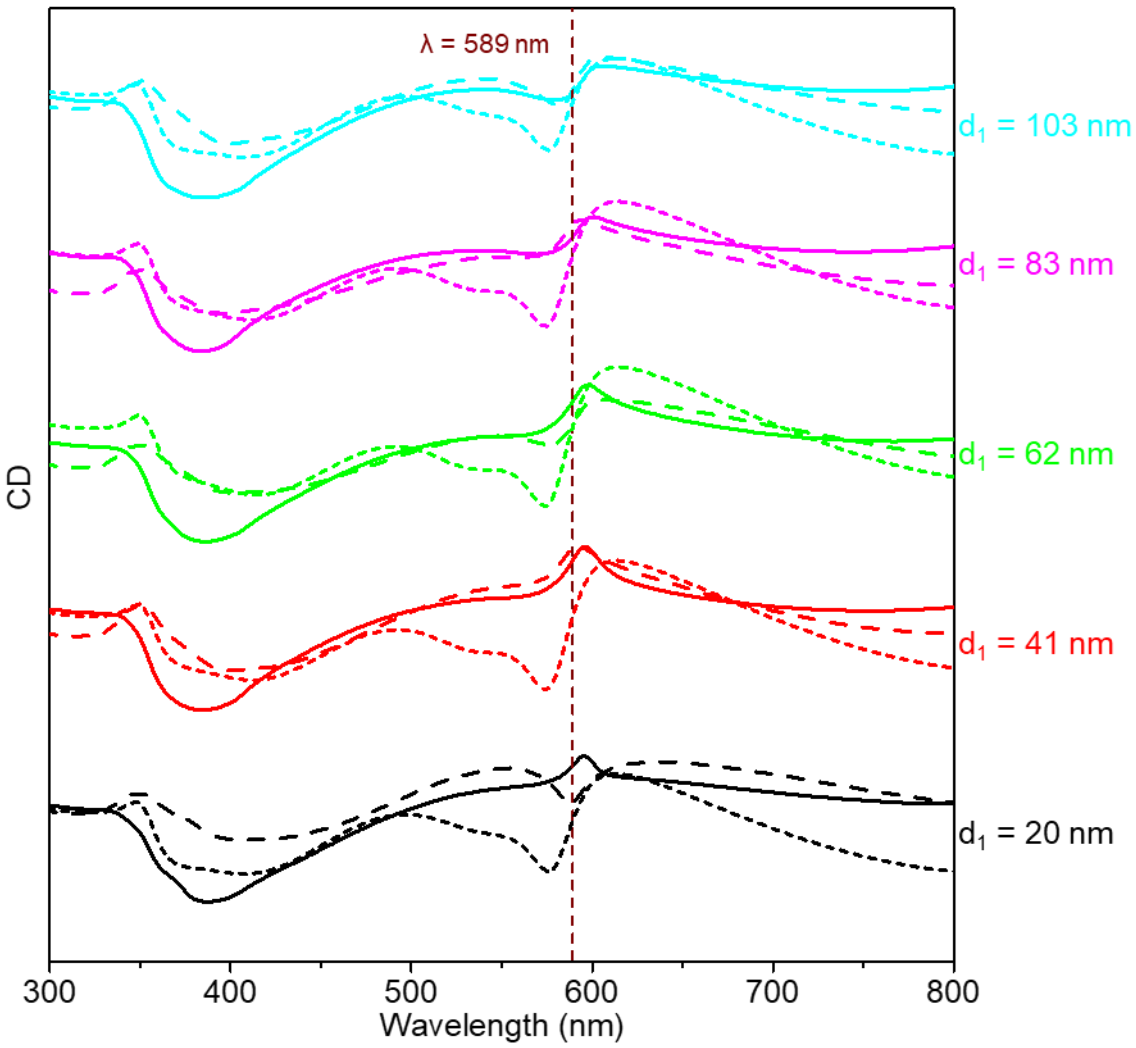

Figure 117. CD by Jasco CD spectroscopy (solid lines), MMP (dashed lines) and simulations (short dashed lines) for different TDBC position (d_1).

We prepared another series of samples similar to the one presented above, while the total interlayer spacing was increased to 294 nm, which is λ/2 of the maximum absorption wavelength of TDBC J-aggregates (589 nm).

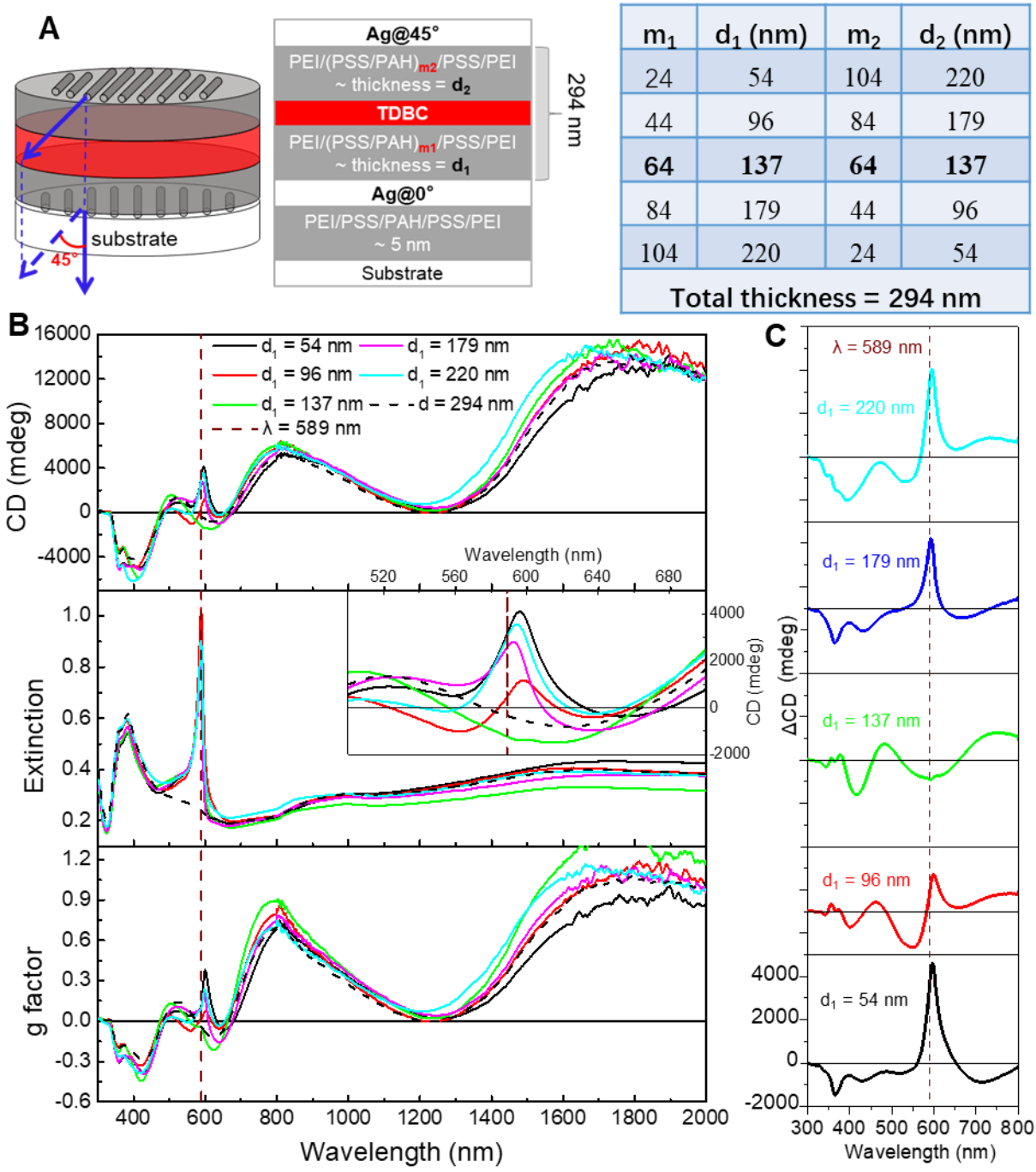

m_1	d_1 (nm)	m_2	d_2 (nm)
24	54	104	220
44	96	84	179
64	**137**	**64**	**137**
84	179	44	96
104	220	24	54
Total thickness = 294 nm			

Figure 118. (A) Sketch of the structures. The total distance between the two layers of AgNWs is fixed at 294 nm. The position of the TDBC layer is varied by changing d_1 (distance from the TDBC layer to the lower layer of AgNWs) and d_2 (distance from the TDBC layer to the top layer of AgNWs). When the TDBC layer is in the middle of the structure, $d_1 = d_2 = 137$ nm. (B) CD, extinction and g-factor spectra of the superstructures for different TDBC layer position (d_1). (C) ΔCD for different TDBC position (d_1), the scale for all the curves is the same.

CD and extinction spectra are similar to the previous series of sample with more oscillations in CD as the interlayer spacing is doubled. The reproducibility of the samples is preserved, which allows to calculate the CD modification due to the TDBC layer (ΔCD). Similar to the previous

series of samples, the ΔCD shows a positive Cotton effect, with however one exception: when the TDBC layer is placed in the middle between the two layers of AgNWs (d_1 = 137 nm), the change in CD is much lower. This confirms our observation in section IV.5 (sample with a very large interlayer spacing).

The Mueller Matrix of these samples were measured and simulated by Yann Battie from the University of Lorraine, from which we obtained the measured (***Figure 119***) and the simulated (***Figure 120***) LD, LB, CD and CB.

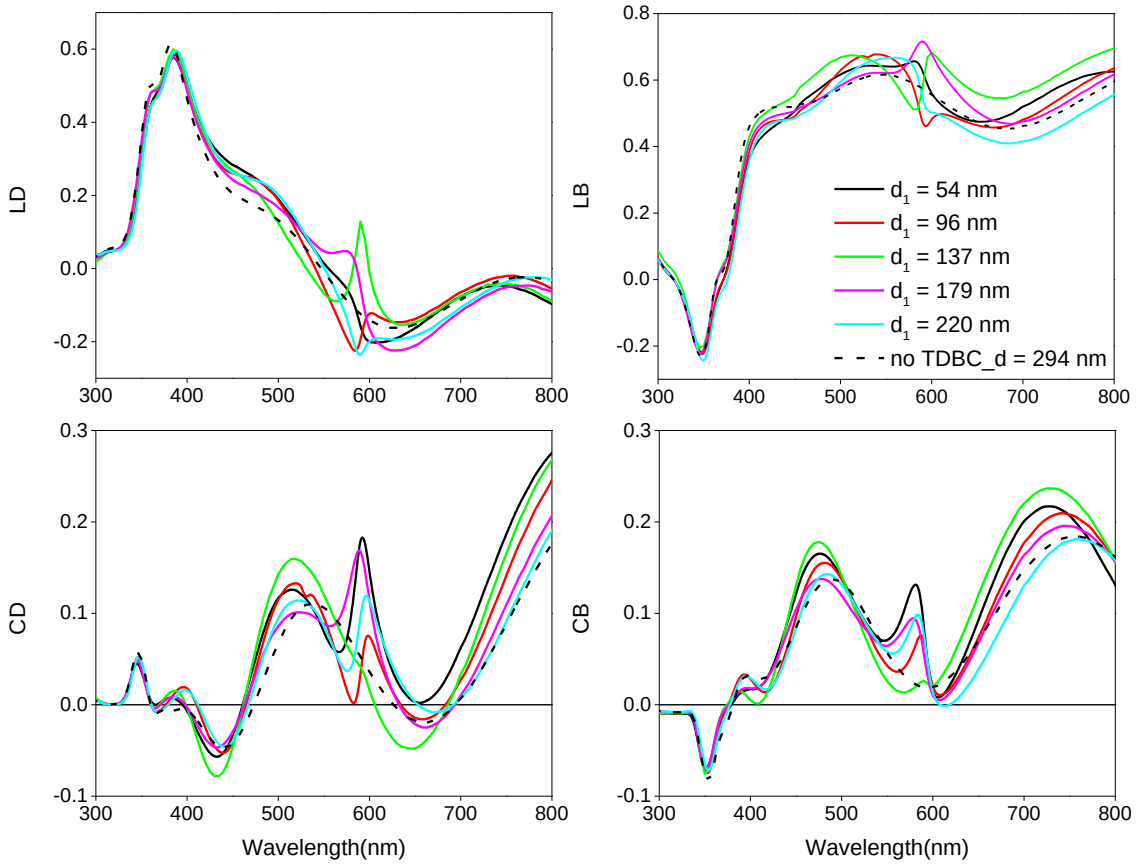

Figure 119. LD, LB, CD and CB measured by MMP for two layers of AgNWs with a fixed interlayer spacing (294 nm) containing a layer of TDBC between them while the position of the TDBC layer (d_1) varies.

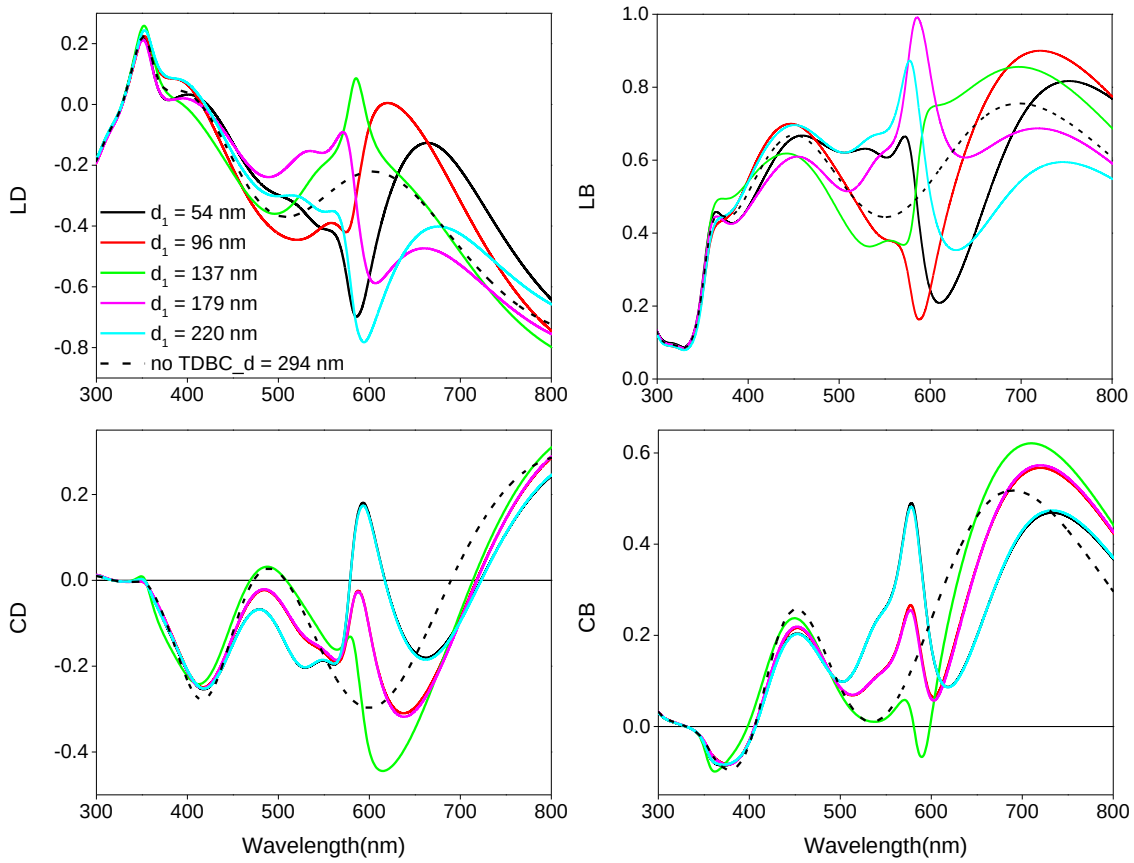

Figure 120. Simulated LD, LB, CD and CB for two layers of AgNWs with a fixed interlayer spacing (294 nm) containing a layer of TDBC between them while the position of the TDBC layer (d_1) varies.

Similar conclusions can be obtained here as previous series of samples. All the LD, LB, CD and CB are modified by the TDBC layer and the modification effect of all the four elements is highly dependent on the TDBC position. Identical CD and CB with symmetric d_1 were obtained in the simulations but not in the measurements for reasons discussion in previous series of samples. The change in LD and LB is much less pronounced in the measured spectra than in the simulated spectra.

The results by MMP and simulations are compared with the measurements made by Jasco in ***Figure 121***. Although the main trends are consistent, significant differences are observed for this series of samples, which may be due to differences in the sample themselves for the different sets of measurements. The general shape of the CD spectra are reasonably well reproduced by the simulations however: a positive peak is observed on the CD close to the

adsorption wavelength of TDBC, and this peak is more intense when the distance between TDBC and the AgNW layers is smaller.

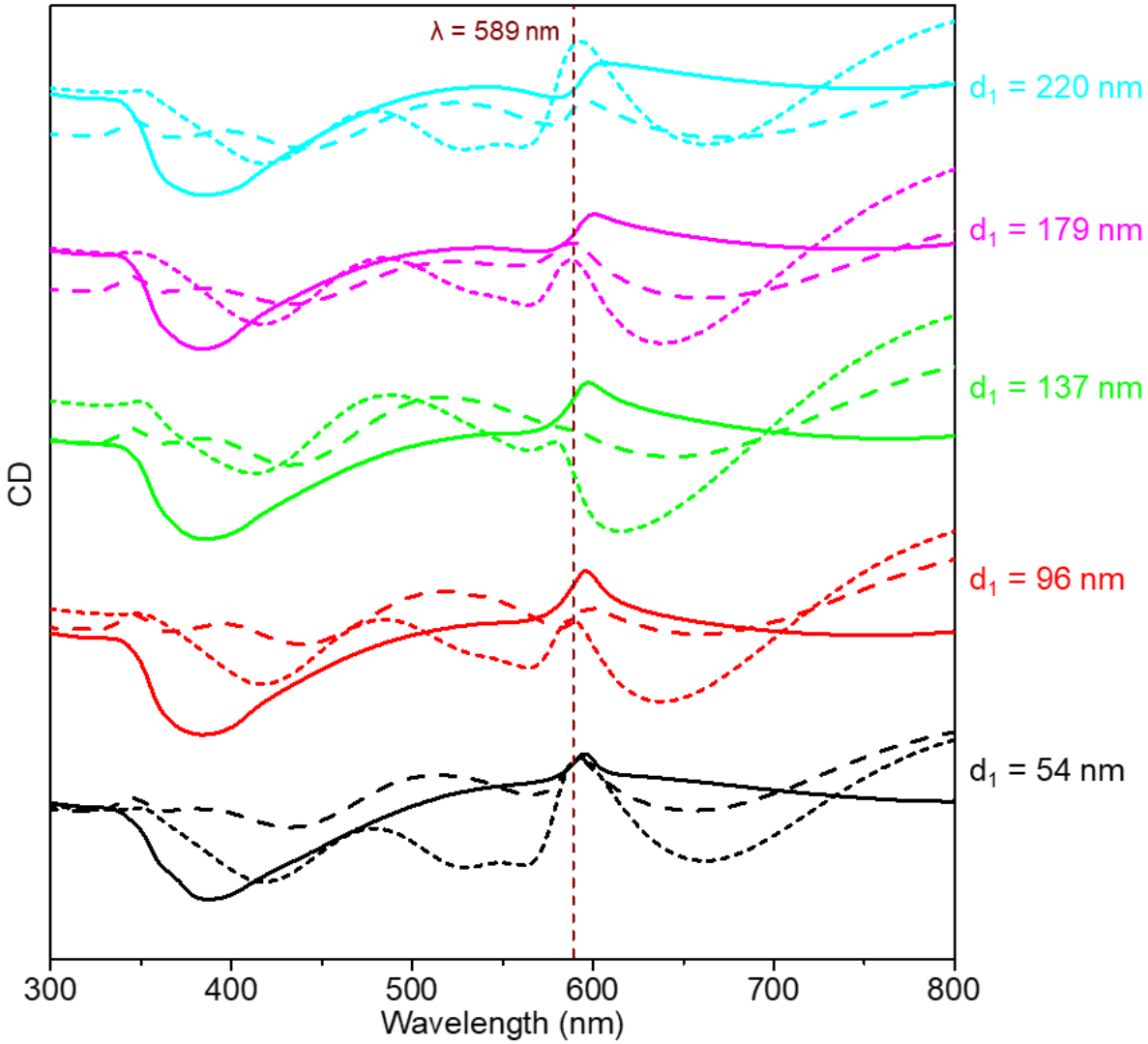

Figure 121. CD by Jasco CD spectroscopy (solid lines), MMP (dashed lines) and simulations (short dashed lines) for different TDBC position (d_1).

The interlayer spacings (147 nm and 294 nm) in the two series of samples above are relatively large, and accordingly all d_1 were relatively large (> 20nm). Therefore, we had only positive Cotton effect for ΔCD, as we demonstrated in section IV.5 that negative Cotton effect only exists for very close distance between TDBC layer and AgNWs. However, the double Cotton effect was reproduced for d_1 = 137 nm (total spacing = 294 nm), that is when the TDBC layer is very far from both the AgNWs layers. This confirms our conclusion in IV.5.

These samples turn out to give optical properties that are complicated to analyze and from which it is hard to obtain solid conclusions. Neither the agreement of the measurements and the simulations were good enough to establish a clear trend and general rules. This is because when changing the TDBC position between two layers of AgNWs, we change the distances of the TDBC layer from both layers of AgNWs. The dependence of the plasmon-exciton coupling strength on d_1 is thus hard to predict. In addition, not only near-field coupling may have an influence but the two AgNW layers may also form a cavity (even of low quality) in which the properties are modified. The observed properties are thus the result of the combination of several phenomena which are hard to disentangle.

For the above reasons, another series of samples with a varying distance between the TDBC layer and the AgNW superstructure were prepared, by depositing the TDBC layer on top of the two layers of AgNWs. We prepared a series of samples containing two layers of AgNWs, with fixed angle $\alpha = 45°$ and fixed interlayer spacing $d = 13$ nm between the AgNW layers, on top of which a PEM film $(PEI/(PSS/PAH)_n/PSS/PEI)$ of varying thickness ($5 \text{ nm} \leq d \leq 100 \text{ nm}$ for $1 \leq n \leq 44$) was deposited on each sample followed by a layer of TDBC deposited by dipping. This protocol allows a more convenient comparison of the CD between samples for following reasons: 1. all the chiral two-layer-AgNW structures are identical ($\alpha = 45°$, $d = 13$ nm) and no variation of interlayer spacing between the two layers of AgNWs is involved here, thus the chiral environment surrounding the AgNWs is similar in all samples; 2. The only variable in this series of samples is the distance between the TDBC layer and the upper layer of AgNWs, which is controlled by the thickness of the PEM film between them; 3. by measuring the CD before and after the deposition of the TDBC layer, it is possible to obtain ΔCD arising from the TDBC layer.

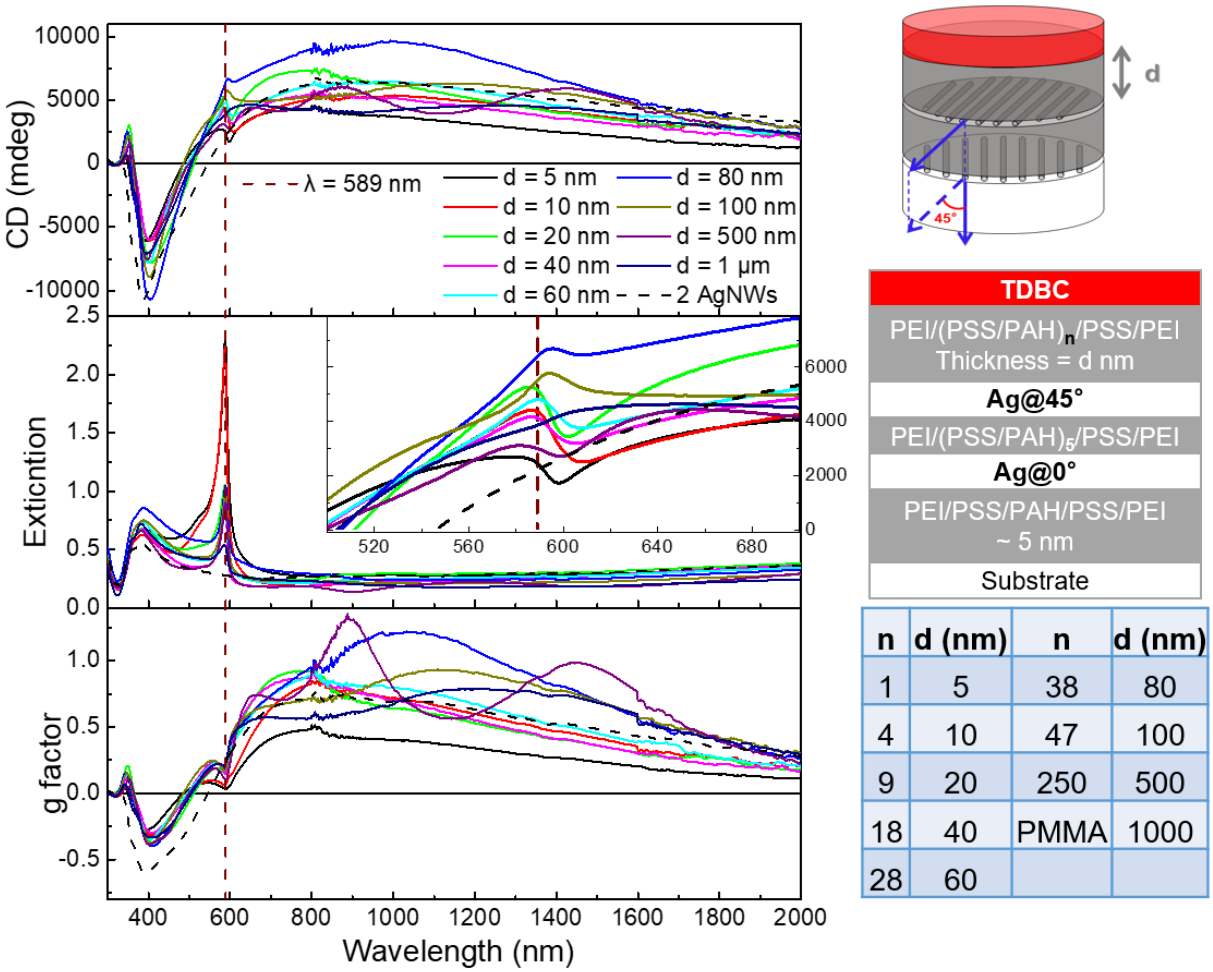

n	d (nm)	n	d (nm)
1	5	38	80
4	10	47	100
9	20	250	500
18	40	PMMA	1000
28	60		

Figure 122. CD, extinction and g-factor spectra of samples composed of a layer of TDBC deposited on two layers of AgNWs separated by a PEM film of different thickness. The interlayer spacing between the two layers of AgNWs is fixed at 13 nm.

Three CD measurements were carried out for each sample: 1. after the deposition of the upper layer of AgNWs and before the deposition of the PEM film separating TDBC and the AgNWs (noted as "2 AgNWs" in ***Figure 123***); 2. after the deposition of the PEM film and before the deposition of the TDBC layer (noted as "2 AgNWs + PEM" in ***Figure 123***); 3. after the deposition of the TDBC layer (noted as "2 AgNWs + PEM + TDBC" in ***Figure 123***). Δ CD in ***Figure 123*** was calculated by subtracting the CD of "2 AgNWs + PEM" from that of "2 AgNWs + PEM + TDBC", and is considered as the modification of CD induced by the TDBC layer (***Figure 123***).

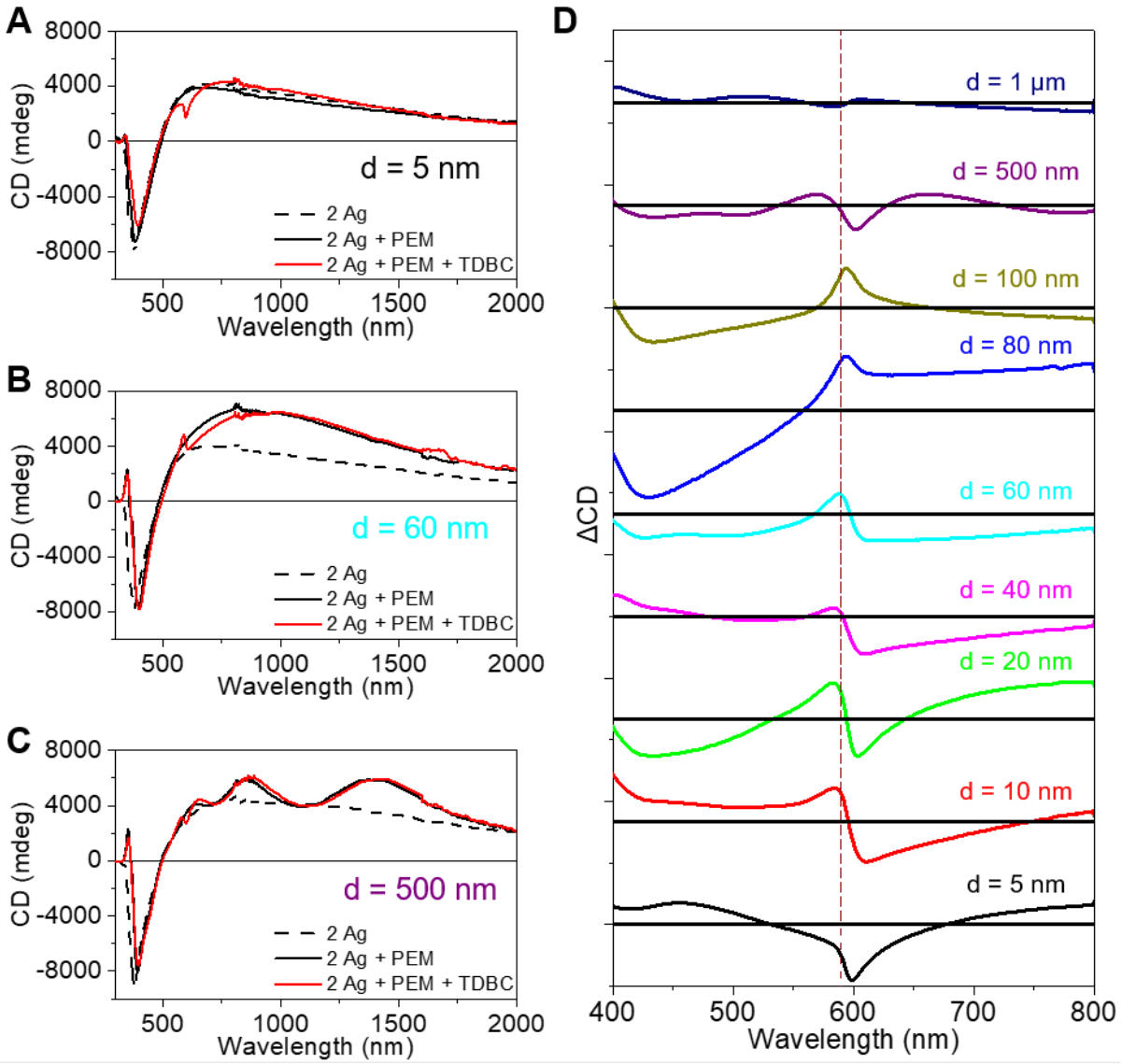

Figure 123. Three measurements of CD for d = 5 nm (A), 60 nm (B) and 500 nm (C), and ΔCD for different d from 5 nm to 1 µm.

For small distance (5 nm $\leqslant$ d $\leqslant$ 60 nm), a negative Cotton effect in ΔCD is observed around maximum absorption wavelength of TDBC (589 nm). The peak is red-shifted with d and the intensity decreases with d. For intermediate distance (d = 80 nm and 100 nm), the ΔCD has a positive Cotton effect, and for large distance (d = 500 nm and 1 µm), double Cotton effect is observed on both side on λ_{abs} of TDBC (589 nm), while for d = 1 µm, the ΔCD is very low. These observations are consistent with those made in section IV.5 and in the previous part of this section.

IV.7. Hybrid chiral superstructures with other materials

In order to know if the chiral plasmonic superstructures can modify the chiroptical properties of materials other than TDBC, we introduced several other materials in the chiral plasmonic superstructures, including other organic dyes and AuNPs.

We first substituted TDBC with three other cyanine dyes labeled S2275, S2165 and S2284 (as from their commercial name) whose structure is given in ***Figure 124***. The structure prepared are composed of two layers of AgNWs oriented at 45° with a layer of S2275, S2165 or S2284 dye between them: PEI/PSS/PAH/PSS/PEI/Ag/PEI/PSS/PAH/PSS/PEI/dye/PEI/PSS/PAH/PSS/PEI/Ag (dye = S2275, S2165 or S2284). The fabrication process is the same as that of samples containing a layer of TDBC.

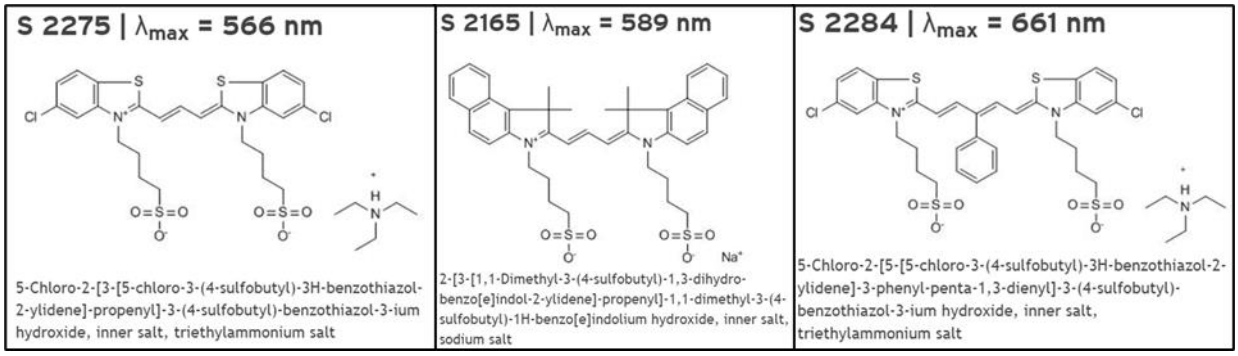

Figure 124. Chemical structures and absorption wavelength of S2275, S2165 and S2284.[260]

CD and extinction spectra were measured and g-factors were calculated for the three samples.

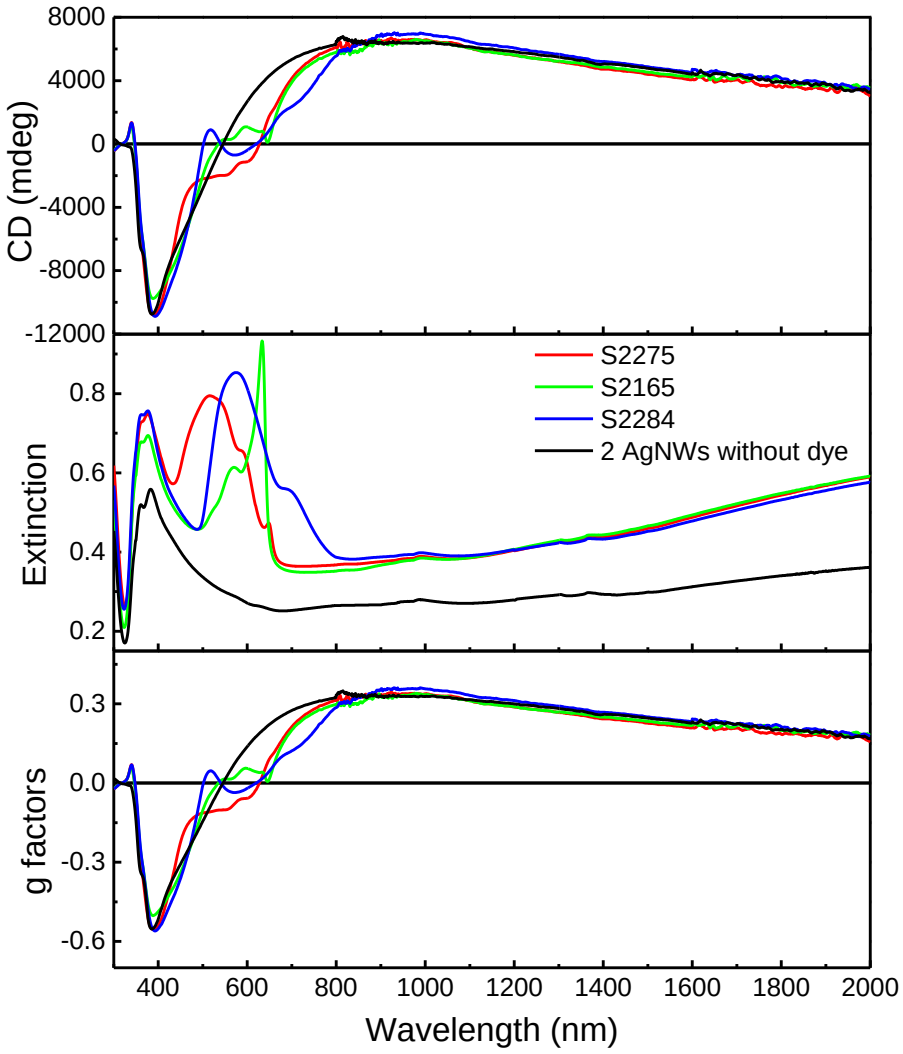

Figure 125. CD, exticniton spectra and g-factors of the two-layer chiral superstructures with a layer of S2275, S2165 or S2284.

We observed also the modification of CD for all the three dyes around their maximum absorption wavelength. However, unlike the narrow peak of J-aggregates of TDBC, these dyes have rather broad absorption peaks thus the modification in CD is also not very well defined.

Copper phthalocyanine-3,4′,4″,4‴ tetra-sulfonated acid tetrasodium salt (TS-CuPc) is another chromophore which interested us. It is a widely used chromophore in studies of organic photovoltaic devices and serving as electron transporting layer in organic solar cells. The TS-CuPc is negatively charged and thus can be LbL-

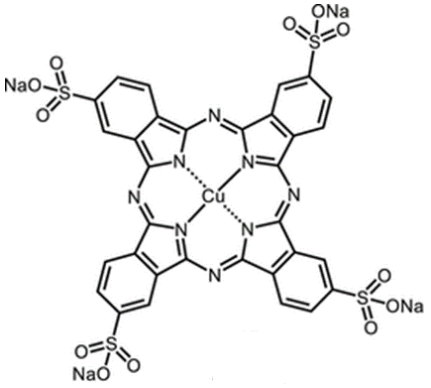

Figure 126. Chemical structure of TS-CuPc.

assembled in a PEM film but its lack of J-aggregate formation makes the electrostatic adsorption less efficient than with TDBC. In fact, the extinction intensity after the deposition of one layer of TS-CuPc is too weak to be observed and cannot induce significant modification in CD. This lead us to insert multiple layers of TS-CuPc in the PEM film instead of a single one. We prepared therefore a sample with 20 layers of TS-CuPc between two layers of AgNWs (PEI/PSS/PAH/PSS/PEI/Ag/(PEI/PSS/PAH/PSS/PEI/TSCuPc)$_{20}$/PEI/PSS/PAH/PSS/PEI/Ag). The angle between the orientation of the two layers of AgNWs is 45°. CD and extinction spectra of the sample were measured and the g-factor spectra was calculated.

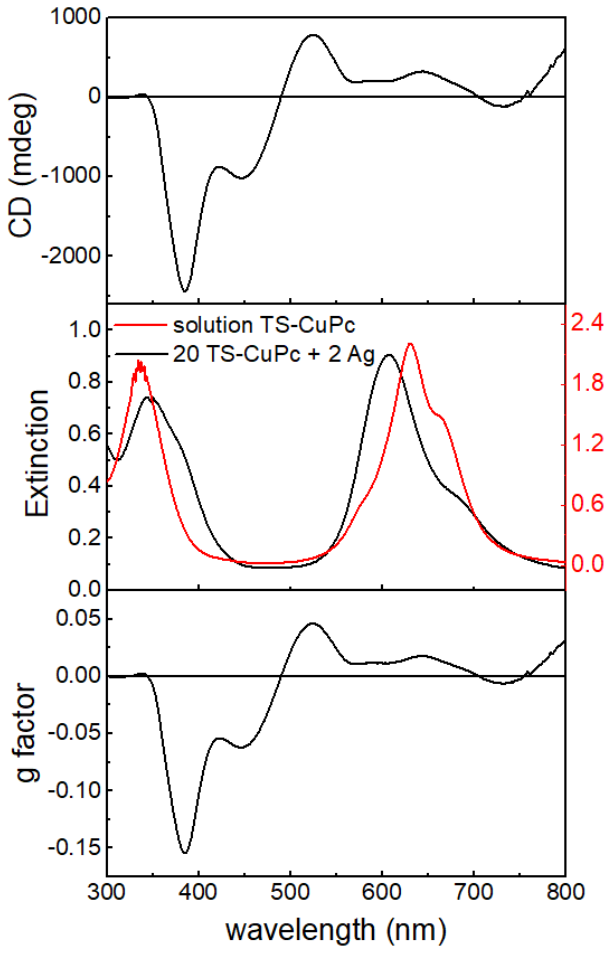

Figure 127. CD, extinction and g-factor spectra of 20 layers of TS-CuPc placed between two layers of AgNWs.

We observe in the extinction spectra that the TS-CuPc has two absorption peaks (in both film and solution), one in the UV range corresponding to the B band of the molecule (arising from n⟶π* transitions) and the other in the visible range corresponding to the Q band of the molecule (arising from π⟶π* transitions)[261]. Although we do not know the exact thickness of the TS-CuPc layer and thus cannot make a corresponding sample without TS-CuPc with identical interlayer spacing for comparison, the CD spectrum around 630 nm (Q band of TS-CuPC) is clearly modified by the TS-CuPc layer, but the CD around 320 nm (B band of TS-CuPc) has not seen apparent signals due to the TS-CuPc layer. This is maybe because the structure has rather weak CD in the region thus a modification of it is not visible even if it may exist. However, it is more likely that the chiral plasmonic structures interact only with the Q band of the molecule but not

the B band, and they can only modify the chiroptical properties of a molecule around its Q band. More studies and modeling are necessary to understand why both optical transitions do not respond similarly.

We are also interested in the CD modification of achiral plasmonic nanoobject by the chiral plasmonic superstructures. More specifically, AuNPs are used here. Alike to the TS-CuPc, one layer of AuNPs has a relatively low density, and we had to build a 30-layer structure (PEI/Ag/(PEI/AuNPs)$_{30}$/PEI/Ag) to see a significant extinction for the AuNPs. The angle between the two layers of AgNWs is 45°. An intense peak around 720 nm is observed in the extinction spectrum of the film, corresponding to the 30 layers of AuNPs. This peak is red-shifted with respect to the AuNPs in solution (maximum absorption at around 520 nm), resulting from the small distance between the AuNPs in the thin film. Although the sample containing two layers of AgNWs without AuNPs ("2 AgNWs" in ***Figure 128***) has not precisely the same interlayer spacing as the sample with 30 layers of AuNPs ("30 AuNPs + 2 AgNWs" in Figure 128), the modification in CD by the introduction of AuNPs in the structure is evidenced, although here again the features are not as sharp as for TDBC.

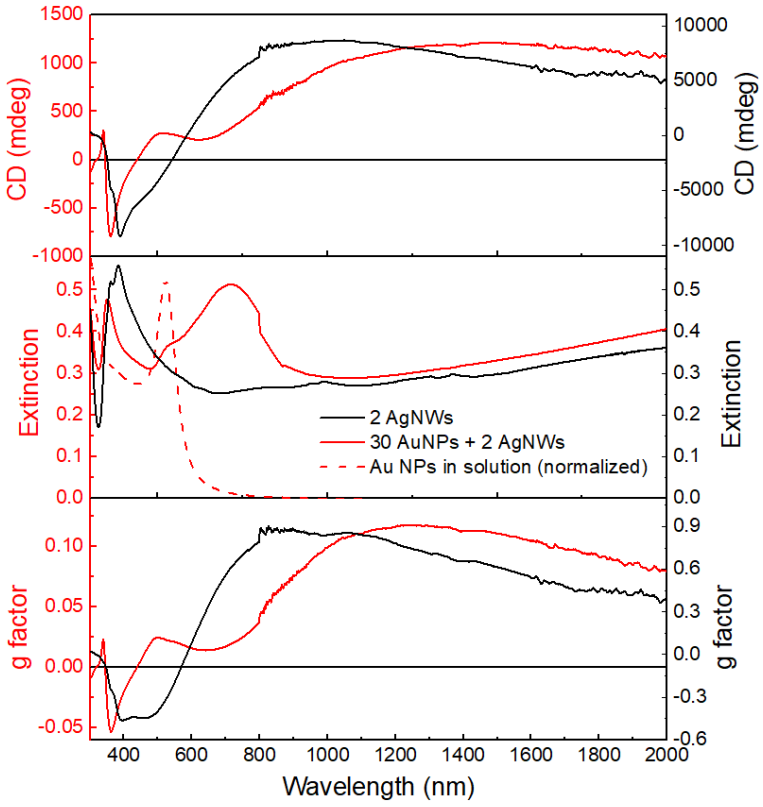

Figure 128. Comparison of CD and extinction spectra and g-factor of two-layer structures with (red) and without (black) AuNPs.

In conclusion, we have shown that the chiroptical properties of the chiral plasmonic superstructures is modified by the insertion of various molecules or nanoparticles, as long as their intensity in the film is high enough to generate noticeable signals. The change of CD

observed is not as sharp and well-defined as for TDBC. The underlying reason of this modification is thus still unclear as we have shown that for a chromophore like TS-CuPc which has two absorption bands namely B band and Q band, the CD modification occurs in the Q band but not in the B band.

IV.8. Coupling of a chiral plasmonic superstructure to a chromophore in solution

We showed in the previous sections how the optical properties of a chromophore are modified when embedded as a solid thin film in a chiral plasmonic environment. It would be interesting to investigate what happens when the molecules are in solution. As we have shown that two layers or AgNWs oriented at a certain angle show some CD even when they are very far away, we aim to deposit one layer of AgNWs by GIS on both side of a spectroscopic cuvette with an optical path length of 0.1 mm, before loading this cuvette with a TDBC solution.

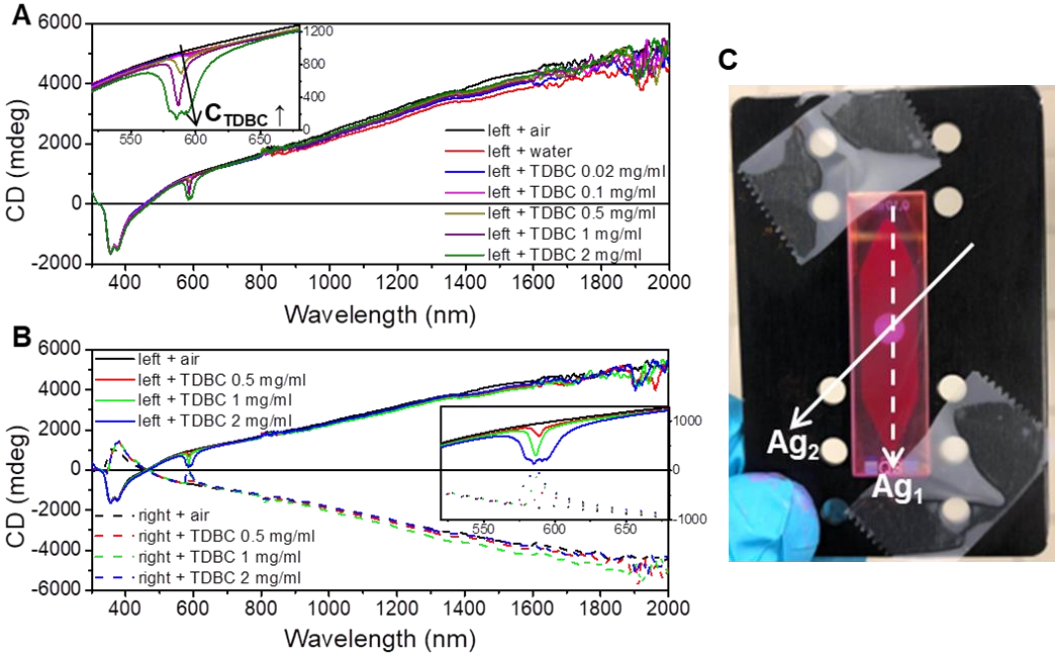

Figure 129. CD spectra of air, water and TDBC solutions of different concentrations in a quartz cuvette with one layer of AgNWs deposited on its both sides, with left- (A) and right-handed (B) structures. The optical path length is 0.1 mm. (C) Photograph of a left-handed cuvette with TDBC solution in it.

By controlling the orientations of the AgNWs on the two sides of the cuvette, we prepared a left-handed structure (angle α between the two AgNWs = 45°), and spectra were measured with air in the cuvette, pure water, and TDBC solutions at different concentration from 0.02 mg/ml to 2 mg/ml.No obvious modification of the CD spectra was observed when the cuvette is filled with air, water or a TDBC solution with a concentration lower than 0.1 mg/ml. From 0.5 mg/ml, a change in the CD spectrum similar to the change observed when TDBC is embedded as a thin film is observed. For a concentration of TDBC of 2 mg/ml, the peak turned to be not well defined since the transmittance is very low at such a high concentration, and thus the CD spectrometer is not sensitive enough in such conditions (***Figure 129***A). The same experiments were realized for right-handed structures, and symmetrical CD spectra were obtained (***Figure 129***B).

These results show that CD modification can be achieved with TDBC in solution. However, the concentration required is very high (> 0.5 mg/ml). We suppose that this is because only J-aggregates in the vicinity of the AgNWs layers, those close to the inner wall of the cuvette, are coupling with the LSPR of AgNWs, while the majority of the molecules dispersed in the cuvette are less effective and contribute less to the CD modification since they are far from the evanescent field of LSPR. These experiments open interesting perspective, as a much simple yet effective geometry is used here, which would allow to easily screen different materials and concentrations on the same nanostructure using for instance a flow cell with oriented AgNW layers deposited on the sides of the cell.

IV.9. Conclusion

We have shown that we are able to build well-controlled hybrid chiral nanostructures composed of oriented AgNW layers and a molecular dye placed at a precise position within the nanostructure. Although the fabrication of such structures requires a large number of steps, the structures formed were highly reproducible and the architecture can be easily tuned with a nm-scale control on the distances between the different constituents.

Using this approach, we have shown that the optical properties of an achiral organic dye are strongly modified when it is placed close to a chiral plasmonic superstructures. This modification includes the enhanced absorption and emission of the dye and the modification in the polarization properties, including LD, LB, CD and CB, among which we are mostly interested in the CD modification.

The surface plasmon enhanced absorption has been observed when a layer of TDBC is in vicinity to AgNW layer(s). This enhancement in absorption increases with the distance d between the TDBC layer and the AgNW layer when d is very small ($d < 10$ nm). The enhancement then decreases with d ($10 \text{ nm} < d < 20 \text{ nm}$) and starting from $d = 20$ nm no more enhancement can be observed. The critical values of d may vary slightly for different structures (one-layer and two-layer), but the general tendency remains unchanged. The surface enhanced emission has also been observed. For the two-layer structures that were prepared, no enhancement in emission was observed for $d < 20$ nm. The enhancement then decreases with d and is negligible for $d > 60$ nm, resulting from the opposite influence of enhanced absorption and fluorescence quenching with distance.

The modification in CD due to the dye layer is characterized by ΔCD, the difference between CD with the dye layer and without the dye layer. We studied the structural parameters which have an influence on the CD modification, in particular the distance from the dye layer to the AgNW layers. In general, ΔCD has relatively high values (up to several degrees) and has a bisignate shape, showing negative / positive / double Cotton effect depending on the distance between the dye layer to the AgNWs. The CD obtained by MMP is generally consistent with the CD measured on a commercial CD spectrometer in the visible range, in terms of shape of the spectra and position of the peaks, while the intensities may be different. This confirms the CD modification phenomenon and related conclusions. The simulations partly reproduce the trend observed but are however less consistent with the measurements. Nonetheless, the important modification in CD is reproduced in the simulations, which reveals that it is possible to generate a modification in CD by considering the samples as a collection of slabs of different

optical properties and without any coupling between them. However, the difference between the simulations and the measurements indicates that possible coupling between the LSPR of AgNWs and the dye molecules may also contribute to the modification in CD. Finally, the structures composed of two semi-reflecting AgNW layers may behave as cavities (although of low quality) which would also modify the optical properties of the dye. The measurements by MMP and the simulations have also shown modifications in LB, LD and CB as important as in the CD. These modifications are also sensitive to the distance d.

We have also shown that the chiral plasmonic superstructures can modify the optical properties of other achiral materials, including three other cyanine dyes, AuNPs and TS-CuPc. In addition, it is possible to obtain a similar phenomenon using TDBC in solution rather than in LbL film, while a relatively high concentration of TDBC solution is required.

In conclusion, we have shown an easy and reproducible way to modify the optical properties of many achiral molecules (not only in film but also in solution) by chiral plasmonic superstructures. These findings fill a gap in the field as this phenomenon is rarely reported although the chirality transfer from chiral molecules to achiral nanostructures is much more studied.

V. Collaborative side-projects: towards more complex chiral metasurfaces

V.1. Oriented assembly of silica nanohelices functionalized with gold nanoparticles

GIS and LbL-assembly have wide applicability in the fabrication of 3D nanostructures thanks to their extensive adaptability, high efficiency and ease to use. In fact, it is possible to align almost any type of rigid elongated nanoparticles on a substrate by GIS and then construct a multilayer superstructure by LbL-assembly. We show here an example of a multilayer structure composed of silica helices functionalized with AuNPs, which displays a significant CD depending on the handedness of the silica helices. This work was done in collaboration with the group of Reiko Oda and Emilie Pouget from the University of Bordeaux, and was published recently[54].

The so-called Goldhelices consist in plasmonic nanoparticles (gold) grafted onto helical templates made from silica nanohelices. The chiral shape of the template combined to the plasmonic properties of the gold nanoparticles give rise to a hybrid nano-object which displays a high CD (***Figure 130***) that depends on the handedness and the pitch of the nanohelix[262].

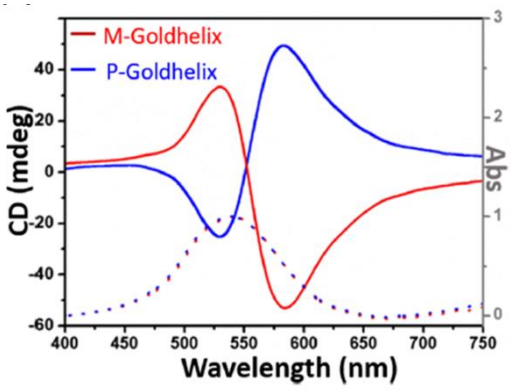

Figure 130. CD (solid line) and absorbance (dashed line) spectra of P- (right-handed) and M-Goldhelix (left-handed) suspensions in water.

The Goldhelices drop-casted on a substrate have a random orientation (***Figure 131a-c***), while aligned Goldhelix thin films (***Figure 131d-f***) were prepared by GIS. The experimental conditions of GIS for Goldhelices are similar to those used

for AgNWs. The optical properties of the assemblies were measured by UV-Vis spectroscopy, CD spectroscopy and Mueller matrix polarimetry.

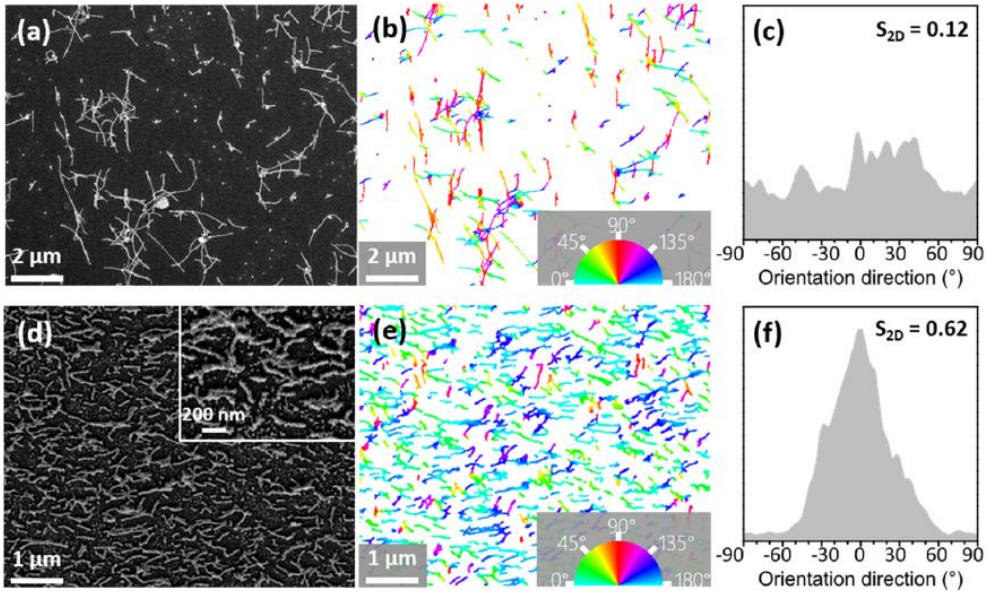

Figure 131. SEM images of a non-oriented thin film (a) and an oriented layer (d) of Goldhelices. Image analysis for the non-oriented (b) and the oriented (e) Goldhelices. The Goldhelices are color-coded according to their orientation (the color scale is shown). The distribution of orientation with respect to the main direction and the corresponding nematic order parameter S_{2D} is extracted from the image analysis (c,f).

The aligned Goldhelix monolayer has similar circular anisotropic properties (g-factor) as the Goldhelix suspension and the non-oriented monolayer, while the linear anisotropies (LB and LD) were only observed for the aligned Goldhelices. The aligned deposition of the Goldhelices also leads to a higher CD. However, the increase in CD arises from the increase of the density of the Goldhelices, but not from a structural dissymmetry, as the three layers of Goldhelices have the same orientation. Therefore, the g-factor is identical for oriented and non-oriented monolayers (***Table 1***).

sample	non-oriented				oriented			
			multilayers			multilayers (3 layers)		
	suspension	monolayer	gap		monolayer	gap		
			0 nm	56 nm		1 nm	22 nm	56 nm
LD	0	0	0	0	0.038	0.051	0.035	0.045
g-factor ($\times 10^{-3}$)	4.4	4.3	0	3.7	4.3	1.3	1.8	4.4

Table 1. LD and g-factor values of samples with or without orientation, with mono- or multilayers with different gaps between the layers.

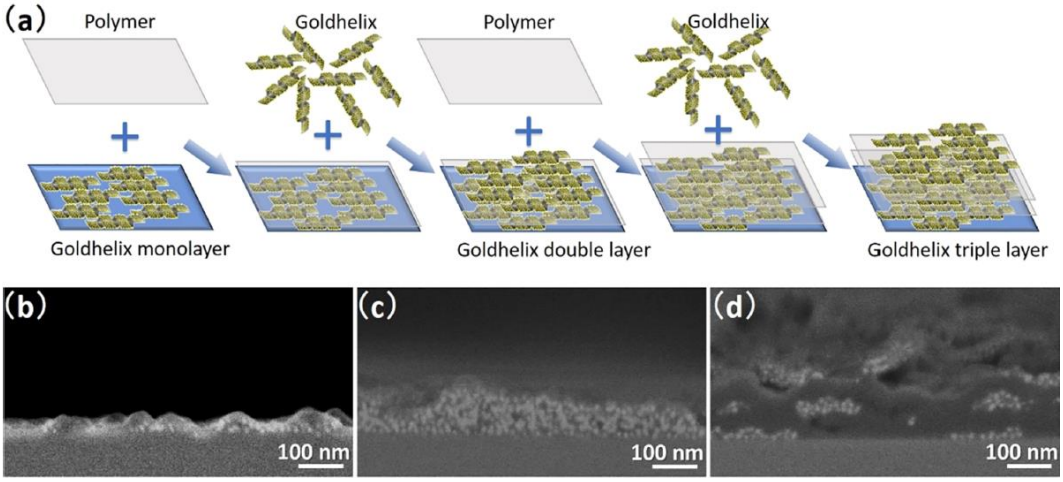

Figure 132. (a) Scheme of the GIS and LbL combined techniques for the creation of Goldhelix multilayer films. Cross-sectional (b–d) SEM images of a monolayer film (b), a triple layer film with a single PEI deposition (thickness = 1 nm) between the Goldhelix layers (c), and a triple layer film with a polyelectrolyte multilayer (PEI/(PSS/PAH)$_{15}$/PSS/PEI, thickness = 56 nm) between the Goldhelix layers (d).

Goldhelix multilayer films (3 layers of Goldhelices oriented in the same direction) were prepared by GIS and LbL-assembly (***Figure 132***). The interlayer spacing were controlled by tuning the number of polyelectrolyte layers between the Goldhelix layers. The three-layer structure has similar linear properties compared to the monolayer structure, while its chiroptical properties depend on the interlayer spacing. For small interlayer spacings (1 nm and 22 nm), the three-layer structure has a decreased g-factor compared to the monolayer structure, while for the larger interlayer spacing (56 nm), the three-layer structure shows a g-factor of the same order than the monolayer structure (***Table 1***). This is because when the layers of the Goldhelices are close to each other, interlayer interactions between the gold nanoparticles occur and cause the loss of the chiral character (***Figure 133***), while if the interlayer distance is large enough, the chiral interaction between the gold nanoparticles on each nanohelix is dominating.

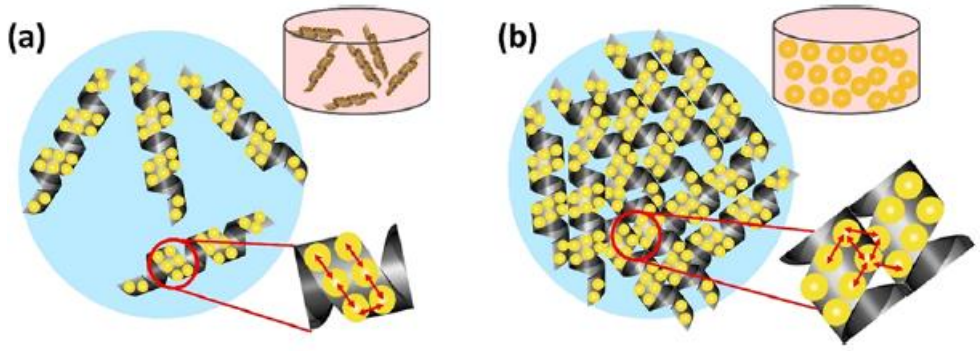

Figure 133. Scheme of the interactions between gold nanoparticles when the Goldhelices are isolated from each other (a) or in close contact (b). In the first case, the gold NPs interact only with their Goldhelix neighbor, whereas in the second case, they can interact with the gold NPs from other Goldhelices, losing the chiral character of the interaction and giving an optical signal close to the one which would be obtained from a homogeneous suspension of GNPs.

This collaboration demonstrated the versatility of the GIS and the LbL-assembly in the 3D assemblies of anisotropic nanoobjects, with good reproducibility maintained. The advantage of the fabrication method is the ease to control the structural parameters (spacing, angle etc.) and thus to tune the properties of the samples, and the high efficiency of the fabrication process. We show that the optical properties and the anisotropy do not only depend on the nature and geometry of the individual nano-objects, but also on their assembly at the mesoscopic scale.

V.2. Oriented AgNWs on Ag mirrors: towards polarizing mirrors and chiral cavities

In the previous chapter, we have studied the interaction of the LSPR of the AgNWs with molecules placed in their vicinity. Our results indicate that two layers of AgNWs may act as an optical cavity with polarizing properties. However, the AgNWs layers were obviously not effective to form optical cavities, for which high-quality semi-reflective surfaces such as Ag mirrors are needed.

We therefore started a collaboration with the group of Prof. Thomas Ebbesen and Cyriaque Genet from ISIS, University of Strasbourg, who has done a lot of research on light-matter strong coupling using optical cavities composed of parallel Ag mirrors. The aim of this collaboration

is to deposit one or more layer(s) of aligned AgNWs on each of the two Ag mirrors to form high-quality polarizing mirrors and ultimately a polarization-dependent cavity, including "chiral" cavities. This would be a first step to observe chiral plasmon-exciton coupling in the strong coupling regime, which has never been done to the best of our knowledge.

The first step is to prepare chiral mirrors, made from AgNW layers deposited on an Ag thin film that acts as a semi-reflecting mirror. The Ag mirrors that consist of a 35 nm thin film sputtered on a glass slide were provided by the group of ISIS. We then deposited one, two or three layers of AgNWs on the mirrors using the GIS and LbL-assembly as previously described (***Figure 134***). The chiral reflection of the samples was measured and simulated by Yann Battie from the Université de Lorraine.

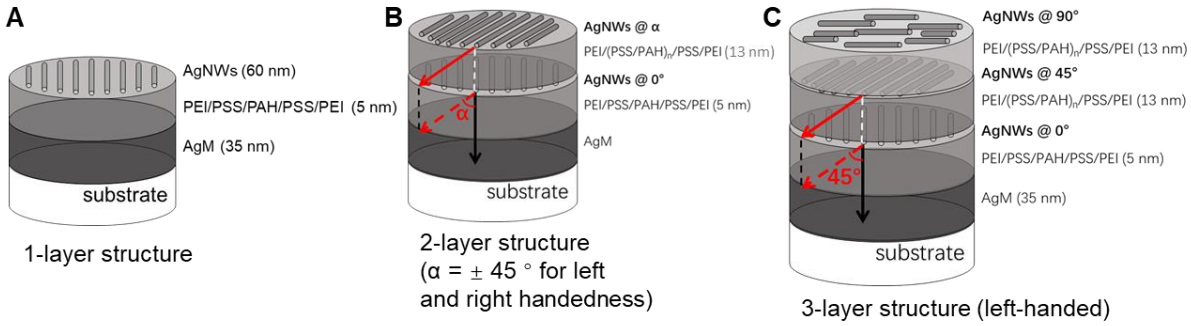

Figure 134. (A) One layer of AgNWs is deposited on an Ag mirror (AgM), separated by a 5-nm PEM film. (B) Two layers of AgNWs are deposited on an Ag mirror, the interlayer spacing between the two layers of AgNWs is 13 nm, the angle between them is α (α = ±45° for left- and right-handed structures). (C) Three layers of AgNWs are deposited on an Ag mirror, the interlayer spacing between the layers of AgNWs is 13 nm, the angle between them is 45° (left-handed).

The Mueller Matrix were measured using MMP in reflection mode. Only the first three rows of the Mueller Matrix were measured due to technical limitations of the setup used, as this is sufficient to obtain the chiral reflection $\Delta R/R = (R_{right} - R_{left})/R = 2 \times M_{41}$. ΔR is the difference of reflections of the sample for right circularly polarized light and left circularly polarized light ($R_{right} - R_{left}$), R is the total reflection for non-polarized light.

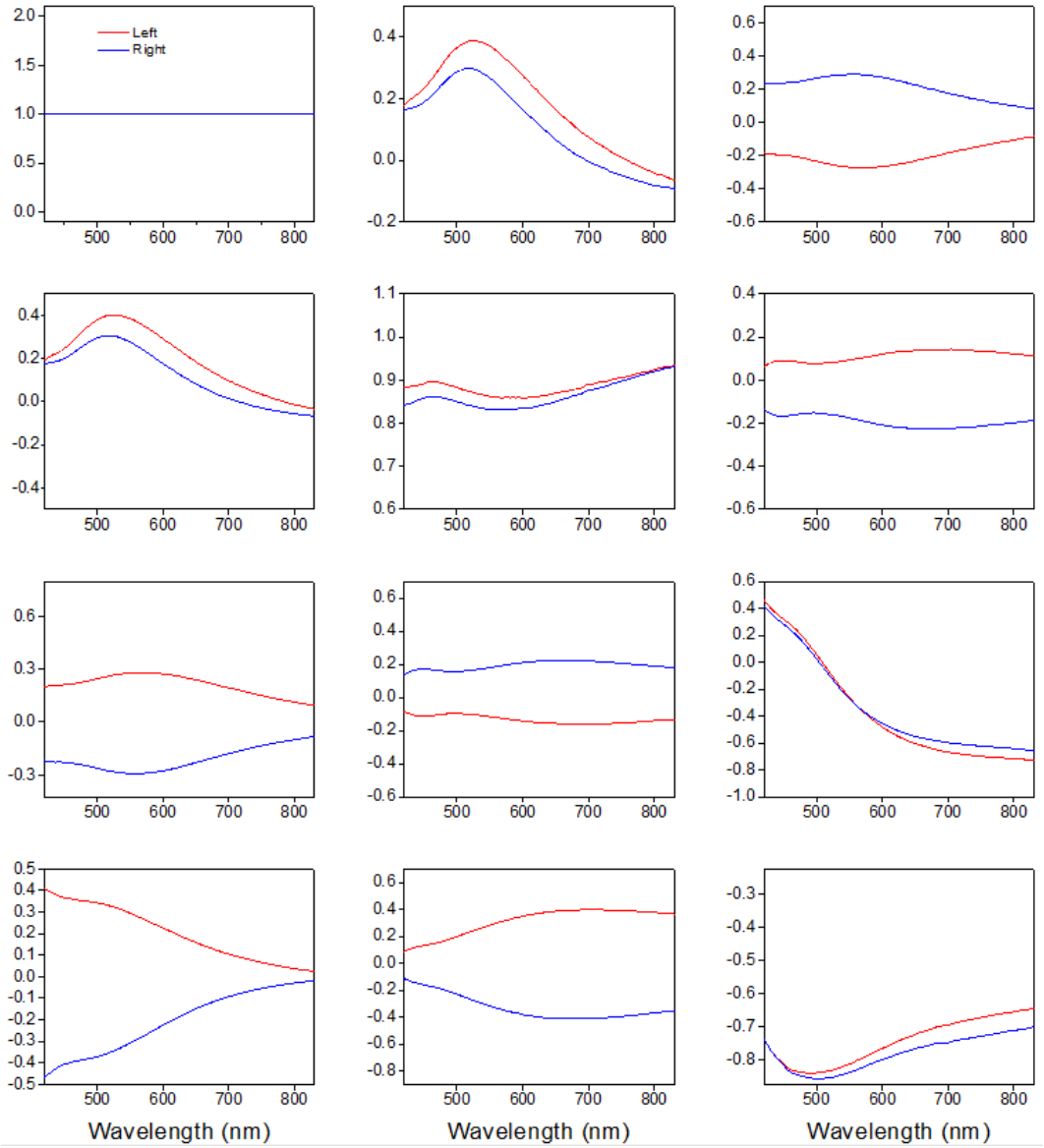

Figure 135. The first three rows of the Mueller Matrix of two layers of AgNWs (left- and right-handed) deposited on an Ag mirror, measured by MMP in reflection mode. The element M41 is used to calculate ΔR/R.

The measurements and simulations of ΔR/R and R for one-layer (non-chiral) and two-layer structures (left- and right-handed) are compared in ***Figure 136***.

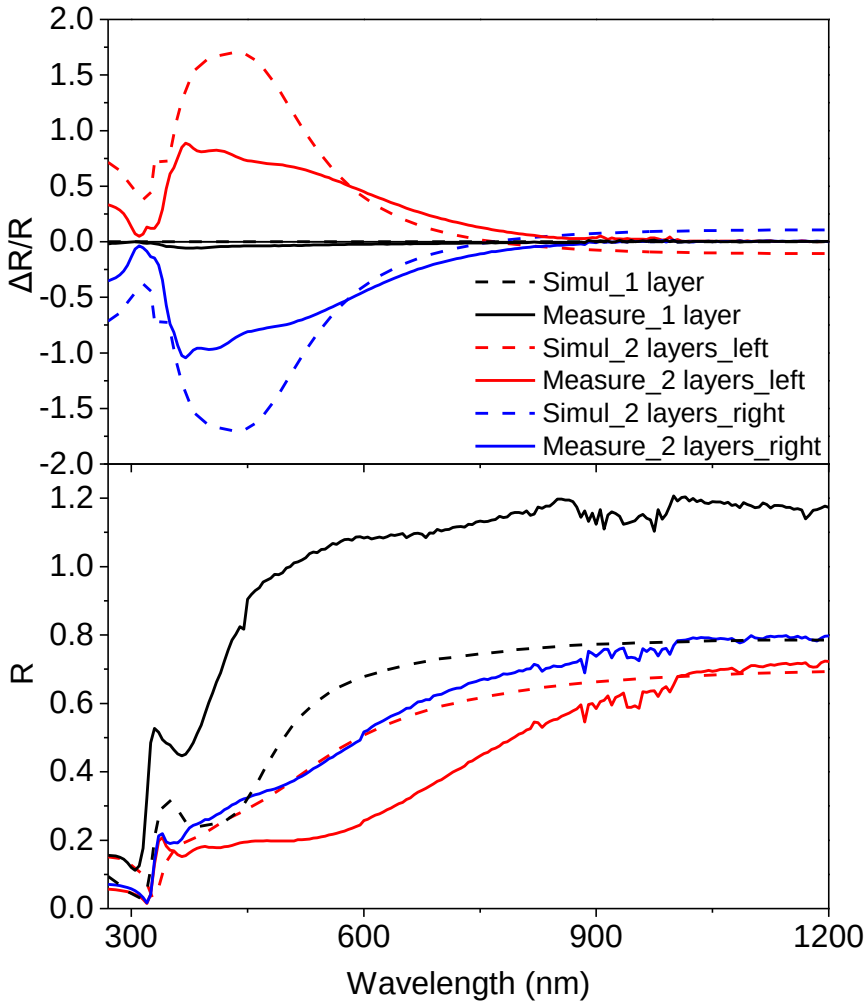

Figure 136. Measured (solid lines) and simulated (dashed lines) ΔR/R and R for one-layer (black) and two-layer structures of both left (red) and right (blue) handedness.

The measured results are very close to the simulations in terms of position of peak and shape of the spectra, while the intensities of ΔR/R differ. The two-layer structures have a reduced Reflectance compared to the one-layer structure, and left- and right-handed two-layer structures have a similar Reflectance. The one-layer structure has no chiral reflection (ΔR/R around 0), while the chiral two-layer structures have very high ΔR/R from 300 nm to 850 nm, with opposite signs for left- and right-handed structures. This is an important result as we show here that our structures have circular polarization-dependent reflections in the visible range, which is a pre-requisite to form chiral cavities.

The measurements and simulations of ΔR/R and R for two-layer (left-handed) and three-layer (left-handed) structures are compared in ***Figure 137***.

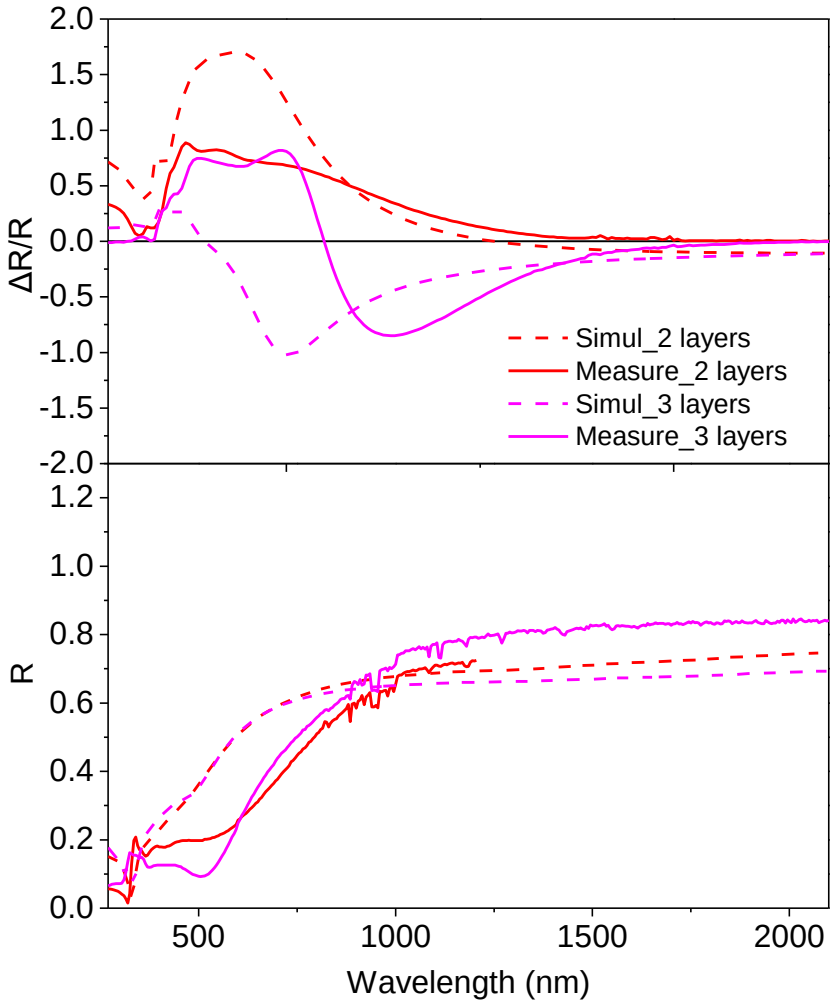

Figure 137. Measured (solid lines) and simulated (dashed lines) ΔR/R and R for two-layer (red) and three-layer (pink) structures, both of them are left-handed.

Comparable Reflectance is obtained for two-layer and three-layer structures, while the ΔR/R are very different. The left-handed two-layer structure has positive ΔR/R from 300 nm – 850 nm, which means that right circularly polarized light is selectively reflected in the visible range. The left-handed three-layer structure shows a ΔR/R spectrum with a bisignate shape, which changes its sign around 550 nm. In another words, the left-handed three-layer structure reflects selectively right circularly polarized light from 300 nm – 550 nm, and left circularly polarized light from 550 nm – 1000 nm.

These preliminary results are very interesting and promising. Further work is needed to explain in more details how the properties depend on the structure, and if the polarization selectivity of the reflection can be enhanced and tuned over a broad wavelength range. However, we show as a proof of principle that chiral semi-reflecting mirrors over the entire visible range can be prepared with our simple approach. With these chiral mirrors, chiral cavities which confine light of a specific polarization can be envisioned and light-matter (strong) coupling of molecules with (circularly) polarized light may be obtained.

V I . General conclusion and perspectives

VI.1. Conclusion

The objectives of this research were to study: 1. the optical properties of multilayer chiral plasmonic superstructures based on aligned silver nanowires (AgNWs) and the tunability of the chiroptical properties by controlling the hierarchical arrangement of the superstructure; 2. the modification of the optical properties of achiral dye molecules by the chiral plasmonic superstructures and the dependence of the modification effect on the structural parameters, in particular the distance between the dye layer and the AgNW layer(s).

The alignment of the AgNWs was realized by Grazing Incidence Spraying (GIS). This technique allows for the alignment of 1D anisotropic nanoobjects by spraying a suspension of the 1D nanoobjects on a pre-treated substrate at a small incidence angle. The nanoobjects are oriented along the flow direction during their adsorption due to the shear force of the flowing liquid. In this manuscript, well aligned AgNW films with high density were obtained using GIS. It was shown that a single layer of aligned AgNWs is highly anisotropic and exhibits linear polarization properties, namely linear birefringence (LB) and linear dichroism (LD).

Multilayer superstructures were fabricated using the Layer-by-Layer (LbL) assembly. The LbL-assembly involves the alternated deposition of oppositely charged materials, in particular polyelectrolytes, by dipping, spraying or spin coating, on a charged substrate. This technique allows to build homogeneous polyelectrolyte multilayer (PEM) films on various substrates, whose thickness can be easily and finely tuned at the nm level by changing the number of polymer layers in the PEM.

Therefore, by combining GIS and LbL-assembly, multilayer chiral plasmonic superstructures can be obtained. Two or more layers of aligned AgNWs were deposited successively. The

orientation of each layer was chosen independently by the GIS and different layers of AgNWs were separated by a LbL-assembled PEM film of selected thickness. The helix-like superstructures are chiral on condition that the angle α between the orientations of neighboring layers of AgNWs is different from 0° or 90°, and the films displayed large circular birefringence (CB) and circular dichroism (CD). For the two-layer structures, the influence of the angle α and the distance d between the two layers of AgNWs on the chiroptical properties of the film have been studied. The structure with α = 45° has been proven to be the most chiral given a fixed distance, while the interlayer spacing also influenced significantly the optical properties at a fixed α.

The optical properties were modeled using a transfer matrix approach based on the measured properties of individual layers and on the experimental geometric parameters (thickness and orientation of each layer). The chiroptical properties could be reasonably well reproduced using the simple model, which considers the multilayer superstructures as a collection of independent slabs interacting with the incident light successively without coupling between them. However, some significant differences exist between the modeling and the measurement, which may indicate that coupling between the localized surface plasmon resonance (LSPR) of different layers of AgNWs may occur and can also contribute to the chiroptical properties of the film.

The modification of the optical properties of an achiral molecule by the chiral plasmonic superstructures has been studied, by introducing a layer of the dye molecule into the multilayer superstructure using LbL-assembly. When the dye layer is close enough to the AgNW layer(s), an enhanced absorption and emission of the dye was observed. These enhancements are dependent on the distance between the dye and the AgNWs. Furthermore, by comparing the LB, LD, CB and CD of the corresponding structures with and without the dye molecule layer, we observed that the polarization properties of the hybrid film were significantly modified by the introduction of the dye layer. In particular, by subtracting the CD of the structure without the dye layer from that with the dye layer, we obtained the ΔCD arising from the introduction of the dye. The ΔCD has a bisignate shape, whose form and intensity depend on the distance of

the dye layer from the AgNW layers. We have also shown that the chiroptical properties are similarly modified if the dye is placed in solution rather than in thin films. Finally, the chiral plasmonic superstructures have been shown to similarly modify the chiroptical properties of many other achiral molecules, as well as gold nanoparticles.

The simple model used in the simulations can reproduce the main features of the observed changes in the chiroptical properties of the hybrid nanostructures. However, the simulated and measured spectra differ in many aspects. Possible reasons may be that plasmon-exciton coupling occurs between the LSPR of the AgNWs and the J-aggregates of the dye molecules, or that the cavity formed by the nanostructure also contributes to the modification of the optical properties of the hybrid film.

In conclusion, we have shown in this manuscript an easy and efficient way to fabricate chiral plasmonic superstructures with precisely controlled structures and reproducible and tunable chiroptical properties. The chiral plasmonic superstructures can modify the chiroptical properties of achiral molecules in its vicinity. This modification is sensitive to the distance between the molecule and the AgNWs. The main features of the chiroptical properties can be reproduced by a simple transfer matrix approach, although a more accurate modeling would certainly require the consideration of possible plasmon-plasmon / plasmon-exciton coupling.

VI.2. Perspectives

Plasmon-exciton strong coupling has been a hot topic in recent years. We have shown that the chiroptical properties of an achiral organic dye is modified by the chiral plasmonic superstructures. It would be interesting to study this phenomenon in the strong coupling regime. For this purpose, high quality polarization-sensitive cavities must be prepared, for which linearly polarized or chiral semi-reflective thin films are needed. Preliminary experiments (section V.2) indicate that by preparing superstructures similar to the one introduced in this thesis on silver mirrors rather than on transparent substrate, such films can be prepared. The

next step will be to fully characterize those films and build cavities of controlled thickness to study the (strong) coupling of molecules in the chiral cavities.

We have restricted ourselves on the interaction between a non-chiral molecule and a chiral plasmonic nanostructure. However, chiral molecules are very important for many fields and in particular for biological functions, and one challenge is to detect and quantify very small amount of those chiral biomolecules. It would thus also be interesting to study the interaction of a chiral molecule with the chiral plasmonic superstructures, which may increase the sensitivity of biosensing.

Plasmonic particles are very often used as catalysts for chemical reactions. It has also been recently reported that chemical reactions are modified when performed in optical cavities.[263,264] As we have shown that the chiral plasmonic superstructures can modify the chiroptical properties of molecules in solution, it would be interesting to look if the chiral plasmonic superstructure could be used to make chiral catalysis, leading to enantio-selective reactions depending on the handedness of the environment.

Finally, we have investigated the surface plasmon enhanced emission of a dye embedded in the chiral plasmonic superstructures, which is a widely studied phenomenon. On the other hand, the circularly polarized luminescence (CPL) has raised recently a lot of interests. Preliminary experiments (***Figure 105***) show that the emission of the achiral dye embedded in the chiral plasmonic superstructures may be circularly polarized. This would be a strong evidence of the plasmon-exciton coupling, which changes the properties of the dye molecules. It would also be a new way to build chiral light sources using non-chiral emitting materials coupled to a chiral environment.

References

(1) Mauskopf, S. CHAPTER 1 - A History of Chirality. In *Chiral Analysis*; Busch, K. W., Busch, M. A., Eds.; Elsevier: Amsterdam, 2006; pp 3–24. https://doi.org/10.1016/B978-044451669-5/50001-6.

(2) Prelog, V. Chirality in Chemistry. *Science* **1976**, *193* (4247), 17–24. https://doi.org/10.1126/science.935852.

(3) Chirality. *Wikipedia*; 2020. https://en.wikipedia.org/wiki/Chirality (accessed Aug 8, 2020)

(4) Bentley, R. Chiral: A Confusing Etymology. *Chirality* **2010**, *22* (1), 1–2. https://doi.org/10.1002/chir.20699.

(5) Flack, H. D. Louis Pasteur's Discovery of Molecular Chirality and Spontaneous Resolution in 1848, Together with a Complete Review of His Crystallographic and Chemical Work. *Acta Crystallogr A Found Crystallogr* **2009**, *65* (5), 371–389. https://doi.org/10.1107/S0108767309024088.

(6) Le Bel, J. A. Sur Les Relations Qui Existent Entre Les Formules Atomiques Des Corps Organiques, et Le Pouvoir Rotatoire de Leurs Dissolutions. *Bull. Soc. Chim. France* **1874**, *22*, 337–347.

(7) Bada, J. Biomolecules - Origins of Homochirality. *Nature* **1995**, *374* (6523), 594–595. https://doi.org/10.1038/374594a0.

(8) Toxvaerd, S. Origin of Homochirality in Biosystems. *IJMS* **2009**, *10* (3), 1290–1299. https://doi.org/10.3390/ijms10031290.

(9) Salam, A. The Role of Chirality in the Origin of Life. *J Mol Evol* **1991**, *33* (2), 105–113. https://doi.org/10.1007/BF02193624.

(10) Johnson, M.; Stokes, R. G.; Arndt, T. *The Thalidomide Catastrophe: How It Happened, Who Was Responsible and Why the Search for Justice Continues after More than Six Decades*; Onwards and Upwards: Cranbrook, 2018.

(11) Ito, T.; Ando, H.; Suzuki, T.; Ogura, T.; Hotta, K.; Imamura, Y.; Yamaguchi, Y.; Handa, H. Identification of a Primary Target of Thalidomide Teratogenicity. *Science* **2010**, *327* (5971), 1345–1350. https://doi.org/10.1126/science.1177319.

(12) Mannschreck, A.; Kiesswetter, R.; von Angerer, E. Unequal Activities of Enantiomers via Biological Receptors: Examples of Chiral Drug, Pesticide, and Fragrance Molecules. *J. Chem. Educ.* **2007**, *84* (12), 2012. https://doi.org/10.1021/ed084p2012.

(13) Green, M. M.; Selinger, J. V. Cosmic Chirality. *Science* **1998**, *282* (5390), 879–879. https://doi.org/10.1126/science.282.5390.879e.

(14) Ma, W.; Xu, L.; de Moura, A. F.; Wu, X.; Kuang, H.; Xu, C.; Kotov, N. A. Chiral Inorganic Nanostructures. *Chem. Rev.* **2017**, *117* (12), 8041–8093. https://doi.org/10.1021/acs.chemrev.6b00755.

(15) Brandt, J. R.; Salerno, F.; Fuchter, M. J. The Added Value of Small-Molecule Chirality in Technological Applications. *Nat Rev Chem* **2017**, *1* (6), 0045. https://doi.org/10.1038/s41570-017-0045.

(16) Keene, F. R. *Chirality in Supramolecular Assemblies: Causes and Consequences*; 2017.

(17) Liu, M.; Zhang, L.; Wang, T. Supramolecular Chirality in Self-Assembled Systems. *Chem. Rev.* **2015**, *115* (15), 7304–7397. https://doi.org/10.1021/cr500671p.

(18) Ziegler, M.; Davis, A. V.; Johnson, D. W.; Raymond, K. N. Supramolecular Chirality: A Reporter of Structural Memory. *Angew. Chem. Int. Ed.* **2003**, *42* (6), 665–668. https://doi.org/10.1002/anie.200390183.

(19) Wang, Z.; Cheng, F.; Winsor, T.; Liu, Y. Optical Chiral Metamaterials: A Review of the Fundamentals, Fabrication Methods and Applications. *Nanotechnology* **2016**, *27* (41), 412001. https://doi.org/10.1088/0957-4484/27/41/412001.

(20) Collins, J. T.; Kuppe, C.; Hooper, D. C.; Sibilia, C.; Centini, M.; Valev, V. K. Chirality and Chiroptical Effects in Metal Nanostructures: Fundamentals and Current Trends. *Advanced Optical Materials* **2017**, *5* (16), 1700182. https://doi.org/10.1002/adom.201700182.

(21) Zheludev, N. I.; Kivshar, Y. S. From Metamaterials to Metadevices. *Nature Mater* **2012**, *11* (11), 917–924. https://doi.org/10.1038/nmat3431.

(22) Flack, H. D. Chiral and Achiral Crystal Structures. *HCA* **2003**, *86* (4), 905–921. https://doi.org/10.1002/hlca.200390109.

(23) *International Tables for Crystallography: Space-Group Symmetry*, 2nd ed.; Aroyo, M. I., Ed.; International Union of Crystallography: Chester, England, 2016; Vol. A. https://doi.org/10.1107/97809553602060000114.

(24) Snatzke, G. J. Jaques, A. Collet, and S. H. Wilen: Enantiomers, Racemates, and Resolutions, J. Wiley & Sons, Inc., New York, Chichester, Brisbane, Toronto 1981. 447 Seiten, Preis: £ 38.75. *Berichte der Bunsengesellschaft für physikalische Chemie* **1982**, *86* (11), 1087–1087. https://doi.org/10.1002/bbpc.198200035.

(25) Flack, H. D.; Bernardinelli, G. The Mirror of Galadriel: Looking at Chiral and Achiral Crystal Structures. *Crystal Engineering* **2003**, *6* (4), 213–223. https://doi.org/10.1016/j.cryseng.2003.10.001.

(26) Berger, A.; Djukic, J.-P.; Pfeffer, M.; Cian, A. de; Kyritsakas-Gruber, N.; Lacour, J.; Vial, L. Novel Heteroleptic Cis-(C_{χ}N)2Pd(II) Chelates for the Preparation of Enantiopure Planar Chiral Cyclopalladated 2-[Tricarbonyl(H6-Phenyl)Chromium]Pyridine. *Chem. Commun.* **2003**, No. 5, 658–659. https://doi.org/10.1039/B211873D.

(27) Dryzun, C.; Avnir, D. On the Abundance of Chiral Crystals. *Chem. Commun.* **2012**, *48* (47), 5874. https://doi.org/10.1039/c2cc17727g.

(28) Ben-Moshe, A.; Govorov, A. O.; Markovich, G. Enantioselective Synthesis of Intrinsically Chiral Mercury Sulfide Nanocrystals. *Angew. Chem.* **2013**, *125* (4), 1313–1317. https://doi.org/10.1002/ange.201207489.

(29) Reilly, A. M.; Middlemiss, D. S.; Siddick, M. M.; Wann, D. A.; Ackland, G. J.; Wilson, C. C.; Rankin, D. W. H.; Morrison, C. A. The Phonon Spectrum of Phase-I Ammonia: Reassignment of Lattice Mode Symmetries from Combined Molecular and Lattice Dynamics Calculations. *J. Phys. Chem. A* **2008**, *112* (6), 1322–1329. https://doi.org/10.1021/jp0757053.

(30) Yeom, J.; Yeom, B.; Chan, H.; Smith, K. W.; Dominguez-Medina, S.; Bahng, J. H.; Zhao, G.; Chang, W.-S.; Chang, S.-J.; Chuvilin, A.; Melnikau, D.; Rogach, A. L.; Zhang, P.; Link, S.; Král, P.; Kotov, N. A. Chiral Templating of Self-Assembling Nanostructures by Circularly Polarized Light. *Nature Mater* **2015**, *14* (1), 66–72. https://doi.org/10.1038/nmat4125.

(31) Liu, H.; Alivisatos, A. P. Preparation of Asymmetric Nanostructures through Site Selective Modification of Tetrapods. *Nano Lett.* **2004**, *4* (12), 2397–2401. https://doi.org/10.1021/nl048523i.

(32) Govan, J. E.; Jan, E.; Querejeta, A.; Kotov, N. A.; Gun'ko, Y. K. Chiral Luminescent CdS Nano-Tetrapods. *Chem. Commun.* **2010**, *46* (33), 6072. https://doi.org/10.1039/c0cc00930j.

(33) Lechtken, A.; Schooss, D.; Stairs, J. R.; Blom, M. N.; Furche, F.; Morgner, N.; Kostko, O.; von Issendorff, B.; Kappes, M. M. Au34−: A Chiral Gold Cluster? *Angew. Chem. Int. Ed.* **2007**, *46* (16), 2944–2948. https://doi.org/10.1002/anie.200604760.

(34) Morito, H.; Yamane, H. Double-Helical Silicon Microtubes. *Angewandte Chemie International Edition* **2010**, *49* (21), 3638–3641. https://doi.org/10.1002/anie.200907271.

(35) Srivastava, S.; Santos, A.; Critchley, K.; Kim, K.-S.; Podsiadlo, P.; Sun, K.; Lee, J.; Xu, C.; Lilly, G. D.; Glotzer, S. C.; Kotov, N. A. Light-Controlled Self-Assembly of Semiconductor Nanoparticles into Twisted Ribbons. *Science* **2010**, *327* (5971), 1355–1359. https://doi.org/10.1126/science.1177218.

(36) Ben-Moshe, A.; Wolf, S. G.; Sadan, M. B.; Houben, L.; Fan, Z.; Govorov, A. O.; Markovich, G. Enantioselective Control of Lattice and Shape Chirality in Inorganic Nanostructures Using Chiral Biomolecules. *Nat Commun* **2014**, *5* (1), 4302. https://doi.org/10.1038/ncomms5302.

(37) Hersam, M. C. Progress towards Monodisperse Single-Walled Carbon Nanotubes. *Nature Nanotechnology* **2008**, *3* (7), 387–394. https://doi.org/10.1038/nnano.2008.135.

(38) González-Rubio, G.; Mosquera, J.; Kumar, V.; Pedrazo-Tardajos, A.; Llombart, P.; Solís, D. M.; Lobato, I.; Noya, E. G.; Guerrero-Martínez, A.; Taboada, J. M.; Obelleiro, F.; MacDowell, L. G.; Bals, S.; Liz-Marzán, L. M. Micelle-Directed Chiral Seeded Growth on Anisotropic Gold Nanocrystals. *Science* **2020**, *368* (6498), 1472–1477. https://doi.org/10.1126/science.aba0980.

(39) Bosnich, B. The Circular Dichoism of [PtXl4]2-Ion. *J. Am. Chem. Soc.* **1966**, *88* (11), 2606–2606. https://doi.org/10.1021/ja00963a053.

(40) Slocik, J. M.; Govorov, A. O.; Naik, R. R. Plasmonic Circular Dichroism of Peptide-Functionalized Gold Nanoparticles. *Nano Lett.* **2011**, *11* (2), 701–705. https://doi.org/10.1021/nl1038242.

(41) Maoz, B. M.; Chaikin, Y.; Tesler, A. B.; Bar Elli, O.; Fan, Z.; Govorov, A. O.; Markovich, G. Amplification of Chiroptical Activity of Chiral Biomolecules by Surface Plasmons. *Nano Lett.* **2013**, *13* (3), 1203–1209. https://doi.org/10.1021/nl304638a.

(42) Tohgha, U.; Deol, K. K.; Porter, A. G.; Bartko, S. G.; Choi, J. K.; Leonard, B. M.; Varga, K.; Kubelka, J.; Muller, G.; Balaz, M. Ligand Induced Circular Dichroism and Circularly Polarized Luminescence in CdSe Quantum Dots. *ACS Nano* **2013**, *7* (12), 11094–11102. https://doi.org/10.1021/nn404832f.

(43) Ortega Lorenzo, M.; Baddeley, C. J.; Muryn, C.; Raval, R. Extended Surface Chirality from Supramolecular Assemblies of Adsorbed Chiral Molecules. *Nature* **2000**, *404* (6776), 376–379. https://doi.org/10.1038/35006031.

(44) Stepanow, S.; Lin, N.; Vidal, F.; Landa, A.; Ruben, M.; Barth, J. V.; Kern, K. Programming Supramolecular Assembly and Chirality in Two-Dimensional Dicarboxylate Networks on a Cu(100) Surface. *Nano Lett.* **2005**, *5* (5), 901–904. https://doi.org/10.1021/nl050362a.

(45) Wan, X.-K.; Yuan, S.-F.; Lin, Z.-W.; Wang, Q.-M. A Chiral Gold Nanocluster Au $_{20}$ Protected by Tetradentate Phosphine Ligands. *Angew. Chem. Int. Ed.* **2014**, *53* (11), 2923–2926. https://doi.org/10.1002/anie.201308599.

(46) Dolamic, I.; Knoppe, S.; Dass, A.; Bürgi, T. First Enantioseparation and Circular Dichroism Spectra of Au38 Clusters Protected by Achiral Ligands. *Nat Commun* **2012**, *3* (1), 798. https://doi.org/10.1038/ncomms1802.

(47) Lopez-Acevedo, O.; Tsunoyama, H.; Tsukuda, T.; Häkkinen, H.; Aikens, C. M. Chirality and Electronic Structure of the Thiolate-Protected Au $_{38}$ Nanocluster. *J. Am. Chem. Soc.* **2010**, *132* (23), 8210–8218. https://doi.org/10.1021/ja102934q.

(48) Wang, S.; Jin, S.; Yang, S.; Chen, S.; Song, Y.; Zhang, J.; Zhu, M. Total Structure Determination of Surface Doping [Ag46Au24(SR)32](BPh4)2 Nanocluster and Its Structure-Related Catalytic Property. *Science Advances* **2015**, *1* (7), e1500441. https://doi.org/10.1126/sciadv.1500441.

(49) Ma, W.; Kuang, H.; Wang, L.; Xu, L.; Chang, W.-S.; Zhang, H.; Sun, M.; Zhu, Y.; Zhao, Y.; Liu, L.; Xu, C.; Link, S.; Kotov, N. A. Chiral Plasmonics of Self-Assembled Nanorod Dimers. *Sci Rep* **2013**, *3* (1), 1934. https://doi.org/10.1038/srep01934.

(50) Hu, L.; Liedl, T.; Martens, K.; Wang, Z.; Govorov, A. O. Long-Range Plasmon-Assisted Chiral Interactions in Nanocrystal Assemblies. *ACS Photonics* **2019**, *6* (3), 749–756. https://doi.org/10.1021/acsphotonics.8b01676.

(51) Guerrero-Martínez, A.; Auguié, B.; Alonso-Gómez, J. L.; Džolić, Z.; Gómez-Graña, S.; Žinić, M.; Cid, M. M.; Liz-Marzán, L. M. Intense Optical Activity from Three-Dimensional Chiral Ordering of Plasmonic Nanoantennas. *Angew. Chem.* **2011**, *123* (24), 5613–5617. https://doi.org/10.1002/ange.201007536.

(52) Fan, Z.; Govorov, A. O. Plasmonic Circular Dichroism of Chiral Metal Nanoparticle Assemblies. *Nano Lett.* **2010**, *10* (7), 2580–2587. https://doi.org/10.1021/nl101231b.

(53) Yan, W.; Xu, L.; Xu, C.; Ma, W.; Kuang, H.; Wang, L.; Kotov, N. A. Self-Assembly of Chiral Nanoparticle Pyramids with Strong *R* / *S* Optical Activity. *J. Am. Chem. Soc.* **2012**, *134* (36), 15114–15121. https://doi.org/10.1021/ja3066336.

(54) Gao, J.; Wu, W.; Lemaire, V.; Carvalho, A.; Nlate, S.; Buffeteau, T.; Oda, R.; Battie, Y.; Pauly, M.; Pouget, E. Tuning the Chiroptical Properties of Elongated Nano-Objects via Hierarchical Organization. *ACS Nano* **2020**, *14* (4), 4111–4121. https://doi.org/10.1021/acsnano.9b08823.

(55) Auguié, B.; Alonso-Gómez, J. L.; Guerrero-Martínez, A.; Liz-Marzán, L. M. Fingers Crossed: Optical Activity of a Chiral Dimer of Plasmonic Nanorods. *J. Phys. Chem. Lett.* **2011**, *2* (8), 846–851. https://doi.org/10.1021/jz200279x.

(56) Zhao, Y.; Belkin, M. A.; Alù, A. Twisted Optical Metamaterials for Planarized Ultrathin Broadband Circular Polarizers. *Nat Commun* **2012**, *3* (1), 870. https://doi.org/10.1038/ncomms1877.

(57) Lan, X.; Liu, T.; Wang, Z.; Govorov, A. O.; Yan, H.; Liu, Y. DNA-Guided Plasmonic Helix with Switchable Chirality. *J. Am. Chem. Soc.* **2018**, *140* (37), 11763–11770. https://doi.org/10.1021/jacs.8b06526.

(58) Pines, D.; Bohm, D. A Collective Description of Electron Interactions: II. Collective vs Individual Particle Aspects of the Interactions. *Phys. Rev.* **1952**, *85* (2), 338–353. https://doi.org/10.1103/PhysRev.85.338.

(59) Vial, A.; Grimault, A.-S.; Macías, D.; Barchiesi, D.; de la Chapelle, M. L. Improved Analytical Fit of Gold Dispersion: Application to the Modeling of Extinction Spectra with a Finite-Difference Time-Domain Method. *Phys. Rev. B* **2005**, *71* (8), 085416. https://doi.org/10.1103/PhysRevB.71.085416.

(60) Johnson, P. B.; Christy, R. W. Optical Constants of the Noble Metals. *Phys. Rev. B* **1972**, *6* (12), 4370–4379. https://doi.org/10.1103/PhysRevB.6.4370.

(61) Klimov, V. *Nanoplasmonics*; CRC Press, 2014.

(62) Surface Plasmon. *Wikipedia*; 2020. https://en.wikipedia.org/wiki/Surface_plasmon (accessed Aug 16, 2020)

(63) Kaya, S. Photo-Thermal Control of Surface Plasmon Mode Propagation at Telecom Wavelengths, 2016.

(64) Otto, A. Excitation of Nonradiative Surface Plasma Waves in Silver by the Method of Frustrated Total Reflection. *Z. Physik* **1968**, *216* (4), 398–410. https://doi.org/10.1007/BF01391532.

(65) Kretschmann, E.; Raether, H. Notizen: Radiative Decay of Non Radiative Surface Plasmons Excited by Light. *Zeitschrift für Naturforschung A* **1968**, *23* (12), 2135–2136. https://doi.org/10.1515/zna-1968-1247.

(66) Raether, H. *Surface Plasmons on Smooth and Rough Surfaces and on Gratings*; Springer Tracts in Modern Physics; Springer Berlin Heidelberg: Berlin, Heidelberg, 1988; Vol. 111. https://doi.org/10.1007/BFb0048317.

(67) Hecht, B.; Bielefeldt, H.; Novotny, L.; Inouye, Y.; Pohl, D. W. Local Excitation, Scattering, and Interference of Surface Plasmons. *Phys. Rev. Lett.* **1996**, *77* (9), 1889–1892. https://doi.org/10.1103/PhysRevLett.77.1889.

(68) Ye, F.; Merlo, J. M.; Burns, M. J.; Naughton, M. J. Optical and Electrical Mappings of Surface Plasmon Cavity Modes. *Nanophotonics* **2014**, *3* (1–2), 33–49. https://doi.org/10.1515/nanoph-2013-0038.

(69) Willets, K. A.; Van Duyne, R. P. Localized Surface Plasmon Resonance Spectroscopy and Sensing. *Annu. Rev. Phys. Chem.* **2007**, *58* (1), 267–297. https://doi.org/10.1146/annurev.physchem.58.032806.104607.

(70) Maier, S. A. *Plasmonics: Fundamentals and Applications*; Springer: New York, 2007.

(71) Jackson, J. D. *Classical Electrodynamics Third Edition*, 3rd edition.; Wiley: New York, 1998.

(72) Cao, J.; Sun, T.; Grattan, K. T. V. Gold Nanorod-Based Localized Surface Plasmon Resonance Biosensors: A Review. *Sensors and Actuators B: Chemical* **2014**, *195*, 332–351. https://doi.org/10.1016/j.snb.2014.01.056.

(73) Kelly, K. L.; Coronado, E.; Zhao, L. L.; Schatz, G. C. The Optical Properties of Metal Nanoparticles: The Influence of Size, Shape, and Dielectric Environment. *J. Phys. Chem. B* **2003**, *107* (3), 668–677. https://doi.org/10.1021/jp026731y.

(74) Peiris, S.; McMurtrie, J.; Zhu, H.-Y. Metal Nanoparticle Photocatalysts: Emerging Processes for Green Organic Synthesis. *Catal. Sci. Technol.* **2016**, *6* (2), 320–338. https://doi.org/10.1039/C5CY02048D.

(75) Kvasnička, P.; Homola, J. Optical Sensors Based on Spectroscopy of Localized Surface Plasmons on Metallic Nanoparticles: Sensitivity Considerations. *Biointerphases* **2008**, *3* (3), FD4–FD11. https://doi.org/10.1116/1.2994687.

(76) Murray, W. A.; Auguié, B.; Barnes, W. L. Sensitivity of Localized Surface Plasmon Resonances to Bulk and Local Changes in the Optical Environment. *J. Phys. Chem. C* **2009**, *113* (13), 5120–5125. https://doi.org/10.1021/jp810322q.

(77) Tréguer-Delapierre, M.; Majimel, J.; Mornet, S.; Duguet, E.; Ravaine, S. Synthesis of Non-Spherical Gold Nanoparticles. *Gold Bull* **2008**, *41* (2), 195–207. https://doi.org/10.1007/BF03216597.

(78) Ma, W.; Xu, L.; Wang, L.; Xu, C.; Kuang, H. Chirality-Based Biosensors. *Adv. Funct. Mater.* **2019**, *29* (1), 1805512. https://doi.org/10.1002/adfm.201805512.

(79) Bochenkov, V.; Shabatina, T. Chiral Plasmonic Biosensors. *Biosensors* **2018**, *8* (4), 120. https://doi.org/10.3390/bios8040120.

(80) Govorov, A. O.; Fan, Z.; Hernandez, P.; Slocik, J. M.; Naik, R. R. Theory of Circular Dichroism of Nanomaterials Comprising Chiral Molecules and Nanocrystals: Plasmon Enhancement, Dipole Interactions, and Dielectric Effects. *Nano Lett.* **2010**, *10* (4), 1374–1382. https://doi.org/10.1021/nl100010v.

(81) García-Etxarri, A.; Dionne, J. A. Surface-Enhanced Circular Dichroism Spectroscopy Mediated by Nonchiral Nanoantennas. *Phys. Rev. B* **2013**, *87* (23), 235409. https://doi.org/10.1103/PhysRevB.87.235409.

(82) Lu, F.; Tian, Y.; Liu, M.; Su, D.; Zhang, H.; Govorov, A. O.; Gang, O. Discrete Nanocubes as Plasmonic Reporters of Molecular Chirality. *Nano Lett.* **2013**, *13* (7), 3145–3151. https://doi.org/10.1021/nl401107g.

(83) McPeak, K. M.; van Engers, C. D.; Bianchi, S.; Rossinelli, A.; Poulikakos, L. V.; Bernard, L.; Herrmann, S.; Kim, D. K.; Burger, S.; Blome, M.; Jayanti, S. V.; Norris, D. J. Ultraviolet Plasmonic Chirality from Colloidal Aluminum Nanoparticles Exhibiting Charge-Selective Protein Detection. *Adv. Mater.* **2015**, *27* (40), 6244–6250. https://doi.org/10.1002/adma.201503493.

(84) Wu, X.; Xu, L.; Liu, L.; Ma, W.; Yin, H.; Kuang, H.; Wang, L.; Xu, C.; Kotov, N. A. Unexpected Chirality of Nanoparticle Dimers and Ultrasensitive Chiroplasmonic Bioanalysis. *J. Am. Chem. Soc.* **2013**, *135* (49), 18629–18636. https://doi.org/10.1021/ja4095445.

(85) Xu, Z.; Xu, L.; Zhu, Y.; Ma, W.; Kuang, H.; Wang, L.; Xu, C. Chirality Based Sensor for Bisphenol A Detection. *Chem. Commun.* **2012**, *48* (46), 5760. https://doi.org/10.1039/c2cc31327h.

(86) Kumar, J.; Eraña, H.; López-Martínez, E.; Claes, N.; Martín, V. F.; Solís, D. M.; Bals, S.; Cortajarena, A. L.; Castilla, J.; Liz-Marzán, L. M. Detection of Amyloid Fibrils in Parkinson's Disease Using Plasmonic Chirality. *Proc Natl Acad Sci USA* **2018**, *115* (13), 3225–3230. https://doi.org/10.1073/pnas.1721690115.

(87) Matuschek, M.; Singh, D. P.; Jeong, H.-H.; Nesterov, M.; Weiss, T.; Fischer, P.; Neubrech, F.; Liu, N. Chiral Plasmonic Hydrogen Sensors. *Small* **2018**, *14* (7), 1702990. https://doi.org/10.1002/smll.201702990.

(88) Inoue, Y.; Ramamurthy, V. *Chiral Photochemistry*; CRC Press: New York, 2004.

(89) Sajonz, P.; Schafer, W.; Gong, X.; Shultz, S.; Rosner, T.; Welch, C. J. Multiparallel Microfluidic High-Performance Liquid Chromatography for High-Throughput Normal-Phase Chiral Analysis. *Journal of Chromatography A* **2007**, *1145* (1), 149–154. https://doi.org/10.1016/j.chroma.2007.01.067.

(90) Chang, C.; Wang, X.; Bai, Y.; Liu, H. Applications of Nanomaterials in Enantioseparation and Related Techniques. *TrAC Trends in Analytical Chemistry* **2012**, *39*, 195–206. https://doi.org/10.1016/j.trac.2012.07.002.

(91) Wang, H.-S.; Wei, J.-P. Emerging Enantiomeric Resolution Materials with Homochiral Nano-Fabrications. *Nanoscale* **2015**, *7* (28), 11815–11832. https://doi.org/10.1039/C5NR03048J.

(92) Zhang, M.; Ye, B.-C. Colorimetric Chiral Recognition of Enantiomers Using the Nucleotide-Capped Silver Nanoparticles. *Anal. Chem.* **2011**, *83* (5), 1504–1509. https://doi.org/10.1021/ac102922f.

(93) Su, H.; Zheng, Q.; Li, H. Colorimetric Detection and Separation of Chiral Tyrosine Based on N-Acetyl-l-Cysteine Modified Gold Nanoparticles. *J. Mater. Chem.* **2012**, *22* (14), 6546. https://doi.org/10.1039/c2jm16746h.

(94) Sun, Y.; Zhang, L.; Li, H. Chiral Colorimetric Recognition of Amino Acids Based on Silver Nanoparticle Clusters. *New J. Chem.* **2012**, *36* (7), 1442. https://doi.org/10.1039/c2nj40098g.

(95) Gan, H.; Tang, K.; Sun, T.; Hirtz, M.; Li, Y.; Chi, L.; Butz, S.; Fuchs, H. Selective Adsorption of DNA on Chiral Surfaces: Supercoiled or Relaxed Conformation. *Angewandte Chemie International Edition* **2009**, *48* (29), 5282–5286. https://doi.org/10.1002/anie.200806295.

(96) Wang, Y.; Zhou, X.; Xu, C.; Jin, Y.; Li, B. Gold Nanorods as Visual Sensing Platform for Chiral Recognition with Naked Eyes. *Sci Rep* **2018**, *8* (1), 5296. https://doi.org/10.1038/s41598-018-23674-y.

(97) Zhang, L.; Xu, C.; Liu, C.; Li, B. Visual Chiral Recognition of Tryptophan Enantiomers Using Unmodified Gold Nanoparticles as Colorimetric Probes. *Analytica Chimica Acta* **2014**, *809*, 123–127. https://doi.org/10.1016/j.aca.2013.11.043.

(98) McFadden, C. F.; Cremer, P. S.; Gellman, A. J. Adsorption of Chiral Alcohols on "Chiral" Metal Surfaces. *Langmuir* **1996**, *12* (10), 2483–2487. https://doi.org/10.1021/la950348l.

(99) Noguez, C.; Garzón, I. L. Optically Active Metal Nanoparticles. *Chem. Soc. Rev.* **2009**, *38* (3), 757. https://doi.org/10.1039/b800404h.

(100) Attard, G. A. Electrochemical Studies of Enantioselectivity at Chiral Metal Surfaces. *J. Phys. Chem. B* **2001**, *105* (16), 3158–3167. https://doi.org/10.1021/jp0041508.

(101) Kühnle, A.; Linderoth, T. R.; Hammer, B.; Besenbacher, F. Chiral Recognition in Dimerization of Adsorbed Cysteine Observed by Scanning Tunnelling Microscopy. *Nature* **2002**, *415* (6874), 891–893. https://doi.org/10.1038/415891a.

(102) Yasukawa, T.; Miyamura, H.; Kobayashi, S. Chiral Metal Nanoparticle-Catalyzed Asymmetric C–C Bond Formation Reactions. *Chem. Soc. Rev.* **2014**, *43* (5), 1450–1461. https://doi.org/10.1039/C3CS60298B.

(103) Mallat, T.; Orglmeister, E.; Baiker, A. Asymmetric Catalysis at Chiral Metal Surfaces. *Chem. Rev.* **2007**, *107* (11), 4863–4890. https://doi.org/10.1021/cr0683663.

(104) Orito, Y.; Imai, S.; Niwa, S.; Nguyengiahung. Asymmetric Hydrogenation of Methyl Benzoylformate Using Platinum-Carbon Catalysts Modified with Cinchonidine. *J. Synth. Org. Chem. Jpn.* **1979**, *37* (2), 173–174. https://doi.org/10.5059/yukigoseikyokaishi.37.173.

(105) Jansat, S.; Gómez, M.; Philippot, K.; Muller, G.; Guiu, E.; Claver, C.; Castillón, S.; Chaudret, B. A Case for Enantioselective Allylic Alkylation Catalyzed by Palladium Nanoparticles. *J. Am. Chem. Soc.* **2004**, *126* (6), 1592–1593. https://doi.org/10.1021/ja036132k.

(106) Okamoto, K.; Akiyama, R.; Kobayashi, S. Recoverable, Reusable, Highly Active, and Sulfur-Tolerant Polymer Incarcerated Palladium for Hydrogenation. *J. Org. Chem.* **2004**, *69* (8), 2871–2873. https://doi.org/10.1021/jo0358527.

(107) Ramírez, J.; Sanaú, M.; Fernández, E. Gold(0) Nanoparticles for Selective Catalytic Diboration. *Angew. Chem. Int. Ed.* **2008**, *47* (28), 5194–5197. https://doi.org/10.1002/anie.200800541.

(108) Chirally Modified Gold Nanoparticles: Nanostructured Chiral Ligands for Catalysis. *Arkivoc* **2006**, *2006* (15), 76. https://doi.org/10.3998/ark.5550190.0007.f10.

(109) Gross, E.; Liu, J. H.; Alayoglu, S.; Marcus, M. A.; Fakra, S. C.; Toste, F. D.; Somorjai, G. A. Asymmetric Catalysis at the Mesoscale: Gold Nanoclusters Embedded in Chiral Self-Assembled Monolayer as Heterogeneous Catalyst for Asymmetric Reactions. *J. Am. Chem. Soc.* **2013**, *135* (10), 3881–3886. https://doi.org/10.1021/ja310640b.

(110) Imai, K.; Takayama, Y.; Murayama, H.; Ohmiya, H.; Shimizu, Y.; Sawamura, M. Asymmetric Synthesis of α-Alkylidene-β-Lactams through Copper Catalysis with a Prolinol-Phosphine Chiral Ligand. *Org. Lett.* **2019**, *21* (6), 1717–1721. https://doi.org/10.1021/acs.orglett.9b00276.

(111) Cano, I.; Tschan, M. J.-L.; Martínez-Prieto, L. M.; Philippot, K.; Chaudret, B.; van Leeuwen, P. W. N. M. Enantioselective Hydrogenation of Ketones by Iridium Nanoparticles Ligated with Chiral Secondary Phosphine Oxides. *Catal. Sci. Technol.* **2016**, *6* (11), 3758–3766. https://doi.org/10.1039/C5CY02206A.

(112) Sawai, K.; Tatumi, R.; Nakahodo, T.; Fujihara, H. Asymmetric Suzuki-Miyaura Coupling Reactions Catalyzed by Chiral Palladium Nanoparticles at Room Temperature. *Angew. Chem. Int. Ed.* **2008**, *47* (36), 6917–6919. https://doi.org/10.1002/anie.200802174.

(113) Hu, A.; Yee, G. T.; Lin, W. Magnetically Recoverable Chiral Catalysts Immobilized on Magnetite Nanoparticles for Asymmetric Hydrogenation of Aromatic Ketones. *J. Am. Chem. Soc.* **2005**, *127* (36), 12486–12487. https://doi.org/10.1021/ja053881o.

(114) Lipkin, D. M. Existence of a New Conservation Law in Electromagnetic Theory. *Journal of Mathematical Physics* **1964**, *5* (5), 696–700. https://doi.org/10.1063/1.1704165.

(115) Tang, Y.; Cohen, A. E. Optical Chirality and Its Interaction with Matter. *Phys. Rev. Lett.* **2010**, *104* (16), 163901. https://doi.org/10.1103/PhysRevLett.104.163901.

(116) Valev, V. K.; Baumberg, J. J.; Sibilia, C.; Verbiest, T. Chirality and Chiroptical Effects in Plasmonic Nanostructures: Fundamentals, Recent Progress, and Outlook. *Adv. Mater.* **2013**, *25* (18), 2517–2534. https://doi.org/10.1002/adma.201205178.

(117) Fedotov, V. A.; Schwanecke, A. S.; Zheludev, N. I.; Khardikov, V. V.; Prosvirnin, S. L. Asymmetric Transmission of Light and Enantiomerically Sensitive Plasmon Resonance in Planar Chiral Nanostructures. *Nano Lett.* **2007**, *7* (7), 1996–1999. https://doi.org/10.1021/nl0707961.

(118) Filonov, D.; Kozlov, V.; Shmidt, A.; Steinberg, B. Z.; Ginzburg, P. Resonant Metasurface with Tunable Asymmetric Reflection. *Appl. Phys. Lett.* **2018**, *113* (9), 094103. https://doi.org/10.1063/1.5046948.

(119) Tranter, G. E. 8.21 Spectroscopic Analysis: Polarimetry and Optical Rotatory Dispersion. In *Comprehensive Chirality*; Elsevier, 2012; pp 411–421. https://doi.org/10.1016/B978-0-08-095167-6.00843-0.

(120) *Circular Dichroism: Principles and Applications, 2nd Edition*, 2nd Edition.; Woody, R. W., Berova, N., Eds.; Wiley-VCH: New York, 2000.

(121) Berova, N.; Bari, L. D.; Pescitelli, G. Application of Electronic Circular Dichroism in Configurational and Conformational Analysis of Organic Compounds. *Chem. Soc. Rev.* **2007**, *36* (6), 914. https://doi.org/10.1039/b515476f.

(122) Some Applications of the Kronig-Kramers Theorem to Optical Activity. *Tetrahedron* **1961**, *13* (1–3), 48–56. https://doi.org/10.1016/S0040-4020(01)92204-5.

(123) Yin, X.; Schäferling, M.; Metzger, B.; Giessen, H. Interpreting Chiral Nanophotonic Spectra: The Plasmonic Born–Kuhn Model. *Nano Lett.* **2013**, *13* (12), 6238–6243. https://doi.org/10.1021/nl403705k.

(124) Modzabi, S. K. Studies on New Approaches of Chiral Discrimination for Chiral Analysis by Regression Modeling of Spectral Data. Thesis, 2009.

(125) Luo, Y.; Chi, C.; Jiang, M.; Li, R.; Zu, S.; Li, Y.; Fang, Z. Plasmonic Chiral Nanostructures: Chiroptical Effects and Applications. *Advanced Optical Materials* **2017**, *5* (16), 1700040. https://doi.org/10.1002/adom.201700040.

(126) Gansel, J. K.; Thiel, M.; Rill, M. S.; Decker, M.; Bade, K.; Saile, V.; von Freymann, G.; Linden, S.; Wegener, M. Gold Helix Photonic Metamaterial as Broadband Circular Polarizer. *Science* **2009**, *325* (5947), 1513–1515. https://doi.org/10.1126/science.1177031.

(127) Jing, L.; Wang, Z.; Yang, Y.; Zheng, B.; Liu, Y.; Chen, H. Chiral Metamirrors for Broadband Spin-Selective Absorption. *Appl. Phys. Lett.* **2017**, *110* (23), 231103. https://doi.org/10.1063/1.4985132.

(128) Zhang, S.; Zhou, J.; Park, Y.-S.; Rho, J.; Singh, R.; Nam, S.; Azad, A. K.; Chen, H.-T.; Yin, X.; Taylor, A. J.; Zhang, X. Photoinduced Handedness Switching in Terahertz Chiral Metamolecules. *Nat Commun* **2012**, *3* (1), 942. https://doi.org/10.1038/ncomms1908.

(129) Rodríguez-Fortuño, F. J.; Engheta, N.; Martínez, A.; Zayats, A. V. Lateral Forces on Circularly Polarizable Particles near a Surface. *Nat Commun* **2015**, *6* (1), 8799. https://doi.org/10.1038/ncomms9799.

(130) Haroche, S.; Kleppner, D. Cavity Quantum Electrodynamics. *Physics Today* **1989**, *42* (1), 24–30. https://doi.org/10.1063/1.881201.

(131) Ebbesen, T. W. Hybrid Light–Matter States in a Molecular and Material Science Perspective. *Acc. Chem. Res.* **2016**, *49* (11), 2403–2412. https://doi.org/10.1021/acs.accounts.6b00295.

(132) Lidzey, D. G.; Bradley, D. D. C.; Skolnick, M. S.; Virgili, T.; Walker, S.; Whittaker, D. M. Strong Exciton–Photon Coupling in an Organic Semiconductor Microcavity. *Nature* **1998**, *395* (6697), 53–55. https://doi.org/10.1038/25692.

(133) Reithmaier, J. P.; Sęk, G.; Löffler, A.; Hofmann, C.; Kuhn, S.; Reitzenstein, S.; Keldysh, L. V.; Kulakovskii, V. D.; Reinecke, T. L.; Forchel, A. Strong Coupling in a Single Quantum Dot–Semiconductor Microcavity System. *Nature* **2004**, *432* (7014), 197. https://doi.org/10.1038/nature02969.

(134) Wang, S.; Chervy, T.; George, J.; Hutchison, J. A.; Genet, C.; Ebbesen, T. W. Quantum Yield of Polariton Emission from Hybrid Light-Matter States. *J. Phys. Chem. Lett.* **2014**, *5* (8), 1433–1439. https://doi.org/10.1021/jz5004439.

(135) Schwartz, T.; Hutchison, J. A.; Léonard, J.; Genet, C.; Haacke, S.; Ebbesen, T. W. Polariton Dynamics under Strong Light-Molecule Coupling. *ChemPhysChem* **2013**, *14* (1), 125–131. https://doi.org/10.1002/cphc.201200734.

(136) Törmä, P.; Barnes, W. L. Strong Coupling between Surface Plasmon Polaritons and Emitters: A Review. *Rep. Prog. Phys.* **2014**, *78* (1), 013901. https://doi.org/10.1088/0034-4885/78/1/013901.

(137) Bellessa, J.; Symonds, C.; Vynck, K.; Lemaitre, A.; Brioude, A.; Beaur, L.; Plenet, J. C.; Viste, P.; Felbacq, D.; Cambril, E.; Valvin, P. Giant Rabi Splitting between Localized Mixed Plasmon-Exciton States in a Two-Dimensional Array of Nanosize Metallic Disks in an Organic Semiconductor. *Phys. Rev. B* **2009**, *80* (3), 033303. https://doi.org/10.1103/PhysRevB.80.033303.

(138) Cao, E.; Lin, W.; Sun, M.; Liang, W.; Song, Y. Exciton-Plasmon Coupling Interactions: From Principle to Applications. *Nanophotonics* **2018**, *7* (1), 145–167. https://doi.org/10.1515/nanoph-2017-0059.

(139) Sukharev, M.; Nitzan, A. Optics of Exciton-Plasmon Nanomaterials. *J. Phys.: Condens. Matter* **2017**, *29* (44), 443003. https://doi.org/10.1088/1361-648X/aa85ef.

(140) Fofang, N. T.; Park, T.-H.; Neumann, O.; Mirin, N. A.; Nordlander, P.; Halas, N. J. Plexcitonic Nanoparticles: Plasmon−Exciton Coupling in Nanoshell−J-Aggregate Complexes. *Nano Lett.* **2008**, *8* (10), 3481–3487. https://doi.org/10.1021/nl8024278.

(141) Schlather, A. E.; Large, N.; Urban, A. S.; Nordlander, P.; Halas, N. J. Near-Field Mediated Plexcitonic Coupling and Giant Rabi Splitting in Individual Metallic Dimers. *Nano Lett.* **2013**, *13* (7), 3281–3286. https://doi.org/10.1021/nl4014887.

(142) Xiong, X.; You, J.-B.; Bai, P.; Png, C. E.; Zhou, Z.-K.; Wu, L. Ultrastrong Coupling in Single Plexcitonic Nanocubes. *Nanophotonics* **2020**, *9* (2), 257–266. https://doi.org/10.1515/nanoph-2019-0333.

(143) Bellessa, J.; Bonnand, C.; Plenet, J. C.; Mugnier, J. Strong Coupling between Surface Plasmons and Excitons in an Organic Semiconductor. *Phys. Rev. Lett.* **2004**, *93* (3), 036404. https://doi.org/10.1103/PhysRevLett.93.036404.

(144) Lan, X.; Zhou, X.; McCarthy, L. A.; Govorov, A. O.; Liu, Y.; Link, S. DNA-Enabled Chiral Gold Nanoparticle–Chromophore Hybrid Structure with Resonant Plasmon–Exciton Coupling Gives Unusual and Strong Circular Dichroism. *J. Am. Chem. Soc.* **2019**, *141* (49), 19336–19341. https://doi.org/10.1021/jacs.9b08797.

(145) Gray, S. K. Surface Plasmon-Enhanced Spectroscopy and Photochemistry. *Plasmonics* **2007**, *2* (3), 143–146. https://doi.org/10.1007/s11468-007-9038-7.

(146) Le Ru, E. C.; Grand, J.; Sow, I.; Somerville, W. R. C.; Etchegoin, P. G.; Treguer-Delapierre, M.; Charron, G.; Félidj, N.; Lévi, G.; Aubard, J. A Scheme for Detecting Every Single Target Molecule with Surface-Enhanced Raman Spectroscopy. *Nano Lett.* **2011**, *11* (11), 5013–5019. https://doi.org/10.1021/nl2030344.

(147) Moskovits, M. Surface-Enhanced Spectroscopy. *Rev. Mod. Phys.* **1985**, *57* (3), 783–826. https://doi.org/10.1103/RevModPhys.57.783.

(148) Rai, V. N.; Srivastava, A. K.; Mukherjee, C.; Deb, S. K. Surface Enhanced Absorption and Transmission from Dye Coated Gold Nanoparticles in Thin Films. *Appl. Opt.* **2012**, *51* (14), 2606. https://doi.org/10.1364/AO.51.002606.

(149) McNay, G.; Eustace, D.; Smith, W. E.; Faulds, K.; Graham, D. Surface-Enhanced Raman Scattering (SERS) and Surface-Enhanced Resonance Raman Scattering (SERRS): A Review of Applications. *Appl. Spectrosc., AS* **2011**, *65* (8), 825–837.

(150) Fort, E.; Grésillon, S. Surface Enhanced Fluorescence. *J. Phys. D: Appl. Phys.* **2007**, *41* (1), 013001. https://doi.org/10.1088/0022-3727/41/1/013001.

(151) Radke, A.; Gissibl, T.; Klotzbücher, T.; Braun, P. V.; Giessen, H. Three-Dimensional Bichiral Plasmonic Crystals Fabricated by Direct Laser Writing and Electroless Silver Plating. *Adv. Mater.* **2011**, *23* (27), 3018–3021. https://doi.org/10.1002/adma.201100543.

(152) Thiel, M.; Rill, M. S.; Freymann, G. von; Wegener, M. Three-Dimensional Bi-Chiral Photonic Crystals. *Advanced Materials* **2009**, *21* (46), 4680–4682. https://doi.org/10.1002/adma.200901601.

(153) Yoon, G.; Kim, I.; So, S.; Mun, J.; Kim, M.; Rho, J. Fabrication of Three-Dimensional Suspended, Interlayered and Hierarchical Nanostructures by Accuracy-Improved Electron Beam Lithography Overlay. *Sci Rep* **2017**, *7* (1), 6668. https://doi.org/10.1038/s41598-017-06833-5.

(154) Leong, E. S. P.; Deng, J.; Khoo, E. H.; Wu, S.; Phua, W. K.; Liu, Y. J. Fabrication of Suspended, Three-Dimensional Chiral Plasmonic Nanostructures with Single-Step Electron-Beam Lithography. *RSC Adv.* **2015**, *5* (117), 96366–96371. https://doi.org/10.1039/C5RA17705G.

(155) Chang, Y.-C.; Lu, S.-C.; Chung, H.-C.; Wang, S.-M.; Tsai, T.-D.; Guo, T.-F. High-Throughput Nanofabrication of Infra-Red and Chiral Metamaterials Using Nanospherical-Lens Lithography. *Sci Rep* **2013**, *3* (1), 3339. https://doi.org/10.1038/srep03339.

(156) Gorkunov, M. V.; Rogov, O. Y.; Kondratov, A. V.; Artemov, V. V.; Gainutdinov, R. V.; Ezhov, A. A. Chiral Visible Light Metasurface Patterned in Monocrystalline Silicon by Focused Ion Beam. *Sci Rep* **2018**, *8* (1), 11623. https://doi.org/10.1038/s41598-018-29977-4.

(157) Dietrich, K.; Lehr, D.; Helgert, C.; Tünnermann, A.; Kley, E.-B. Circular Dichroism from Chiral Nanomaterial Fabricated by On-Edge Lithography. *Adv. Mater.* **2012**, *24* (44), OP321–OP325. https://doi.org/10.1002/adma.201203424.

(158) Shen, B.; Linko, V.; Tapio, K.; Pikker, S.; Lemma, T.; Gopinath, A.; Gothelf, K. V.; Kostiainen, M. A.; Toppari, J. J. Plasmonic Nanostructures through DNA-Assisted Lithography. *Sci. Adv.* **2018**, *4* (2), eaap8978. https://doi.org/10.1126/sciadv.aap8978.

(159) Yang, S.-M.; Jang, S. G.; Choi, D.-G.; Kim, S.; Yu, H. K. Nanomachining by Colloidal Lithography. *Small* **2006**, *2* (4), 458–475. https://doi.org/10.1002/smll.200500390.

(160) Wang, Z.; Ai, B.; Möhwald, H.; Zhang, G. Colloidal Lithography Meets Plasmonic Nanochemistry. *Advanced Optical Materials* **2018**, *6* (18), 1800402. https://doi.org/10.1002/adom.201800402.

(161) Wu, Z.; Zheng, Y. Moiré Chiral Metamaterials. *Advanced Optical Materials* **2017**, *5* (16), 1700034. https://doi.org/10.1002/adom.201700034.

(162) Urban, M. J.; Shen, C.; Kong, X.-T.; Zhu, C.; Govorov, A. O.; Wang, Q.; Hentschel, M.; Liu, N. Chiral Plasmonic Nanostructures Enabled by Bottom-Up Approaches. *Annu. Rev. Phys. Chem.* **2019**, *70* (1), 275–299. https://doi.org/10.1146/annurev-physchem-050317-021332.

(163) van Dorp, W. F.; Hagen, C. W. A Critical Literature Review of Focused Electron Beam Induced Deposition. *Journal of Applied Physics* **2008**, *104* (8), 081301. https://doi.org/10.1063/1.2977587.

(164) Randolph, S. J.; Fowlkes, J. D.; Rack, P. D. Focused, Nanoscale Electron-Beam-Induced Deposition and Etching. *Crit. Rev. Solid State Mat. Sci.* **2006**, *31* (3), 55–89. https://doi.org/10.1080/10408430600930438.

(165) Esposito, M.; Tasco, V.; Cuscunà, M.; Todisco, F.; Benedetti, A.; Tarantini, I.; Giorgi, M. D.; Sanvitto, D.; Passaseo, A. Nanoscale 3D Chiral Plasmonic Helices with Circular Dichroism at Visible Frequencies. *ACS Photonics* **2015**, *2* (1), 105–114. https://doi.org/10.1021/ph500318p.

(166) Yeom, B.; Zhang, H.; Zhang, H.; Park, J. I.; Kim, K.; Govorov, A. O.; Kotov, N. A. Chiral Plasmonic Nanostructures on Achiral Nanopillars. *Nano Lett.* **2013**, *13* (11), 5277–5283. https://doi.org/10.1021/nl402782d.

(167) Hou, Y.; Li, S.; Su, Y.; Huang, X.; Liu, Y.; Huang, L.; Yu, Y.; Gao, F.; Zhang, Z.; Du, J. Design and Fabrication of Three-Dimensional Chiral Nanostructures Based on Stepwise Glancing Angle Deposition Technology. *Langmuir* **2013**, *29* (3), 867–872. https://doi.org/10.1021/la304122f.

(168) Mark, A. G.; Gibbs, J. G.; Lee, T.-C.; Fischer, P. Hybrid Nanocolloids with Programmed Three-Dimensional Shape and Material Composition. *Nature Mater* **2013**, *12* (9), 802–807. https://doi.org/10.1038/nmat3685.

(169) Peinado, P.; Sangiao, S.; De Teresa, J. M. Focused Electron and Ion Beam Induced Deposition on Flexible and Transparent Polycarbonate Substrates. *ACS Nano* **2015**, *9* (6), 6139–6146. https://doi.org/10.1021/acsnano.5b01383.

(170) Nicolis, G.; Prigogine, I. *Self-Organization in Nonequilibrium Systems: From Dissipative Structures to Order through Fluctuations*, 1st edition.; Wiley: New York, 1977.

(171) Whitesides, G. M.; Grzybowski, B. Self-Assembly at All Scales. *Science* **2002**, *295* (5564), 2418–2421. https://doi.org/10.1126/science.1070821.

(172) Yashima, E.; Maeda, K.; Nishimura, T. Detection and Amplification of Chirality by Helical Polymers. *Chem. Eur. J.* **2004**, *10* (1), 42–51. https://doi.org/10.1002/chem.200305295.

(173) Cecconello, A.; Besteiro, L. V.; Govorov, A. O.; Willner, I. Chiroplasmonic DNA-Based Nanostructures. *Nat Rev Mater* **2017**, *2* (9), 17039. https://doi.org/10.1038/natrevmats.2017.39.

(174) Kuzyk, A.; Schreiber, R.; Fan, Z.; Pardatscher, G.; Roller, E.-M.; Högele, A.; Simmel, F. C.; Govorov, A. O.; Liedl, T. DNA-Based Self-Assembly of Chiral Plasmonic Nanostructures with Tailored Optical Response. *Nature* **2012**, *483* (7389), 311–314. https://doi.org/10.1038/nature10889.

(175) Querejeta-Fernández, A.; Chauve, G.; Methot, M.; Bouchard, J.; Kumacheva, E. Chiral Plasmonic Films Formed by Gold Nanorods and Cellulose Nanocrystals. *J. Am. Chem. Soc.* **2014**, *136* (12), 4788–4793. https://doi.org/10.1021/ja501642p.

(176) Song, C.; Blaber, M. G.; Zhao, G.; Zhang, P.; Fry, H. C.; Schatz, G. C.; Rosi, N. L. Tailorable Plasmonic Circular Dichroism Properties of Helical Nanoparticle Superstructures. *Nano Lett.* **2013**, *13* (7), 3256–3261. https://doi.org/10.1021/nl4013776.

(177) Ma, W.; Kuang, H.; Xu, L.; Ding, L.; Xu, C.; Wang, L.; Kotov, N. A. Attomolar DNA Detection with Chiral Nanorod Assemblies. *Nat Commun* **2013**, *4* (1), 2689. https://doi.org/10.1038/ncomms3689.

(178) Rothemund, P. W. K. Folding DNA to Create Nanoscale Shapes and Patterns. *Nature* **2006**, *440* (7082), 297–302. https://doi.org/10.1038/nature04586.

(179) Douglas, S. M.; Dietz, H.; Liedl, T.; Högberg, B.; Graf, F.; Shih, W. M. Self-Assembly of DNA into Nanoscale Three-Dimensional Shapes. *Nature* **2009**, *459* (7245), 414–418. https://doi.org/10.1038/nature08016.

(180) Kneer, L. M.; Roller, E.-M.; Besteiro, L. V.; Schreiber, R.; Govorov, A. O.; Liedl, T. Circular Dichroism of Chiral Molecules in DNA-Assembled Plasmonic Hotspots. *ACS Nano* **2018**, *12* (9), 9110–9115. https://doi.org/10.1021/acsnano.8b03146.

(181) Kuzyk, A.; Schreiber, R.; Zhang, H.; Govorov, A. O.; Liedl, T.; Liu, N. Reconfigurable 3D Plasmonic Metamolecules. *Nature Mater* **2014**, *13* (9), 862–866. https://doi.org/10.1038/nmat4031.

(182) Zhou, C.; Duan, X.; Liu, N. A Plasmonic Nanorod That Walks on DNA Origami. *Nat Commun* **2015**, *6* (1), 8102. https://doi.org/10.1038/ncomms9102.

(183) Hu, H.; Wang, S.; Feng, X.; Pauly, M.; Decher, G.; Long, Y. In-Plane Aligned Assemblies of 1D-Nanoobjects: Recent Approaches and Applications. *Chem. Soc. Rev.* **2020**, *49* (2), 509–553. https://doi.org/10.1039/C9CS00382G.

(184) Tao, A. R.; Huang, J.; Yang, P. Langmuir−Blodgettry of Nanocrystals and Nanowires. *Acc. Chem. Res.* **2008**, *41* (12), 1662–1673. https://doi.org/10.1021/ar8000525.

(185) Bensimon, A.; Simon, A.; Chiffaudel, A.; Croquette, V.; Heslot, F.; Bensimon, D. Alignment and Sensitive Detection of DNA by a Moving Interface. *Science* **1994**, *265* (5181), 2096–2098. https://doi.org/10.1126/science.7522347.

(186) Huang, J.; Fan, R.; Connor, S.; Yang, P. One-Step Patterning of Aligned Nanowire Arrays by Programmed Dip Coating. *Angew. Chem. Int. Ed.* **2007**, *46* (14), 2414–2417. https://doi.org/10.1002/anie.200604789.

(187) Yu, G.; Cao, A.; Lieber, C. M. Large-Area Blown Bubble Films of Aligned Nanowires and Carbon Nanotubes. *Nat Nanotechnol* **2007**, *2* (6), 372–377. https://doi.org/10.1038/nnano.2007.150.

(188) Javey, A.; Nam; Friedman, R. S.; Yan, H.; Lieber, C. M. Layer-by-Layer Assembly of Nanowires for Three-Dimensional, Multifunctional Electronics. *Nano Lett.* **2007**, *7* (3), 773–777. https://doi.org/10.1021/nl063056l.

(189) He, J.; Zhang, Q.; Gupta, S.; Emrick, T.; Russell, T. P.; Thiyagarajan, P. Drying Droplets: A Window into the Behavior of Nanorods at Interfaces. *Small* **2007**, *3* (7), 1214–1217. https://doi.org/10.1002/smll.200700055.

(190) Lu, X.; Wang, C.; Wei, Y. One-Dimensional Composite Nanomaterials: Synthesis by Electrospinning and Their Applications. *Small* **2009**, *5* (21), 2349–2370. https://doi.org/10.1002/smll.200900445.

(191) Yang, P. Wires on Water. *Nature* **2003**, *425* (6955), 243–244. https://doi.org/10.1038/425243a.

(192) Whang, D.; Jin, S.; Wu, Y.; Lieber, C. M. Large-Scale Hierarchical Organization of Nanowire Arrays for Integrated Nanosystems. *Nano Lett.* **2003**, *3* (9), 1255–1259. https://doi.org/10.1021/nl0345062.

(193) Zhang, C.; Zhang, X.; Zhang, X.; Ou, X.; Zhang, W.; Jie, J.; Chang, J. C.; Lee, C.-S.; Lee, S.-T. Facile One-Step Fabrication of Ordered Organic Nanowire Films. *Adv. Mater.* **2009**, *21* (41), 4172–4175. https://doi.org/10.1002/adma.200802793.

(194) Feng, J.; Xia, H.; You, F.; Mao, H.; Ma, X.; Tao, H.; Zhao, X.; Wang, M.-C. Alignment of Ag Nanowires on Glass Sheet by Dip-Coating Technique. *Journal of Alloys and Compounds* **2018**, *735*, 607–612. https://doi.org/10.1016/j.jallcom.2017.09.154.

(195) Qi, X.; Lu, Z.; You, E.-M.; He, Y.; Zhang, Q.; Yi, H.-J.; Li, D.; Ding, S.-Y.; Jiang, Y.; Xiong, X.; Xu, J.; Ge, D.; Liu, X. Y.; Bai, H. Nanocombing Effect Leads to Nanowire-Based, in-Plane, Uniaxial Thin Films. *ACS Nano* **2018**, *12* (12), 12701–12712. https://doi.org/10.1021/acsnano.8b07671.

(196) Hu, H.; Pauly, M.; Felix, O.; Decher, G. Spray-Assisted Alignment of Layer-by-Layer Assembled Silver Nanowires: A General Approach for the Preparation of Highly Anisotropic Nano-Composite Films. *Nanoscale* **2017**, *9* (3), 1307–1314. https://doi.org/10.1039/C6NR08045F.

(197) Sekar, S.; Lemaire, V.; Hu, H.; Decher, G.; Pauly, M. Anisotropic Optical and Conductive Properties of Oriented 1D-Nanoparticle Thin Films Made by Spray-Assisted Self-Assembly. *Faraday Discuss.* **2016**, *191*, 373–389. https://doi.org/10.1039/C6FD00017G.

(198) Blell, R.; Lin, X.; Lindström, T.; Ankerfors, M.; Pauly, M.; Felix, O.; Decher, G. Generating In-Plane Orientational Order in Multilayer Films Prepared by Spray-Assisted Layer-by-Layer Assembly. *ACS Nano* **2017**, *11* (1), 84–94. https://doi.org/10.1021/acsnano.6b04191.

(199) Decher, G.; Schlenoff, J. B. *Multilayer Thin Films: Sequential Assembly of Nanocomposite Materials*; John Wiley & Sons, 2012.

(200) Iler, R. K. Multilayers of Colloidal Particles. *Journal of Colloid and Interface Science* **1966**, *21* (6), 569–594. https://doi.org/10.1016/0095-8522(66)90018-3.

(201) Langmuir, I.; Schaefer, V. J. Composition of Fatty Acid Films on Water Containing Calcium or Barium Salts. *J. Am. Chem. Soc.* **1936**, *58* (2), 284–287. https://doi.org/10.1021/ja01293a028.

(202) Blodgett, K. B. Films Built by Depositing Successive Monomolecular Layers on a Solid Surface. *J. Am. Chem. Soc.* **1935**, *57* (6), 1007–1022. https://doi.org/10.1021/ja01309a011.

(203) Roberts, G. *Langmuir-Blodgett Films*; Springer Science & Business Media, 2013.

(204) Mrksich, M.; Whitesides, G. M. Using Self-Assembled Monolayers to Understand the Interactions of Man-Made Surfaces with Proteins and Cells. *Annu Rev Biophys Biomol Struct* **1996**, *25*, 55–78. https://doi.org/10.1146/annurev.bb.25.060196.000415.

(205) Mrksich, M. A Surface Chemistry Approach to Studying Cell Adhesion. *Chem. Soc. Rev.* **2000**, *29* (4), 267–273. https://doi.org/10.1039/A705397E.

(206) Decher, G. Fuzzy Nanoassemblies: Toward Layered Polymeric Multicomposites. *Science* **1997**, *277* (5330), 1232–1237. https://doi.org/10.1126/science.277.5330.1232.

(207) Decher, G.; Hong, J.-D. Buildup of Ultrathin Multilayer Films by a Self-Assembly Process, 1 Consecutive Adsorption of Anionic and Cationic Bipolar Amphiphiles on Charged Surfaces. *Makromolekulare Chemie. Macromolecular Symposia* **1991**, *46* (1), 321–327. https://doi.org/10.1002/masy.19910460145.

(208) Decher, G.; Hong, J. D.; Schmitt, J. Buildup of Ultrathin Multilayer Films by a Self-Assembly Process: III. Consecutively Alternating Adsorption of Anionic and Cationic Polyelectrolytes on Charged Surfaces. *Thin Solid Films* **1992**, *210–211*, 831–835. https://doi.org/10.1016/0040-6090(92)90417-A.

(209) Decher, G.; Lehr, B.; Lowack, K.; Lvov, Y.; Schmitt, J. New Nanocomposite Films for Biosensors: Layer-by-Layer Adsorbed Films of Polyelectrolytes, Proteins or DNA. *Biosensors and Bioelectronics* **1994**, *9* (9), 677–684. https://doi.org/10.1016/0956-5663(94)80065-0.

(210) Lvov, Y.; Ariga, K.; Kunitake, T. Layer-by-Layer Assembly of Alternate Protein/Polyion Ultrathin Films. *Chem. Lett.* **1994**, *23* (12), 2323–2326. https://doi.org/10.1246/cl.1994.2323.

(211) Lvov, Y.; Haas, H.; Decher, G.; Moehwald, H.; Mikhailov, A.; Mtchedlishvily, B.; Morgunova, E.; Vainshtein, B. Successive Deposition of Alternate Layers of Polyelectrolytes and a Charged Virus. *Langmuir* **1994**, *10* (11), 4232–4236. https://doi.org/10.1021/la00023a052.

(212) Kleinfeld, E. R.; Ferguson, G. S. Stepwise Formation of Multilayered Nanostructural Films from Macromolecular Precursors. *Science* **1994**, *265* (5170), 370–373. https://doi.org/10.1126/science.265.5170.370.

(213) Keller, S. W.; Kim, H.-N.; Mallouk, T. E. Layer-by-Layer Assembly of Intercalation Compounds and Heterostructures on Surfaces: Toward Molecular “Beaker” Epitaxy. *J. Am. Chem. Soc.* **1994**, *116* (19), 8817–8818. https://doi.org/10.1021/ja00098a055.

(214) Kotov, N. A.; Dekany, I.; Fendler, J. H. Layer-by-Layer Self-Assembly of Polyelectrolyte-Semiconductor Nanoparticle Composite Films. *J. Phys. Chem.* **1995**, *99* (35), 13065–13069. https://doi.org/10.1021/j100035a005.

(215) Schmitt, J.; Decher, G.; Dressick, W. J.; Brandow, S. L.; Geer, R. E.; Shashidhar, R.; Calvert, J. M. Metal Nanoparticle/Polymer Superlattice Films: Fabrication and Control of Layer Structure. *Advanced Materials* **1997**, *9* (1), 61–65. https://doi.org/10.1002/adma.19970090114.

(216) Keller, S. W.; Johnson, S. A.; Brigham, E. S.; Yonemoto, E. H.; Mallouk, T. E. Photoinduced Charge Separation in Multilayer Thin Films Grown by Sequential Adsorption of Polyelectrolytes. *J. Am. Chem. Soc.* **1995**, *117* (51), 12879–12880. https://doi.org/10.1021/ja00156a034.

(217) Gittins, D. I.; Caruso, F. Multilayered Polymer Nanocapsules Derived from Gold Nanoparticle Templates. *Advanced Materials* **2000**, *12* (24), 1947–1949. https://doi.org/10.1002/1521-4095(200012)12:24<1947::AID-ADMA1947>3.0.CO;2-8.

(218) Gittins, D. I.; Caruso, F. Tailoring the Polyelectrolyte Coating of Metal Nanoparticles. *J. Phys. Chem. B* **2001**, *105* (29), 6846–6852. https://doi.org/10.1021/jp0111665.

(219) Schneider, G.; Decher, G.; Nerambourg, N.; Praho, R.; Werts, M. H. V.; Blanchard-Desce, M. Distance-Dependent Fluorescence Quenching on Gold Nanoparticles Ensheathed with Layer-by-Layer Assembled Polyelectrolytes. *Nano Lett.* **2006**, *6* (3), 530–536. https://doi.org/10.1021/nl052441s.

(220) Schneider, G. F.; Subr, V.; Ulbrich, K.; Decher, G. Multifunctional Cytotoxic Stealth Nanoparticles. A Model Approach with Potential for Cancer Therapy. *Nano Lett.* **2009**, *9* (2), 636–642. https://doi.org/10.1021/nl802990w.

(221) Richardson, J. J.; Bjornmalm, M.; Caruso, F. Technology-Driven Layer-by-Layer Assembly of Nanofilms. *Science* **2015**, *348* (6233), aaa2491–aaa2491. https://doi.org/10.1126/science.aaa2491.

(222) Gill, R.; Mazhar, M.; Félix, O.; Decher, G. Covalent Layer-by-Layer Assembly and Solvent Memory of Multilayer Films from Homobifunctional Poly(Dimethylsiloxane). *Angewandte Chemie International Edition* **2010**, *49* (35), 6116–6119. https://doi.org/10.1002/anie.200907161.

(223) Sun, J.; Wu, T.; Liu, F.; Wang, Z.; Zhang, X.; Shen, J. Covalently Attached Multilayer Assemblies by Sequential Adsorption of Polycationic Diazo-Resins and Polyanionic Poly(Acrylic Acid). *Langmuir* **2000**, *16* (10), 4620–4624. https://doi.org/10.1021/la991482z.

(224) Wang, L.; Wang, Z.; Zhang, X.; Shen, J.; Chi, L.; Fuchs, H. A New Approach for the Fabrication of an Alternating Multilayer Film of Poly(4-Vinylpyridine) and Poly(Acrylic

Acid) Based on Hydrogen Bonding. *Macromolecular Rapid Communications* **1997**, *18* (6), 509–514. https://doi.org/10.1002/marc.1997.030180609.

(225) Kharlampieva, E.; Kozlovskaya, V.; Sukhishvili, S. A. Layer-by-Layer Hydrogen-Bonded Polymer Films: From Fundamentals to Applications. *Advanced Materials* **2009**, *21* (30), 3053–3065. https://doi.org/10.1002/adma.200803653.

(226) Stockton, W. B.; Rubner, M. F. Molecular-Level Processing of Conjugated Polymers. 4. Layer-by-Layer Manipulation of Polyaniline via Hydrogen-Bonding Interactions. *Macromolecules* **1997**, *30* (9), 2717–2725. https://doi.org/10.1021/ma9700486.

(227) Wang, F.; Ma, N.; Chen, Q.; Wang, W.; Wang, L. Halogen Bonding as a New Driving Force for Layer-by-Layer Assembly. *Langmuir* **2007**, *23* (19), 9540–9542. https://doi.org/10.1021/la701969q.

(228) Serizawa, T.; Yamashita, K.; Akashi, M. Unique Physical Adsorption of Proteins onto Double Stranded Stereocomplex Films Composed of Stereoregular Poly(Methyl Methacrylate)s. *Polymer Journal* **2006**, *38* (5), 503–506. https://doi.org/10.1295/polymj.38.503.

(229) Schomaker, E.; Challa, G. Complexation of Stereoregular Poly(Methyl Methacrylates). 14. The Basic Structure of the Stereocomplex of Isotactic and Syndiotactic Poly(Methyl Methacrylate). *Macromolecules* **1989**, *22* (8), 3337–3341. https://doi.org/10.1021/ma00198a025.

(230) Xiong, H.; Cheng, M.; Zhou, Z.; Zhang, X.; Shen, J. A New Approach to the Fabrication of a Self-Organizing Film of Heterostructured Polymer/Cu2S Nanoparticles. *Advanced Materials* **1998**, *10* (7), 529–532. https://doi.org/10.1002/(SICI)1521-4095(199805)10:7<529::AID-ADMA529>3.0.CO;2-E.

(231) Hao, E.; Wang, L.; Zhang, J.; Yang, B.; Zhang, X.; Shen, J. Fabrication of Polymer/Inorganic Nanoparticles Composite Films Based on Coordinative Bonds. *Chem. Lett.* **1999**, *28* (1), 5–6. https://doi.org/10.1246/cl.1999.5.

(232) Schlenoff, J. B.; Dubas, S. T.; Farhat, T. Sprayed Polyelectrolyte Multilayers. *Langmuir* **2000**, *16* (26), 9968–9969. https://doi.org/10.1021/la001312i.

(233) Chiarelli, P. A.; Johal, M. S.; Casson, J. L.; Roberts, J. B.; Robinson, J. M.; Wang, H.-L. Controlled Fabrication of Polyelectrolyte Multilayer Thin Films Using Spin-Assembly. *Advanced Materials* **2001**, *13* (15), 1167–1171. https://doi.org/10.1002/1521-4095(200108)13:15<1167::AID-ADMA1167>3.0.CO;2-A.

(234) Chiarelli, P. A.; Johal, M. S.; Holmes, D. J.; Casson, J. L.; Robinson, J. M.; Wang, H.-L. Polyelectrolyte Spin-Assembly. *Langmuir* **2002**, *18* (1), 168–173. https://doi.org/10.1021/la011333s.

(235) Sun, J.; Gao, M.; Feldmann, J. Electric Field Directed Layer-by-Layer Assembly of Highly Fluorescent CdTe Nanoparticles. *Journal of Nanoscience and Nanotechnology* **2001**, *1* (2), 133–136. https://doi.org/10.1166/jnn.2001.029.

(236) Hong, X.; Li, J.; Wang, M.; Xu, J.; Guo, W.; Li, J.; Bai, Y.; Li, T. Fabrication of Magnetic Luminescent Nanocomposites by a Layer-by-Layer Self-Assembly Approach. *Chem. Mater.* **2004**, *16* (21), 4022–4027. https://doi.org/10.1021/cm049422o.

(237) Picart, C.; Lavalle, Ph.; Hubert, P.; Cuisinier, F. J. G.; Decher, G.; Schaaf, P.; Voegel, J.-C. Buildup Mechanism for Poly(l-Lysine)/Hyaluronic Acid Films onto a Solid Surface. *Langmuir* **2001**, *17* (23), 7414–7424. https://doi.org/10.1021/la010848g.

(238) Han, J. T.; Zheng, Y.; Cho, J. H.; Xu, X.; Cho, K. Stable Superhydrophobic Organic-Inorganic Hybrid Films by Electrostatic Self-Assembly. *J Phys Chem B* **2005**, *109* (44), 20773–20778. https://doi.org/10.1021/jp052691x.

(239) Lee, D.; Rubner, M. F.; Cohen, R. E. All-Nanoparticle Thin-Film Coatings. *Nano Lett.* **2006**, *6* (10), 2305–2312. https://doi.org/10.1021/nl061776m.

(240) Wang, Y.; Tang, Z.; Podsiadlo, P.; Elkasabi, Y.; Lahann, J.; Kotov, N. A. Mirror-Like Photoconductive Layer-by-Layer Thin Films of Te Nanowires: The Fusion of Semiconductor, Metal, and Insulator Properties. *Advanced Materials* **2006**, *18* (4), 518–522. https://doi.org/10.1002/adma.200501465.

(241) Fou, A. C.; Onitsuka, O.; Ferreira, M.; Rubner, M. F.; Hsieh, B. R. Fabrication and Properties of Light-emitting Diodes Based on Self-assembled Multilayers of Poly(Phenylene Vinylene). *Journal of Applied Physics* **1996**, *79* (10), 7501–7509. https://doi.org/10.1063/1.362421.

(242) Lvov, Y.; Yamada, S.; Kunitake, T. Non-Linear Optical Effects in Layer-by-Layer Alternate Films of Polycations and an Azobenzene-Containing Polyanion. *Thin Solid Films* **1997**, *300* (1), 107–112. https://doi.org/10.1016/S0040-6090(96)09494-1.

(243) Liu, S.; Kurth, D. G.; Möhwald, H.; Volkmer, D. A Thin-Film Electrochromic Device Based on a Polyoxometalate Cluster. *Advanced Materials* **2002**, *14* (3), 225–228. https://doi.org/10.1002/1521-4095(20020205)14:3<225::AID-ADMA225>3.0.CO;2-F.

(244) Agrios, A. G.; Cesar, I.; Comte, P.; Nazeeruddin, M. K.; Grätzel, M. Nanostructured Composite Films for Dye-Sensitized Solar Cells by Electrostatic Layer-by-Layer Deposition. *Chem. Mater.* **2006**, *18* (23), 5395–5397. https://doi.org/10.1021/cm061679u.

(245) Cui, T.; Liu, Y.; Zhu, M. Field-Effect Transistors with Layer-by-Layer Self-Assembled Nanoparticle Thin Films as Channel and Gate Dielectric. *Appl. Phys. Lett.* **2005**, *87* (18), 183105. https://doi.org/10.1063/1.2123390.

(246) Tang, Z.; Wang, Y.; Podsiadlo, P.; Kotov, N. A. Biomedical Applications of Layer-by-Layer Assembly: From Biomimetics to Tissue Engineering. *Adv. Mater.* **2006**, *18* (24), 3203–3224. https://doi.org/10.1002/adma.200600113.

(247) Cini, N.; Tulun, T.; Decher, G.; Ball, V. Step-by-Step Assembly of Self-Patterning Polyelectrolyte Films Violating (Almost) All Rules of Layer-by-Layer Deposition. *J. Am. Chem. Soc.* **2010**, *132* (24), 8264–8265. https://doi.org/10.1021/ja102611q.

(248) Zhang, L.; Sun, J. Layer-by-Layer Deposition of Polyelectrolyte Complexes for the Fabrication of Foam Coatings with High Loading Capacity. *Chem. Commun.* **2009**, No. 26, 3901. https://doi.org/10.1039/b907691c.

(249) Tang, Z.; Kotov, N. A.; Magonov, S.; Ozturk, B. Nanostructured Artificial Nacre. *Nature Mater* **2003**, *2* (6), 413–418. https://doi.org/10.1038/nmat906.

(250) Schneider, G.; Decher, G. From Functional Core/Shell Nanoparticles Prepared via Layer-by-Layer Deposition to Empty Nanospheres. *Nano Lett.* **2004**, *4* (10), 1833–1839. https://doi.org/10.1021/nl0490826.

(251) Nogueira, G. M.; Banerjee, D.; Cohen, R. E.; Rubner, M. F. Spray-Layer-by-Layer Assembly Can More Rapidly Produce Optical-Quality Multistack Heterostructures. *Langmuir* **2011**, *27* (12), 7860–7867. https://doi.org/10.1021/la200790g.

(252) Circular Dichroism https://chem.libretexts.org/Bookshelves/Physical_and_Theoretical_Chemistry_Textbook_Maps/Supplemental_Modules_(Physical_and_Theoretical_Chemistry)/Spectroscopy/Electronic_Spectroscopy/Circular_Dichroism (accessed Aug 3, 2020).

(253) Schubert, M. Polarization-Dependent Optical Parameters of Arbitrarily Anisotropic Homogeneous Layered Systems. *Phys. Rev. B* **1996**, *53* (8), 4265–4274. https://doi.org/10.1103/PhysRevB.53.4265.

(254) Palik, E. D. *Handbook of Optical Constants of Solids*; Academic Press, 1998.

(255) Scanning Electron Microscope. *Wikipedia*; 2020. https://en.wikipedia.org/wiki/Scanning_electron_microscope (accessed Sept 13, 2020)

(256) Claudionico~commonswiki. *English: Illustration of the Phenomena That Occur from the Interaction of Highly Energetic Electrons with Matter, Also Depicting the Pear Shape Interaction Volume Which Is Typically Observed in This Type of Interactions.*; 2013.

(257) Lemaire, V. Dépôts Alignés de Nanofils d'argent Au Sein de Films Multicouches Pour Des Propriétés Conductrices et Optiques. These de doctorat, Strasbourg, 2017.

(258) von Berlepsch, H.; Böttcher, C.; Ouart, A.; Burger, C.; Dähne, S.; Kirstein, S. Supramolecular Structures of *J* -Aggregates of Carbocyanine Dyes in Solution. *J. Phys. Chem. B* **2000**, *104* (22), 5255–5262. https://doi.org/10.1021/jp000220z.

(259) Kirstein, S.; Bourbon, S.; Gao, M.; De Rossi, U. Layer-by-Layer Deposition of J-Aggregates and Polyelectrolytes for Electroluminescence Applications: A Spectroscopic Study. *Isr. J. Chem.* **2000**, *40* (2), 129–138. https://doi.org/10.1560/4CGH-9ECB-9VFK-1PL6.

(260) FEW Chemicals GmbH: 400-599 nm https://www.few.de/en/menue-oben/spezialchemikalien/funktionelle-farbstoffe/loesungsmittelloesliche-cyanine/400-599-nm/ (accessed Oct 26, 2020).

(261) Cataldo, F. Synthesis and Study of Electronic Spectra of Planar Polymeric Phthalocyanines. *Dyes and Pigments* **1997**, *34* (1), 75–85. https://doi.org/10.1016/S0143-7208(96)00059-9.

(262) Cheng, J.; Le Saux, G.; Gao, J.; Buffeteau, T.; Battie, Y.; Barois, P.; Ponsinet, V.; Delville, M.-H.; Ersen, O.; Pouget, E.; Oda, R. GoldHelix: Gold Nanoparticles Forming 3D Helical Superstructures with Controlled Morphology and Strong Chiroptical Property. *ACS Nano* **2017**, *11* (4), 3806–3818. https://doi.org/10.1021/acsnano.6b08723.

(263) Hutchison, J. A.; Schwartz, T.; Genet, C.; Devaux, E.; Ebbesen, T. W. Modifying Chemical Landscapes by Coupling to Vacuum Fields. *Angewandte Chemie International Edition* **2012**, *51* (7), 1592–1596. https://doi.org/10.1002/anie.201107033.

(264) Thomas, A.; George, J.; Shalabney, A.; Dryzhakov, M.; Varma, S. J.; Moran, J.; Chervy, T.; Zhong, X.; Devaux, E.; Genet, C.; Hutchison, J. A.; Ebbesen, T. W. Ground-State Chemical Reactivity under Vibrational Coupling to the Vacuum Electromagnetic Field. *Angewandte Chemie* **2016**, *128* (38), 11634–11638. https://doi.org/10.1002/ange.201605504.

Wenbing WU

Propriétés optiques de films minces plasmoniques hybrides à superstructure chirale contrôlée

Résumé:

Cette thèse présente l'étude des propriétés optiques de superstructures plasmoniques chirales composées de nanofils d'argent alignés par pulvérisation à incidence rasante (GIS) et organisés en structures multicouche par assemblage couche-par-couche (LbL). Cette approche permet d'obtenir des superstructures multicouches hélicoïdales avec des propriétés optiques reproductibles et modulables en contrôlant précisément l'organisation des nanoobjets. Les propriétés optiques sont systématiquement caractérisées par différentes méthodes (spectroscopie de dichroïsme circulaire et polarimétrie à matrice de Mueller en particulier) et modélisées par matrices de transfert en utilisant le formalisme de Berreman. Les superstructures chirales présentent un dichroïsme circulaire extrêmement élevé (au-delà de 10 000 mdeg). Ces structures peuvent également modifier fortement les propriétés de molécules achirales situées dans leur voisinage par couplage entre les nanofils d'argent et la molécule, avec une influence prépondérante de la position du colorant dans la superstructure.

Mots-clés: *chiralité, nanofils d'argent, pulvérisation à incidence rasante, assemblage couche-par-couche, dichroïsme circulaire, métamatériaux hybrides*

Abstract:

This thesis presents the study of the optical properties of chiral plasmonic superstructures composed of silver nanowires aligned by grazing incidence spraying (GIS) and organized in multilayer structures by Layer-by-Layer (LbL) assembly. This approach allows to obtain helical multilayer superstructures with reproducible and tunable optical properties by precisely controlling the organization of the nanoobjects. The optical properties are systematically characterized by different methods (in particular circular dichroism spectroscopy and Mueller matrix polarimetry) and modelled by transfer matrices using the Berreman formalism. The chiral superstructures present an extremely high circular dichroism (above 10,000 mdeg). These structures can also strongly modify the properties of achiral molecules placed in their vicinity by coupling between the silver nanowires and the molecule, with a preponderant influence of the position of the dye in the superstructure.

Keywords: *chirality, silver nanowires, grazing incidence spraying, Layer-by-Layer assembly, circular dichroism, hybrid metamaterials*